ABSTRACT

Title of thesis: INVESTIGATION INTO THE EFFECTS OF AEOLIAN SCALING PARAMETERS ON SEDIMENT MOBILIZATION BELOW A HOVERING ROTOR

Ajay Baharani, Master of Science, 2011

Thesis directed by: Professor J. Gordon Leishman
Department of Aerospace Engineering

Flow visualization and particle image velocimetry (PIV) experiments were conducted on a small-scale rotor hovering over a ground plane covered with a mobile sediment bed to help understand the effects of certain selected scaling parameters on the processes of sediment mobilization, entrainment, and uplift as induced by the rotor. Flow visualization using high-speed videography was used to study the rotor flow structures, their evolution in the rotor wake, and their interaction with the ground plane. Time-resolved PIV measurements of the rotor wake flow at the sediment bed quantified the flow velocities where most of the sediment mobilization was observed to occur. Dual-phase PIV experiments were conducted using ten different sediment samples of known characteristics to vary the values of five of the similarity parameters: 1. Particle diameter-to-rotor radius ratio, 2. Particle-to-fluid density ratio, 3. Ratio of characteristic flow (or wind) speed to particle terminal speed, 4. Densimetric Froude number, and 5. Threshold friction velocity ratio. The particle-to-fluid density ratio was shown to have the greatest effect on the resulting two-phase flow, followed by the threshold friction velocity ra-

tio. The flow was also sensitive to changes in the particle diameter-to-rotor radius ratio. Changes in the densimetric Froude number and ratio of the characteristic flow speed to particle terminal speed also showed good correlations to observations of the quantity of uplifted particles. The effects of the passage of the tip vortex near the bed was shown to increase the shear stresses on the bed, which was observed to be closely correlated to an increase in the quantity of entrained sediment particles if the threshold conditions for particle mobility was exceeded. The observations and results were used to make recommendations regarding scaling on dual-phase experiments to better simulate the problem of rotorcraft brownout in the laboratory environment.

EFFECTS OF AEOLIAN SCALING PARAMETERS ON SEDIMENT MOBILIZATION BELOW A HOVERING ROTOR

by

Ajay Baharani

Thesis submitted to the Faculty of the Graduate School of the
University of Maryland, College Park in partial fulfillment
of the requirements for the degree of
Master of Science
2011

Advisory Committee:
Professor J. Gordon Leishman, Chair/Advisor
Associate Professor James D. Baeder
Assistant Professor Anya R. Jones

Acknowledgments

First I would like to thank my advisor, Professor J. Gordon Leishman, for giving me the opportunity to work under his guidance on this project. I have learned so much from him during my time as a graduate student at the University of Maryland, and it was a privilege to have worked in his lab.

I would like to thank Dr. Anya Jones and Dr. James Baeder for their contributions and for serving as members of my thesis committee.

I would also like to thank the entire faculty and staff of the Aerospace Department. It has been a privilege to have done my undergraduate and graduate work here in this prestigious program.

Special thanks to Anish Sydney for his mentorship, expertise, and humor. I don't think I would have had as much fun on Team Dust Chamber if it weren't for him.

I want to thank everyone on Team Leishman: Bharath Govindarajan, Monica Syal, Joe Ramsey, Ben Hance, Joe Milluzzo, Dave Mayo, Jaime Reel, Juergen Rauleder, Grant Barrett, Nick Amen, Harrison Chau, Natalie Jones, and Nate Doane. It's because of you guys that coming to work everyday was fun and memorable.

A very special thanks to Sharada for always being there for me and supporting me through the hardest of times. I couldn't have done this without her supporting me every step of the way.

Finally I want to thank my family: Mom, Dad, Grandma, Reena, Vijay, and Sunny. Their unwavering love and support has allowed me to accomplish what I have in life and has made me who I am today. Words can never express what they have done for me.

Table of Contents

List of Tables vii

List of Figures vii

Nomenclature xv

1 Introduction 1

1.1 Background to the Problem of Brownout 1

1.2 Physics of Brownout 5

1.2.1 Flow Physics 7

1.2.2 Particle Physics 10

1.3 Principles of Sediment Transport 10

1.3.1 Threshold Criteria 12

1.3.2 Shields Parameter 13

1.3.3 Saltation 13

1.3.4 Vortex Induced Sediment Trapping 14

1.3.5 Bombardment 15

1.4 Consideration for Scaling of the Brownout Problem 17

1.4.1 Scaling of the Carrier Phase 18

1.4.2 Scaling of Dispersed Phase 20

1.5 Objectives of the Present Work 22

1.6 Organization of Thesis 23

2 Description of the Experiments 25

2.1 Overview . . . 25

2.2 Experimental Setup . . . 26

2.2.1 Rotor System and Ground Plane . . . 26

2.2.2 Dust Chamber . . . 29

2.2.3 Regions of Interest . . . 31

2.3 Time-Resolved Flow Visualization . . . 32

2.4 Particle Image Velocimetry . . . 34

2.4.1 Method of PIV . . . 34

2.4.2 Phase-Resolved PIV . . . 37

2.4.3 Time-Resolved PIV . . . 38

2.4.4 Dual-Phase PIV . . . 39

2.4.5 Particle Recognition Technique . . . 41

2.4.6 Challenges in the Flow Measurements . . . 43

2.4.7 Uncertainties in PIV Measurements . . . 45

2.4.8 Particle Identification Errors . . . 46

2.5 Summary . . . 48

3 Results and Discussion 49

3.1 Overview . . . 49

3.2 Time-Resolved Flow Visualization . . . 49

3.2.1 Single-Phase Flow Visualization . . . 50

3.2.2 Dual-Phase Flow Visualization . . . 55

3.2.3 Summary . . . 57
3.3 Phase-Resolved PIV Results . . . 57
3.3.1 Vortex Characteristics . . . 58
3.3.2 Wall Flow Characteristics . . . 62
3.3.3 Summary . . . 67
3.4 Time-Resolved PIV Results . . . 68
3.4.1 Time-Averaged Wall Flow . . . 69
3.4.2 Particle Characteristics . . . 70
3.4.3 Dual-Phase TR-PIV Results . . . 79
3.4.4 Effect of Particle Size on Entrainment . . . 88
3.4.5 Effect of Density Ratio on Entrainment . . . 89
3.4.6 Effect of Particle Terminal Velocity . . . 91
3.4.7 Effect of Froude Number . . . 94
3.4.8 Effect of Threshold Friction Velocity on Sediment Entrainment . 95
3.4.9 Friction Velocity at the Ground . . . 100
3.4.10 Summary . . . 135
3.5 Ranking of Similarity Parameters . . . 136
3.6 Summary . . . 137

4 Conclusions 139
4.1 Summary . . . 139
4.2 Specific Conclusions . . . 141
4.3 Suggestions for Future Work . . . 144

4.3.1 Measurements of Threshold Friction Velocity 144

4.3.2 Effects of Unsteadiness 145

4.3.3 Phase Separation 145

4.3.4 Selection of Sediment Particles 147

4.3.5 Experiments in Water 147

A Mineral Composition for Naturally Occurring Sediment Samples 149

B Particle Sizing Data 151

C Estimation of Full-Scale Similarity Parameters 192

Bibliography 194

List of Tables

1.1 Nondimensional similarity parameters for aeolian transport. 21

3.1 Calculated mean particle size and mass density measurements for each sediment sample. 78

3.2 Calculated similarity parameters for each sediment sample for this flow. . 87

3.3 Calculated velocity gradient, wall shear stress, and friction velocity before ($\psi = 160°$) and during ($\psi = 210°$) the passage of a tip vortex. 104

A.1 Mineral content of the naturally occurring sediment samples as determined by X-ray diffraction. 150

B.1 Method used to determine PSD for each sediment sample. 151

C.1 Values of the dimensional variables at full-scale for a CH-54. 192

C.2 Values of similarity parameters at full-scale for a CH-54. 192

List of Figures

1.1 A helicopter encountering brownout conditions during a landing maneuver. (Courtesy of Optical Air Data Systems LLC.) 2

1.2 A schematic of some of the fluid dynamic mechanisms involved in the uplift and transport of sediment in the development of brownout conditions. 5

1.3 A toroidal brownout cloud produced by a helicopter. (Courtesy of AWI). . 6

1.4 Flow visualization images of a two-bladed rotor operating IGE and OGE [1]. 9

1.5 Forces acting on a particle while in a mobile sediment bed and while in suspension. 11
1.6 Mechanisms of sediment entrainment in brownout [2]. 12
1.7 Schematic of particles undergoing saltation and creep. 14
1.8 Schematic of vortex induced trapping mechanism. 15
1.9 Local bombardment in a vortex flow. 16

2.1 Photograph of the rotor blade and its principal dimensions. 26
2.2 Schematic showing the components of the small-scale rotor system used for the present experiments. 27
2.3 Schematic of the experimental setup. 28
2.4 Dust chamber facility used to conduct flow diagnostic experiments. 30
2.5 Schematic showing the flow regions of interest. 32
2.6 Schematic showing PIV methodology. 36
2.7 Particles were identified by connecting neighboring pixels that met the intensity threshold. 43
2.8 Reduction of laser light reflections near the ground by better alignment of the laser light sheet. 45

3.1 Single-phase flow visualization of a rotor in ground effect, $z/R = 1.0$. . . . 51
3.2 Flow visualization of the rotor flow in ground effect at a blade azimuth angle of $\psi = 0^\circ$ to show the relatively low levels of aperiodicity and the repeatability of the flow induced by a one-bladed rotor at wake ages of $\xi = 360^\circ$, 720°, and 1080°. 52

3.3 Flow visualization of near wall region, $y/R = 1.75$ to $y/R = 2.60$. 54

3.4 Dual-phase flow visualization with a sediment bed consisting of 45–63 μm glass microspheres on the ground plane. 55

3.5 Circulation box method used to estimate the circulation of a vortex. . . . 59

3.6 Integration process around the vortex (in this case at $\xi = 210^\circ$) to estimate its circulation. 59

3.7 PIV velocity field of a vortex at a wake age of $\xi = 210^\circ$ and the resulting swirl velocity profile. 61

3.8 Phase-averaged velocity fields of the wall-parallel velocity shown for blade azimuth angles of $\psi = 0^\circ$ to 150° in 30° increments. 63

3.8 (Cont'd) Phase-averaged velocity fields of the wall-parallel velocity shown for blade azimuth angles of $\psi = 180^\circ$ to 330° in 30° increments. 64

3.9 Fluctuation of flow velocity profile at the ground at $y/R = 2.07$ with the passage of a tip vortex at blade azimuth angles of $\psi = 0^\circ$, 150°, 330°. . . 66

3.10 Contour plot of time-averaged wall flow in ROI 2. 70

3.11 PSD and microscope image of the 1–38 μm microspheres. 74

3.12 PSD and microscope image of the 45–63 μm microspheres. 74

3.13 PSD and microscope image of the 90–125 μm microspheres. 75

3.14 PSD and microscope image of the kaolinite sediment sample. 75

3.15 PSD and microscope image of the Arizona Test Dust 0–5 μm sediment sample. 76

3.16 PSD and microscope image of the Arizona Test Dust 0–10 μm sediment sample. 76

3.17 PSD and microscope image of the Ottawa sand sediment sample. 77
3.18 Combined PSDs of the glass microsphere particles. 77
3.19 Example of process used to generate particle concentration maps. 80
3.20 Particle concentration maps showing the variance in the quantity and location of particles uplifted between glass microsphere sediment samples. . 81
3.20 (Cont'd) Particle concentration maps showing the variance in the quantity and location particles uplifted between the naturally occurring sediment samples. Images are from ROI 2. 82
3.21 Time-averaged particle concentration maps. 84
3.21 (Cont'd) Time-averaged particle concentration maps. 85
3.22 Normalized quantity of uplifted particles plotted against the particle diameter-to-rotor radius ratio, D_p/R. 88
3.23 Normalized quantity of uplifted particles plotted against the particle-to-fluid density ratio, ρ_s/ρ. 90
3.24 Normalized number of sediment particles plotted against the characteristic velocity-to-terminal velocity ratio. 93
3.25 Number of sediment particles plotted against the densimetric Froude number. 95
3.26 Particle uplift versus threshold friction velocity using Shao-Lu model. . . 96
3.27 Threshold friction velocity plotted against particle size using three different models. 98
3.28 Particle uplift versus threshold friction velocity using Greeley model. . . . 99
3.29 Particle uplift versus threshold friction velocity using Bagnold model. . . 100

3.30 turbulent shear stress profile. 102

3.31 Schematic of the velocity profile at the ground and the laminar sublayer region. 103

3.32 Unsteady excursions in the wall flow velocity profile from the passage of a tip vortex at $y/R = 2.0$. 104

3.33 Friction velocity, u_* plotted with threshold friction velocity values for kaolinite at $y/R = 2.0$. 105

3.34 Velocity profile before the passage of a vortex at $y/R = 2.0$ and corresponding dual-phase measurement using kaolinite. 106

3.35 Velocity profile during the passage of a vortex at $y/R = 2.0$ and corresponding dual-phase measurement using kaolinite. 107

3.36 Particle concentration maps of kaolinite before and during the passage of a tip vortex at $y/R = 2.0$. 108

3.37 Friction velocity at $y/R = 2.0$ versus degrees of blade rotation. Lines denoting the threshold friction velocity for Ottawa sand using three models are also given. 110

3.38 Velocity profile before the passage of a vortex at $y/R = 2.0$ and corresponding dual-phase measurement with Ottawa sand. 111

3.39 Velocity profile during the passage of a vortex at $y/R = 2.0$ and corresponding dual-phase measurement with Ottawa sand. 112

3.40 Particle concentration maps of Ottawa sand before and during the passage of a tip vortex at $y/R = 2.0$. 113

3.41 Friction velocity at y/R = 2.0. Threshold friction velocity for 1–38 μm glass microspheres using three models is also given. 115

3.42 Friction velocity at y/R = 2.0. Threshold friction velocity for 45–53 μm glass microspheres using three models is also given. 115

3.43 Friction velocity at y/R = 2.0. Threshold friction velocity for 53–63 μm glass microspheres using three models is also given. 116

3.44 Friction velocity at y/R = 2.0. Threshold friction velocity for 45–63 μm glass microspheres using three models is also given. 116

3.45 Friction velocity at y/R = 2.0. Threshold friction velocity for 90–106 μm glass microspheres using three models is also given. 117

3.46 Friction velocity at y/R = 2.0. Threshold friction velocity for 90–125 μm glass microspheres using three models is also given. 117

3.47 Friction velocity at y/R = 2.0 versus degrees of blade rotation. Threshold friction velocity for AZTD 0–5 μm particles using three models is also given. 118

3.48 Friction velocity at y/R = 2.0 versus degrees of blade rotation. Threshold friction velocity for AZTD 0–10 μm particles using three models is also given. 118

3.49 Dual-phase measurement with 1–38 μm diameter glass microspheres before and during the passage of a tip vortex 119

3.50 Particle concentration maps of 1–38 μm diameter glass microspheres before and during the passage of a tip vortex at y/R = 2.0. 120

3.51 Dual-phase measurement with 45–53 μm diameter glass microspheres before and during the passage of a tip vortex 121

3.52 Particle concentration maps of 45–53 μm diameter glass microspheres before and during the passage of a tip vortex at $y/R = 2.0$. 122

3.53 Dual-phase measurement with 53–63 μm diameter glass microspheres before and during the passage of a tip vortex 123

3.54 Particle concentration maps of 53–63 μm diameter glass microspheres before and during the passage of a tip vortex at $y/R = 2.0$. 124

3.55 Dual-phase measurement with 45–63 μm diameter glass microspheres before and during the passage of a tip vortex 125

3.56 Particle concentration maps of 45–63 μm diameter glass microspheres before and during the passage of a tip vortex at $y/R = 2.0$. 126

3.57 Dual-phase measurement with 90–106 μm diameter glass microspheres before and during the passage of a tip vortex 127

3.58 Particle concentration maps of 90–106 μm diameter glass microspheres before and during the passage of a tip vortex at $y/R = 2.0$. 128

3.59 Dual-phase measurement with 90–125 μm diameter glass microspheres before and during the passage of a tip vortex 129

3.60 Particle concentration maps of 90–125 μm diameter glass microspheres before and during the passage of a tip vortex at $y/R = 2.0$. 130

3.61 Dual-phase measurement with AZTD 0–5 μm diameter particles before and during the passage of a tip vortex 131

3.62 Particle concentration maps of AZTD 0–5 μm diameter glass microspheres before and during the passage of a tip vortex at $y/R = 2.0$. 132

3.63 Dual-phase measurement with AZTD 0–10 μm diameter particles before and during the passage of a tip vortex 133

3.64 Particle concentration maps of AZTD 0–10 μm diameter glass microspheres before and during the passage of a tip vortex at $y/R = 2.0$. 134

Nomenclature

a	speed of sound, ms^{-1}
A	particle cross-sectional area, m^{-2}
c_{tip}	chord length at blade tip, m
C	contour of integration
C_D	particle drag coefficient
C_T	thrust coefficient = $T/\rho\pi\Omega^2 R^4$
d	sediment bed deflation or deposition, m
D	aerodynamic drag force, N
D_p	particle diameter, m
e	coefficient of restitution
F^*	densimetric Froude number = $U_{\mathrm{char}}/\sqrt{(\rho_s\rho - 1)gD_p}$
F_b	buoyancy force, N
g	gravitational acceleration, ms^{-2}
I	pixel intensity, (grayscale value)
I_d	dispersed phase image subset, (grayscale value)
I_{thresh}	threshold intensity, (grayscale value)
L^*	Monin-Obhukov atmospheric stability length, m
L_i	all other topographical horizontal dimensions, m
M	magnification factor, $\mathrm{m\,pixel}^{-1}$
M_{tip}	blade tip Mach number
R	rotor radius, m
$\mathbf{R}$	particle location, m

Re_p	particle Reynolds number = $\rho U_F D_p/\mu$
Re_{tip}	blade tip Reynolds number = $\rho V_{\text{tip}} c_{\text{tip}}/\mu$
Re_v	vortex Reynolds number = Γ/ν
t	time, s
u_*	friction velocity, ms^{-1}
u_{*_t}	threshold friction velocity, ms^{-1}
U	wall parallel velocity, ms^{-1}
u', v'	velocity fluctuations, ms^{-1}
$\overline{U}$, $\overline{V}$	mean velocity, ms^{-1}
U_{avg}	average U velocity, ms^{-1}
U_{char}	characteristic flow velocity, ms^{-1}
U_F	particle terminal (or settling) velocity, ms^{-1}
U_T, V_T	tangential velocities along integration contour, ms^{-1}
V	wall normal velocity, ms^{-1}
$\mathbf{V}$	fluid velocity vector, ms^{-1}
V_{tip}	blade tip speed, ms^{-1}
$V_\theta(r)$	vortex swirl velocity, ms^{-1}
W	particle weight, N
x, y, z	Cartisian coordinate system, m
X_c, Y_c	particle centroid location, m
z	height above ground or sediment bed, m
z^+	nondimensional height in boundary layer
z_o	surface aerodynamic roughness height, m

Greek Symbols

γ	particle cohesiveness, Nm^{-1}
Γ_v	vortex circulation, ms^{-1}
ε_{A_b}	uncertainty in bin area, m^2
$\varepsilon_{\Delta t}$	uncertainty in pulse separation time, s
$\varepsilon_{\Delta x}$	uncertainty of particle displacement in x, m
$\varepsilon_{\Delta X_c}$, $\varepsilon_{\Delta Y_c}$	uncertainty in particle centroid, m
ε_N	uncertainty in number of particles per bin
η	all other topographical vertical dimensions, m
μ	coefficient of dynamic viscosity, $\mathrm{kg\,m}^{-1}\mathrm{s}^{-1}$
ν	coefficient of kinematic viscosity, $\mathrm{m}^2\mathrm{s}^{-1}$
ξ	wake age, deg.
ρ	air density, $\mathrm{kg\,m}^{-3}$
ρ_s	sediment density, $\mathrm{kg\,m}^{-3}$
σ	rotor solidity = $N_b c/\pi R$
σ_p	submerged specific gravity
τ_w	wall shear stress, Nm^{-2}
τ_*	nondimensional shear stress (Shields parameter)
ψ	blade azimuth angle, deg.
Ω	rotational frequency, $\mathrm{rad\,s}^{-1}$

Abbreviations

AZTD	Arizona Test Dust
CCD	charge coupled device
CMOS	complementary metal oxide semiconductor
FFT	Fast Fourier Transform
fps	frames-per-second
FV	flow visualization
MP	megapixel
PIV	particle image velocimetry
PR-PIV	phase-resolved particle image velocimetry
PSD	particle size distribution
ROI	region of interest
TPP	tip path plane
TR-FV	time-resolved flow visualization
TR-PIV	time-resolved particle image velocimetry
XRD	X-ray diffraction

Chapter 1

Introduction

1.1 Background to the Problem of Brownout

The phenomenon of "brownout" has been a continuing problem for rotorcraft that operate in dry, dusty environments. Brownout occurs when a rotorcraft is operating in close proximity to terrain covered with loose sediment such as dust or sand (e.g., during takeoff and landing maneuvers in a desert environment). As the rotor wake interacts with the loose material on the ground, it causes the uplift and suspension of small sediment particles into the air. A helicopter photographed during a landing in which it encounters brownout conditions is shown in Fig. 1.1.

The practical consequence of brownout conditions is that the suspended dust can build to sufficient concentrations such that it leads to a rapid loss of visual references for the pilot and the development of various visual anomalies and vection (apparent motion) illusions, possibly leading to spatial disorientation. Vision is the predominant coordinating sense that pilots rely upon for a safe landing, so being suddenly immersed in a blinding dust cloud can be catastrophic for the pilot if such a situation occurs close to the ground. The loss of visual cues combined with spatial disorientation increases the risk for mishaps such as collisions with nearby objects. In fact, as many as 60% of human-factor related accidents in military helicopters (many of them involving fatalities) have resulted from encounters with brownout conditions [3], although civilian helicopters also suffer

Figure 1.1: A helicopter encountering brownout conditions during a landing maneuver. (Courtesy of Optical Air Data Systems LLC.)

from the problem [4].

In addition to the piloting problems associated with brownout occurrences, other consequences of the dust cloud include a harsh working environment for ground personnel and mechanical wear and tear of vital drivetrain components. Rotor blades, bearings, and engine components all suffer a severely reduced operational life because of the abrasion caused by the sediment particles, creating a serious and costly maintenance issue [5].

Several technical efforts have been undertaken to attempt to mitigate the piloting risks associated with the occurrence of brownout. Much of the work has been focused on developing advanced sensing and display technologies. These sensors are intended to be integrated into the vehicle's avionics package, the intent being to provide vital information to the pilot, allowing the pilot to effectively "see" though the dust cloud during brownout conditions [6–9]. The overarching goal of these important programs is to develop systems

that can increase the situational awareness of the pilot during an encounter with brownout and, therefore, increase the safety of flight.

In addition to the available technical solutions, pilots have adopted certain operational tactics in the form of flight path management to avoid or minimize the impact of the developing brownout cloud on their visibility of the ground and surrounding features. These tactics usually involve flying at high speeds close to the ground to outpace the developing dust cloud, or increasing the rate of descent to try and land before being engulfed in the cloud. Although these tactics are sometimes successful in avoiding the dust cloud, they may not be unique and usually result in "hard" landings in an attempt to get the vehicle on the ground as quickly as possible before brownout conditions develop.

While the role of sensing/display technologies and effective piloting strategies for brownout mitigation should not be underestimated, they do nothing to reduce the intensity or development of the dust cloud, and therefore the maintenance and abrasion issues still remain, reducing mission readiness rates and driving up operational costs. Overall, the problem of brownout is serious enough in terms of loss of life, hull damage, wear and tear on the aircraft, etc. to warrant a detailed scientific study of its characteristics, with the longer-term view of understanding the underlying mechanisms that may lead to its eventual mitigation.

It seems unlikely that future generations of military rotorcraft could be fielded without brownout considerations being part of the constraints imposed during their design. The challenge for the research community is to ultimately understand all aspects of the brownout problem such that mitigation strategies can be properly formulated and eventually practically implemented. Brownout has not yet proved predictable, although this

is not for want of gallant efforts [10–16]. Published dust cloud simulations, while often looking realistic to the casual observer, are but tentative. When examined critically in terms of optical properties, such dust cloud simulations generally fall well short of the needed fidelity. As of yet, quantitative prediction of brownout has not been shown by any method, and appreciating the overall complexity of the fluid dynamics of the problem suggests that reaching a true predictive capability is a longer way off. To this end, a necessary prerequisite is the characterization of the dust cloud by using meaningful quantitative metrics. The creation of high quality experimental measurements of the two-phase fluid dynamics of the wake near the ground is also badly needed, including the boundary layer characteristics, turbulence spectra, and quantification of the mechanisms by which dust is uplifted and entrained into the rotor flow. Such measurements are essential for the validation of modeling efforts, which will always remain tentative unless they can be shown to quantitatively predict the dust clouds for the correct reasons.

It is impractical to make most of the needed measurements of brownout phenomena in the field, and laboratory experiments performed under controlled conditions are required. For example, the measurement of the two-phase nature of the problem with sufficient spatial resolution when using dual-phase particle image velocimetry is limited to relatively small fields of view, and to much smaller fields if the details of the sediment mobility and uplift mechanisms are to be documented. The need for laboratory experiments, however, brings to the forefront the issues of scaling, both in terms of the aerodynamics and of the transport of the sediment. While the aerodynamic similarity parameters and the scaling issues for rotor flows by themselves are fairly well understood, there are additional similarity parameters that will govern the movement of sediment and

dust. In fact, according to Greeley and Iversen [17] there are at least fifteen similarity parameters that must all be satisfied to obtain dynamic similarity in aeolian flows. Clearly, there are significant challenges in satisfying both aerodynamic and aeolian similarity in laboratory-scale experiments, such as with sub-scale rotors operated in dust chambers or in wind tunnels. To this end, the purpose of this thesis is to begin to expose the dynamic scaling factors governing the problem of brownout, with a view to understanding the types of experiments that will provide the highest value in future validation studies.

1.2 Physics of Brownout

Fundamentally, brownout is a complex, three-dimensional, unsteady, two-phase, fluid dynamics problem. A schematic illustrating some of the fluid dynamic mechanisms involved in brownout is shown in Fig 1.2. Clearly, there are many factors involved in the development of the dust cloud, including the characteristics of the rotor wake in ground effect (i.e., downwash, vortices, turbulence) and the sediment characteristics (i.e., particle

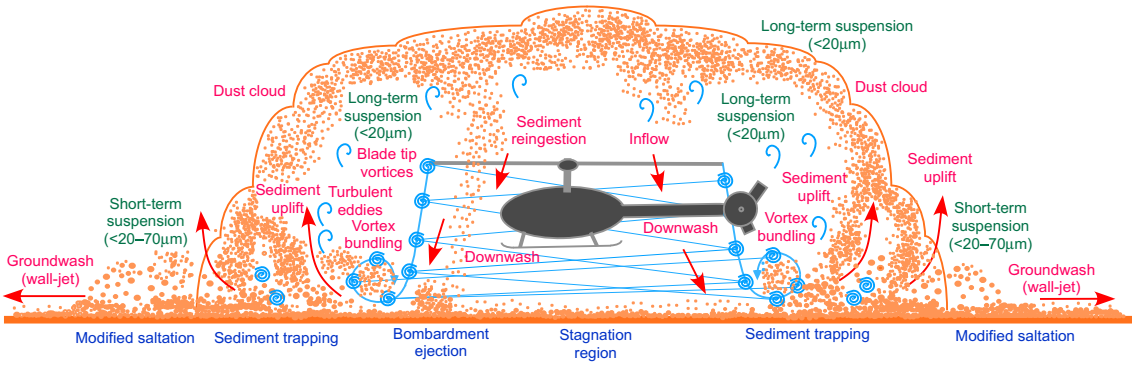

Figure 1.2: A schematic of some of the fluid dynamic mechanisms involved in the uplift and transport of sediment in the development of brownout conditions.

size, mass density, mineral content, moisture content, etc.). The two-phase flow consists of: 1) the carrier phase, which is represented by the unsteady flow induced by a rotorcraft operating in ground effect and 2) the dispersed phase, which is represented by the sediment particles suspended in the flow. It is imperative to understand the physics and mechanisms of each phase to gain a better overall understanding of the formation of dust clouds in brownout conditions.

Some helicopters appear to be more susceptible to brownout problems and others somewhat less so. For example, a helicopter with a toroidal shaped brownout cloud is shown in Fig. 1.3. This cloud seems to be blown away further from the landing area, leaving zones of better visibility for the pilot. The more severe brownout problems arise because of a susceptibility to re-ingest the uplifted dust back through the rotor disk, fol-

Figure 1.3: A toroidal brownout cloud produced by a helicopter. (Courtesy of AWI).

lowed by the bombardment of dust back onto the sediment bed at high velocity [18]. The ejection of more dust then follows through a cascading process, rapidly intensifying the brownout cloud surrounding the helicopter. While the reasons for favorable or unfavorable brownout characteristics still need to be understood, the severity of a brownout cloud can be correlated to several interdependent design parameters including (but not limited to) rotor disk loading, blade loading, rotor height off the ground, number and placement of rotors, number of blades, blade twist, blade tip shape, fuselage shape, etc. [19].

1.2.1 Flow Physics

Challenges in understanding the fluid dynamic processes involved in the problem of brownout include the measurement and prediction of the rotor wake flow near the ground, as well as the need to expose the detailed processes of sediment lift-off from the underlying bed. The sedimentology or aeolian transport aspects of the problem are obviously related to the properties of the particles, but also to the condition of the particles on the surface of the bed (e.g., whether they are compacted or not) as well as the topology of the surface (e.g., smooth or with troughs and dunes). The flow below the rotor, however, is obviously of primary concern, especially as it approaches the ground. An understanding of this flow is obviously a necessary prerequisite to understand the complex phenomenon of brownout.

The flow induced by a rotorcraft is complicated enough, but it is significantly different when the vehicle is operating in close proximity to the ground. The problem of rotors operating in ground effect has been studied extensively in [20–25]. However, most

of these studies have focused on the aerodynamic effects of operating in ground effect on rotor performance. Only recently have several studies been conducted to understand the detailed fluid dynamics of the flow below a rotor near the ground [1,26,27]. These studies have shown that the rotor wake in ground effect is intricately complex and contains turbulence, unsteadiness, and helicoidal tip vortices that persist to relatively old wake ages. It is these flow features that are responsible for the mobilization and entrainment of sediment particles in brownout conditions [1,2,28].

Flow visualization images showing the differences in the wake structure between out-of-ground-effect (OGE) and in-ground-effect (IGE) conditions are shown in Figs. 1.4(a) and 1.4(b), respectively. The structure of the flow induced below a rotor IGE obviously changes considerably to when the rotor is operating OGE. In OGE operations, as shown in Fig. 1.4(a), the rotor wake flows down axially, initially contracting and then expanding only slightly and progressively further downstream. Helicoidal tip vortices trail from each blade and convect along the wake slipstream boundary, but then begin to diffuse after only two or three rotor revolutions, resulting in a mostly turbulent far wake downstream.

In the IGE case, however, the flow is very different, as shown in Fig. 1.4(b). The rotor wake in this case initially contracts, but because an impermeable surface must be a streamline of the flow, the flow turns sharply in the radial (outward) direction, expanding over the ground plane and developing into a turbulent wall flow. The tip vortices in this case persist significantly longer (six or eight rotor revolutions) than when the rotor is operating OGE because of a reintensification of the vorticity from the stretching of the vortex filaments [29,30]. More details about the aerodynamics of the rotor wake for IGE conditions are explained by Lee [1].

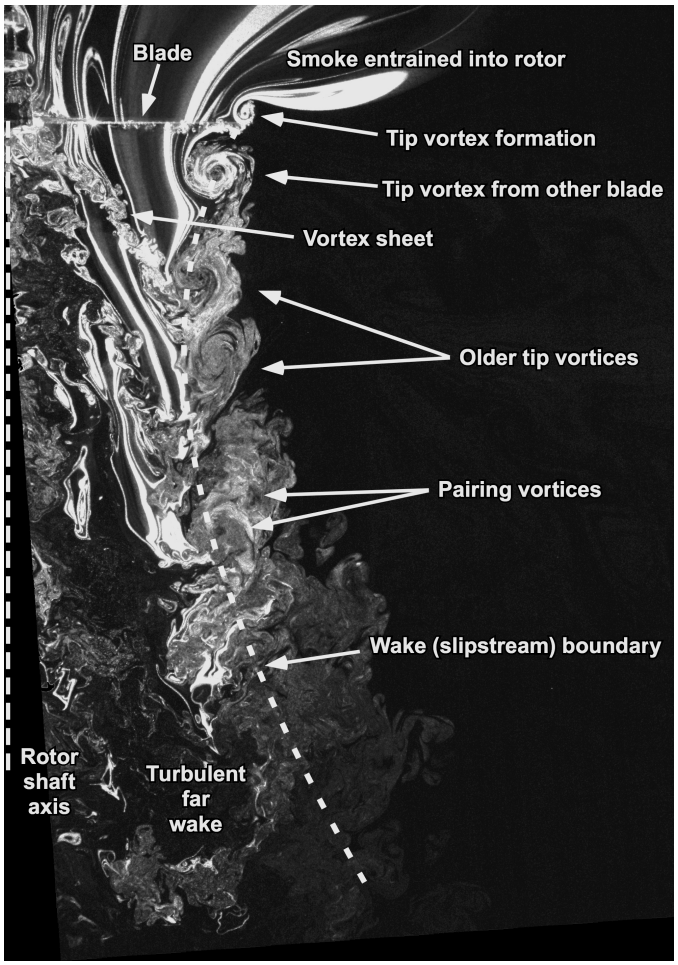

(a) Flow visualization of a two-bladed rotor operating OGE

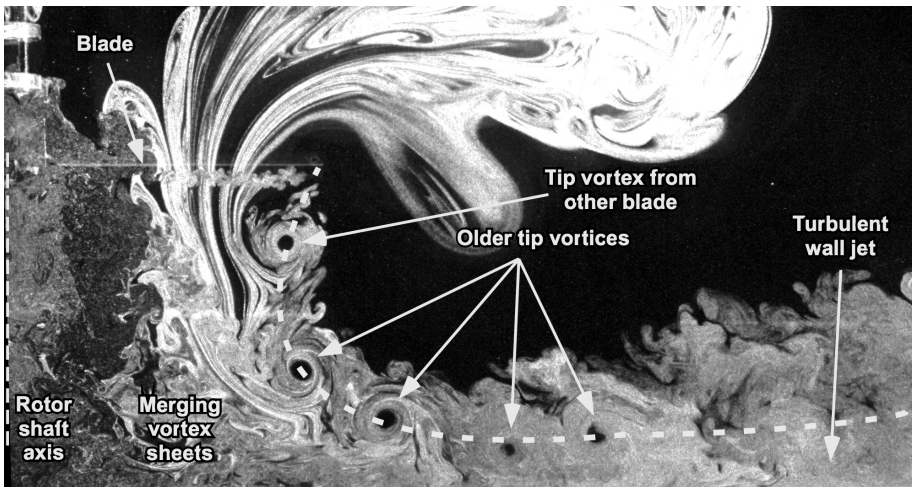

(b) Flow visualization of a two-bladed rotor operating IGE

Figure 1.4: Flow visualization images of a two-bladed rotor operating IGE and OGE [1].

1.2.2 Particle Physics

Understanding the formation of the dust cloud also requires an understanding of the particle physics involved. Fundamentally, the uplift of sediment is caused by the interaction of the rotor wake with the particle bed. The forces acting on a particle on the ground include shear forces from the boundary layer, gravitational forces, unsteady pressure effects, and cohesive forces between particles [17, 31]. A schematic of the forces acting on a particle comprising a sediment bed is shown in Fig. 1.5(a). For a particle to become mobilized, the gravitational and cohesive forces must be overcome by the aerodynamic forces. Once entrained, the dominant forces on the particle are the aerodynamic lift, drag, and the weight of the particle. A schematic of the forces on an airborne particle is shown in Fig. 1.5(b).

1.3 Principles of Sediment Transport

To understand the effects of scaling on the uplift of sediment particles first requires knowledge of the fundamental sediment entrainment and transport physics. In the aeolian sciences, the principles of sediment entrainment and transport have been well established for wind and riverine flows. These include particle creep, saltation, bombardment, among others [17,31]. However, these mechanisms occur in modified forms for a rotor flow. The mechanisms responsible for brownout have been identified by Sydney [2]. A schematic showing each of the mechanisms is given in Fig. 1.6.

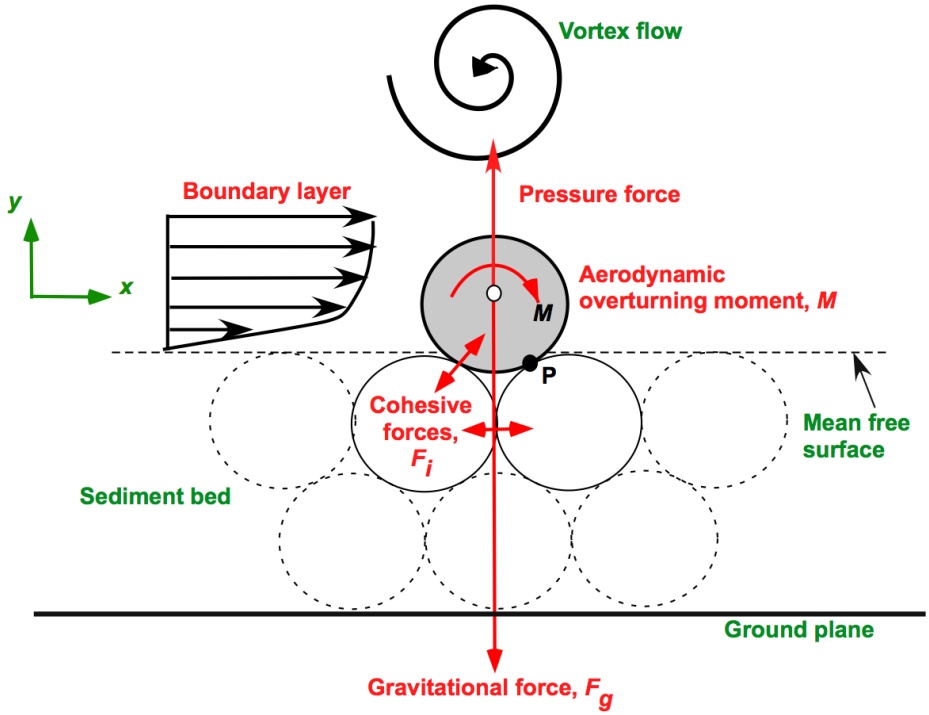

(a) Particle in mobile sediment bed

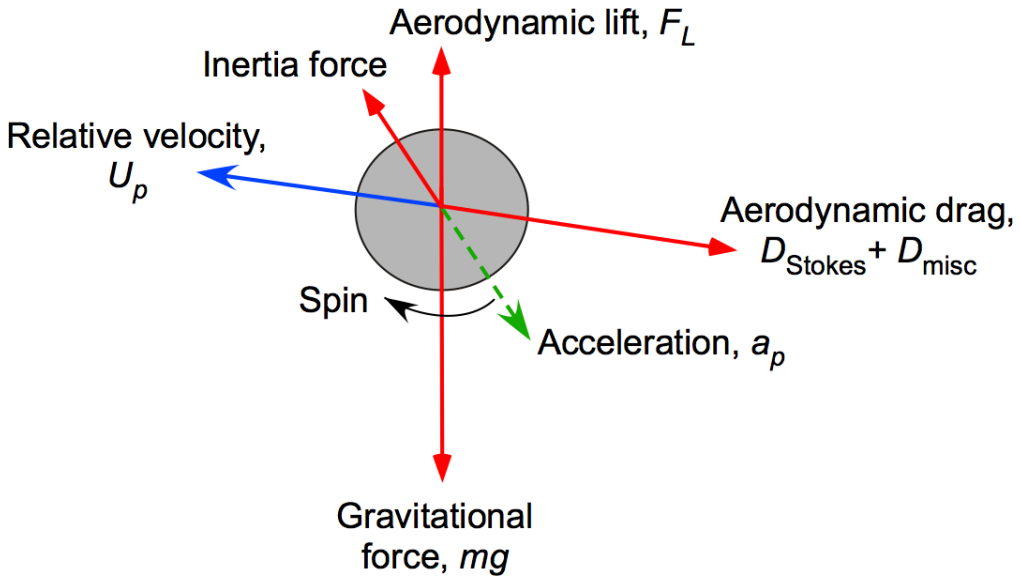

(b) Airborne particle

Figure 1.5: Forces acting on a particle while in a mobile sediment bed and while in suspension.

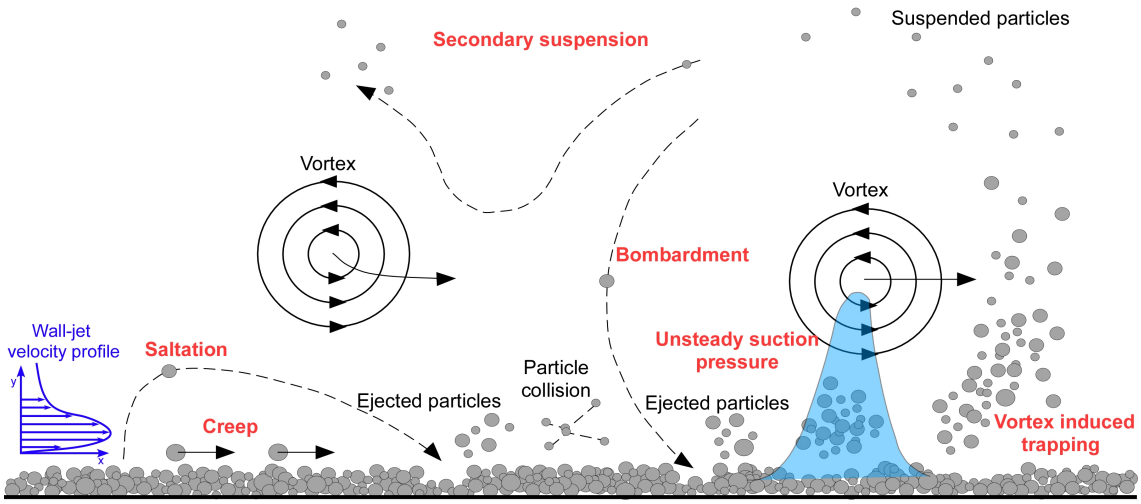

Figure 1.6: Mechanisms of sediment entrainment in brownout [2].

1.3.1 Threshold Criteria

Identifying the threshold of motion for sediment particles is an important and highly studied topic in the aeolian sciences. The shear stress on the sediment bed can be given as an equivalent velocity, u_*, known as the friction velocity. According to boundary layer theory, u_* is related to the shear stress by

$$u_* = \sqrt{\frac{\tau_w}{\rho}} \tag{1.1}$$

where τ_w is the shear stress at the surface and ρ is the density of the fluid. The threshold for mobility can also be expressed as an equivalent velocity, known as the threshold friction velocity, u_{*_t}. This quantity is representative of the minimum shear stress required to overcome the gravitational and cohesive forces that resist particle motion. When the friction velocity, u_*, exceeds the threshold friction velocity, sediment particles will start to become mobilized from the sediment bed, i.e., when the condition$u_* \geq u_{*_t}$ is met.

1.3.2 Shields Parameter

The Shields parameter is another parameter that is used in the field of sedimentology to establish a threshold for sediment mobility, i.e.,

$$\tau_* = \frac{\tau}{(\rho_s - \rho) g D_p} \tag{1.2}$$

This parameter gives a relationship between the fluid forces on the particle and the gravitational forces on the particles. It can also be viewed as a non-dimensionalization of the shear stress on the sediment bed. It has been a common practice to use a Shields diagram to calculate the incipient motion of sediment particles. However, there has been controversy around the work of Shields regarding inconsistencies in his data [32,33]. Furthermore, this parameter is difficult to use in practice because it requires trial and error to establish the threshold for mobility for a given set of fluid and sediment parameters. This iterative process can make its application rather inconvenient [34]. Therefore, the present work uses the threshold friction velocity rather than the Shields parameter to define the threshold of particle motion.

1.3.3 Saltation

Particles larger than about 50 μm in diameter tend to exhibit an initial motion from the bed known as saltation. In this type of motion, particles are uplifted off the bed by shear, pressure, or other external forces, and then follow ballistic trajectories until they fall back and impact the bed [17]. A schematic of a particle undergoing saltation is shown in Fig. 1.7. This process can repeat, resulting in many particles hopping and bouncing along the surface. When many such particles undergo saltation, they form a layer known

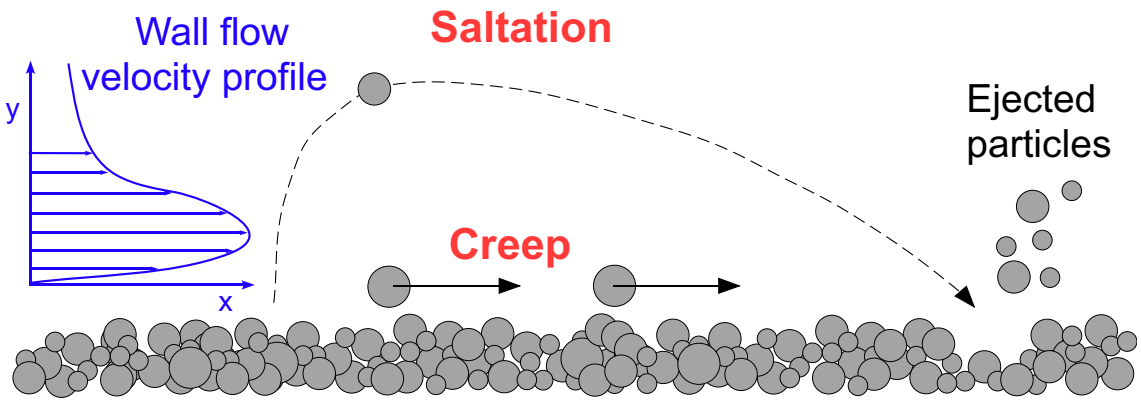

Figure 1.7: Schematic of particles undergoing saltation and creep.

as the saltation layer. Notice that individually saltating particles can impact the bed and eject many more particles into the saltation layer, resulting in a cascading process that entrains more and more particles [35]. Particles that are too big and heavy to undergo saltation, simply roll along the surface in a type of motion known as particle creep [31].

1.3.4 Vortex Induced Sediment Trapping

The mechanism of vortex-induced sediment trapping was first identified for a rotor flow in proximity to a sediment bed by Johnson et al. [28] and Sydney et al. [2]. The vortices were seen as the primary drivers in the processes of sediment mobilization and uplift. In this mechanism, as a vortex passes over the sediment bed, it causes increased shear and mobilizes and uplifts particles from the bed. The high swirl velocities of the vortex causes particles to become trapped in the strong upwash of the flow, resulting in a wave of uplifted sediment. The schematic shown in Fig. 1.8 illustrates this process of vortex-induced sediment trapping.

The heavier particles that have been entrained by the vortex flow are usually spun

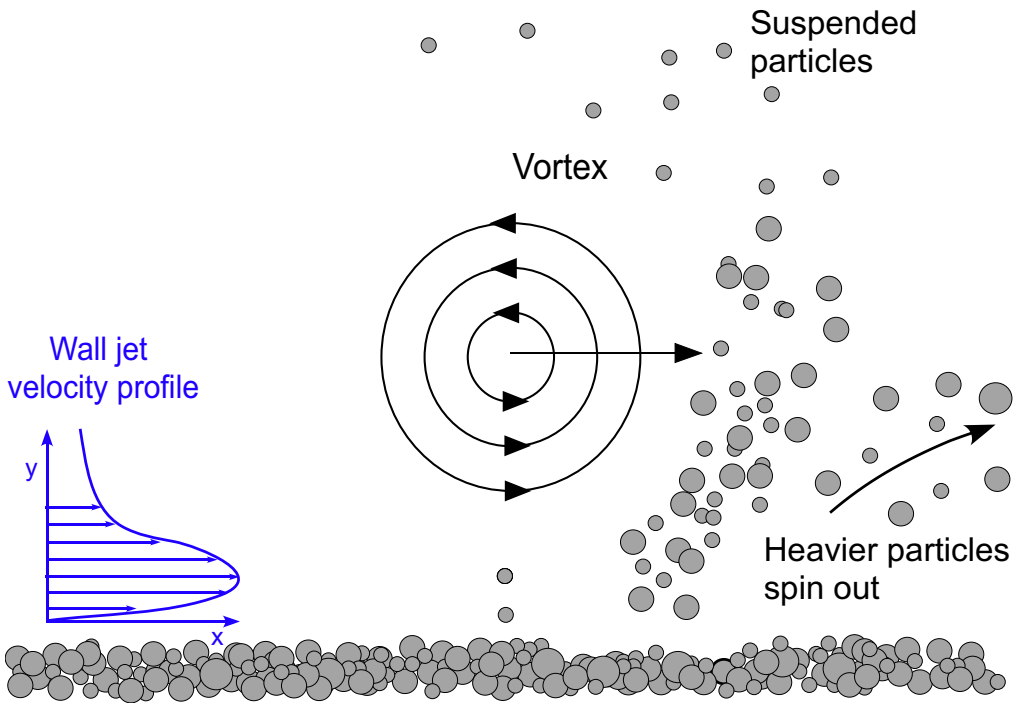

Figure 1.8: Schematic of vortex induced trapping mechanism.

out under the action of centrifugal forces. They then follow ballistic trajectories back toward the bed. For the smaller particles, the momentum they extract from the flow is sufficient to convect them well above the flow near the bed and into suspension. Particle suspension occurs when the balance of forces on the particle from the vertical flow and turbulent fluctuations in the surrounding flow is greater than the gravitational effects on the particle. In general, mostly the smaller particles tend to remain in suspension for the periods of time over which brownout occurs.

1.3.5 Bombardment

Bombardment is a mechanism by which particles impact the bed and can eject even more particles into the flow. In a rotor flow, there are three types of bombardment: salta-

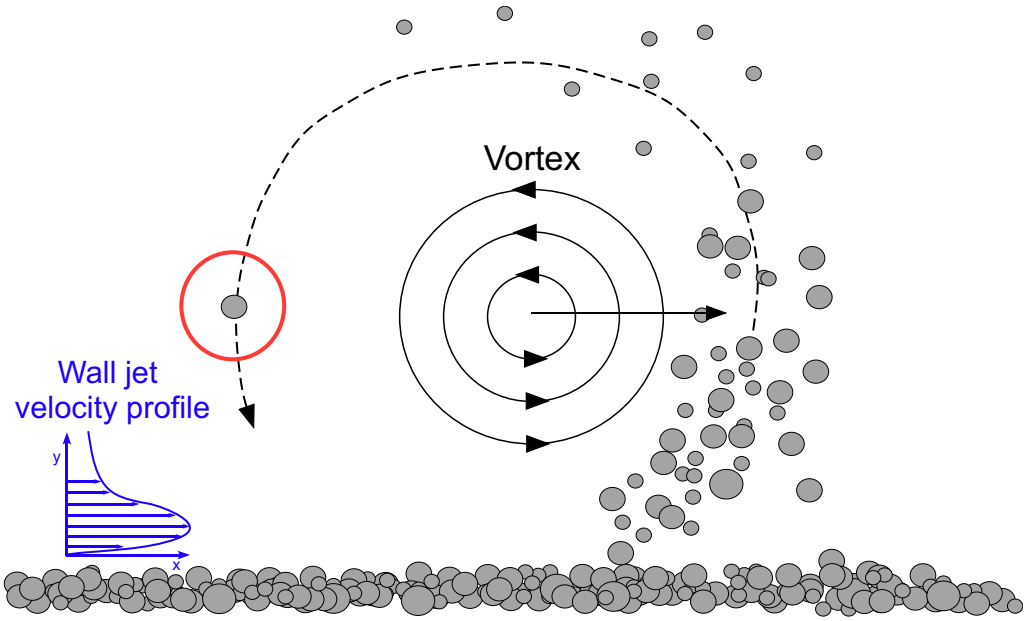

(a)

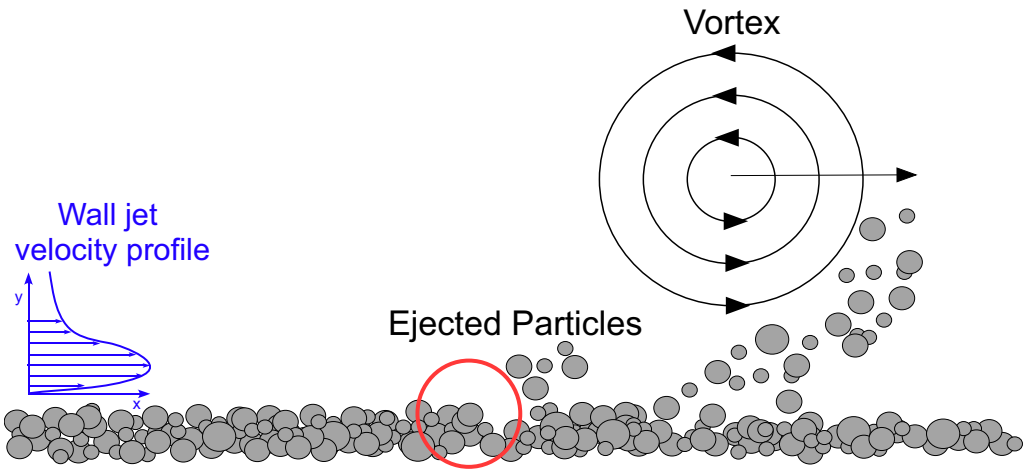

(b)

Figure 1.9: Local bombardment in a vortex flow.

tion bombardment (as previously described), local bombardment, and global (or reingestion) bombardment [2]. Saltation bombardment occurs when a saltating particle impacts the bed and transfers its momentum to other particles, causing them to become mobilized. In local bombardment, a particle is uplifted into the flow, such as by a vortex or a large turbulent eddy. The particle then follows a circular path around the vortex flow and impacts the ground with greater momentum and energy, ejecting even more particles in the process. A schematic of the process of local bombardment is shown in Fig. 1.9. Global or reingestion bombardment occurs when suspended particles become uplifted high enough to be ingested through the rotor disk before impacting the ground and then ejecting more particles in the process.

1.4 Consideration for Scaling of the Brownout Problem

Most of the previous experimental studies on brownout [2, 28, 36], while providing valuable results, have not addressed dynamic similarity or scaling issues. Therefore, it is difficult to know if the results obtained from such studies are, in fact, representative of the brownout problem at full-scale. Conducting full-scale tests [37, 38], while potentially very valuable, can be highly expensive and time consuming because of the size, complexity of the setup, and the cost of specialized equipment needed to conduct flow field measurements at full-scale, if indeed this is even possible. Therefore, laboratory scale tests must be considered to gather experimental data and so to develop a detailed understanding of the problem of brownout. While the efforts to simulate brownout conditions in a small-scale laboratory experiment are certainly important, the effects of scaling down

such a complex problem are also important to address.

It is expected that most (if not all) detailed fluid mechanics studies of brownout will have to be conducted in a laboratory environment using small-scale rotor models. In these experiments, scaling becomes an issue because it may alter the physics of both the flow problem and the behavior of the dust and, therefore, the overall results that are obtained. The effect of scaling needs to be explored to establish a better understanding of how it affects the measurements, so that future experiments that simulate the brownout problem with small-scale models can be properly designed to give the best and most representative types of results.

As stated previously, the problem of brownout is fundamentally a two-phase problem. The proper scaling of both the phases needs to be understood to have a good overall understanding of the effect that scaling has on the brownout problem. For this problem, there are two groups of similarity parameters: 1) The classic aerodynamic scaling for flow similitude, and 2) Similarity parameters associated with the sediment or aeolian similarity parameters. The issues with scaling for each type are outlined in the subsequent sections.

1.4.1 Scaling of the Carrier Phase

In the field of aerodynamics, there are two primary nondimensional flow similarity parameters that need to be matched with full-scale values to achieve flow similitude: 1) Reynolds number and 2) Mach number [39]. There may be other scaling parameters too, such as reduced frequencies, but they are generally of lesser importance in all flows other than those with high levels of unsteadiness. It is well known that closely matching

these parameters in a controlled experiment to the full-scale values can be a challenge because of the dependencies on geometric quantities such as the model size (in the case of Reynolds number), fluid properties (i.e., viscosity, density, temperature), and also their interdependencies [40].

For rotorcraft, the reference values for Reynolds number and Mach number are usually referenced to the tip of the rotor blade. The equations for the Reynolds number and Mach number at the blade tip are given by

$$Re_{\text{tip}} = \frac{\rho V_{\text{tip}} c_{\text{tip}}}{\mu} \tag{1.3}$$

$$M_{\text{tip}} = \frac{V_{\text{tip}}}{a} \tag{1.4}$$

where $V_{\text{tip}} = \Omega R$ is the blade tip speed in hover. Clearly, the Reynolds number and Mach number are related by V_{tip}. Solving for V_{tip} in Eq. 1.4 and substituting the result into Eq. 1.3 gives

$$Re_{\text{tip}} = \left(\frac{\rho a c_{\text{tip}}}{\mu} \right) M_{\text{tip}} \tag{1.5}$$

It is clear, therefore, that using scaled down models for aerodynamic testing can raise concerns about aerodynamic scaling and flow similitude. For example, if a 1/10th scale model of a rotor was tested in air (assuming all other parameters are the same as the full-scale), the tip speed would have to be increased to 10 times the full-scale value to match the tip Reynolds number. Obviously, compressibility effects would then become an issue when using such high tip speeds. Assuming the same 1/10th scale model, if the Mach number were matched to full-scale (i.e., V_{tip} is equivalent to full-scale value), then the ratio between ρ and μ would have to increase by 10 times the full-scale value to also match the Reynolds number. Achieving this condition would either require changing the

fluid properties via temperature changes, or using a different fluid altogether (e.g., with the use of a gas such as Freon), which would require specialized facilities [40]. Clearly, with only two similarity parameters, it is a challenge to achieve flow similitude in the laboratory.

1.4.2 Scaling of Dispersed Phase

Scaling parameters also govern similitude of the dispersed phase. Greeley and Iversen [17] have listed potentially up to 18 physical variables that govern the characteristics of sediment mobilization, entrainment, and uplift. These parameters include variables such as particle diameter, particle density, a characteristic length (the rotor radius in this case), wind speed, fluid viscosity, among others. The complete list of variables is given in [17]. Assuming that p is equal to the number of physical variables (18 in this case) and k is equal to the number of independent fundamental physical quantities or dimensions used to express those variables (3 in this case: mass, length, and time), the methods of dimensional analysis can be applied to this set of variables giving $p-k = 18-3 = \mathbf{15}$ independent nondimensional similarity parameters. The expressions and descriptions of these parameters are given in Table 1.1.

From a first examination, the number of parameters appears rather daunting from a scaling point of view. The challenges associated with matching just the Reynolds number and Mach number for aerodynamic scaling of the model rotor are significant on their own, as previously discussed in Section 1.4.1. To match 15 more parameters would be extraordinarily difficult, if not impossible. For example, if just parameters 2 and 3 are

#	Expression	Description
(1)	d/R	Deposition or deflation depth ratio
(2)	D_p/R	Particle diameter-to-rotor radius ratio
(3)	U_{char}^2/gR	Froude number
(4)	e	Coefficient of restitution
(5)	U_{char}/U_F	Ratio of windspeed to particle terminal speed
(6)	$L_i/R, (z/R)/R, \eta/R$	Topographical geometric similarity
(7)	z_o/R	Roughness similarity
(8)	L^*/R	Boundary layer stability similarity
(9)	$U_{\text{char}}R/\nu$	Reynolds number
(10)	$U_{\text{char}}/u_{*_t}, U_{\text{char}}/u_*$	Friction speed ratios
(11)	ρ_s/ρ	Density ratio
(12)	$U_{\text{char}}t/R$	Time scale

Table 1.1: Nondimensional similarity parameters for aeolian transport.

considered for a 1/10th scale model rotor system, the particle diameter, D_p, would have to be 10 times smaller than what is found at full-scale to have similitude. Similarly, to satisfy scaling of the Froude number, the characteristic velocity will also have to be significantly reduced, possibly reducing it to below the threshold friction velocity for particle motion, resulting in no particle entrainment at all.

In light of the foregoing issues, the goal of this thesis was to explore the effects of scaling on the processes of sediment uplift and entrainment and attempt to establish the sensitivity of the problem to the similarity parameters. While studying the effects of every parameter would be ideal, in the present work the effects of only a few of the relevant parameters were studied, namely:

1. Particle diameter-to-rotor radius ratio, D_p/R

2. Particle-to-fluid density ratio, ρ_s/ρ

3. Ratio of characteristic flow (or wind) speed to particle terminal speed, U_{char}/U_F

4. Densimetric Froude number, $U_{\text{char}}/(\sqrt{(\rho_s/\rho - 1)gD_p})$

5. Threshold friction speed ratio, U_{char}/u_{*_t}

In the present work, the densimetric Froude number was substituted for the Froude number given by Greeley and Iversen [17] because it was particle specific, while the original definition was not.

All of the similarity parameters could not be studied because of the sheer number of parameters as previously discussed, as well as the fact that some parameters do not change from sediment to sediment and are flow specific. These values will change between sediment samples so they can be studied using the same flow while only changing the type of sediment.

1.5 Objectives of the Present Work

The main goal of the present work was to help improve the fundamental understanding of the effects of scaling on the mobilization, uplift, and entrainment of sediment particles below a rotor operating in ground effect above a sediment bed. The relative importance of each of the studied similarity parameters was also established. The work also contributed by providing quantitative measurements of the two-phase flow in response

to changes in the similarity parameters. Apart from one study done on saltation threshold [41], there is a dearth of information on the effects of variations in the other similarity parameters, and none at all on particle entrainment below a rotor flow.

To provide an understanding of the effects of the similarity parameters on the mobilization and uplift of sediment particles, a series of experiments were performed with a small-scale, one-bladed rotor system operating above a ground plane. Different particle species of known size range, density, and mineral composition were distributed on the ground plane to simulate a sediment bed below the rotor. Various flow diagnostic techniques were used to measure the two-phase flow. The use of a particle tracking and identification algorithm allowed for separate measurements of the flow and sediment phases. High resolution phase-resolved particle image velocimetry allowed the characteristics of the tip vortex and the turbulent wall flow formed by the rotor flow to be studied. These measurements established the characteristics of the flow near the ground that were used in calculating the various similarity parameters. The results obtained establish the significance of scaling for brownout experimental studies and help to make recommendations regarding scaling for future small-scale brownout experiments.

1.6 Organization of Thesis

A background to the brownout problem has been given in the present chapter, along with the fundamentals of the rotor flow in ground effect and sediment transport processes. A discussion of scaling and its significance to experimental studies on brownout was also given, along with an explanation of the similarity parameters that govern the physics

of the problem. Chapter 2 provides a comprehensive explanation of the experimental techniques and instrumentation used to study the rotor flow field, as well as how scaling affects the particle mobilization and entrainment into the rotor flow. These descriptions include the flow diagnostic techniques of flow visualization and particle image velocimetry. Chapter 3 discusses the results in terms of flow field characterization, single-phase flow velocity measurements of just the rotor flow in ground effect, and dual-phase flow measurements of the combined air-sediment environment near the ground. Finally, Chapter 4 discusses some of the conclusions of the present study, and suggests direction for future experimental research toward better understanding of the effects of scaling on brownout experimental studies.

Chapter 2

Description of the Experiments

2.1 Overview

Experiments were performed to explore both the single-phase and dual-phase flow environments below a rotor in simulated hovering flight above a mobile sediment bed. The goals were to better understand the effects of varying the selected aeolian similarity parameters on particle mobility and uplift, and how the type and characteristics of the particles may contribute to the problem of rotorcraft brownout. To recap what was explained in Chapter 1, the similarity parameters that were studied in the present work were:

1. Particle diameter-to-rotor radius ratio, D_p/R
2. Particle-to-fluid density ratio, ρ_s/ρ
3. Ratio of characteristic flow (or wind) speed to particle terminal speed, U_{char}/U_F
4. Densimetric Froude number, $U_{\text{char}}/(\sqrt{(\rho_s/\rho - 1)gD_p})$
5. Threshold friction speed ratio, U_{char}/u_{*_t}

The present chapter describes the experimental setup and instrumentation, as well as the flow diagnostic techniques and data processing techniques that were used. This chapter also discusses the numerous challenges in performing such measurements.

2.2 Experimental Setup

This section gives a description of the rotor system, the ground plane and the dust chamber, as well as a description of the regions of interest (ROI) that were studied in the flow.

2.2.1 Rotor System and Ground Plane

A small, laboratory scale, one-bladed rotor, with a radius of 77 mm (3.03 inches) was used to generate the rotor wake for these experiments. The blade used was an untwisted, cambered flat plate with a sharpened leading edge and a rectangular (i.e., constant chord) planform shape. Figure 2.1 shows a photograph of the blade and its principal dimensions. These cambered flat plates are known to be more aerodynamically efficient than traditional airfoil shapes in the low Reynolds number regime [26]. The blade was constructed out of a single piece of thin carbon fiber sheet and was mounted to a teetering hub to allow for small flapping displacements. A counter-mass was placed on the hub

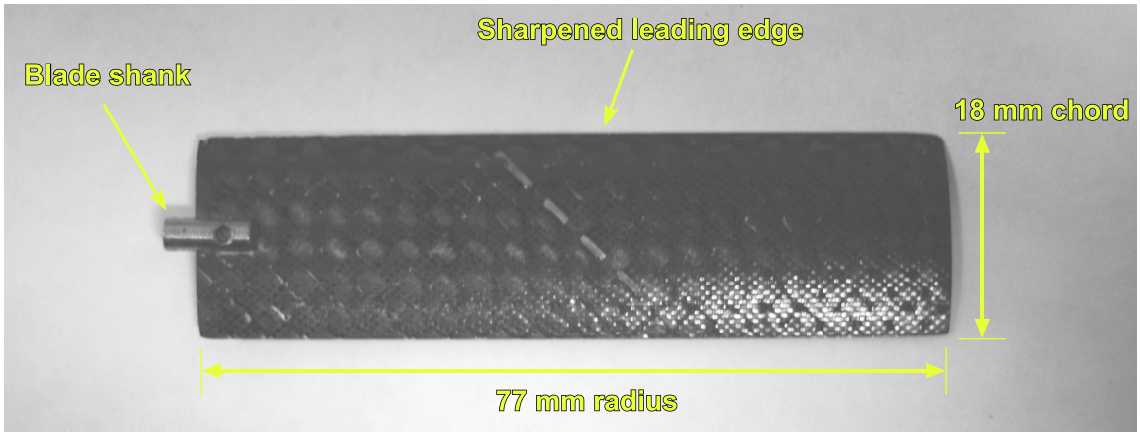

Figure 2.1: Photograph of the rotor blade and its principal dimensions.

opposite to the blade. The rotor was driven by a small DC motor coupled to a 4:1 gear reduction unit. The frequency of rotation was controlled by varying the input voltage to the DC motor. A schematic of the rotor system is shown in Fig. 2.2.

The rotor was adjusted to operate in hover at a height of one rotor radius ($z/R = 1.0$) centered over a rectangular horizontal ground plane. A schematic of the overall setup is shown in Fig. 2.3. The ground plane was constructed from a stiff, rigid PVC material. The surface of the ground plane was dulled by sanding and then painted matte-black to limit laser light reflections. The ground plane extended seven rotor radii outwards from the rotor shaft to allow enough clearance from the rotor to the edge of the plane. The

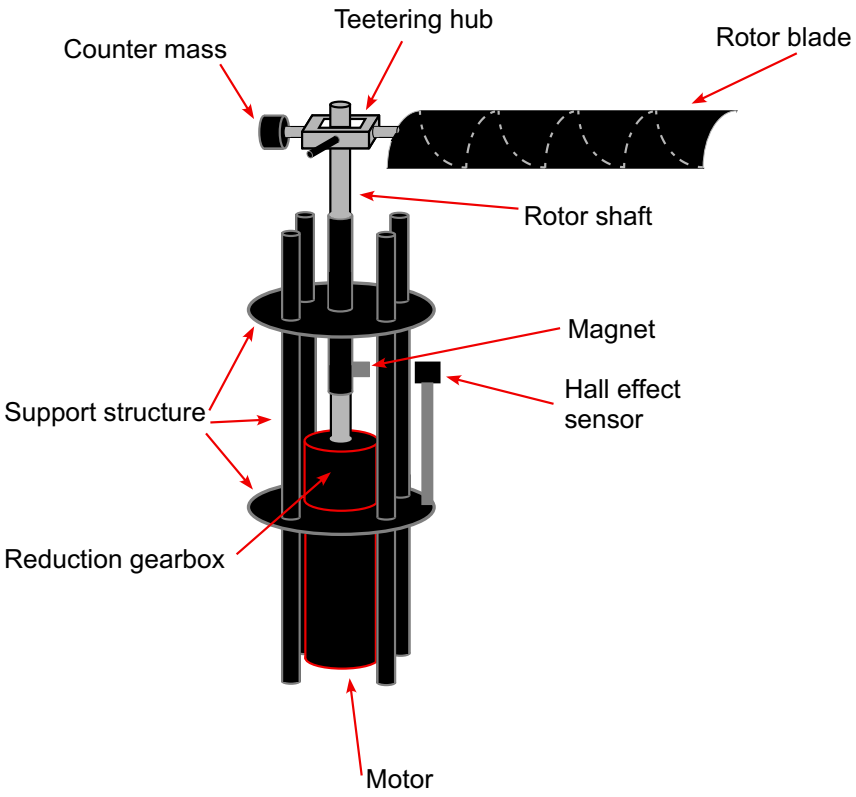

Figure 2.2: Schematic showing the components of the small-scale rotor system used for the present experiments.

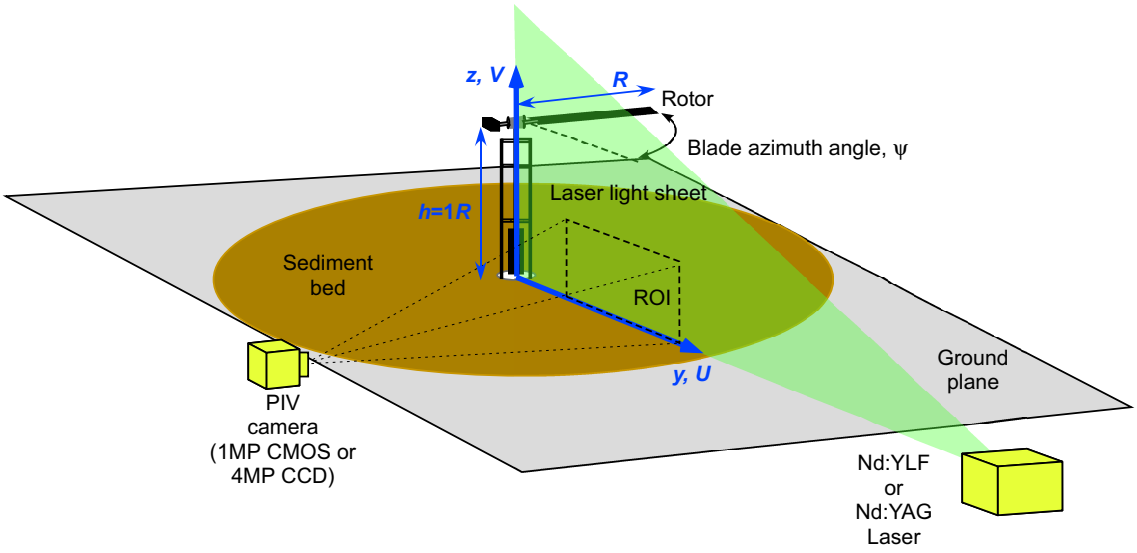

Figure 2.3: Schematic of the experimental setup.

reference coordinate system was centered directly below the rotor shaft at the center of the ground plane, as defined in Fig. 2.3.

For the present experiments, the rotor was operated at a nominal rotational frequency of 85 Hz, which corresponds to a blade tip speed of 41.12 ms^{-1} and a chord Reynolds number at the blade tip of approximately 47,000. The solidity of the rotor was $\sigma = 0.074$. The pitch of the blade was fixed to 12° using a known reference angle measured with a digital inclinometer. Under these operating conditions, the rotor produced a thrust of 31.3 ± 0.1 grams when measured using a micro-balance, which corresponds to a thrust coefficient of $C_T = 0.00828$ and a blade loading coefficient of, $C_T/\sigma = 0.111$. These values are representative of those found on an actual helicopter rotor. The rotor was operated at this condition to give the same flow conditions for each experiment.

The main goal of the research was to identify changes in the entrainment and uplift of sediment particles from changes in the values of the particle parameters alone. To

this end, a mobile sediment bed consisting of dust particles of known characteristics (i.e., known size and mass density) was laid out over the ground plane in a circular disk with an approximate thickness of 11 mm. The top of the sediment bed was made smooth with a scraper to ensure that the surface was consistent between the experiments that were performed with the different sediment samples.

For both the single-phase and dual-phase experiments, a laser light sheet was oriented parallel to the rotor shaft axis and orthogonal to the ground plane to illuminate the region of interest. This light sheet was used for both particle image velocimetry (PIV) and flow visualization (FV) experiments. A digital CCD or CMOS camera was aligned to be orthogonal to the light sheet and was uniformly focused on the region of interest to capture the images. As shown in Fig. 2.3, the blade azimuth angle, ψ, is defined to be $\psi = 0^\circ$ when the quarter-chord location at the blade tip passes through the plane of the light sheet.

2.2.2 Dust Chamber

All of the experiments were performed inside a dust chamber, as shown in Fig. 2.4. This chamber provided a controlled environment for conducting the experiments and also fully contained any suspended dust particles that were uplifted from the sediment bed during the dual-phase tests. The 2 x 2 x 2 meter chamber was also large enough to limit significant flow recirculation effects from the operation of the small rotor.

The frame of the chamber was constructed using slotted aluminum beams. Optically clear Plexiglas was seated in the slots and served as the dust chamber walls. The

Plexiglas allowed for unattenuated transmission of the laser light into the test section and also for unimpeded image capturing. All sensitive instrumentation (i.e., laser, PIV camera, synchronizer, optics) were kept outside of the chamber and safely away from the dust particles.

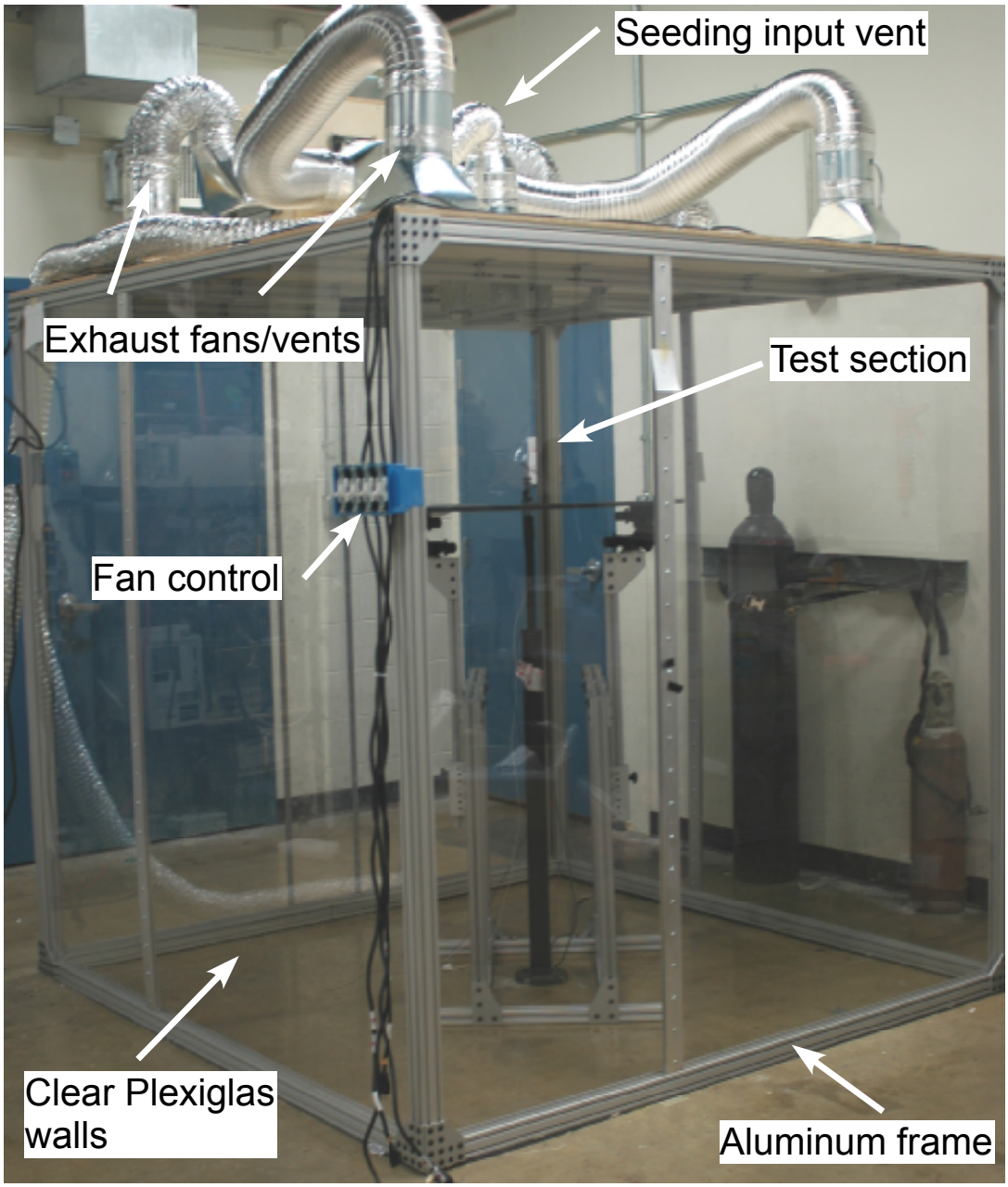

Figure 2.4: Dust chamber facility used to conduct flow diagnostic experiments.

The dust chamber was also designed with an input vent in the ceiling to allow for the introduction of seeding particles into the test section and an exhaust ventilation system to evacuate the chamber. The input vent was connected to a smoke generator with flexible aluminum ducting. During experiments, the exhaust fans could be turned on to draw the smoke into the chamber. The multiple exhaust fans could be independently turned on or off to precisely control the flow seeding to the desired seed concentration. The fans could also be used to vent out suspended sediment particles after a dual-phase experiment. Specific portions of the chamber were lined with black cloth to limit reflections from the laser light.

2.2.3 Regions of Interest

Several regions of interest (ROI) in the flow were studied to explore the effects of the similarity parameters on sediment uplift. The ROIs studied are shown in Fig. 2.5. ROI 1, which consisted of the region from $y/R = 0.50$ to $y/R = 2.50$, allowed measurements to be made of the entire flow field to gain an overall understanding of what flow features were present and what areas in the flow then needed to be studied in greater detail. This region was used for the single-phase and dual-phase FV, as well as PIV. ROI 2, which consisted of the near wall region from $y/R = 1.75$ to $y/R = 2.60$, was used to study the region where much of the sediment was found to be mobilized. Single-phase and dual-phase PIV and FV were also conducted in ROI 2 to characterize the flow and to quantify the sediment uplift off the ground plane as it was affected by changes to the various particle similarity parameters.

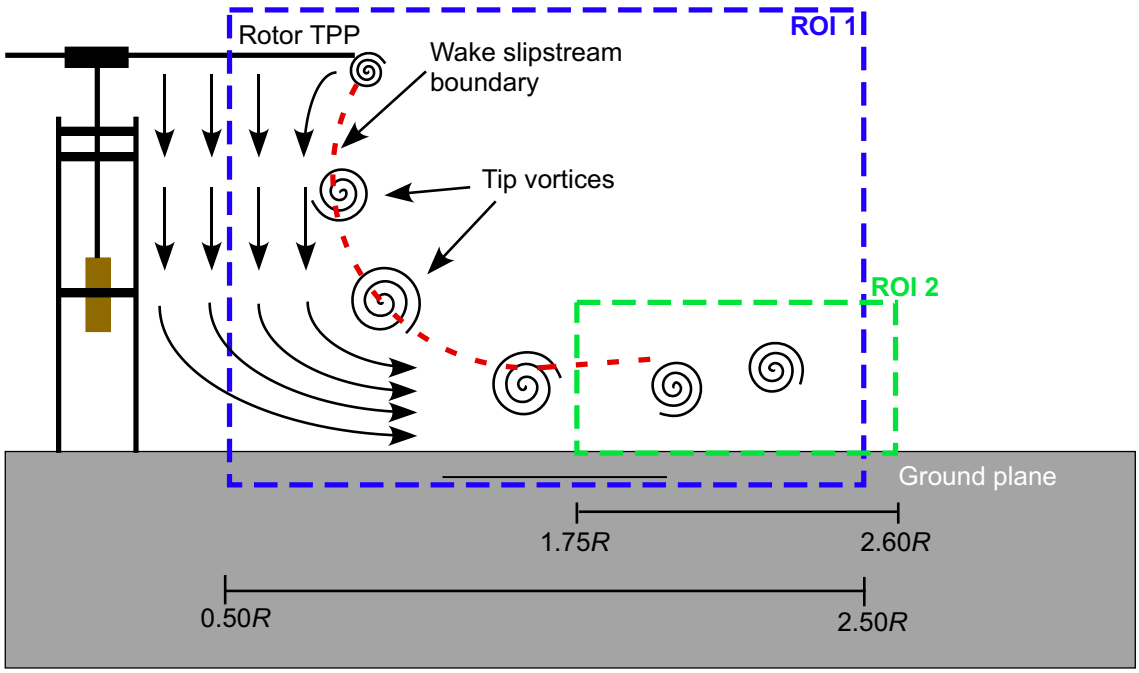

Figure 2.5: Schematic showing the flow regions of interest.

2.3 Time-Resolved Flow Visualization

The complex flow induced by the rotor in ground effect was first qualitatively studied using high-speed imaging of the flow field. This flow consisted in part, of vortices trailed from the blade tips. Time-resolved flow visualization (TR-FV) allowed for the temporal tracking of the vortical flow structures in the rotor wake and of the development of the turbulent wall flow on the ground plane. In the dual-phase FV, the region of maximum particle uplift could also be identified and studied using FV.

The FV images were captured with the camera viewing axis orthogonal to the plane of the laser light sheet. A high-speed CMOS camera was used in conjunction with a high-speed Nd:YLF laser to capture these images. The CMOS camera was able to capture images at a maximum rate of 3,000 fps with a pixel resolution of 1,024-by-1,024 pixels

(1 Mp). The Nd:YLF laser emitted light at a wavelength of 527 nm with 20 mJ per pulse. Given the large number of high-resolution images being transferred to the data acquisition system in a relatively short time, a hyperstreaming system was used to provide a temporary data buffer before the images were sent to the data acquisition system.

During the TR-FV, the flow field was more heavily seeded with smoke to highlight and track the individual flow structures, as well as to visualize the flow field as a whole. A smoke generator was used to produce submicron seed particles. Inside this generator, high pressure nitrogen was mixed with a mineral oil solution, which was then vaporized after being heated to its boiling point. As the vapor left the nozzle, it mixed with the air, producing a dense white smoke containing the tracer particles, and was routed to the input vent in the ceiling of the dust chamber. These seed particles were passed through a plenum and honeycomb structure under the influence of a weak pressure gradient, which helped to remove most of the larger turbulence and eddies from entering the test section.

A calibration determined that the seed particles contained in the smoke had a nominal diameter of 0.2 μm [42]. These submicron particles were large enough to produce enough Mie scattering of the laser light, but also small enough to faithfully follow the rotor wake flow [43–45].

For the present TR-FV measurements, the frame rate of the camera was chosen to be 1,000 fps. There was a trade-off between the frame rate and image intensity because at higher frame rates there was less time for the camera to capture the available light energy. Therefore, at very high frame rates the camera captures darker images, which can sometimes be unusable for analysis. A frame rate of 1,000 fps was found to be satisfactory between balancing the temporal resolution with the image intensity. In each run, 1,000

sequential images were captured, which corresponded to about 85 revolutions of the rotor.

2.4 Particle Image Velocimetry

Particle image velocimetry was used to quantitatively study the flow field in both ROIs, as previously discussed in Section 2.2.3. Both the phase-resolved PIV (PR-PIV) and time-resolved PIV (TR-PIV) techniques were used. Dual-phase PIV was also performed to study the detailed mobilization, uplift, and entrainment of particles from the ground plane, and how they were affected by the similarity parameters.

2.4.1 Method of PIV

PIV is a non-invasive flow diagnostic technique that allows for an instantaneous measurement of the entire two-dimensional velocity field in a given ROI. To perform the PIV measurements, the flow is first carefully seeded with small (usually micron or submicron) tracer particles, as previously discussed. The selection of an appropriate tracer particle is critical for PIV because the particles must be small and light enough to be able to follow the flow faithfully without significant tracking errors, but also large enough to scatter enough light and be captured by the imaging sensor on the camera. Furthermore, for PIV a uniform distribution of tracer particles in the flow is desired to give the best results.

A planar laser light sheet is used to illuminate the seed particles present in the flow, and a digital camera is oriented orthogonally with respect to the light sheet, as previously discussed. The light sheet is created by passing the laser beams through a series of cylin-

drical and spherical lenses. The light sheet thickness for the current experiments was less than 2 mm at its waist. The camera was then uniformly focused over the ROI illuminated by the sheet.

In PIV, the entire illuminated flow field is imaged twice by the camera in quick succession. The two images are separated by a small pulse separation time, Δt, (a few microseconds); the first image is denoted Frame A, and the second is denoted Frame B. These image pairs comprise the raw data used for the cross-correlation process; the image pairs together contain the relative pixel displacements of the tracer particles over the prescribed pulse separation time, providing the spatial information needed to calculate the local flow velocity.

To derive the PIV results, the images are first sub-divided into many smaller interrogation windows of a given size, which for the present experiments was 24-by-24 pixels (TR-PIV) or 16-by-16 pixels (PR-PIV). The PR-PIV measurements could be analyzed with a finer grid because the raw images were of higher spatial resolution. To calculate the displacements, an image cross-correlation procedure is used to match the unique intensity pattern produced by the group of tracer particles in a single interrogation window between Frame A and Frame B. This cross-correlation process was conducted by performing a Fast Fourier Transform (FFT) on the data and conducting the analysis in the frequency domain [46].

The resulting pixel displacements of the group of tracer particles, $(\Delta x, \Delta y)$, are calculated to sub-pixel precision, and can then be used to accurately calculate the local flow

velocity using the equation

$$\left\{ \begin{array}{c} U \\ V \end{array} \right\} = \frac{1}{M\Delta t} \left\{ \begin{array}{c} \Delta x \\ \Delta y \end{array} \right\} \tag{2.1}$$

where U and V are the wall-parallel and wall-normal velocity components, respectively, and M is the magnification factor that depends on the camera resolution and lens used to capture the image. The magnification factor, M, was calculated within the PIV software by imaging an object of known dimension (usually a ruler or scale), which allows a calibration ratio between pixels and millimeters to be computed.

The cross-correlation sequence is then repeated for each set of the remaining interrogation windows in the image pair, resulting in velocity measurements for the entire

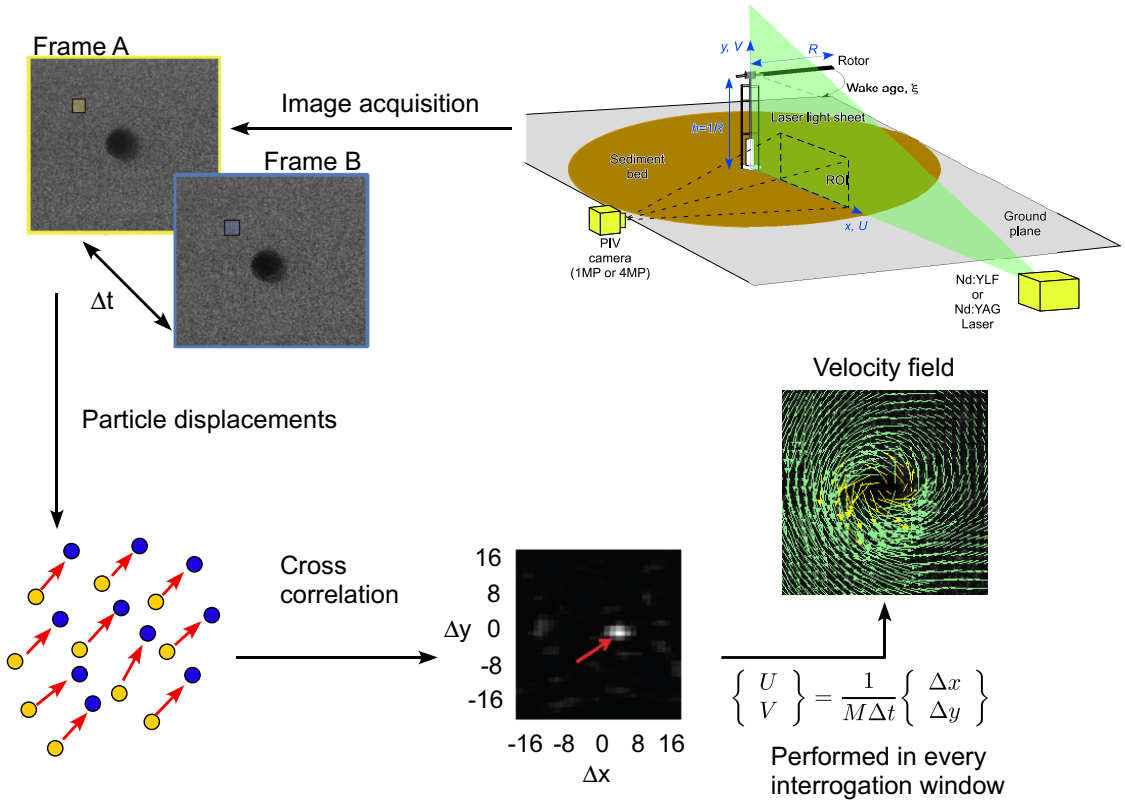

Figure 2.6: Schematic showing PIV methodology.

planar flow field. This sequence is shown for a vortex flow in Fig. 2.6. In the present work, all the PIV cross-correlation calculations utilized a deformation grid algorithm, which is discussed by Scarano in [47]. Additional information about the PIV technique can be found in [48–52].

2.4.2 Phase-Resolved PIV

In the present work, phase-resolved PIV was used to characterize the flow field and the properties of the wall flow at the ground. In this particular setup, a Nd:YAG dual laser that emitted light at a wavelength of 532 nm with 90 mJ per pulse was used to illuminate the flow field, and a 4 Mp CCD camera was used to capture the images. The pulse separation time, Δt, for these set of experiments was chosen to be 20 μs, which corresponded to only 0.612° of blade rotation. 1,000 image pairs were collected for each data set to provide enough data from a statistical viewpoint. A lens with a focal length of 105 mm was used to capture the entire flow field that measured approximately 13.5 cm-by-13.5 cm. Only single-phase measurements were conducted using PR-PIV (i.e., no sediment particles were used).

In the PR-PIV experiments, images were captured when the blade was at a defined azimuthal position, ψ. This technique allowed the blade tip vortices to be studied as a function of wake age, ξ, which is defined as the time the flow structures (e.g., the vortices) have been in the wake in terms of degrees of blade rotation since they were formed. To this end, the rotor was instrumented with a Hall effect sensor that allowed measurements of rotational frequency. The sensor was mounted onto the rotor shaft support.

When a magnet on the rotor shaft passed by the sensor while the rotor was spinning, the changing magnetic field induced a current in the sensor. This once-per-revolution signal was conditioned and used to trigger and synchronize the laser and camera. A time delay could be implemented from the acquisition of the reference signal to capture images at a desired blade azimuth position. The blade azimuth angles studied with the PR-PIV were $\psi = 0^\circ$ to $\psi = 330^\circ$ in 30° increments.

2.4.3 Time-Resolved PIV

Because of the unsteadiness and aperiodicity of the flow, time-resolved PIV was used to study the time-history of the flow field and the entrained dust particles, i.e., this type of PIV allowed for high temporal resolution measurements of the flow field to be obtained. The principles of TR-PIV are similar to those of PR-PIV, except that instead of capturing images at prescribed azimuthal blade locations the images are recorded as a continuous time-history at a high frame-rate. The high-speed capability of TR-PIV allowed for the evolution of the tip vortices, as well as the developing flow over the ground plane, to be studied in some detail.

The same Nd:YLF high-speed laser and CMOS camera setup, as discussed previously in Section 2.3, were used to make the TR-PIV measurements. In this case, the laser and camera were both synchronized with a timing hub to allow image capturing at a frame rate of 1,000 fps. This high frame rate allowed enough light to enter the camera, while still preserving the full spatial resolution of the images. The pulse separation time in this case was set to $\Delta t = 20\ \mu$s, and 1,000 image pairs were recorded for each condition. Both

ROIs were studied using TR-PIV, with ROI 1 being imaged with a 105 mm focal length lens (15 cm-by-15 cm field of view) and ROI 2 being imaged with a 200 mm focal length lens (6.7 cm-by-6.7 cm field of view).

While a higher temporal resolution is the main benefit of using the TR-PIV system, the spatial resolution is lower than the resolution possible with the PR-PIV system. The high repetition rates of the TR-PIV system also requires the need to stream large amounts of data over short periods of time, the resolution of the high-speed camera used for the present work was limited to 1 Mp. In comparison, the PR-PIV system is only capable of making measurements at a maximum rate of 15 fps, but as previously mentioned, a 4 Mp resolution camera was used in this case.

2.4.4 Dual-Phase PIV

Dual-phase experiments were conducted using the TR-PIV system. In these experiments, the rotor was impulsively started and image capturing was initiated approximately 3 seconds (or 255 revolutions) later to allow the rotor to reach the desired rotational speed of 85 Hz. As previously described, the rotor was operated at a height of $z/R = 1.0$ off the ground plane for all of the experiments.

In each case, the sediment bed consisted of ten different sediment species. Each sediment sample had different properties that affected the values of the similarity parameters that were studied. The particle samples that were used were:

1. Glass microspheres of diameters 1–38 μm

2. Glass microspheres of diameters 45–63 μm

3. Glass microspheres of diameters 90–125 μm

4. Glass microspheres of diameters 53–63 μm (from sieving)

5. Glass microspheres of diameters 45–53 μm (from sieving)

6. Glass microspheres of diameters 90–106 μm (from sieving)

7. Kaolinite

8. Ottawa sand

9. Arizona Test Dust of diameters 0–5 μm

10. Arizona Test Dust of diameters 0–10 μm

Glass microspheres were chosen because they were well characterized with respect to their shape and size. Kaolinite was used because it is a naturally occurring clay-like material that is comprised of very small, non-cohesive particles. Ottawa sand was chosen because it has larger naturally occurring round particles and has become a standard material to use in the field of sedimentology and sediment transport science; see also Section 3.4.2. The two varieties of Arizona Test Dust (AZTD) were chosen because they were naturally occurring sediment samples that were also characterized by a consistent average particle size.

A sieving procedure was used to separate some of the species of glass microspheres (as noted above) and to narrow the range of particles so that the effects of particle size could be more precisely studied. The 45–63 μm diameter glass microspheres were passed through a sieve with a 53 μm mesh to yield the samples containing 53–63 μm and 45–53

μm particle diameters. The 90–125 μm diameter glass microspheres were passed through a sieve with a 106 μm mesh to yield the sample containing 90–106 μm diameter particles. Although sieving the 90–125 μm diameter particles also yielded 106–125 μm diameter particles, there was not enough sediment of this size to create a full bed, so it was not used.

2.4.5 Particle Recognition Technique

One challenge of making dual-phase measurements was in the proper separation of the dispersed-phase from the carrier-phase such that it could be analyzed independently with minimal cross-talk. In the present work, a thresholding technique [53] was used to discriminate between the two flow phases based on the intensity of laser light that was scattered by each phase. The light that was scattered by the dispersed-phase particles produced a higher intensity signal than the light scattered by carrier-phase particles. This property of the phases allowed a thresholding technique to be used to discriminate between the sediment particles and the tracer particles in each image.

To this end, a subset of dispersed phase images with pixel values $I_d(m,n)$ was created by using an algorithm that checked the intensity grayscale value of each pixel in a given image against a specified minimum threshold value, I_{thresh}. The integers m and n represent the pixel location in the image. If the pixel intensity was above the threshold value, it was considered part of the dispersed phase, otherwise it was considered part of

the carrier phase, i.e.,

$$I_d(m,n) = \begin{cases} I(m,n) & \text{if } I(m,n) \geq I_{\text{thresh}} \\ 0 & \text{otherwise} \end{cases} \tag{2.2}$$

The value of I_{thresh} is a user-defined grayscale value between 1 and 255, and was chosen as 40 for the present work because almost all of the sediment particles had an intensity above this value.

After thresholding, a particle identification algorithm was used to recognize groups of connected pixels as sediment particles. For example, if a pixel at location (i, j) possessed an intensity value of $I(i, j)$ that was greater than the threshold intensity value, I_{thresh}, the algorithm would then examine each of its eight neighboring pixels. Each neighboring pixel that met or exceeded the threshold intensity value was connected with pixel (i, j). This process was repeated until each particle in the thresholded image was identified by a connected group of pixels. Figure 2.7 illustrates this process, with the shaded squares representing pixels that have met the threshold and the arrows representing the checking of neighboring pixels.

The geometric center of each identified particle was then determined by finding the average X and Y coordinates of the connected pixels, i.e.,

$$X_c = \frac{1}{N}\sum_{k=1}^{N} X(i,j); \qquad Y_c = \frac{1}{N}\sum_{k=1}^{N} Y(i,j) \tag{2.3}$$

where N is the total number of pixels in the connected group, k is an integer assigned to each pixel in the group, and $X(i, j)$ and $Y(i, j)$ are the spatial locations of each pixel with respect to the entire image. The particle center, (X_c, Y_c), represents the location of the particle within the image.

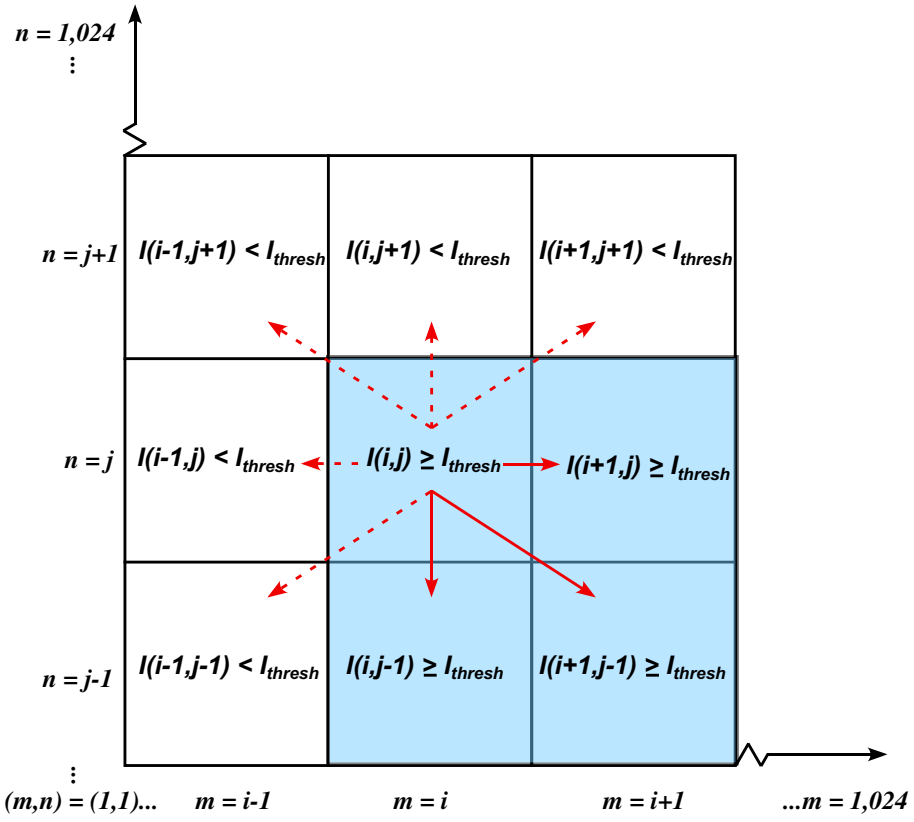

Figure 2.7: Particles were identified by connecting neighboring pixels that met the intensity threshold.

2.4.6 Challenges in the Flow Measurements

Making the various types of flow measurements described above presented several unique experimental and other challenges. For the FV, the smoke had to be introduced in a precise location to be entrained into the flow and illuminate the vortical flow structures in the rotor wake. The FV also required precise timing of the image capture system because the smoke would otherwise quickly saturate the dust chamber.

Accomplishing successful PIV measurements also posed several challenges. For example, the concentration of seeding had to be sufficient such that there were enough seed particles in the flow to allow for accurate cross-correlations, but not over-seeded to

the point where individual seed particles could no longer be discerned from other nearby seed particles. Also, careful selection of a Δt between image pairs was needed because it depends on several factors such as the maximum flow velocities and the size of the interrogation windows to be used for the cross-correlation process. On one hand, if Δt is too large, the tracer particles may have displacements that are too high, which can give inaccurate measurements of the flow velocities. Also, the particles may move out of the interrogation window, resulting in poor cross-correlations. On the other hand, if Δt is too small, then the particles may have sub-pixel displacements that cannot be accurately quantified.

Laser reflections from the ground plane made the cross-correlations here rather difficult. For example, Fig. 2.8(a) shows a region near the ground that is affected by such reflections. The individual seed particles there are masked by bright reflections and are no longer visible in the images, obviously preventing any PIV measurements in the near wall region. Such reflections were reduced by carefully aligning the laser light sheet such that the rays of light traveled more parallel to the ground plane and so passed directly above the surface without significant reflections being produced. Figure 2.8(b) shows the same region near the ground after such an alignment. Although this technique reduced the reflections, some reflections were inevitable when attempting to make velocity measurements directly above the ground plane.

In the dual-phase measurements, saltating sediment particles can saturate the images in the near-bed region, making the recognition of individual particles impossible. Regions of the flow that had the highest quantities of sediment uplift also had similar issues because the particles were so close together. In this case, the scattered light from

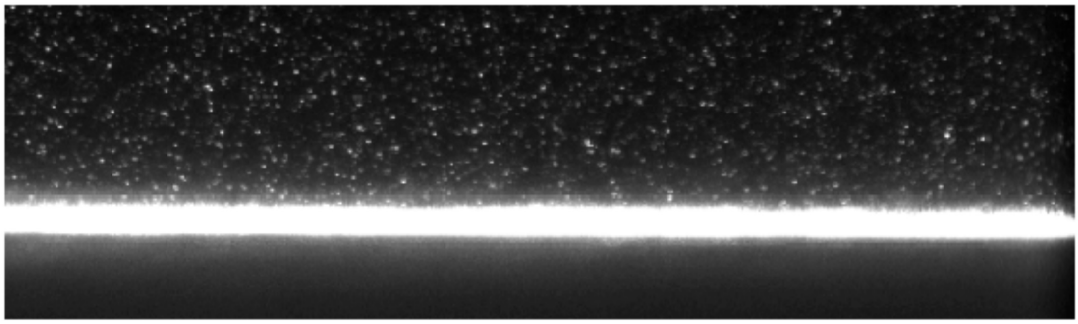

(a) Intense laser light sheet reflection at the ground

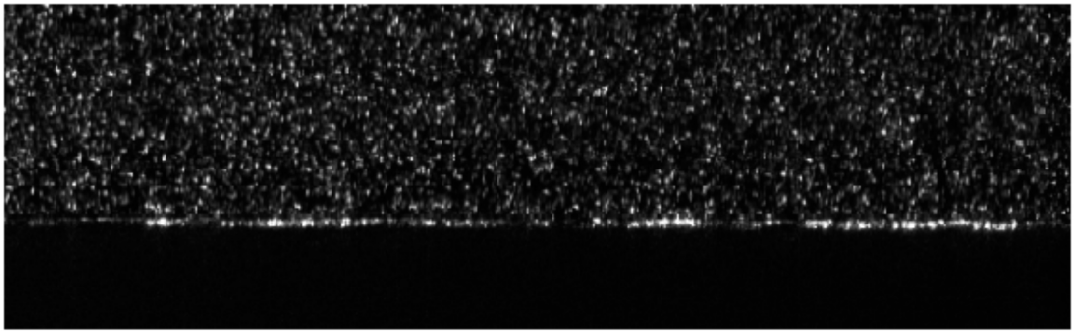

(b) Reduction of reflections after laser light sheet alignment

Figure 2.8: Reduction of laser light reflections near the ground by better alignment of the laser light sheet.

one particle merged from the scattered light from another, appearing as one large particle instead of two or more smaller ones. Consequently, the particle recognition algorithm can interpret this result as just one particle, or it may not recognize it at all based on the settings used in the particle identification analysis.

2.4.7 Uncertainties in PIV Measurements

Sources of uncertainty in the flow measurements using PIV include tracking errors of the tracer particles, background noise, interrogation window size, and others [48, 54]. Tracking errors are a result of the inability of the tracer particles to perfectly respond to

changes in flow velocities (i.e., the particles experience a finite amount of slip). Background noise in the image sensor of the cameras can cause spurious peaks in the cross-correlation, and may make it difficult to accurately determine the particle displacements if the signal-to-noise ratio is too low. All these sources of error affect the ability to accurately calculate the pixel displacements for the cross-correlation process. Another source of error in the PIV measurements is the uncertainty in the magnification factor, M, because there are always some uncertainties in the measurement of the size of the reference object. There is also some uncertainty in the determination of the pulse separation time, although it is very small.

For the present work, the uncertainty in the pixel displacements used to measure the velocity fields was estimated to be 4.7%. When combined with the uncertainties in the values of the pulse separation time, Δt (0.005%), and magnification factor, M (0.95%), the total propagated uncertainty in the flow velocity measurements was estimated to be 4.9% when using

$$\Delta U = \sqrt{\left(\Delta\varepsilon_{\Delta x}\frac{\partial U}{\partial \Delta x}\right)^2 + \left(\varepsilon_{\Delta t}\frac{\partial U}{\partial \Delta t}\right)^2 + \left(\varepsilon_M \frac{\partial U}{\partial M}\right)^2} \tag{2.4}$$

where $\varepsilon_{\Delta x}$, $\varepsilon_{\Delta t}$, and ε_M are the uncertainties in the pixel displacement, pulse separation time, and magnification factor, respectively.

2.4.8 Particle Identification Errors

In general, all of the particles in the imaged dual-phase flow cannot be identified because of limitations with the particle identification algorithm. For example, some particles may not scatter enough light and so will not be registered as a single sediment particle

because the signal is below the intensity threshold. Lowering the threshold is only effective up to a point because the grayscale values at the edges of a particle are typically lower than at the center, and so this approach may cause the inclusion of pixels that are actually part of the tracer particles rather than sediment particles. Furthermore, a lowered threshold would most likely increase the number of neighboring pixels that are part of a single particle, leading to artificially larger particles.

Such errors will also affect the calculation of the particle centroid, (X_c, Y_c). The uncertainty in the pixel location of X_c and Y_c was estimated to be 5 pixels for each value. If a position vector of the particle centroid is defined as $\mathbf{R} = (X_c, Y_c)$ with length $|\mathbf{R}| = \sqrt{X_c^2 + Y_c^2}$, then the uncertainty in $|\mathbf{R}|$ is

$$\Delta|\mathbf{R}| = \sqrt{\left(\varepsilon_{X_c}\frac{\partial|\mathbf{R}|}{\partial X_c}\right)^2 + \left(\varepsilon_{Y_c}\frac{\partial|\mathbf{R}|}{\partial Y_c}\right)^2} \tag{2.5}$$

where ε_{X_c} and ε_{Y_c} are the uncertainties in X_c and Y_c, respectively. The resulting uncertainty in the particle centroid was estimated to be 1.0% of the particle location. These errors also resulted in an uncertainty of 3.4% in particle concentration maps which was estimated by using

$$\Delta C = \sqrt{\left(\varepsilon_N\frac{\partial C}{\partial N}\right)^2 + \left(\varepsilon_{A_b}\frac{\partial C}{\partial A_b}\right)^2} \tag{2.6}$$

where N is the number of particles in a bin and A_b is the area of the bin, with ε_N and ε_{A_b} representing their uncertainties, respectively.

Another source of error is the high sediment particle concentration that occurs near the ground plane (as discussed in Section 2.4.6). If the edges of any particles overlap each other, then it is impossible to distinguish one particle from another, resulting in the recognition of fewer particles than are actually present in the flow. Because of such

errors, it was estimated that only 85% of the particles that were uplifted were actually successfully identified by the particle identification algorithm.

2.5 Summary

This chapter has described the experimental setup and methods used in the current work. The rotor system, ground plane, and dust chamber were described. The flow visualization technique and operating principles of PIV have been explained, and the experimental equipment used in each setup has been given. The present work utilized time-resolved flow visualization (TR-FV) to qualitatively study the single and dual-phase flows and PIV to gather quantitative data relevant to the problem. Phase-resolved particle image velocimetry (PR-PIV) and time-resolved particle image velocimetry (TR-PIV) were used to acquire velocity field measurements of the full flow field and of a near wall region. Dual-phase tests were conducted in both regions with different sediment samples using the time-resolved system. A particle thresholding technique was utilized to discriminate between the two phases, and a particle identification algorithm was used to identify individual particles as a group of connected pixels. Several challenges of performing flow measurements were also discussed.

Chapter 3

Results and Discussion

3.1 Overview

This chapter describes the results and analysis from the measurements made during the single-phase and dual-phase flow experiments with the rotor and the beds comprising the different sediment particles. Flow visualization was used to make qualitative observations of the rotor wake flow, especially as it convected in proximity to the ground plane, and to identify the regions of interest in the flow that needed to be studied in greater detail. Single-phase particle image velocimetry measurements were used to make quantitative measurements of the flow field, which better characterized the carrier flow near the ground plane. Dual-phase PIV experiments were performed and a particle identification algorithm was utilized to identify the airborne particles in the flow for the different sediment samples. The resulting data were used, in part, to generate suspended particle concentration maps to quantify and compare the effects of varying the selected similarity parameters on the uplift of sediment from the ground plane below the rotor.

3.2 Time-Resolved Flow Visualization

Single-phase, time-resolved flow visualization (FV) was primarily used to identify the flow structures present within the rotor wake as the rotor was operating near the ground

plane. FV was also used to qualitatively characterize certain significant features in the flow and to study their evolution over time. The dual-phase FV provided considerable insight into the regions of the flow where the majority of sediment mobilization and uplift was observed from the ground plane.

3.2.1 Single-Phase Flow Visualization

A precursor to understanding the much more complex dual-phase flow, is to properly understand the single-phase flow environment below the rotor. Figure 3.1 shows an instantaneous FV image of the flow field beneath the rotor at the ground plane with the rotor operating at a height of one rotor radius. Even superficially it can be seen that the flow is rather complex, consisting of a blade tip vortex embedded in the turbulent rotor wake, turbulent vortex sheets trailed behind the blade, and a developing turbulent wall flow at the ground plane. Notice that because a one-bladed rotor was used, the rotor trails a single helicoidal tip vortex in this case. This helicoidal wake initially contracts below the rotor disk, but quickly begins to radially expand as it encounters the presence of the ground plane. The concentrated vortex trailed from the blade tip convects along the wake slipstream boundary and then approaches the ground plane at a radial location of about $y/R = 1.4$ where y is the radial distance measured from the rotor shaft.

The darker voids seen in the FV images are characteristic signatures left by the blade tip vortex. These seed voids form primarily because of centrifugal effects on the seed particles resulting from the high swirl velocities in the vortex core, which causes them to spin outward away from the vortex axis [45]. As the parts of the vortex filament

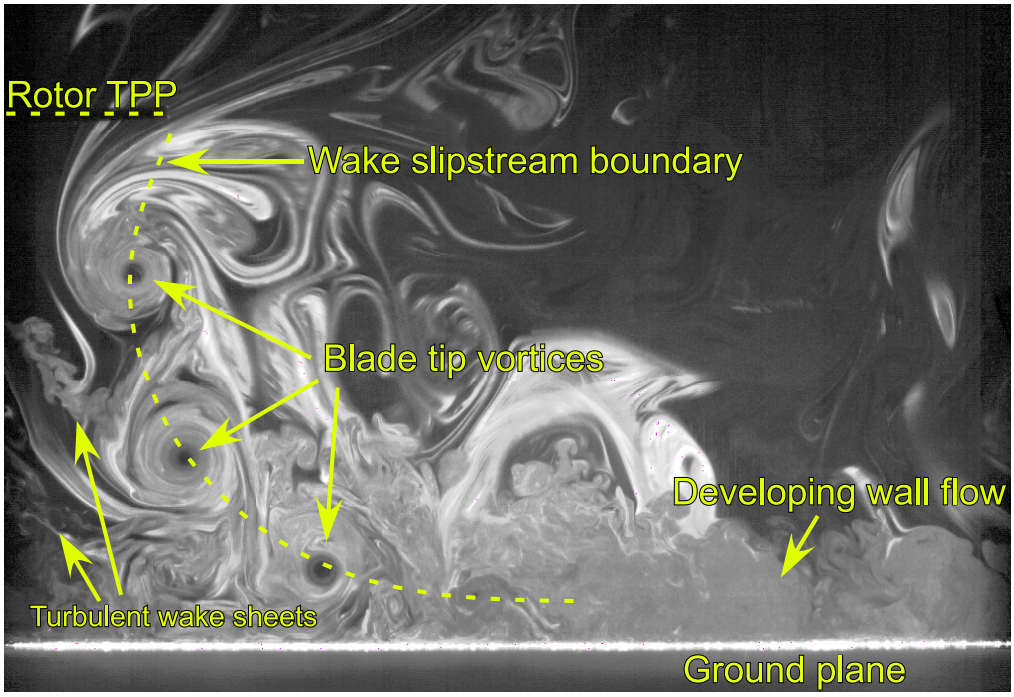

Figure 3.1: Single-phase flow visualization of a rotor in ground effect, $z/R = 1.0$.

impinge on the ground and reach older wake ages (3 to 4 revolutions old), the coherent vortex structure begins to break down and mix with the remainder of the flow, resulting in little or no visible seed void signatures of the vortex further downstream. Furthermore, the vortex has a tendency to persist to older wake ages than when the rotor is operating out of ground effect [1]. This behavior arises because of vortex stretching, which intensifies vorticity and commensurately increases the swirl velocity. The persistence of the tip vortex near the ground, as will be elaborated in later sections, greatly affects the flow as it develops over the ground plane.

The set of FV images shown in Fig. 3.2 also reveals that the flow induced by a one-bladed rotor has relatively low levels of aperiodicity compared to previous similar experimental studies such as [2] and [28], both of which have used a two-bladed rotor configuration. Although the flow generated here with the single bladed rotor is consid-

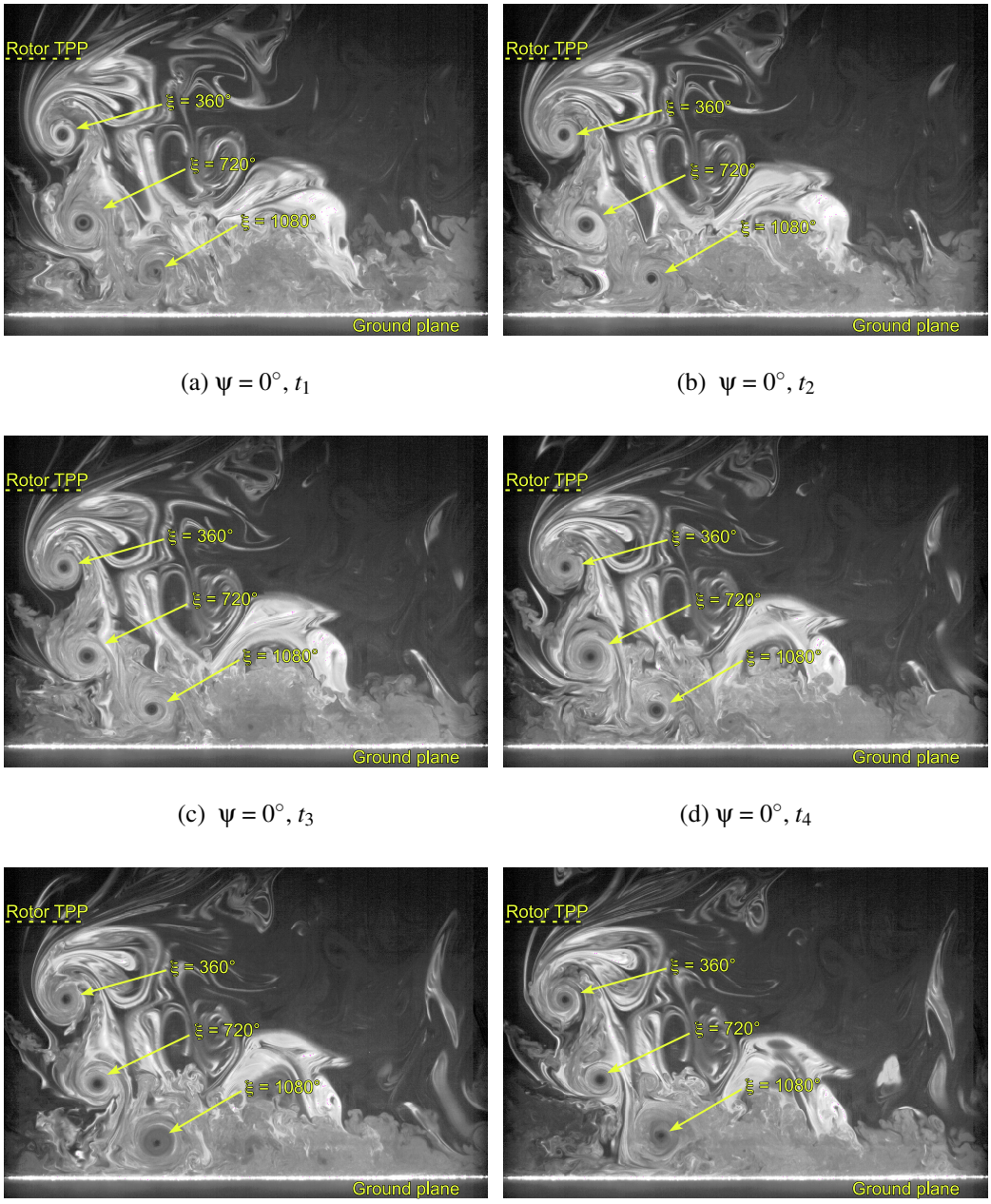

(a) $\psi = 0°, t_1$ (b) $\psi = 0°, t_2$

(c) $\psi = 0°, t_3$ (d) $\psi = 0°, t_4$

(e) $\psi = 0°, t_5$ (f) $\psi = 0°, t_6$

Figure 3.2: Flow visualization of the rotor flow in ground effect at a blade azimuth angle of $\psi = 0°$ to show the relatively low levels of aperiodicity and the repeatability of the flow induced by a one-bladed rotor at wake ages of $\xi = 360°$, 720°, and 1080°.

erably simplified compared to an actual helicopter rotor, it was still representative of the rotor wake flow and highly suitable for this study because of its relative simplicity. Each image in Fig. 3.2 was taken at a different instant in time, denoted by t_n.

It was noted that the rotor flow was very repeatable at the same wake age; this repeatability is highly desirable for the present study because the variability (i.e., non-repeatability) in the flow realizations between sequential test cases was all but eliminated. It is well known that adjacent vortices in a rotor wake can often pair and merge into a "supervortex," especially in multi-bladed rotor systems, mainly as a result of the relatively low helical pitch between vortex filaments and the excitation of unstable wake deformation modes [55]. This combined vortex flow can have significantly higher swirl velocities than a single vortex, and may significantly affect the uplift of sediment particles at the ground [28]. However, the wake generated by a one-bladed rotor is very periodic because it is more difficult to excite its unstable modes. Using the one-bladed rotor all but eliminated the occurrence of these aperiodic pairing and merging events, resulting in a cleaner and more periodic flow, and ensured that any major changes in the processes of sediment uplift would be attributed mostly to changes in the particle parameters rather than to the flow parameters.

More detailed FV was also performed for a near wall region imaging a field of view from $y/R = 1.75$ to $y/R = 2.60$ (i.e., ROI 2); see Fig. 3.3. This region was chosen because it was observed to be the region where the maximum quantity of sediment uplift occurred, and so it contained relatively high quantities of airborne sediment particles (as determined from the dual-phase measurements—see later in Section 3.2.2).

Figure 3.3 shows a FV image of the flow near the ground plane. In this case, the tip

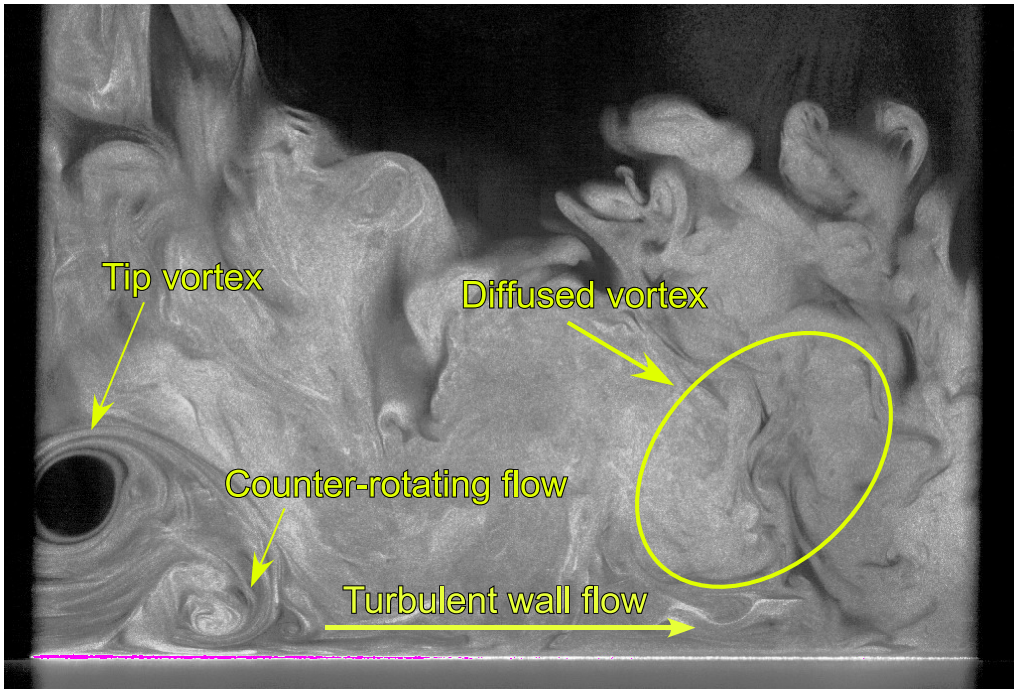

Figure 3.3: Flow visualization of near wall region, $y/R = 1.75$ to $y/R = 2.60$.

vortex has entered the image from the left. Notice that the vortex is inducing a counter-rotating flow region just ahead of it near the ground. Further downstream, the remnants of the previous (i.e., older) parts of the tip vortex are found; the elements of the vortex here quickly diffuse and the flow becomes more turbulent in this region. With parts of the vortex continuously passing by at once-per-rotor revolution, the near-wall flow is both unsteady and is still somewhat aperiodic. As will be described in the following sections, the overall unsteadiness in the flow significantly affects the flow velocity at a fixed point on the ground.

3.2.2 Dual-Phase Flow Visualization

Dual-phase FV was performed to study the corresponding two-phase flow. In this case, the sediment bed consisted of glass microspheres with diameters in the range of 45–63 μm and a mass density of 2,230 kg m^{-3}. Figure 3.4 shows an image taken during dual-phase tests when the blade was at an azimuth angle of $\psi = 0^\circ$ (i.e., the blade is in the plane of the light sheet and moving away from the observer). Immediately noticeable is that the region of sediment uplift is confined to downstream regions, although the vortices actually come close or impinge on the ground plane further upstream. Waves of sediment

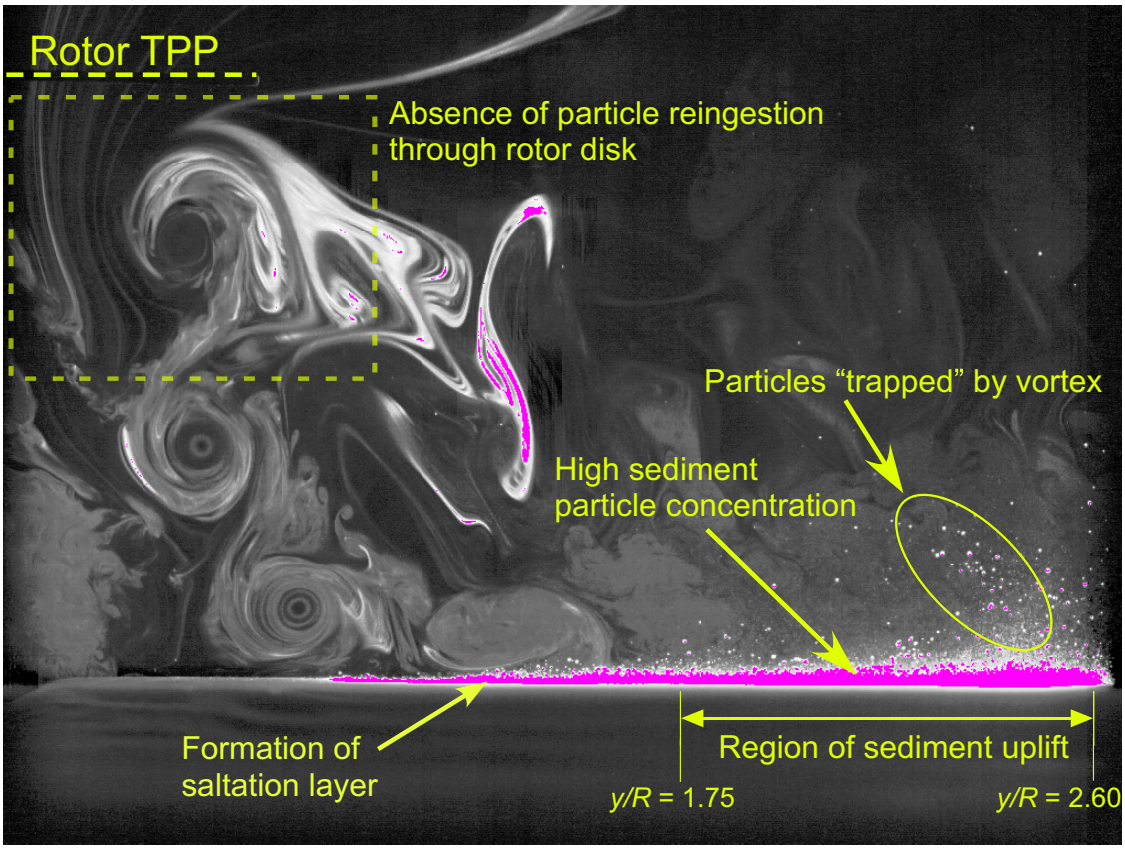

Figure 3.4: Dual-phase flow visualization with a sediment bed consisting of 45–63 μm glass microspheres on the ground plane.

particles are observed because the vortices uplift and "trap" sediment [28]. Closer to the rotor, there is little to no observable occurrence of particles there. However, it was observed that there was a forming saltation layer above the sediment bed that gradually thickens along the bed surface.

Also notable, is the concentrated region of sediment particles directly above the sediment bed in the downstream region. PIV measurements in the near bed region are challenging because no seed particles can be identified to establish cross-correlations (i.e., no PIV measurements can be made in this region). The sediment particle concentration also poses a problem for particle identification and tracking because the individual sediment particles in this region are no longer discernible as a consequence of the sheer number of particles that are present in the flow.

While there are waves of dust that are uplifted and suspended by the tip vortices, the particle field near the ground is relatively dilute and high particle concentrations are limited to the near wall region, at least when using this particular type of sediment. Furthermore, little in the way of uplift and reingestion of suspended particles through the rotor disk is seen, whereas this particular behavior seems to be a key feature in the formation of the most severe brownout clouds with actual rotorcraft [19].

Obviously, the properties of the sediment used as well as the operating conditions of the rotor will affect the processes of sediment entrainment and transport. To study the effects that scaling has on the uplift of sediment particles, various similarity parameters can be varied by using sediment samples with different properties, and the differences seen in the uplift of particles from the bed can then be measured. This was an important goal of subsequent parts of the present work, as will be described.

3.2.3 Summary

Single-phase and dual-phase flow visualization measurements were performed on the flow beneath a rotor hovering above a ground plane. The nature of the flow was studied and the flow structures present were identified. The flow generated by the rotor was observed to be very repeatable with low occurrences of vortex pairing and merging, as previously described. With the rotor operating in ground effect, the tip vortices were observed to persist to older wake ages because of reintensification of the vorticity from filament stretching. A near wall region from y/R = 1.75 to y/R = 2.60 was also studied because this region was identified to be a region responsible for much of the sediment uplift. The high particle concentration in the saltation layer, as will be described in detail later in this chapter, impeded the ability to perform PIV and particle identification in the region directly above the sediment bed.

3.3 Phase-Resolved PIV Results

This section describes the results from the phase-resolved PIV (PR-PIV) experiments. Measurements were taken over a range of blade azimuth angles from ψ= 0° to 330° in increments of 30°. Each data set consisted of 1,000 separate measurements. Phase-averaging of the measurements at each ψ was performed; the resulting phase-averaged measurements were used to characterize the properties of the tip vortex and to study the developing turbulent flow above the ground plane.

3.3.1 Vortex Characteristics

The blade tip vortices have previously been identified as a primary mechanism for sediment uplift in [2] and [28]. Therefore, it is important to precisely quantify the characteristics of the vortices that were produced by the rotor. Such quantities include the circulation, vortex Reynolds number, and swirl velocity profile. Measurements of other properties such as turbulence spectra may be useful, but were not performed in the present study.

The vortex Reynolds number is given by

$$Re_v = \frac{\Gamma_v}{\nu} \tag{3.1}$$

where Γ_v is the circulation contained in the vortex flow and ν is the coefficient of kinematic viscosity. The circulation is given by the closed loop line integral

$$\Gamma_v = \oint_C \mathbf{V} \cdot \mathbf{ds} \tag{3.2}$$

where $\mathbf{V}$ is the local fluid velocity and $\mathbf{ds}$ is the directed line segment aligned tangentially to the closed contour of integration, C. The circulation in the vortex was calculated using a circulation box method, as illustrated in Fig. 3.5. Any closed curve that does not intersect the vortex can be used, but for ease of calculation a rectangular contour was chosen in the present case. Because the velocity data calculated from the PIV were given at discrete locations over the flow field, a discrete form of the integral in Eq. 3.2 must be used. In this case, the integral in Eq. 3.2 can be written as

$$\Gamma_v = \oint_C \mathbf{V} \cdot \mathbf{ds} = \sum U_T \Delta x + V_T \Delta y \tag{3.3}$$

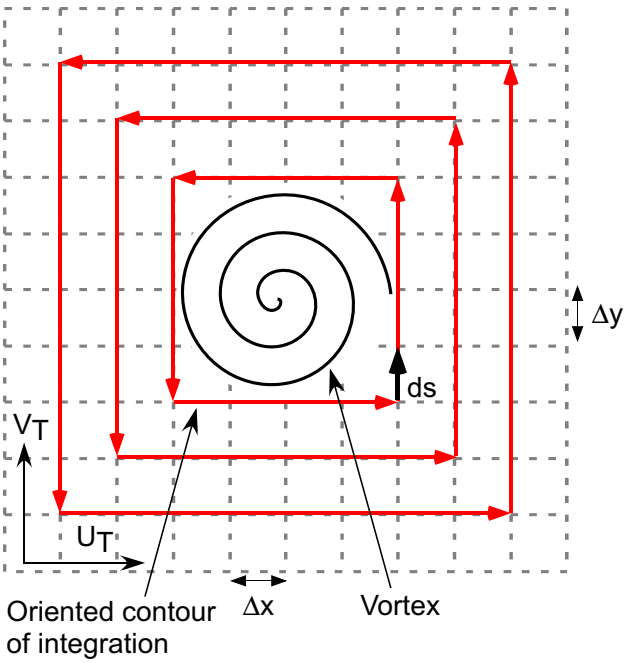

Figure 3.5: Circulation box method used to estimate the circulation of a vortex.

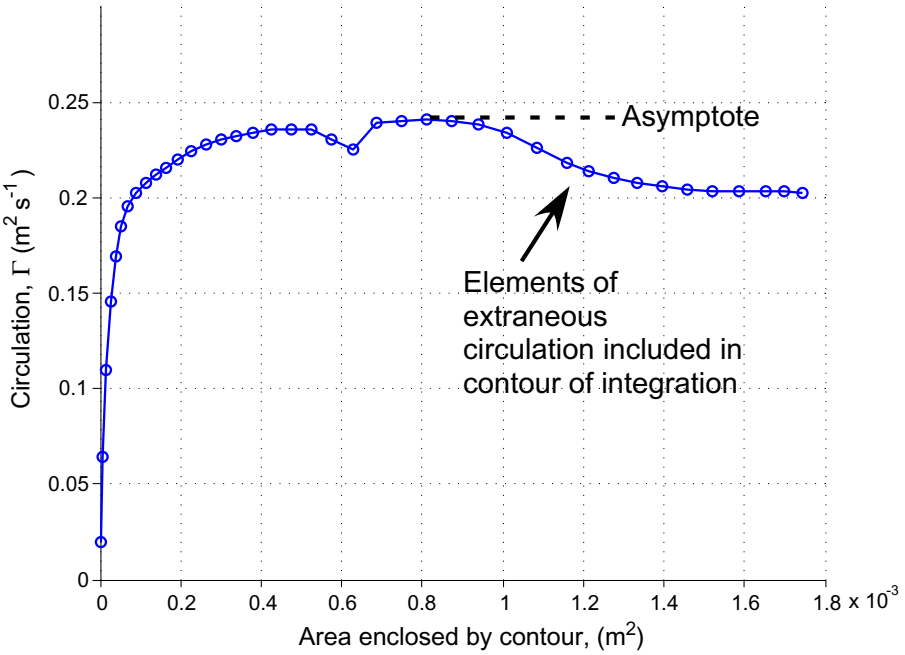

Figure 3.6: Integration process around the vortex (in this case at $\xi = 210°$) to estimate its circulation.

where U_T and V_T are the horizontal and vertical velocity components of the flow, tangential to the integration contour, respectively, and Δx and Δy are the corresponding grid spacings of the velocity field measurements.

A value for the circulation was found by first starting with a small closed contour, and then increasing its size until the calculated circulation reached a nominally constant value, as shown in Fig. 3.6. Care was taken not to encompass areas containing extraneous sources of circulation, such as nearby vortices or the blade itself, so that only the circulation of the vortex would be determined.

Using this contour integration method, the circulation contained in the vortex, for the given operating conditions of the rotor, was estimated to be 0.2410 m^2s^{-1} (2.594 ft^2s^{-1}), giving a vortex Reynolds number of about 16,000. Notice that these quantities were calculated for a vortex at a wake age of $\xi = 210^\circ$ because measurements of the entire vortex flow are available at this wake age. However the circulation is known to be relatively constant for all wake ages [56] because dissipation is a relatively slow process.

The swirl velocities in the vortex flow were also extracted from the PIV data. First, the center of the vortex was located and a vertical cut was taken through the data at that location, as shown in Fig. 3.7(a). The U velocity along the cut was then plotted as shown in Fig. 3.7(b) (in this case, the data shown are for a vortex at a wake age of $\xi = 210^\circ$). The velocity in Fig. 3.7(b) is the swirl or tangential velocity, $V_\theta(r)$, because with a vertical cut, the U and V velocities at the cut location represent the tangential and radial velocities of the flow, respectively. The maximum swirl velocity of the vortex was found to be about 10 ms^{-1}. From the location of the maximum swirl velocity, the core radius was estimated to be about 2 mm (0.0787 inches). In this case, the U velocity of the core is nearly

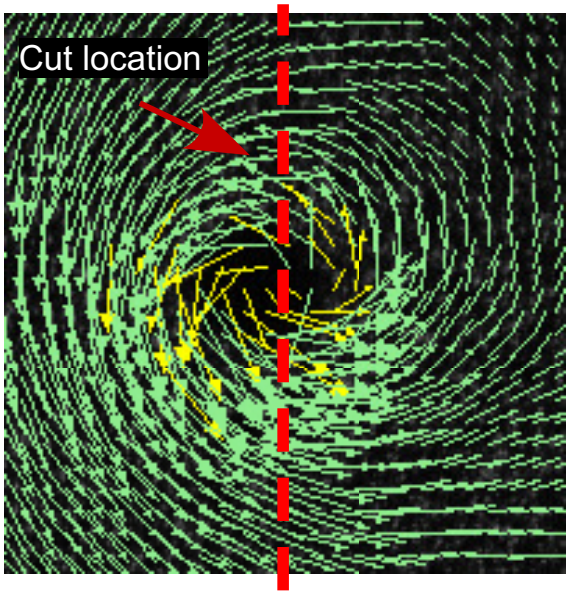

(a) Cut location in vortex flow

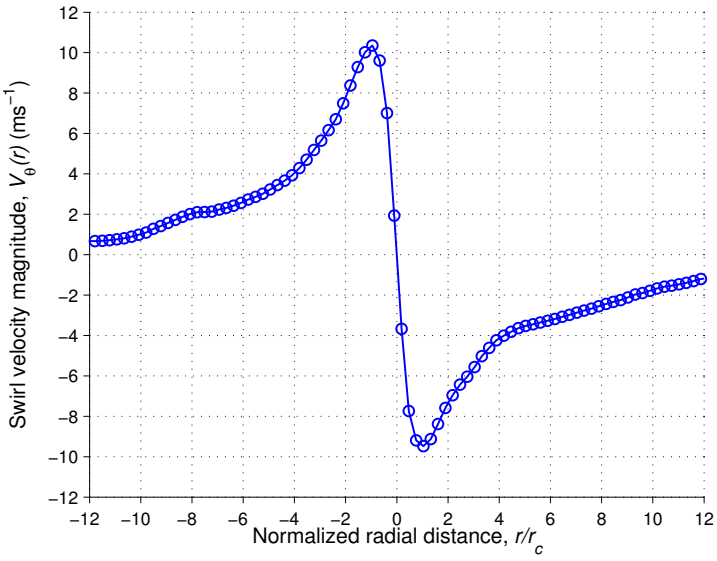

(b) Vortex swirl velocity, $V_\theta(r)$

Figure 3.7: PIV velocity field of a vortex at a wake age of $\xi = 210^\circ$ and the resulting swirl velocity profile.

zero because the cut is taken at a relatively early wake age when the vortex is primarily convecting vertically through the wake (i.e., the horizontal convection velocity of the core is very low).

Notice the relatively few number of points in the immediate core region, which is a result of the lower spatial resolution of the measurements relative to the magnitude of the velocity gradients; greater spatial resolution in the measurements would be required to increase the number of data points inside of the vortex core. Nevertheless, the present measurements still have sufficiently high spatial resolution to resolve the flow in the core region.

3.3.2 Wall Flow Characteristics

In the field of classical aeolian sciences, sediment uplift is often studied by assuming the flow above the particle bed is a steady uniform flow. However, directly underneath a rotor the flow is clearly different because of the unsteady effects caused by the passage of individual tip vortices.

Figure 3.8 shows contours of the wall-parallel or U velocity for the flow field for blade positions at $\psi = 0^\circ$ to 330° in 30° increments. Each measurement is an ensemble average of 1,000 PR-PIV images captured with the blade "phase-locked" at a given azimuth angle (i.e., they were phase-averaged). A red colored contour signifies that the flow is traveling to the right, or away from the rotor, and a blue colored contour signifies that the flow is traveling to the left, or towards the rotor; a red-blue pair signifies the "signature" of a vortex flow. On examining the velocity field near the ground, it is clear that

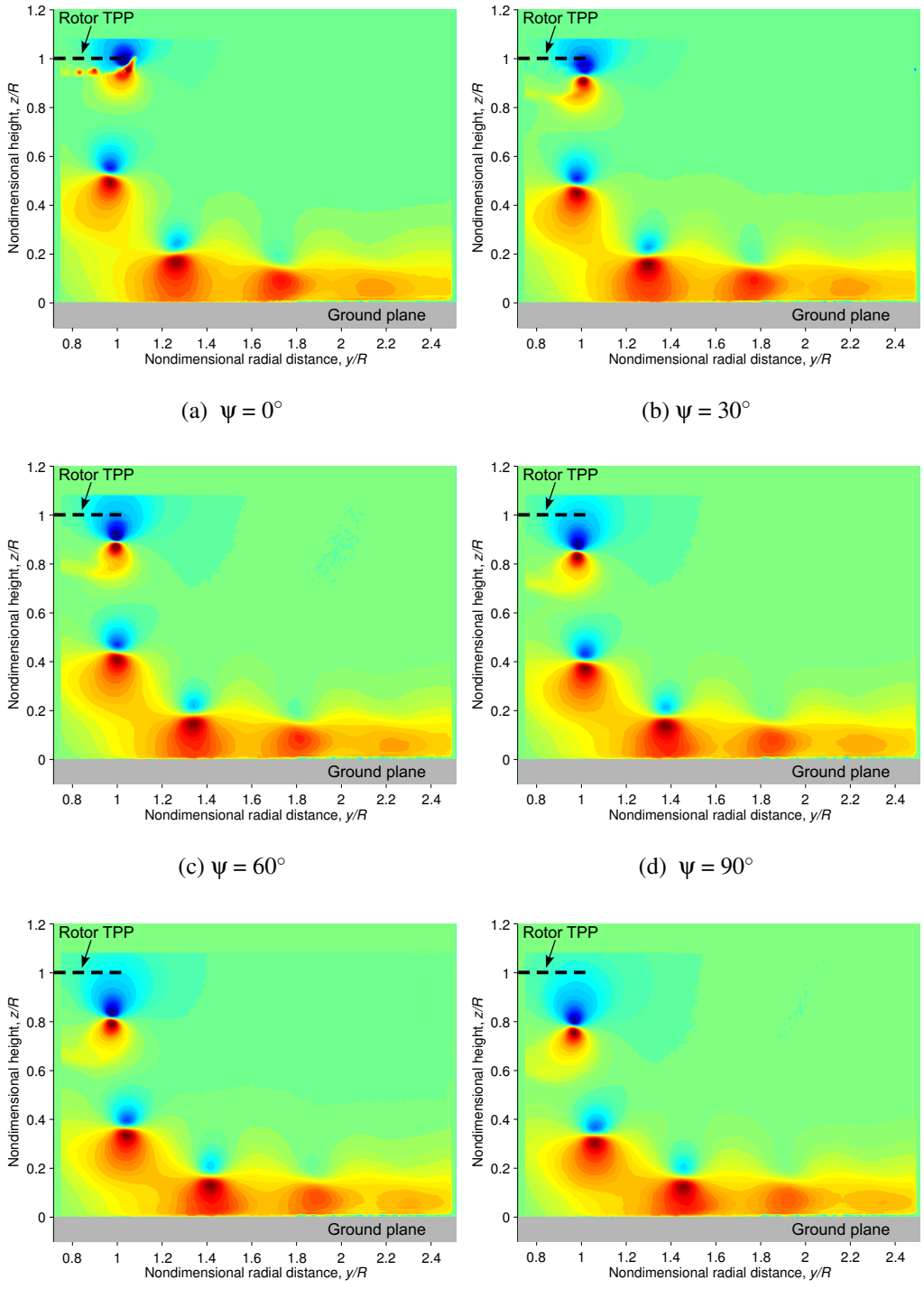

(a) $\psi = 0^\circ$ (b) $\psi = 30^\circ$

(c) $\psi = 60^\circ$ (d) $\psi = 90^\circ$

(e) $\psi = 120^\circ$ (f) $\psi = 150^\circ$

Figure 3.8: Phase-averaged velocity fields of the wall-parallel velocity shown for blade azimuth angles of $\psi = 0^\circ$ to 150° in 30° increments.

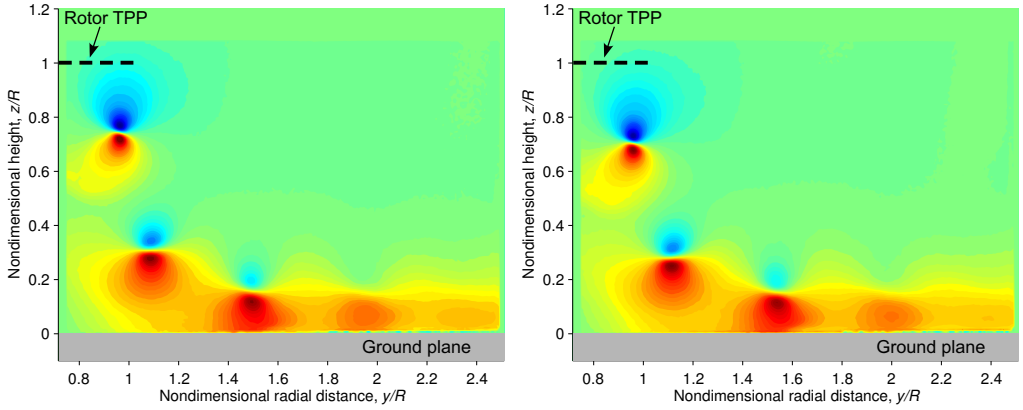

(g) $\psi = 180^\circ$ (h) $\psi = 210^\circ$

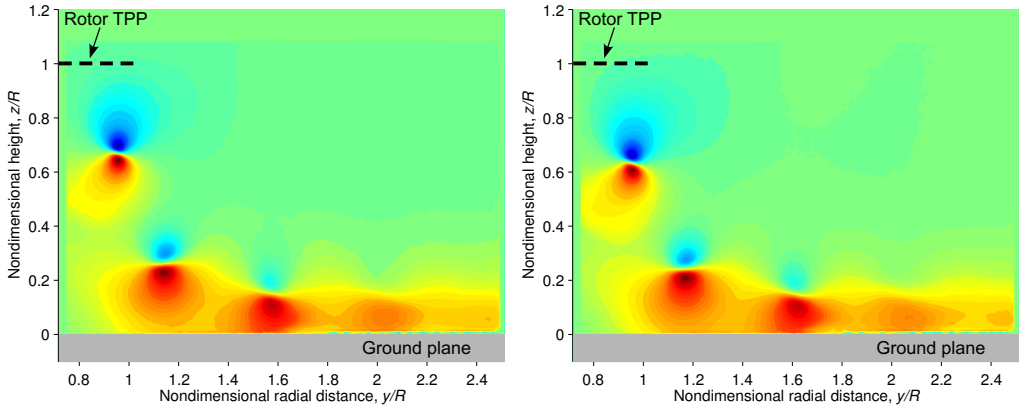

(i) $\psi = 240^\circ$ (j) $\psi = 270^\circ$

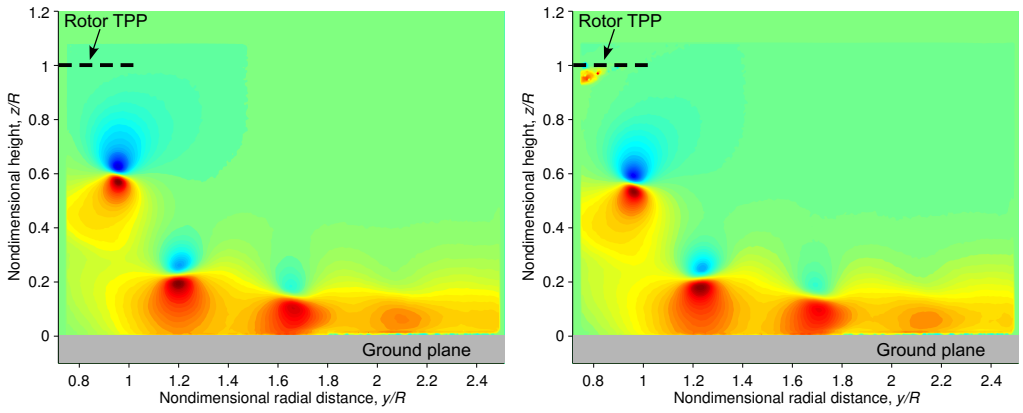

(k) $\psi = 300^\circ$ (l) $\psi = 330^\circ$

Figure 3.8: (Cont'd) Phase-averaged velocity fields of the wall-parallel velocity shown for blade azimuth angles of $\psi = 180^\circ$ to 330° in 30° increments.

the presence of a tip vortex alters the magnitude of the velocity of the flow at the wall, thereby causing significant unsteady fluctuations in the overall flow as it passes by.

To better show the influence of a passing vortex on the near-wall flow, a vertical cut through a radial location at $y/R = 2.07$ on the ground is plotted in Fig. 3.9. In Figs. 3.9(a), 3.9(c), and 3.9(e), contours of the phase-averaged wall-parallel velocity at the ground are shown with every 10th vector plotted along the x-axis to avoid congestion; all vectors are plotted along the y-axis. The corresponding plots of the wall flow velocity profile, as shown in Figs. 3.9(b), 3.9(d), and 3.9(f), illustrate the influence of a passing tip vortex on the phase-averaged velocity profile.

In Fig. 3.9(a), at a blade azimuth angle of $\psi = 0^\circ$, a vortex is convecting over and near to the ground plane and is just about to intersect the location of the defined cut. The corresponding velocity profile, as shown in Fig. 3.9(b), indicates that the flow there is still uninfluenced by the incoming vortex. Figure 3.9(d) shows the increased peak velocity of the wall flow from the vortex passing through the cut region at $\psi = 150^\circ$. Finally, Fig. 3.9(f) shows the velocity profile after the vortex has passed the cut location, and the wall flow velocity has returned to its more steady condition. Notice that the gray colored areas above the ground in Figs. 3.9(b), 3.9(d), and 3.9(f) indicate regions where the PIV cross-correlation algorithm produced erroneous data points. These "bad" vectors were caused by the laser light reflecting off the ground plane, which could only be minimized to a certain level.

As previously mentioned, in the field of aeolian sciences particle entrainment is often studied by using a uniform flow of velocity U. In that case, it is clear that the characteristic velocity of the flow, denoted by U_{char}, is defined as $U_{\text{char}} = U$. However,

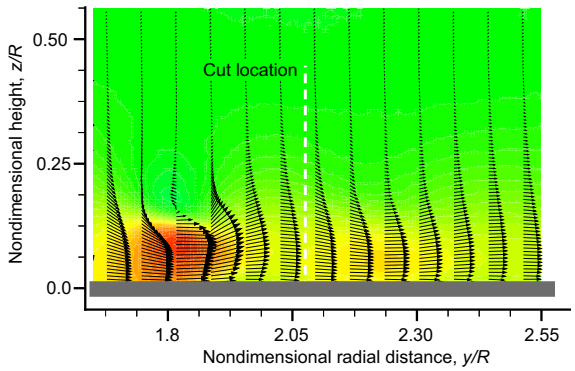

(a) Flow field at the ground, $\psi = 0°$

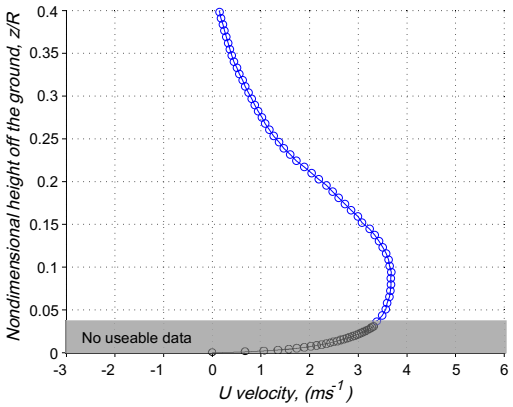

(b) Velocity profile at the ground, $\psi = 0°$

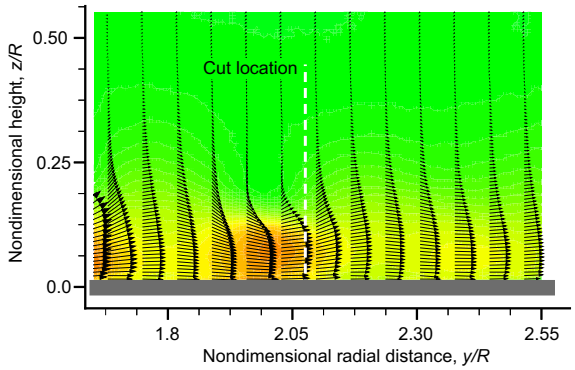

(c) Flow field at the ground, $\psi = 150°$

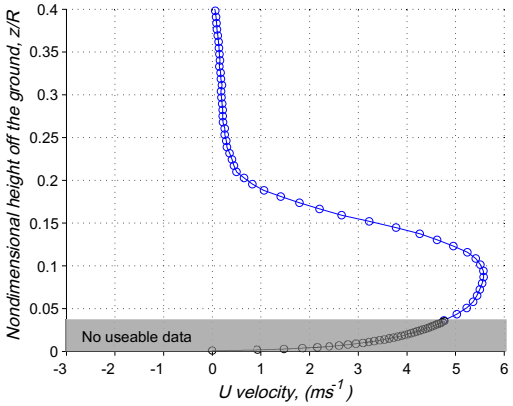

(d) Velocity profile at the ground, $\psi = 150°$

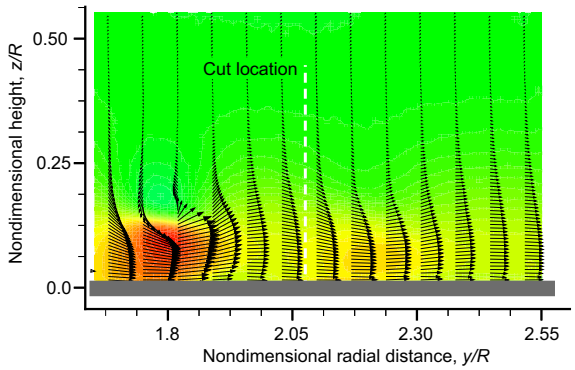

(e) Flow field at the ground, $\psi = 330°$

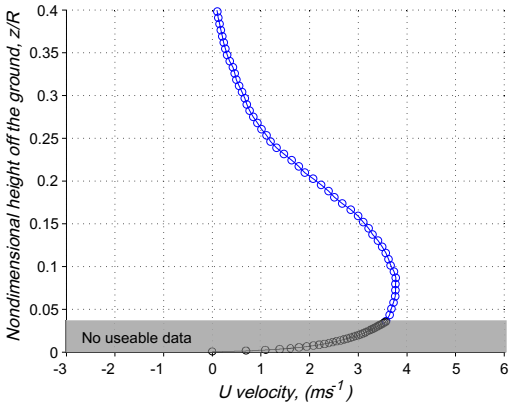

(f) Velocity profile at the ground, $\psi = 330°$

Figure 3.9: Fluctuation of flow velocity profile at the ground at $y/R = 2.07$ with the passage of a tip vortex at blade azimuth angles of $\psi = 0°, 150°, 330°$.

In the present work, the sequence of plots in Fig. 3.9 show the unsteady nature of the near-wall flow under the rotor, i.e., the velocity is not constant over time. Therefore, it is not immediately clear as to how to define U_{char} for the vortical rotor flow. However, it is clear that U_{char} must be characterized carefully because it is a key variable used for calculating many of the similarity parameters, such as the terminal velocity ratio, (U_{char}/U_F), the threshold velocity ratio, $(U_{\text{char}}/u_{*_t})$, and the densimetric Froude number, $U_{\text{char}}/(\sqrt{(\rho_s/\rho - 1)gD_p})$.

In the present work, U_{char} was defined as the average peak wall-parallel velocity over the ground plane from y/R = 1.75 to y/R = 2.60 because this was the region of the flow where many sediment particles were mobilized. The processes of sediment entrainment and transport are time-dependent phenomena, so time-resolved measurements were used to calculate U_{char}, as described in Section 3.4.1. The resulting velocity would be representative of the flow velocities (on average) over the sediment bed.

3.3.3 Summary

The results obtained from the phase-resolved PIV experiments have been analyzed. The blade tip vortices were studied and quantified by calculating their circulation, vortex Reynolds number, and by extracting the swirl velocity profile from the phase-averaged PIV measurements. The primary characteristics of the wall flow were also studied using PIV, and it was shown to be highly unsteady, exhibiting large velocity excursions from the mean flow with the passage of each blade tip vortex. In the aeolian sciences, particle entrainment is studied with uniform flows where the characteristic velocity is easily

defined. However the unsteady nature of the wall flow below a rotor makes it difficult to define a characteristic velocity for this flow. In this case, a method of averaging was proposed to calculate the characteristic velocity of the unsteady wall flow using time-resolved measurements, which is described later in Section 3.4.1.

3.4 Time-Resolved PIV Results

Single-phase and dual-phase measurements of the flow field under a rotor were acquired using time-resolved PIV (TR-PIV) where a continuous time-history of measurements could be taken. These measurements helped to characterize the wall flow as well as to quantify the effects of changing the similarity parameters on the entrainment of sediment particles. The similarity parameters for the two-phase flow were

1. Particle diameter-to-rotor radius ratio, D_p/R
2. Particle-to-fluid density ratio, ρ_s/ρ
3. Ratio of characteristic flow (or wind) speed to particle terminal speed, U_{char}/U_F
4. Densimetric Froude number, $U_{\text{char}}/(\sqrt{(\rho_s/\rho - 1)gD_p})$
5. Threshold friction speed ratio, U_{char}/u_{*_t}

The values of the similarity parameters were calculated for each type of sediment using the flow velocity measurements, along with results from the particle characterization studies. Instantaneous and time-averaged particle concentration maps of the flow were produced for each sediment sample. From this form of analysis, the effects of the similarity parameters on the processes of sediment uplift were then investigated.

3.4.1 Time-Averaged Wall Flow

The flow at the near wall region from y/R = 1.75 to y/R = 2.60 (i.e., ROI 2) was measured using single-phase, time-resolved PIV. The objective in this case was to extract a characteristic velocity, U_{char}, for the flow that could be used in calculating the selected nondimensional similarity parameters.

As previously mentioned, the wall flow is unsteady because of the passage of the tip vortex. To address this issue, a time-average of the flow field near the ground plane was computed. In the current work, 1,000 PIV images were captured in ROI 2, which corresponded to approximately 85 revolutions of the rotor. The data were then averaged using Eq. 3.4 where N is the total number of measurements (1,000 in this case), m is an integer denoting the measurement number, and (i, j) denotes the spatial location in the PIV measurement, i.e.,

$$U_{avg}(i,j) = \frac{1}{N}\sum_{m=1}^{N} U_m(i,j) \tag{3.4}$$

The result in this case is a time-average of the flow field near the ground plane, as shown in Fig. 3.10. Again, every 10th vector along the x-axis is shown here to avoid image congestion. It can be seen that the time-averaged wall flow no longer contains the unsteady velocity fluctuations from the tip vortices because they have been averaged out. The maximum velocity of the wall flow in this region is located at a height of about z/R = 0.10.

Using this averaged flow, a characteristic velocity then can be extracted. First, the peak U velocity of the wall flow was found for each radial station in the time-averaged PIV data. Then, the average of those peak velocities was computed, giving an average of

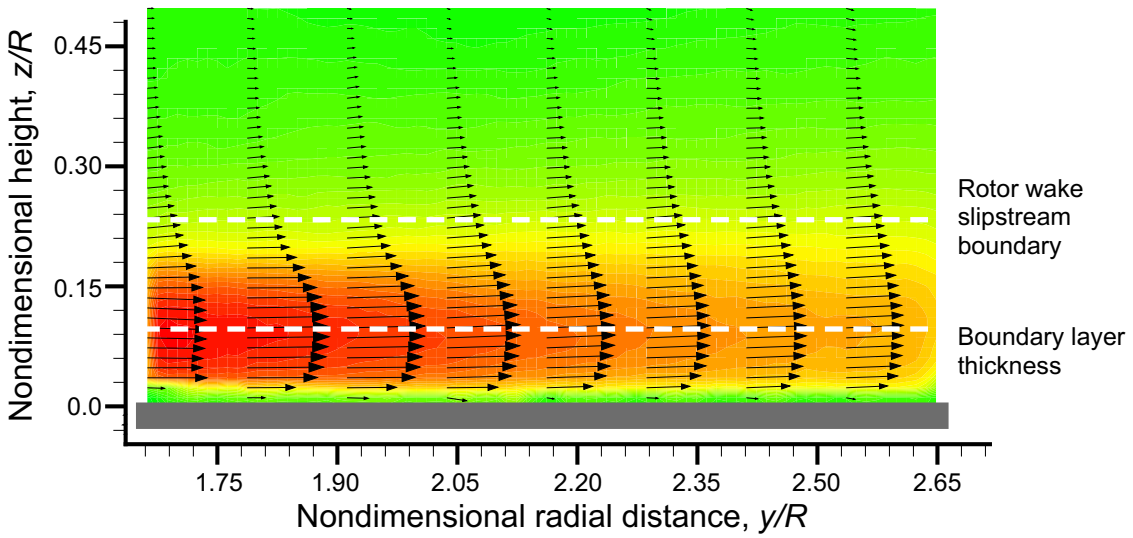

Figure 3.10: Contour plot of time-averaged wall flow in ROI 2.

the peak wall flow velocity, U_{char}, over this region. This result is given by

$$U_{\text{char}} = \frac{1}{N}\sum_{i=1}^{k} max(U(i)) \tag{3.5}$$

where k is the total number of data points in the radial direction, and $max(U(i))$ is the peak U velocity in the wall flow at radial index i in the time-averaged wall flow measurement. Using this process, the characteristic flow velocity of the wall flow at the conditions being studied was found to be $U_{\text{char}} = 4.104$ ms^{-1}.

3.4.2 Particle Characteristics

The selected similarity parameters depend on the physical properties of the particles (i.e., particle diameter and density) so it is important to accurately quantify these properties. As discussed in Chapter 2, ten different sediment samples were used in the current work to represent the particle bed. Each sample had unique size and material properties that will affect the aeolian similarity parameters. The properties quantified in this thesis

are the particle diameter and particle density, but the particle properties are not just limited to these quantities. The mineral composition for the naturally occurring samples was also obtained, and is given in Appendix A.

The particle size is used in calculating the ratio between the particle diameter, D_p, and the characteristic length, R (i.e., D_p/R). This ratio would be trivial to calculate if the sediment bed consisted of monodispersed particles (i.e., all particles were of the same diameter). However, a monodispersed particle bed is impossible to achieve in practice, and the sediment samples actually consist of a range of particle sizes. In this regard, it was necessary to measure the particle size distribution (PSD) for each sample. The information from a PSD can then be used to calculate a mean or effective diameter for each sample.

Two techniques were used to measure the particle sizes: 1. X-ray sedigraph and 2. Laser light scattering. Both tests were conducted by an outside laboratory. The X-ray sedigraph technique determined particle size by measuring the gravity induced settling rates of different size particles in a liquid with known properties. By using Stokes' law, the particle size can be calculated from the measured settling velocity. For this method to work successfully, the particle Reynolds number while settling must be less than 0.3 to use Stokes' law (i.e., laminar flow around a spherical particle). The mass frequency for each size was determined by using a beam of X-rays directed towards the settling particles in the liquid medium. The transmittance was measured as the particles settled and the attenuated intensity was used to calculate the mass fraction for a given particle size in the measuring zone. This technique can measure particle sizes within a range of D_p = 0.1–300 μm [57].

The laser light scattering technique is used to measure particles with a size range of $D_p = 0.1$–$1500\,\mu$m. This technique was used on the samples that have particles larger than could be measured by the sedigraph technique. The basic principle behind this method is that suspended particles in a liquid medium are illuminated with a laser light source. The light scattered by the particles is then captured by a photodetector device. Using Mie theory, the light scattering pattern data can be reduced and used to characterize the particles by size [58]. More detailed information on these methods can be found in [57] and [58].

Figures 3.11–3.17 show the results of the PSD tests for each sediment sample and a corresponding photograph taken with a microscope at 5x magnification. For each PSD, the mass frequency is plotted against the particle diameter. Notice that most of the samples have a Gaussian-like distribution with a single defining peak. The exception is the kaolinite, as shown in Fig. 3.14(a), which has a double peak in its PSD because it contains an increased frequency of two primary particle sizes rather than just one.

Once the particle size distribution is known, a mean value of the particle diameter for each sample can be calculated by using a weighted mean, as given by

$$D_{p,\text{mean}} = \frac{D_{p_1} p_1 + D_{p_2} p_2 + \ldots D_{p_n} p_n}{p_1 + p_2 \ldots + p_n} \tag{3.6}$$

because the distribution may be skewed towards a certain particle diameter. In this equation, D_{p_n} and p_n are the particle diameter and the corresponding mass frequency, respectively.

The mass density of each sample was also measured by taking a known mass of each sample and submerging it in a known volume of vegetable oil. Oil was used instead

of water because some compounds in the sediment could be soluble and would dissolve in water. The volume displacement of the oil was measured after adding the sediment, and the density for each sample was then calculated. The uncertainty in the density measurements was estimated to be $\pm$ 0.011 g cm^{-3}. Both the calculated mean particle diameter and the mass density for each sample is given in Table 3.1.

The microscope images shown in Figs. 3.12(b) and 3.13(b), indicate that the glass microspheres of diameter ranges 45–63 μm and 90–125 μm are almost uniformly spherical in shape and also exhibit little cohesion. As for the 1–38 μm diameter glass microspheres, it was difficult to confirm from the photograph in Fig. 3.11(b) if the particles were spherical or not. However, a photograph taken at 20-times magnification confirmed that those particles were indeed closely spherical. Figure 3.17(b) shows that the Ottawa sand has remarkably round-shaped grains, while the other naturally occurring samples contained more irregularly shaped grains, as shown in Figs, 3.14(b), 3.15(b), and 3.16(b). The finer samples were also observed to form aggregates and clumps of particles because of the greater levels cohesiveness between such particles.

In Fig. 3.18, the PSD for each of the glass microsphere samples are plotted together. Notice that the 45–63 μm and 90–125 μm diameter glass microspheres have a much narrower distribution than the 1–38 μm glass microspheres, which have a wider spread. Figure 3.18 shows that the two larger size ranges contain more particles that are closer to the calculated mean particle size than the smaller size range.

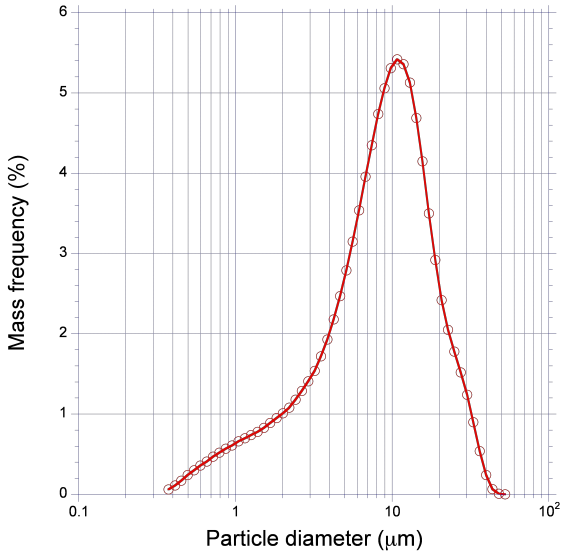

(a) PSD of 1–38 μm glass microspheres

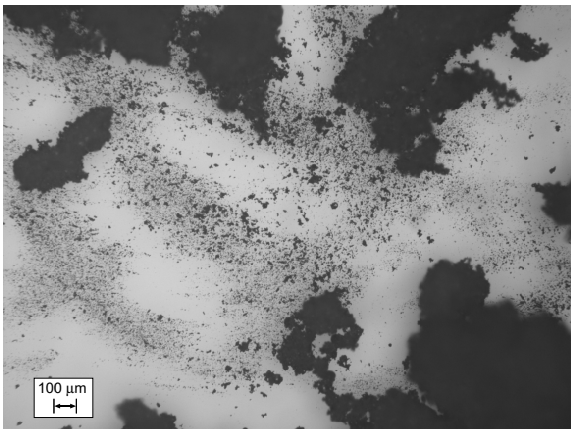

(b) 1–38 μm glass microspheres under a microscope

Figure 3.11: PSD and microscope image of the 1–38 μm microspheres.

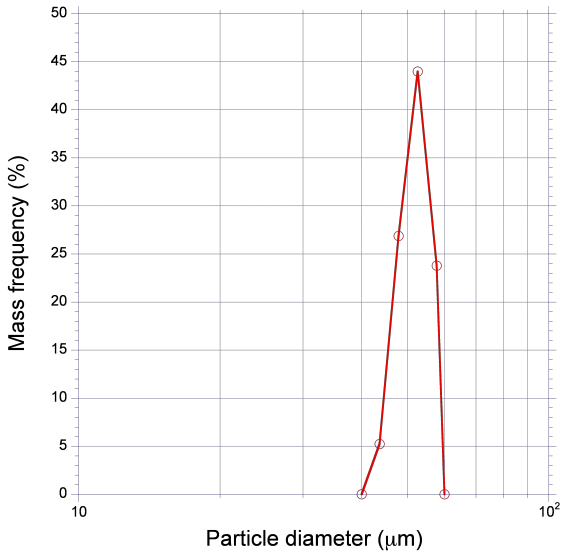

(a) PSD of 45–63 μm glass microspheres

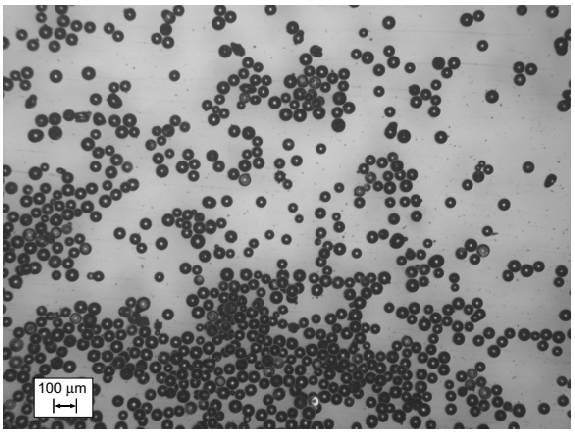

(b) 45–63 μm glass microspheres under a microscope

Figure 3.12: PSD and microscope image of the 45–63 μm microspheres.

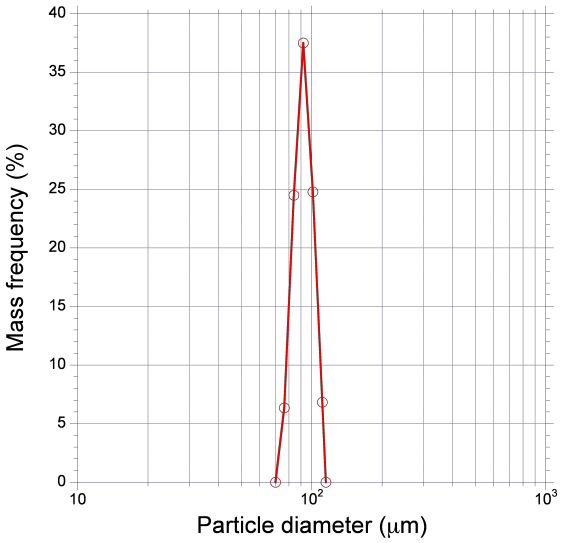

(a) PSD of 90–125 μm glass microspheres

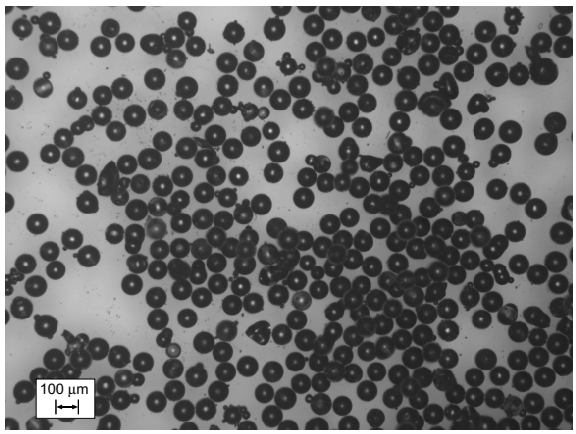

(b) 90–125 μm glass microspheres under a microscope

Figure 3.13: PSD and microscope image of the 90–125 μm microspheres.

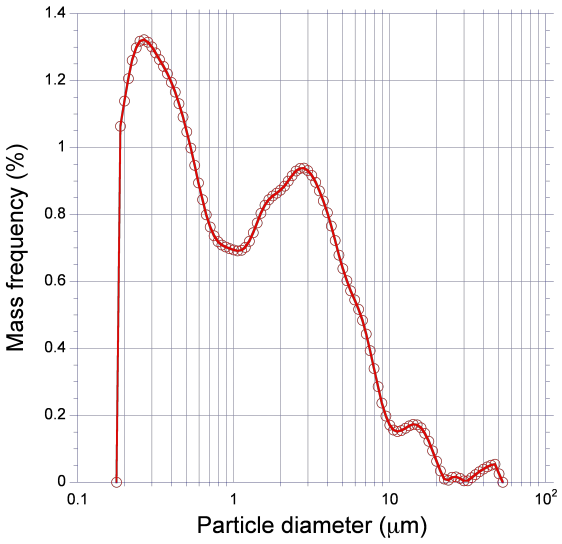

(a) PSD of Kaolinite

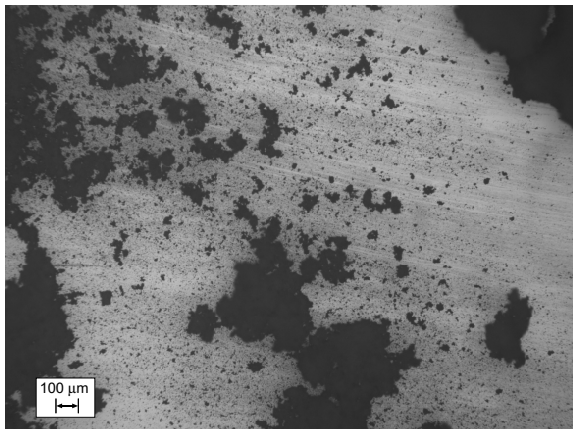

(b) Kaolinite under a microscope

Figure 3.14: PSD and microscope image of the kaolinite sediment sample.

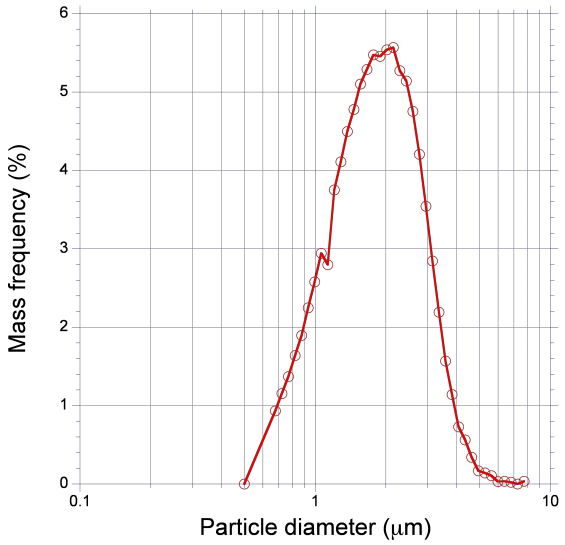

(a) PSD of Arizona Test Dust 0–5 μm

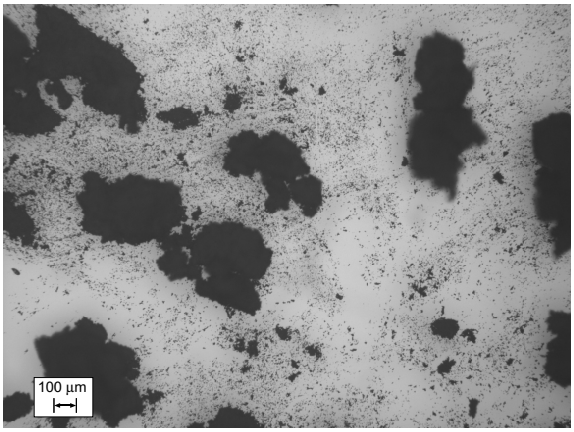

(b) Arizona Test Dust 0–5 μm under a microscope

Figure 3.15: PSD and microscope image of the Arizona Test Dust 0–5 μm sediment sample.

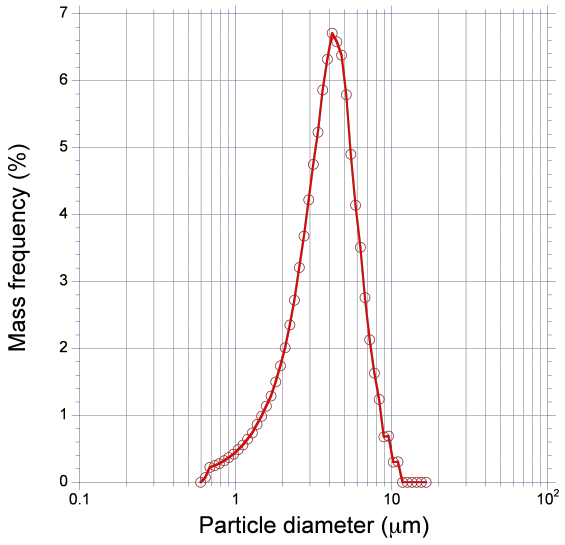

(a) PSD of Arizona Test Dust 0–10 μm

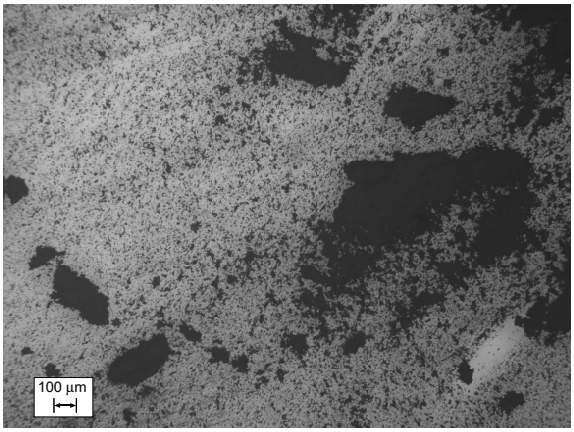

(b) Arizona Test Dust 0–10 μm under a microscope

Figure 3.16: PSD and microscope image of the Arizona Test Dust 0–10 μm sediment sample.

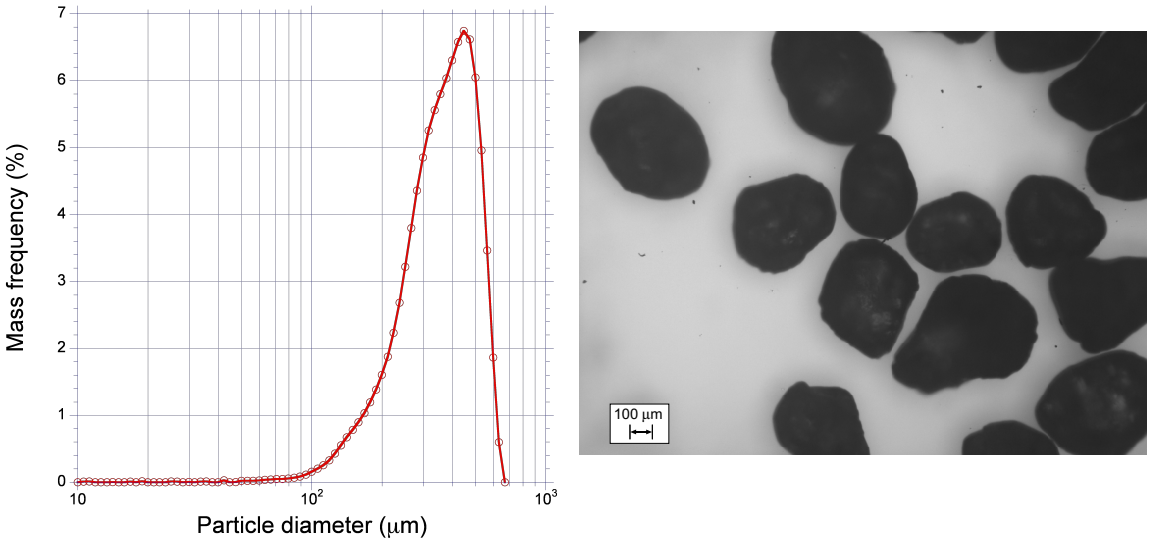

(a) PSD of Ottawa sand

(b) Ottawa sand under a microscope

Figure 3.17: PSD and microscope image of the Ottawa sand sediment sample.

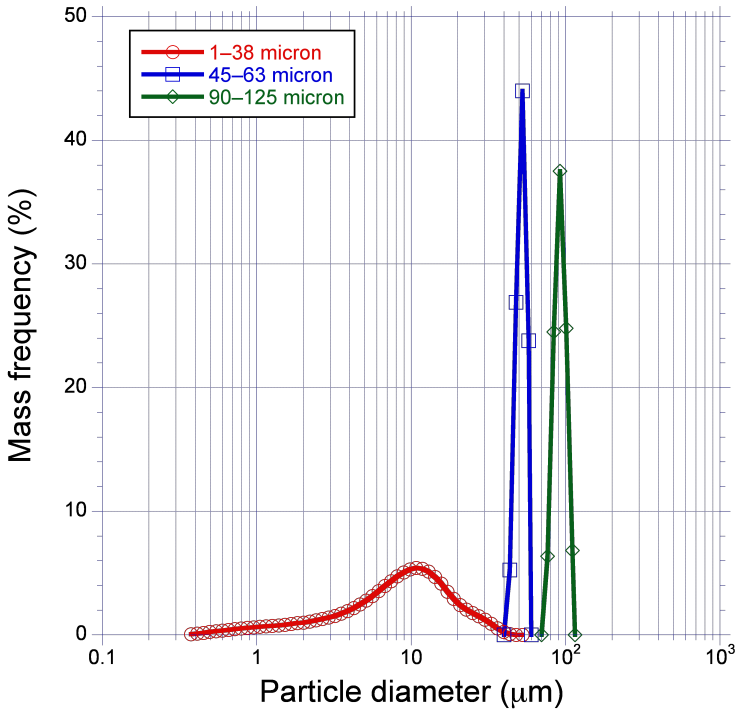

Figure 3.18: Combined PSDs of the glass microsphere particles.

Sediment sample	**Mean diameter, D_p (μm)**	**Mass density, ρ_s ($\mathbf{kg\,m^{-3}}$)**
Glass microspheres, 1–38 μm	10.80	2,475
Glass microspheres, 45–53 μm	47.24	2,535
Glass microspheres, 53–63 μm	54.43	2,578
Glass microspheres, 45–63 μm	54.61	2,238
Glass microspheres, 90–106 μm	91.26	2,453
Glass microspheres, 90–125 μm	97.04	2,217
Arizona Test Dust, 0–5 μm	1.81	2,630
Arizona Test Dust, 0–10 μm	3.549	2,640
Ottawa Sand	359.92	2,650
Kaolinite	1.49	2,160

Table 3.1: Calculated mean particle size and mass density measurements for each sediment sample.

3.4.3 Dual-Phase TR-PIV Results

Measurements of the dual-phase flow environment were made with each of the sediment samples placed on the bed below the rotor. A particle identification algorithm was used to give the location of each identified particle in the dual-phase measurements, as described previously in Section 2.4.5. This information was used to generate particle concentration maps that showed the location and relative concentration of the mobilized and uplifted particles over the measurement region. The basic idea in the use of this method was to expose the differences between sediment samples in the volume and spatial distribution of sediment particles that were uplifted from the bed by the action of the rotor flow.

An example of the process used for computing the concentration maps from the measured data is illustrated in Fig. 3.19. A raw dual-phase image, as shown in Fig. 3.19(a), is first analyzed with the particle identification software. Then, the resulting particle field is divided into a specified number of boxes or bins (32-by-32 bins in this case), as shown in Fig. 3.19(b). Each particle is then sorted into one of these bins by using the corresponding x- and y-coordinates of the particle centroid. After the binning procedure is complete, the number of particles in each bin is divided by the area of the bin to give a value with units of particles per unit area, which is a measure of the effective particle concentration in the flow. This concentration value can then be plotted as a contour map, as shown in Fig. 3.19(c). The areas of high particle concentration are represented by red colored contours and levels of low concentration are represented by blue colored contours.

Figure 3.20 shows the particle concentration maps generated from the instantaneous

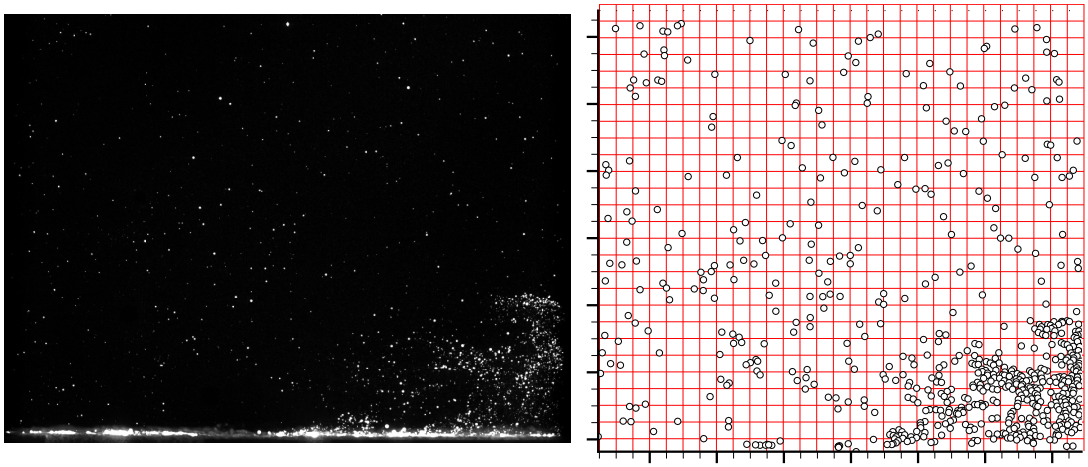

(a) Raw image of particle field

(b) Gridded image after particle identification

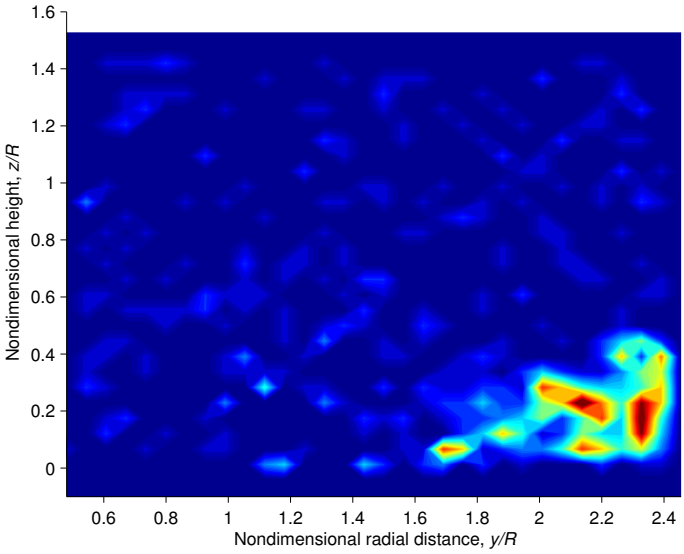

(c) Resulting particle concentration map

Figure 3.19: Example of process used to generate particle concentration maps.

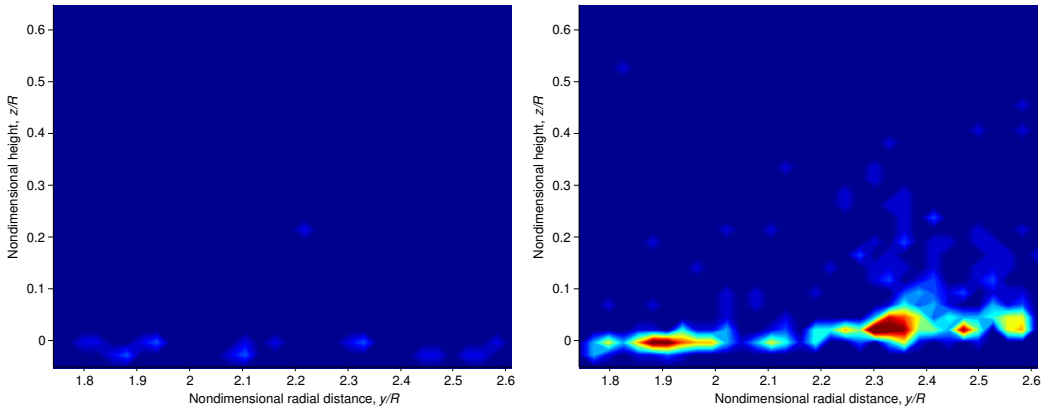

(a) 1–38 μm glass microspheres

(b) 45–53 μm glass microspheres

(c) 45–63 μm glass microspheres

(d) 53–63 μm glass microspheres

(e) 90–106 μm glass microspheres

(f) 90–125 μm glass microspheres

Figure 3.20: Particle concentration maps showing the variance in the quantity and location of particles uplifted between glass microsphere sediment samples.

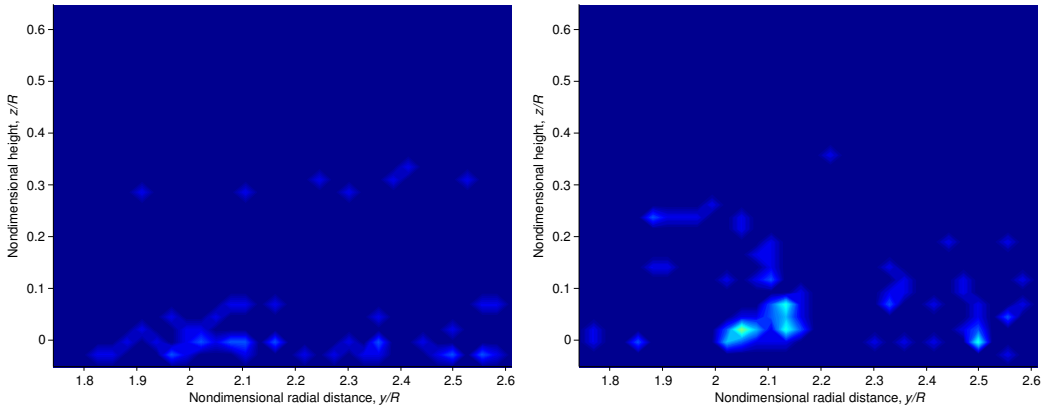

(g) AZTD 0–5 μm

(h) AZTD 0–10 μm

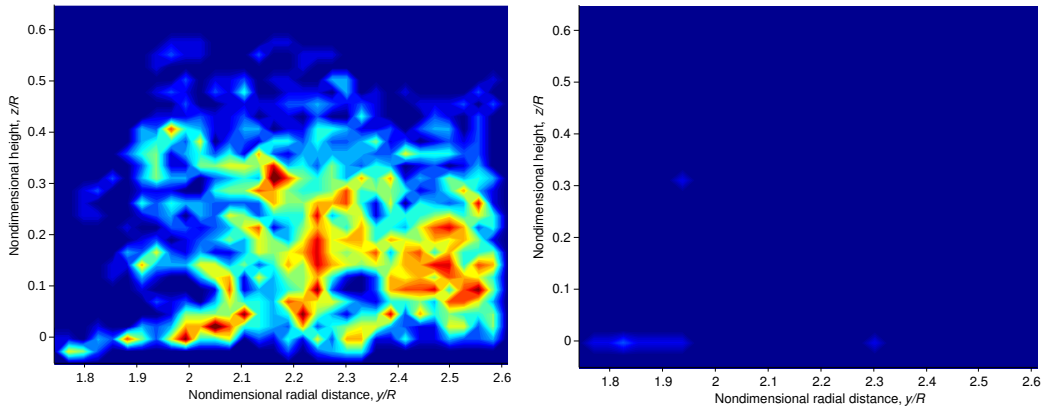

(i) Kaolinite

(j) Ottawa sand

Figure 3.20: (Cont'd) Particle concentration maps showing the variance in the quantity and location particles uplifted between the naturally occurring sediment samples. Images are from ROI 2.

measurements for each sediment sample in ROI 2. The data shown are from rotor wake flows that are at approximately the same wake ages. Figures 3.20(a)–3.20(f) show the concentration maps for the different samples of glass microspheres, and Figs. 3.20(g)–3.20(j) show the concentration maps for the remainder of the sediment samples. All of the glass microspheres tend to have similar uplift patterns, with the exception of the 1–

38 μm diameter glass microspheres where significantly fewer suspended particles were observed. The 90–125 μm and 90–106 μm diameter glass microspheres showed slightly fewer particles higher above the bed compared to the 45–53 μm, 53–63 μm, and 45–63 μm diameter glass microspheres, but in general, the concentration maps were similar near the ground. As shown in Figs. 3.20(g) and 3.20(h), the Arizona Test Dust (AZTD) samples experienced relatively low levels of uplift, and no significant difference was observed in this case between the two diameter ranges.

In Fig. 3.20(i), it is apparent that the kaolinite exhibited a tremendous amount of uplift, with many regions in the flow having high particle concentrations. The particles are also transported to greater heights above the sediment bed as compared to the other samples. In contrast, the Ottawa sand exhibits almost no particle uplift, as shown in Fig. 3.20(j), which is a result of its greater threshold conditions for the onset of mobility, as explained later in Section 3.4.9.

While analyzing the instantaneous measurements is useful, any aperiodic pairing and merging of adjacent parts of the vortex filament can lead to increased sediment uplift and can artificially skew the comparison. To address this issue, time-average particle concentration maps were also generated by averaging 1,000 instantaneous TR-PIV measurements. Figure 3.21 shows the results of this time-averaging. Time-averaging reveals that the particle concentration maps for most of the glass microspheres, as shown in Fig. 3.21(b)–3.21(f), are almost identical over time with respect to the location of particles and the particle concentration. Once again, the 1–38 μm particle sample, on average, exhibits very little uplift from below the rotor, as shown in Fig. 3.21(a).

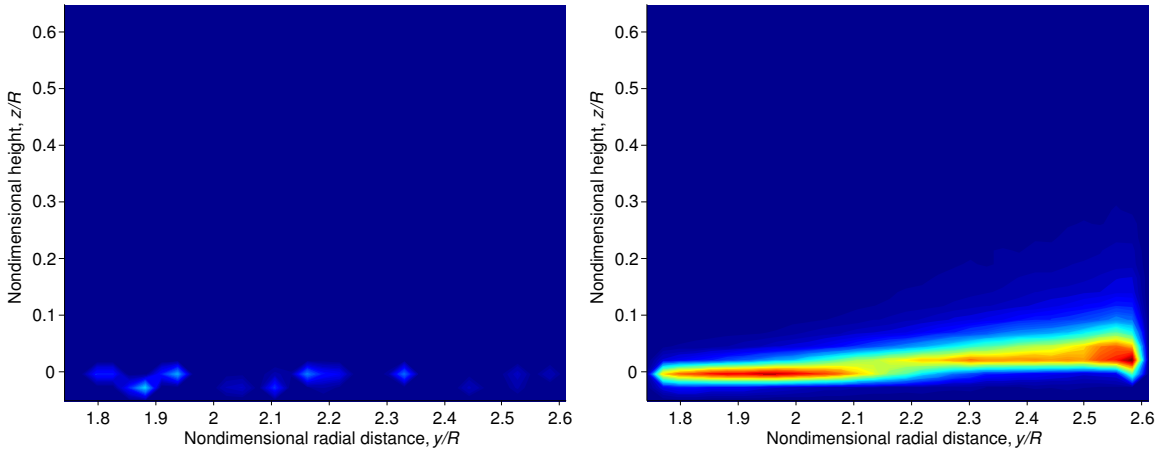

(a) 1–38 μm glass microspheres

(b) 45–53 μm glass microspheres

(c) 45–63 μm glass microspheres

(d) 53–63 μm glass microspheres

(e) 90–106 μm glass microspheres

(f) 90–125 μm glass microspheres

Figure 3.21: Time-averaged particle concentration maps.

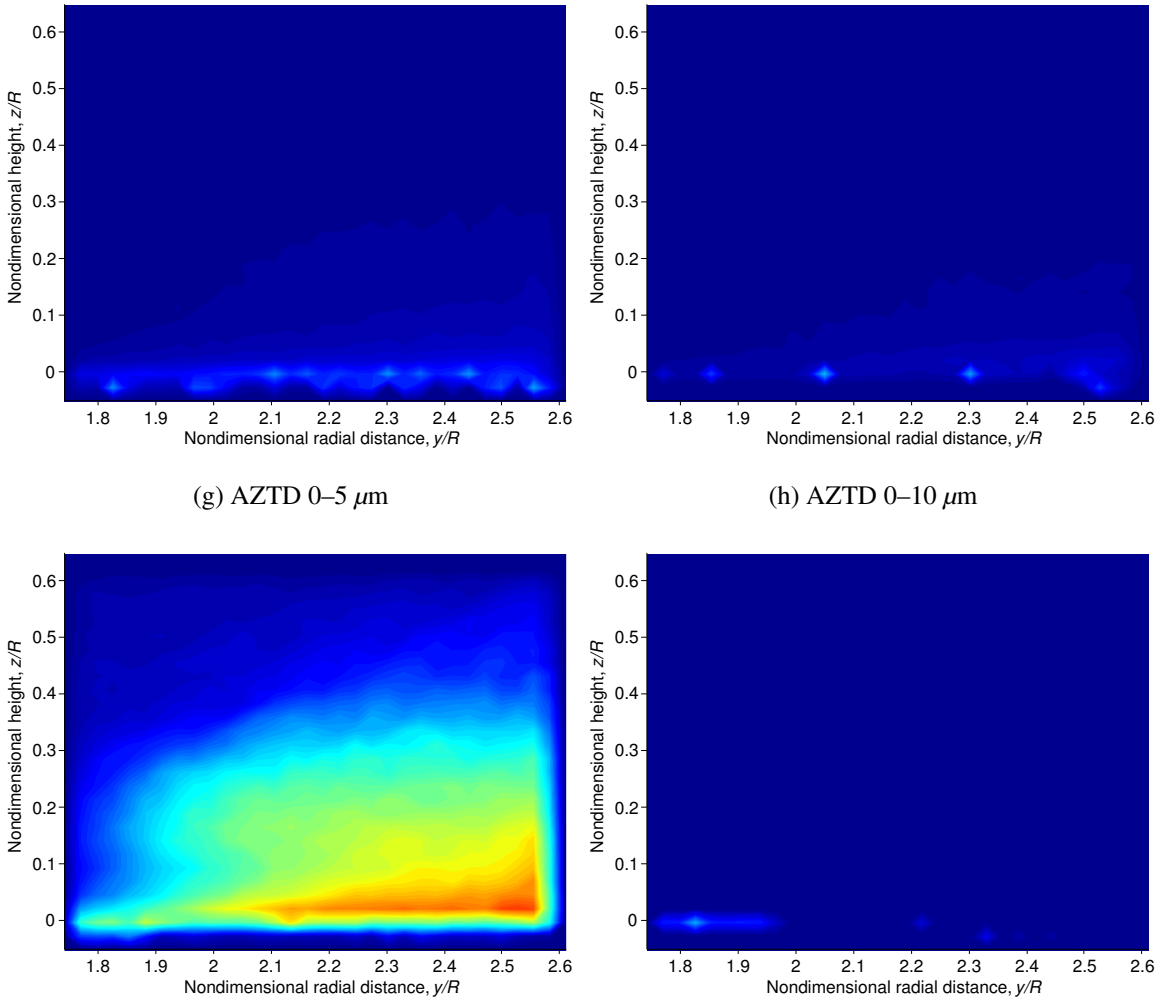

(g) AZTD 0–5 μm

(h) AZTD 0–10 μm

(i) Kaolinite

(j) Ottawa sand

Figure 3.21: (Cont'd) Time-averaged particle concentration maps.

In Figs. 3.21(g) and 3.21(h), the Arizona Test Dust samples both experienced low levels of uplift, with the 0–5 μm diameter range showing slightly more particles suspended above the bed as compared to particles in the 0–10 μm diameter range. Again, the kaolinite occupied most of the region, although the regions of higher particle concentration in this case were limited to near the bed surface, as shown in Fig. 3.21(i). In Fig. 3.21(j), it is clear that the Ottawa sand showed little uplift because of its greater threshold for mobility,

as will be discussed further later.

A study was conducted to examine whether the differences seen in the particle concentration maps between the samples can be correlated with the changes in the values of the five selected aeolian similarity parameters, as given in Table 3.2. Using the wall flow and particle characteristics that have been calculated in the previous sections, the similarity parameters for each sediment group were calculated and are listed in Table 3.2. Notice that large (sometimes orders of magnitude) differences were obtained between the samples. Although the threshold friction velocity, u_{*t}, was not directly measured in the present work, a semi-empirical model was used to estimate its value for each sample, which is explained in Section 3.4.8.

Sediment sample	D_p/R	ρ_s/ρ	U_{char}/U_F	$U_{\text{char}}/\sqrt{(\rho_s/\rho-1)gD_p}$	U_{char}/u_{*_t}
Glass microspheres, 1–38 μm	1.40×10^{-4}	2,101	493	8.70	86.97
Glass microspheres, 45–53 μm	6.13×10^{-4}	2,153	27	4.11	41.08
Glass microspheres, 53–63 μm	7.09×10^{-5}	1,900	23	3.80	37.95
Glass microspheres, 45–63 μm	7.07×10^{-5}	2,189	20	4.06	40.67
Glass microspheres, 90–106 μm	1.18×10^{-3}	2,083	8.53	3.01	30.05
Glass microspheres, 90–125 μm	1.26×10^{-3}	1,883	8.42	3.06	30.65
Arizona Test Dust, 0–5 μm	2.35×10^{-5}	2,233	16,291	20.6	205.89
Arizona Test Dust, 0–10 μm	4.61×10^{-5}	2,241	4,243	14.7	146.90
Ottawa Sand	4.67×10^{-3}	2,250	1.21	1.46	14.56
Kaolinite	1.93×10^{-5}	1,834	29,362	25.1	250.60

Table 3.2: Calculated similarity parameters for each sediment sample for this flow.

3.4.4 Effect of Particle Size on Entrainment

The effect of particle size on entrainment is shown in Fig. 3.22. On the y-axis is the normalized number of uplifted particles, and on the x-axis is the particle diameter-to-rotor radius ratio, D_p/R. The average number of particles per measurement for each sediment group was normalized by the sample that had the highest average number of uplifted particles, which was the kaolinite in this case. Figure 3.22 suggests that the changes in the quantity of entrained sediment particles can be correlated with changes in particle size. As the size increases, the number of suspended particles drops off sharply,

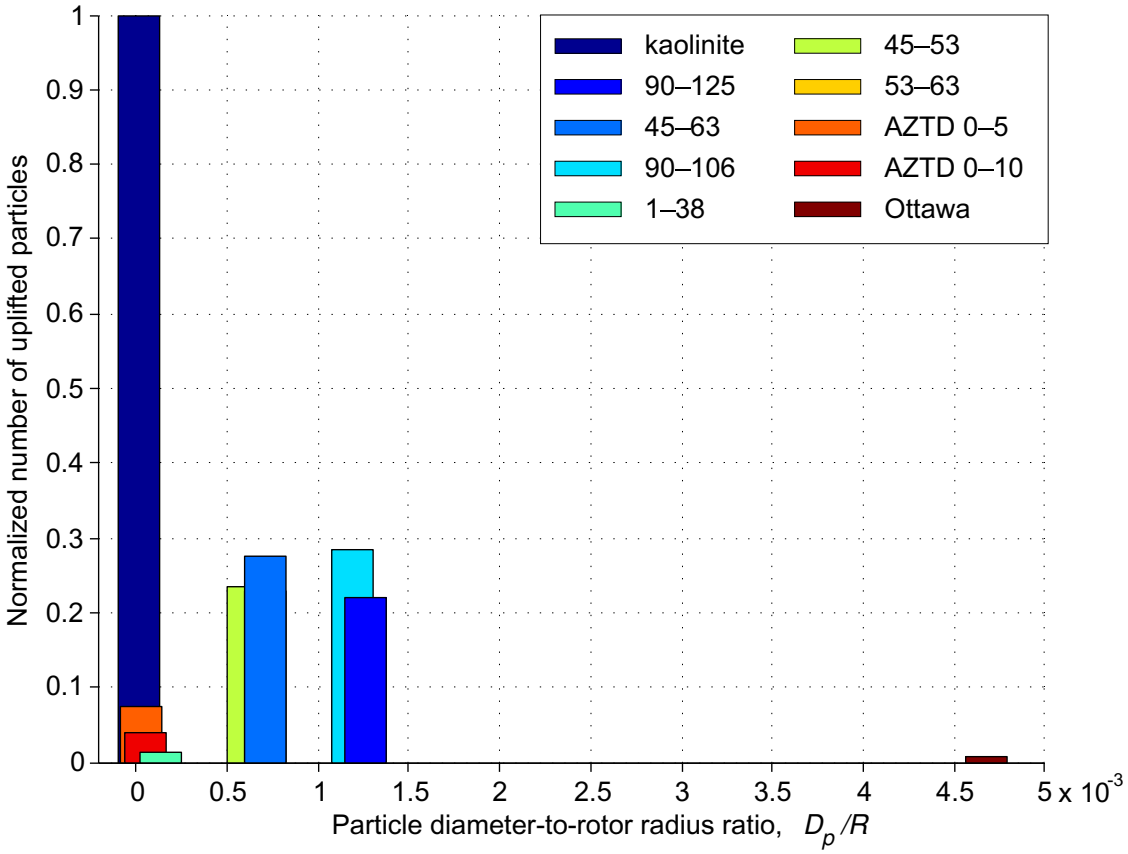

Figure 3.22: Normalized quantity of uplifted particles plotted against the particle diameter-to-rotor radius ratio, D_p/R.

with very few particles being entrained and uplifted for the Ottawa sand, which has the largest particle size. The kaolinite, which had the smallest sized particles, exhibited the most uplift. However, the other samples with particles of small sizes had relatively very little uplift, most likely because of cohesive effects between particles. Although more data might be needed to establish specific trends, the results of the current work clearly suggest that particle entrainment is sensitive to changes the particle diameter-to-rotor radius ratio, D_p/R; as D_p/R increased the quantity of suspended particles decreased.

3.4.5 Effect of Density Ratio on Entrainment

The effect of particle-to-fluid density ratio, ρ_s/ρ, was also investigated. The temperature of the test section was nominally 80 °F, and the corresponding density of the air was calculated using the measured ambient pressure. Figure 3.23 shows the normalized quantity of uplifted particles plotted against the particle-to-fluid density ratio, ρ_s/ρ, of each sample. It is clear that a correlation exists between the density ratio and the quantity of sediment particles being uplifted. In this case, the kaolinite, which showed the highest quantity of uplifted particles, also had the lowest density ratio. In contrast, the Ottawa sand, which showed the lowest quantity of uplifted particles, also had the highest density ratio.

Recall that the density ratio, ρ_s/ρ is important because it affects the amount of time that a particle will spend in the flow after it is uplifted off the bed; a denser particle will tend to fall more quickly under the influence of gravity, while a less dense particle will fall slower and will tend to stay airborne longer. The glass microspheres had some variations

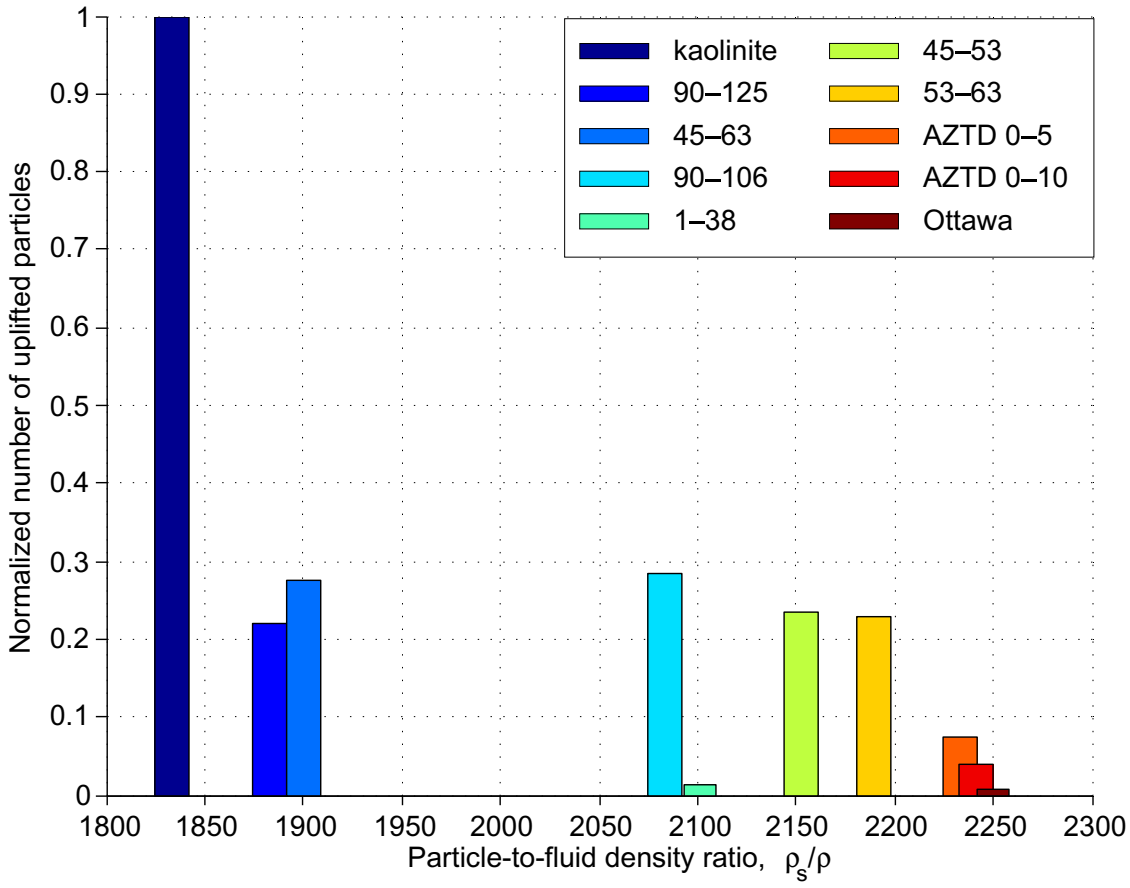

Figure 3.23: Normalized quantity of uplifted particles plotted against the particle-to-fluid density ratio, ρ_s/ρ.

in their density, although they were made of the same material. However, the quantity of particles that were uplifted did not differ greatly, except for the 1–38 μm diameter glass microspheres, which exhibited very little uplift. The trend observed here is that for the same flow, as the density ratio was increased the quantity of sediment particles that were uplifted and suspended decreased.

3.4.6 Effect of Particle Terminal Velocity

The terminal or settling velocity of a particle is defined as the maximum speed it attains while in free fall through a fluid under the influence of gravity. This terminal condition occurs when the forces acting on the particle (weight, drag, and buoyancy) are in equilibrium, i.e.,

$$W = F_b + D \tag{3.7}$$

where W is the weight of the particle, F_b is the buoyancy force on the particle, and D is the drag force. Assuming a spherical particle, the weight and buoyancy forces on the particle are

$$W = \frac{\pi}{6} D_p^3 \rho_s g \tag{3.8}$$

and

$$F_b = \frac{\pi}{6} D_p^3 \rho g \tag{3.9}$$

respectively, then the drag force in the particle at its terminal velocity is

$$D = \frac{1}{2} \rho U_F^2 C_D A \tag{3.10}$$

where C_D is the particle drag coefficient, A is the cross sectional area of the particle, and U_F is the terminal velocity. Substituting Eq. 3.8, 3.9, and 3.10 into Eq. 3.7, and solving for U_F gives

$$U_F = \sqrt{\frac{4 g D_p}{3 C_D} \left(\frac{\rho_s - \rho}{\rho} \right)} \tag{3.11}$$

For very small particles, Stokes' law can be used to estimate the drag coefficient, which is given by

$$C_D = \frac{24}{Re_p} \tag{3.12}$$

where Re_p is the particle Reynolds number ($Re_p = \rho U_F D_p/\mu$). Substituting Eq. 3.12 into Eq. 3.11 gives

$$U_F = \frac{gD_p^2}{18\mu}(\rho_s - \rho) \tag{3.13}$$

However, Stokes' law is only valid when the particle Reynolds number while settling is less than 0.3 because it assumes only laminar flow around a spherical particle; this assumption is only valid for particles with very small diameters (D_p <50 μm); larger particles will have higher Reynolds numbers because of the larger diameter and higher falling velocity. For example, consider a particle with 100 μm diameter. The maximum settling velocity allowed for the particle Reynolds number to be less than 0.3 is only 0.15 ms^{-1}. This velocity is much slower than what would practically occur for a particle of that size. Therefore, another model is needed that is valid over a larger range of particle Reynolds numbers to account for larger particle sizes.

The following model from [59] predicts the terminal velocity for both smaller particles, (where Stokes's law is valid), and for larger ones (where it no longer holds). In this case

$$U_F = \frac{\sigma_p g D_p^2}{C_1 \nu + \left(0.75 C_2 \sigma_p g D_p^3\right)^{0.5}} \tag{3.14}$$

In Eq. 3.14, C_1 and C_2 are constants that depend on the shape of the particles and σ_p is the submerged specific gravity of the particles, as given by

$$\sigma_p = \left(\frac{\rho_s - \rho}{\rho}\right) \tag{3.15}$$

For this analysis, values of C_1 =18 and C_2 = 0.4 were assumed, corresponding to smooth, spherical particles, as explained in [59].

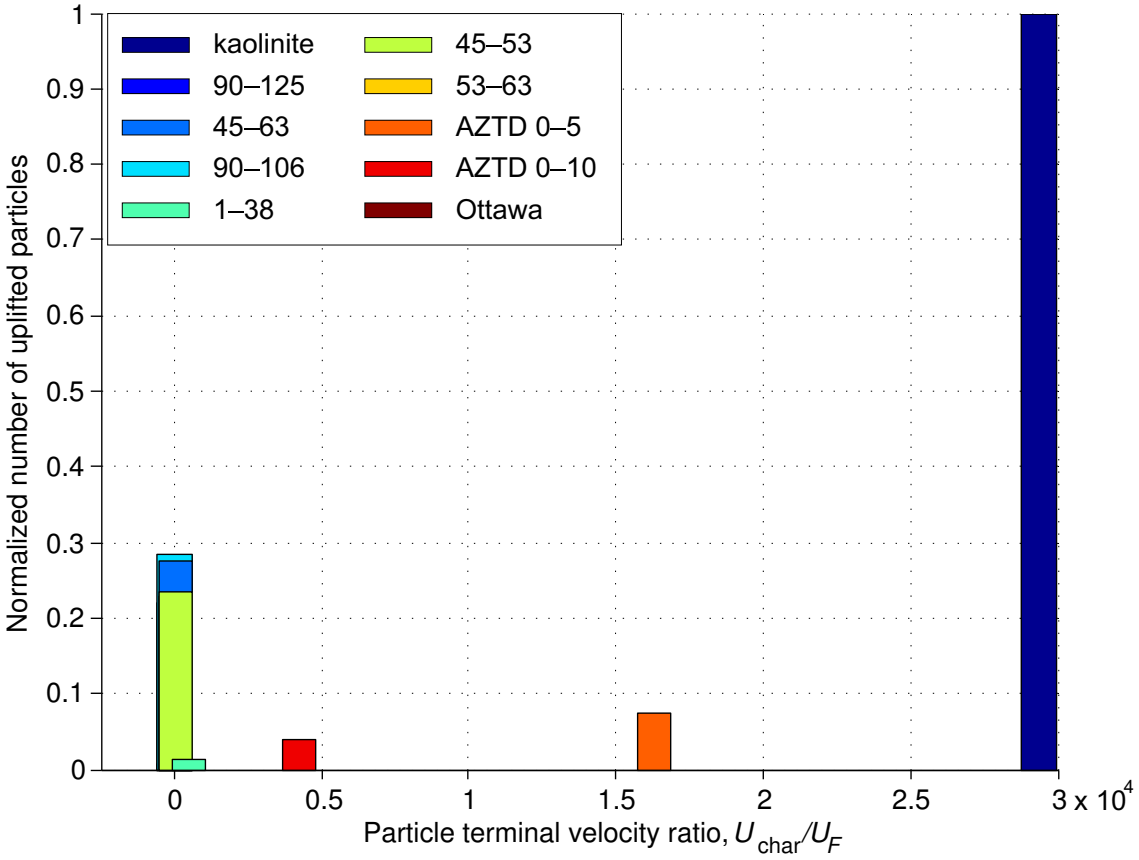

Figure 3.24: Normalized number of sediment particles plotted against the characteristic velocity-to-terminal velocity ratio.

Figure 3.24 shows the normalized number of particles plotted versus the characteristic velocity-to-terminal velocity ratio, U_{char}/U_F. Kaolinite has the highest terminal velocity ratio, and also showed the highest quantity of uplifted particles. As this ratio decreases, there is a sharp drop in the quantity of uplifted material. Most of the glass particle samples have similar values of terminal velocity, and are grouped close together. Notice that the quantity of uplift for these samples is higher than some of the samples that have a larger ratio of U_{char}/U_F. The reason for this behavior might be because of the low cohesiveness between the particles. However, to determine a complete explanation

of the behavior would require further study. Nonetheless, the correlation observed from the measurements is that an increase in the terminal velocity ratio results in an increase in the quantity of uplifted particles.

3.4.7 Effect of Froude Number

The densimetric Froude number, F^*, was calculated for each sediment sample using

$$F^* = \frac{U_{\text{char}}}{\sqrt{(\rho_s/\rho - 1)gD_p}} \tag{3.16}$$

This expression for the Froude number was taken from [60], where F^* was used as a parameter to help predict the onset of sediment mobility. Recall that, in general, the Froude number is the ratio between inertial forces and gravitational forces. This means that a higher Froude number conveys that the inertia of the particle is dominant, and a lower Froude number means that gravity has more influence on the particle.

Figure 3.25 shows the normalized number of uplifted particles for each sediment sample plotted versus the densimetric Froude number. The kaolinite had the highest Froude number (i.e., less influenced by gravity) and also had the highest number of uplifted sediment particles for the flow studied here. The particle count decreased as the Froude number decreased because gravity had more influence on these particles, causing fewer particles to remain suspended. Most of the glass microsphere samples have low Froude numbers, but unlike the other samples, they showed larger quantities of uplifted particles. Once again, to fully explain the behavior of the glass microspheres would require further studies.

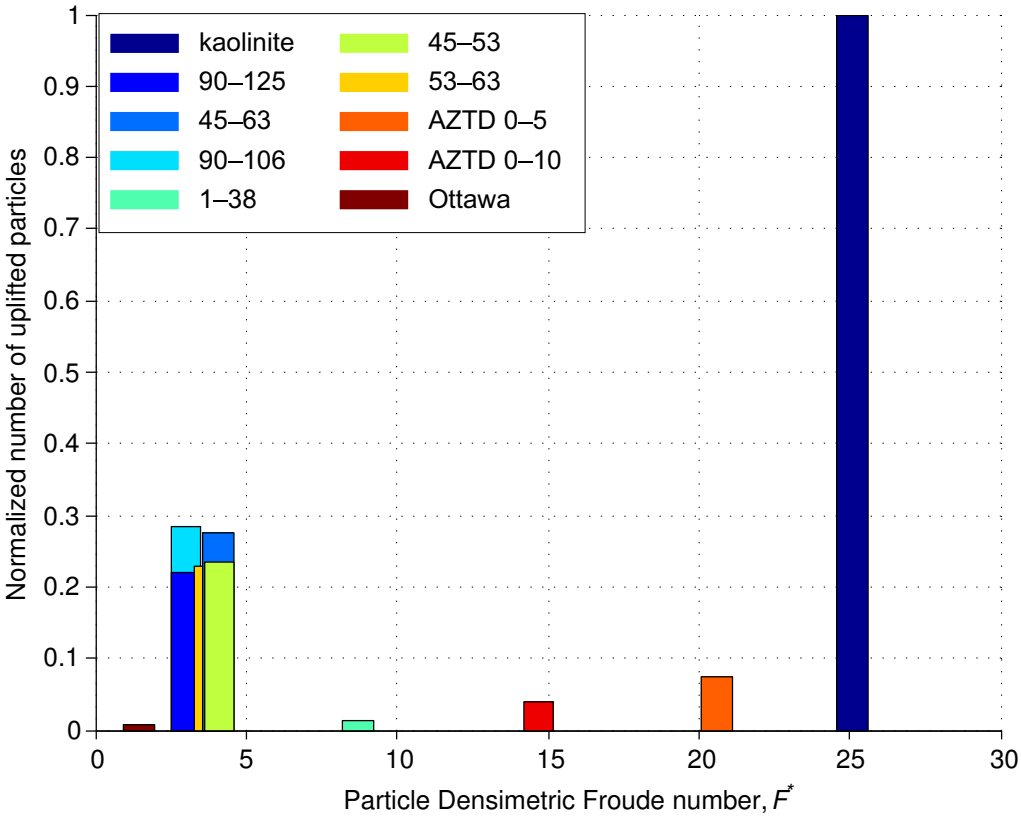

Figure 3.25: Number of sediment particles plotted against the densimetric Froude number.

3.4.8 Effect of Threshold Friction Velocity on Sediment Entrainment

Measurements of the threshold friction velocity, u_{*_t}, were not obtained during the course of the present studies. To this end, measuring u_{*_t} would require a steady, uniform wall flow in which the velocity can be precisely controlled, i.e., the wall flow would have to be directed over a sediment bed with the velocity incrementally being increased until the point of mobilization is achieved. Flow field measurements would then be taken at this condition to identify the threshold friction velocity using a procedure similar to that used in estimating the friction velocity, u_*. This procedure is described in Section 3.4.9.

In the present work, u_{*t} was calculated using a semi-empirical model [61], which is

given by

$$u_{*t} = \sqrt{f(Re_{*t})\left(\frac{\rho_s}{\rho} g d + \frac{\gamma}{\rho d}\right)} \tag{3.17}$$

where $f(Re_{*t})$ is a function of the particle Reynolds number at the threshold friction velocity and γ is a constant representing the cohesiveness of the particles. From [61], the recommended values for $f(Re_{*t})$ and γ were 0.0123 and 3×10^{-4} kg s^{-2}, respectively.

Figure 3.26 shows the normalized quantity of uplifted particles plotted against the threshold friction velocity ratio, U_{char}/u_{*_t}. Notice that the sample with the greatest quantity of uplift has the lowest threshold friction velocity ratio (i.e., they are more difficult to mobilize) and the samples that have lower quantities of uplift have higher friction velocity

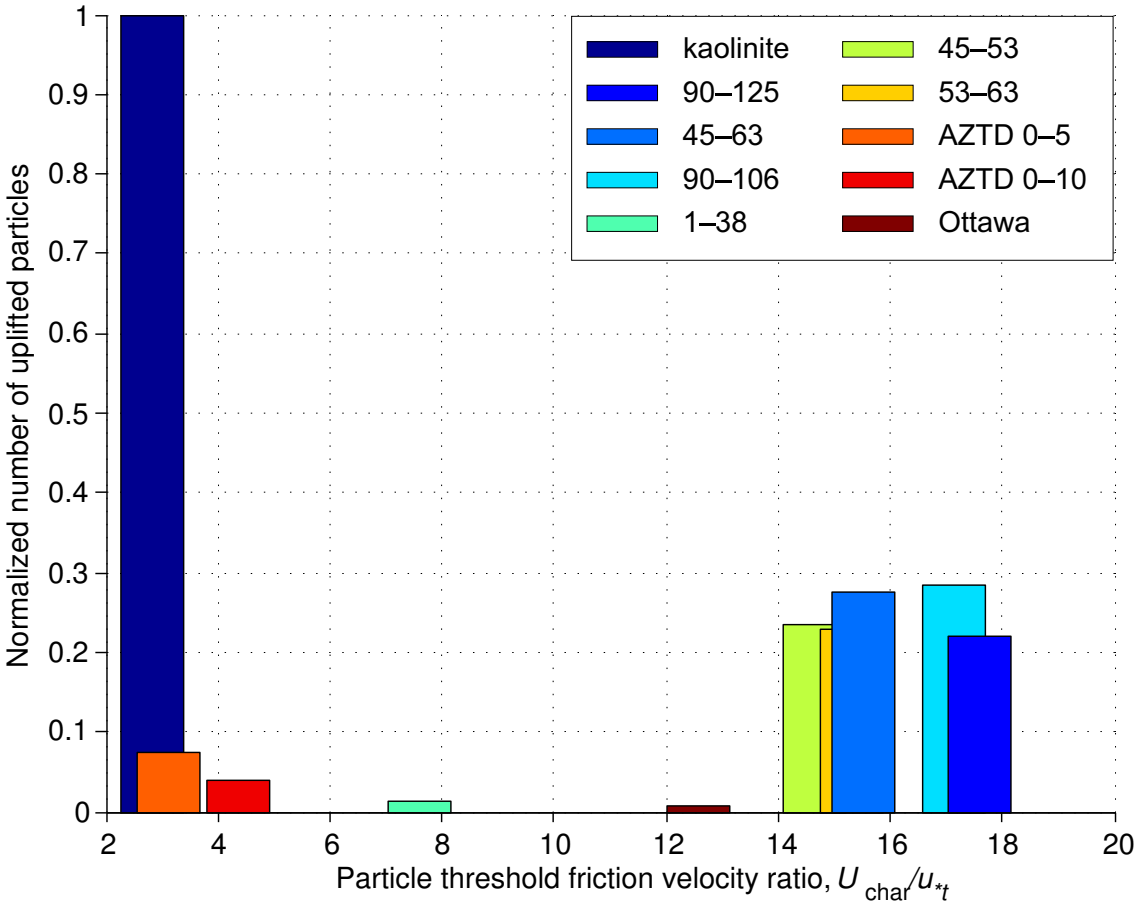

Figure 3.26: Particle uplift versus threshold friction velocity using Shao-Lu model.

ratios (i.e., they are less difficult to mobilize). The results from this model suggests that the kaolinite had the highest threshold to achieve mobilization. However, this result is the opposite to what was observed in the experiments because the kaolinite was actually seen to be the most mobile of all the samples.

Two other threshold friction velocity models, given by Eq. 3.18 and 3.19, were subsequently explored to determine if they could predict the trends that were seen in the present experiments. The first was developed by Bagnold [31] and the second was developed by Greeley and Iversen [17], i.e., in this case

$$\text{Bagnold model,} \quad u_{*t} = A_B(Re_{*t})\sqrt{\frac{\rho_s}{\rho} g D_p} \tag{3.18}$$

$$\text{Greeley and Iversen model,} \quad u_{*t} = A_1\sqrt{\frac{\rho_s}{\rho} g D_p F(Re_{*t}) G(D_p)} \tag{3.19}$$

where A_B is a function of Re_{*t} but is a constant between 0.1 and 0.2 for $Re_{*t} > 3.5$. Here it was assumed that A_B = 0.1 from [31]. In Eq. 3.19, A_1 is a constant, F is a function of Re_{*t}, and G is a function of the particle diameter, D_p. The detailed expressions for $F(Re_{*t})$ and $G(D_p)$ are given elsewhere [17].

The predicted threshold friction velocity, u_{*_t}, as a function of particle diameter using each model is plotted in Fig. 3.27. The Bagnold model predicts u_{*t} to steadily decrease with decreasing particle diameter. The models of Greeley and Shao-Lu, however, predict the value of u_{*t} to decrease with decreasing particle diameter to a minimum value and then increase again, which physically represents the effects of the greater cohesion between the smaller particle diameters.

Now using the Greeley and Bagnold models, the quantity of uplifted particles is plotted against U_{char}/u_{*t} in Figs. 3.28 and 3.29. While the Shao-Lu and Greeley models

make similar predictions of the threshold velocity, Bagnold's model predicts the behavior to be more closely aligned with that observed in the present experiments. The trend here using the Bagnold model is that as U_{char}/u_{*_t} increases, the quantity of particles uplifted also increases.

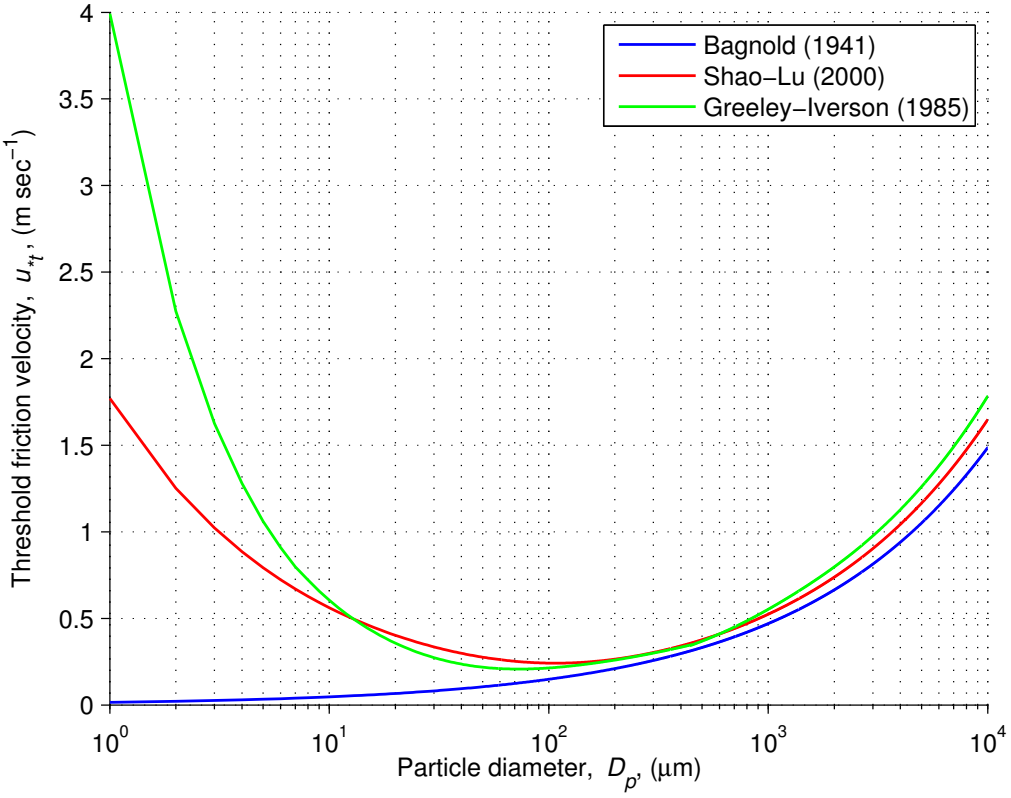

Figure 3.27: Threshold friction velocity plotted against particle size using three different models.

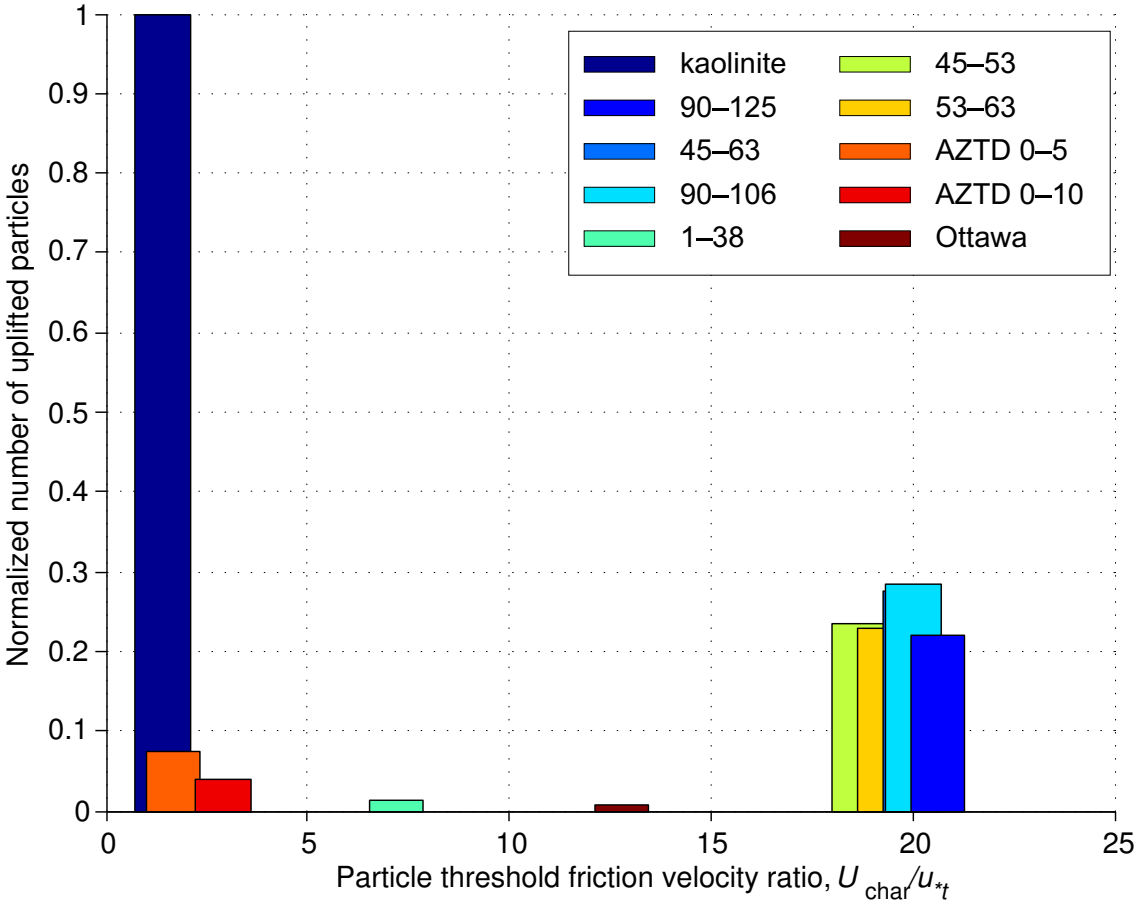

Figure 3.28: Particle uplift versus threshold friction velocity using Greeley model.

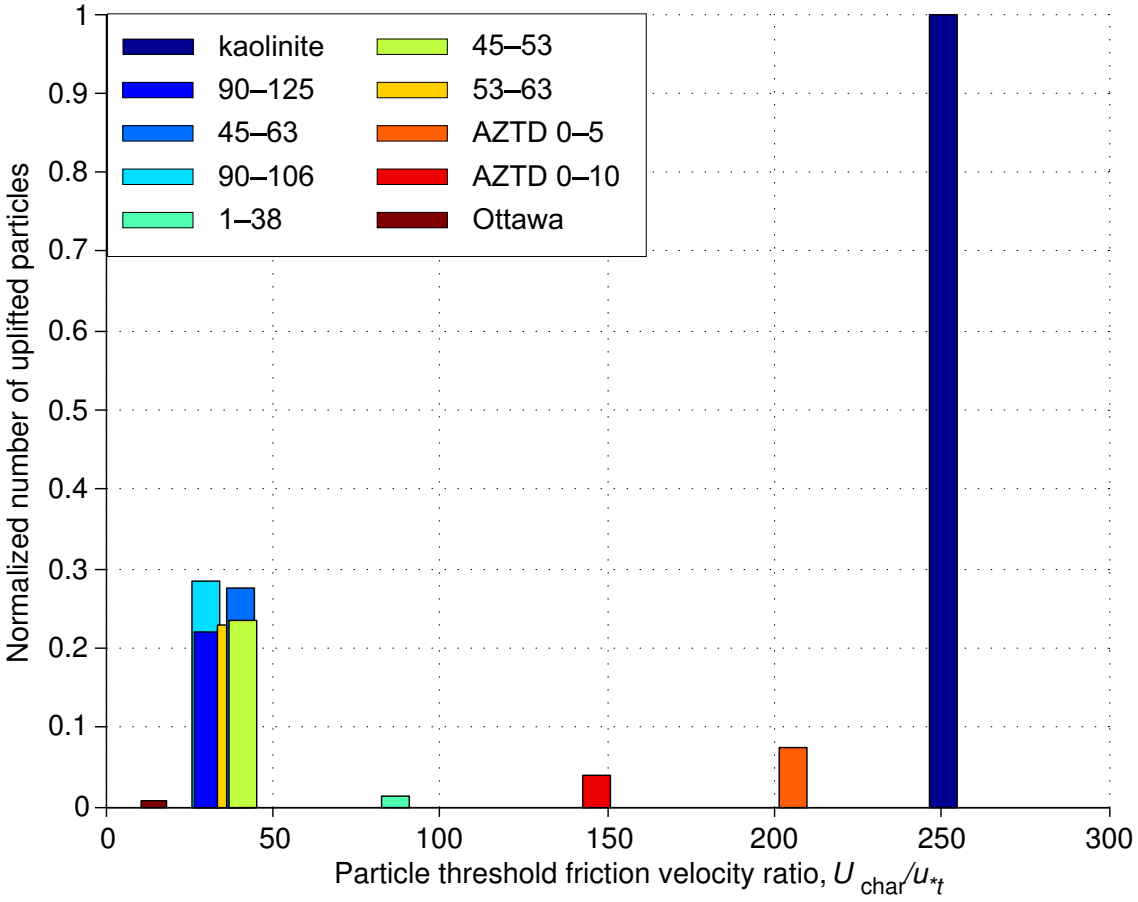

Figure 3.29: Particle uplift versus threshold friction velocity using Bagnold model.

3.4.9 Friction Velocity at the Ground

The friction velocity, u_*, was measured from the TR-PIV data. Measuring this quantity is very challenging because it requires acquiring velocity measurements very close to the ground plane, which has several problems including laser light reflections. The value of u_* is given in boundary layer theory by

$$u_* = \sqrt{\frac{\tau_w}{\rho}} \tag{3.20}$$

where τ_w is the shear stress at the wall. The wall shear stress, τ_w, is comprised of two components, the viscous shear stress, τ_v, and the turbulent shear stress, τ_t, i.e.,

$$\tau_w = \tau_v + \tau_t \tag{3.21}$$

The viscous component of τ_w is given by

$$\tau_v = \mu \left(\frac{dU}{dz} \right) \Bigg|_{z \to 0} \tag{3.22}$$

where dU/dz is the velocity gradient and and z is the distance above the ground. The turbulent component of the wall shear stress is given by

$$\tau_t = -\rho \overline{u'v'} \tag{3.23}$$

where U' and V' are the instantaneous velocity fluctuations from the mean velocities.

$$U = \overline{U} + u'; \qquad V = \overline{V} + v' \tag{3.24}$$

$\overline{u'v'}$ is calculated by taking the mean of the product $u'v'$ over all the PIV measurements.

The turbulent shear stress can be a significant component of the total shear stress, and therefore it was important to quantify its value for the present flow. A profile of the turbulent shear stress at multiple radial locations is given in Fig. 3.30. In this case, the turbulent shear stress near the ground was observed to go nearly to zero, and so it can be safely ignored for the purposes of calculating the wall shear stress, i.e., in the present case it is sufficient to assume that

$$\tau_w = \tau_v = \mu \left(\frac{dU}{dz} \right) \Bigg|_{z \to 0} \tag{3.25}$$

To measure the velocity gradient, dU/dz, velocity measurements must be taken down into the laminar sublayer of the boundary layer, where the velocity profile is linear

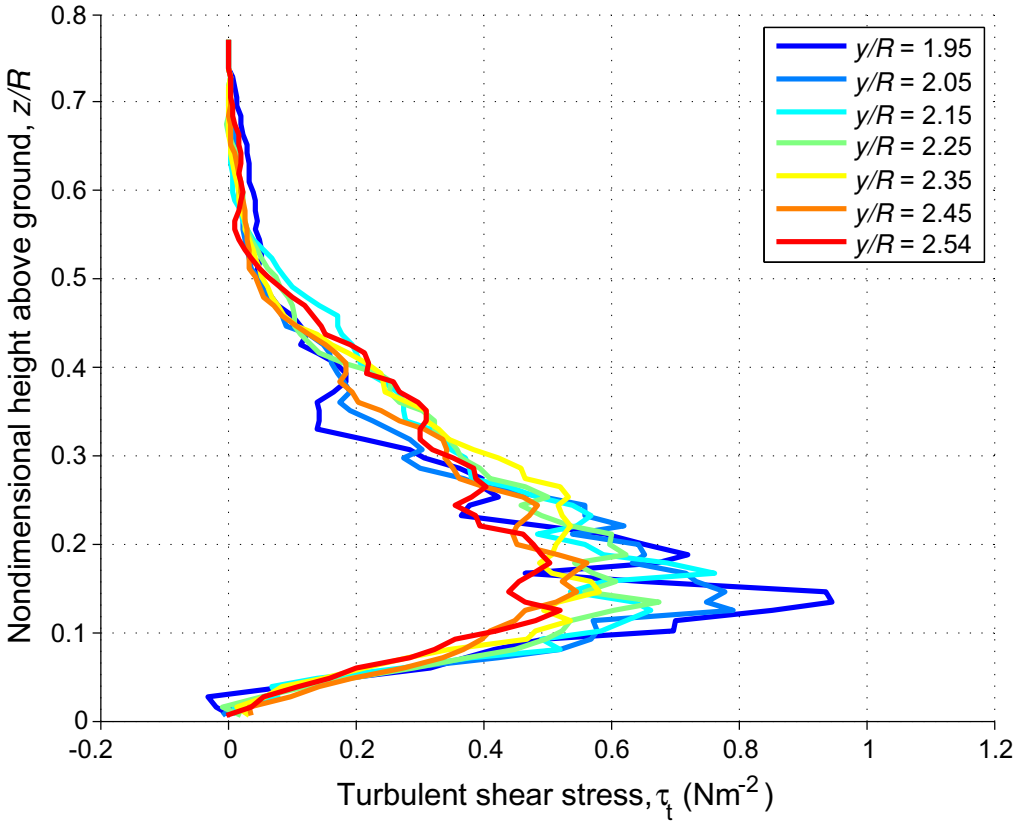

Figure 3.30: turbulent shear stress profile.

and the velocity gradient is nominally constant. A schematic of this flow region is shown in Fig. 3.31.

To establish a criteria for whether a flow measurement is in the sublayer, a nondimensional height, z^+, can be defined as

$$z^+ = \frac{z\, u_*}{\nu} \tag{3.26}$$

Normally, the viscous sublayer region is defined as $z^+ < 5$ [62]. In the present experiments, the last valid data point closest to the wall was at a z^+ just above 5 and, therefore, just at the edge of the sublayer. Therefore, by assuming a linear velocity profile (i.e., constant velocity gradient) to the ground plane from this last valid data point while en-

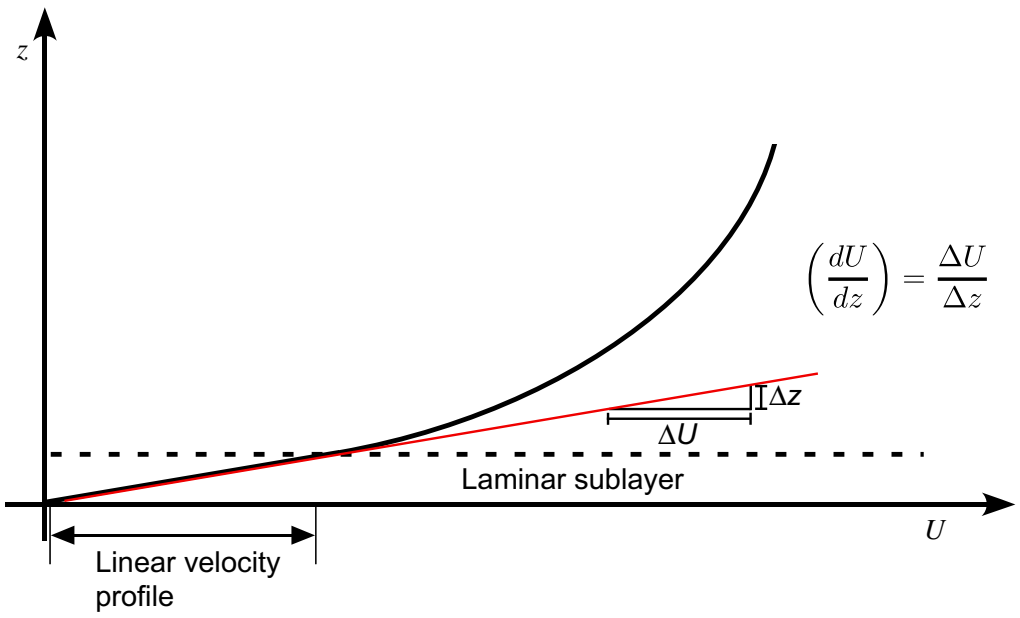

Figure 3.31: Schematic of the velocity profile at the ground and the laminar sublayer region.

forcing the no-slip condition, is a reasonable assumption for the purposes of estimating the friction velocity, u^*.

Shown in Fig. 3.32 are the instantaneous velocity profiles at the ground at a radial location of $y/R = 2.0$. The blue curve shows the velocity profile before the passage of a tip vortex with $\psi = 160^\circ$, and the red curve shows the velocity profile during the passage of a tip vortex with $\psi = 210^\circ$. There are obviously significant excursions from the mean flow resulting from the relatively high swirl velocities near the vortex core. The last valid data points near the ground are highlighted. If the shear stress and friction velocity are calculated using these points, the shear stress is more than doubled when the vortex passes by, as given in Table 3.3.

It is known from [2] and [28], and also from the present work, that the tip vortices in the rotor wake are responsible for the mobilization and uplift of much sediment. Fig-

Blade azimuth angle	(dU/dz) (s^{-1})	τ_w (Nm^{-2})	u_* (ms^{-1})
$\psi = 160°$	1,843	0.0341	0.1702
$\psi = 210°$	5,227	0.0968	0.2867

Table 3.3: Calculated velocity gradient, wall shear stress, and friction velocity before ($\psi = 160°$) and during ($\psi = 210°$) the passage of a tip vortex.

ure 3.33(a) shows the fluctuations in u_* as a function of degrees of blade rotation. Lines denoting the threshold friction velocity values for kaolinite using each of the three models (Bagnold, Shao, and Greeley) are also given.

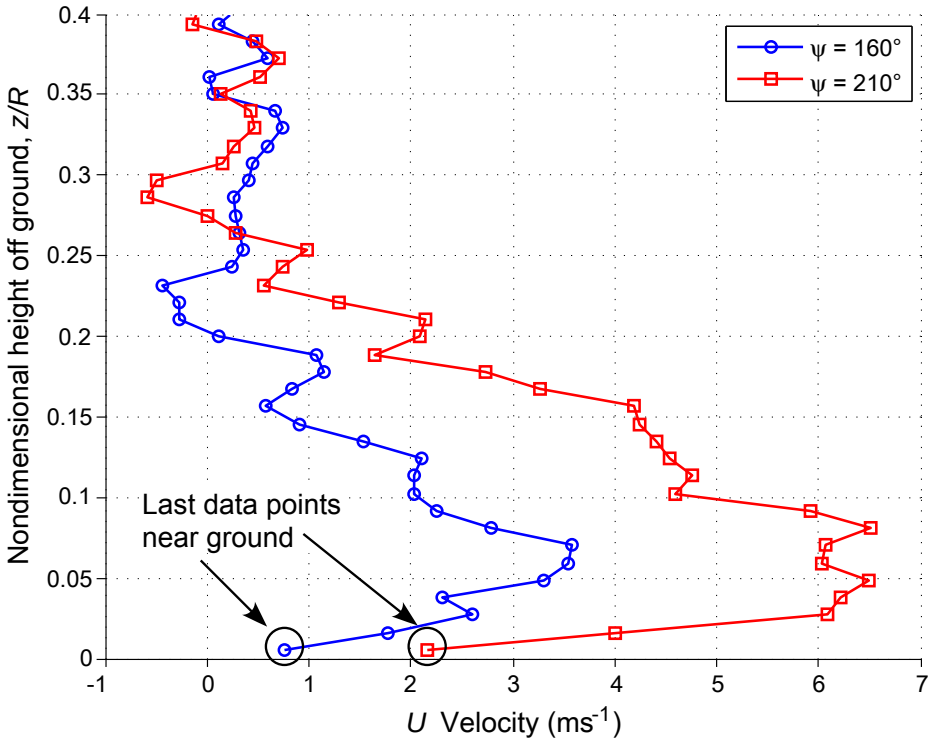

Figure 3.32: Unsteady excursions in the wall flow velocity profile from the passage of a tip vortex at $y/R = 2.0$.

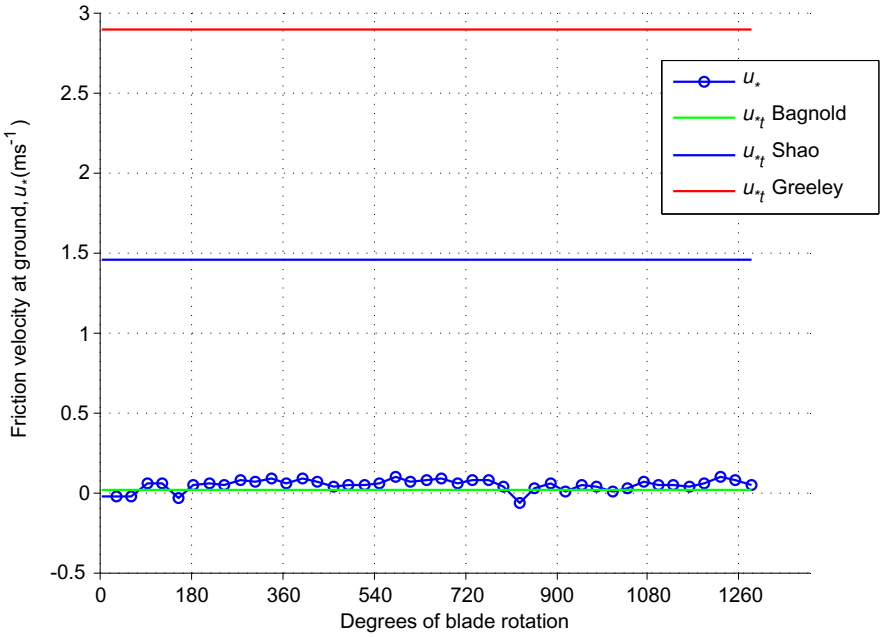

(a) Friction velocity at $y/R = 2.0$ versus degrees of blade rotation. Lines denoting the threshold friction velocity for kaolinite using three models are also given.

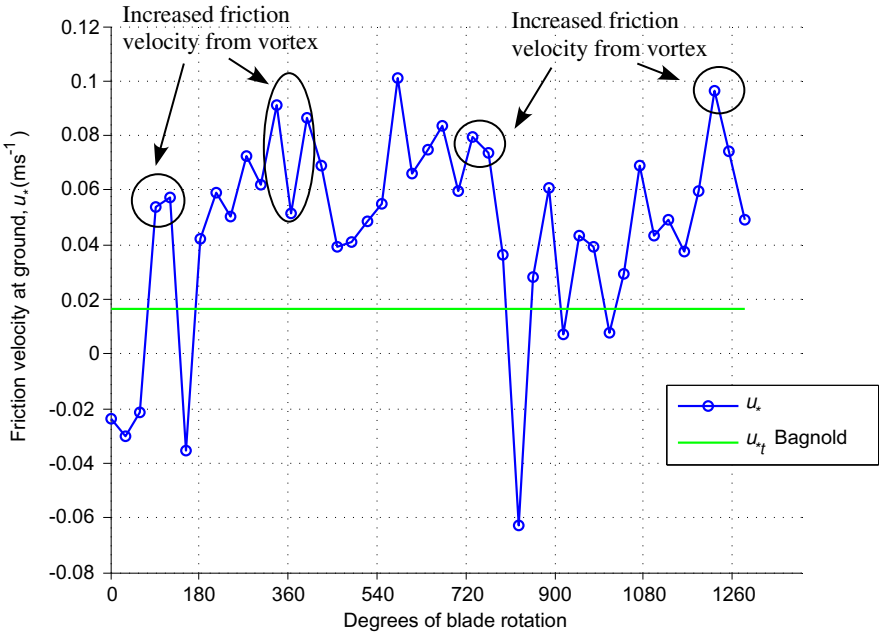

(b) Close up of Fig. 3.33(a) showing the fluctuations in u_*. Increases in u_* are observed with the passage of a tip vortex.

Figure 3.33: Friction velocity, u_* plotted with threshold friction velocity values for kaolinite at $y/R = 2.0$.

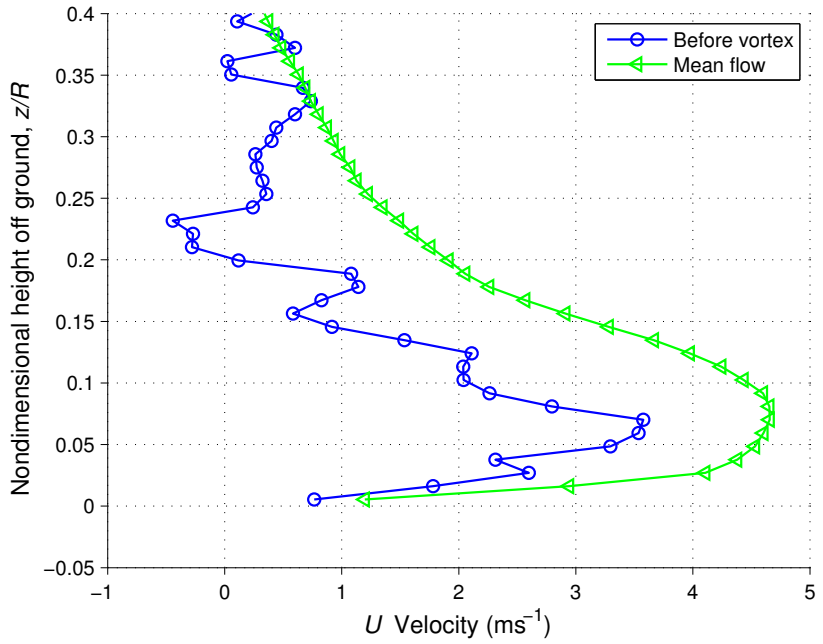

(a) Instantaneous velocity profile before the passage of a tip vortex at $y/R = 2.0$

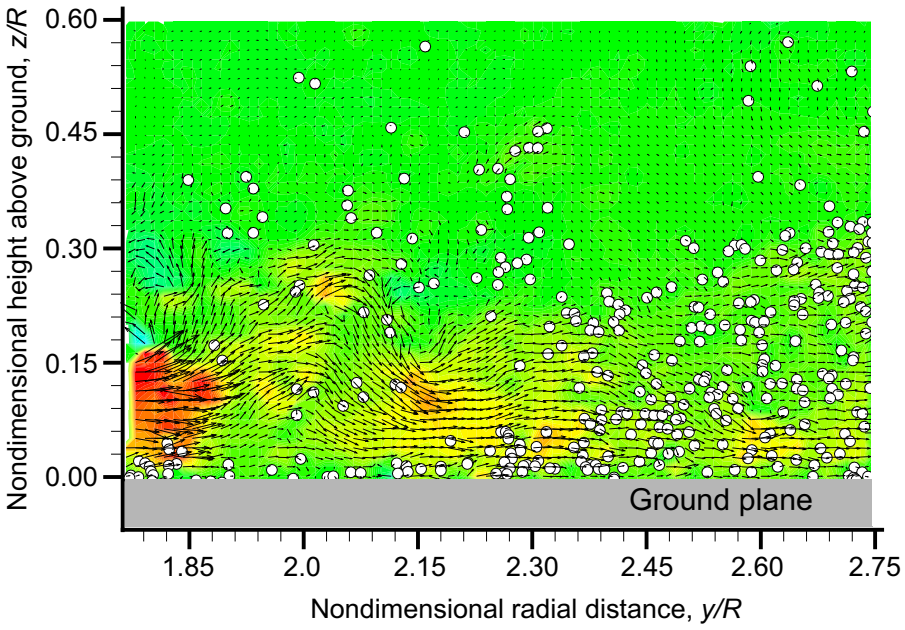

(b) Dual-phase measurement with kaolinite before the passage of a tip vortex

Figure 3.34: Velocity profile before the passage of a vortex at $y/R = 2.0$ and corresponding dual-phase measurement using kaolinite.

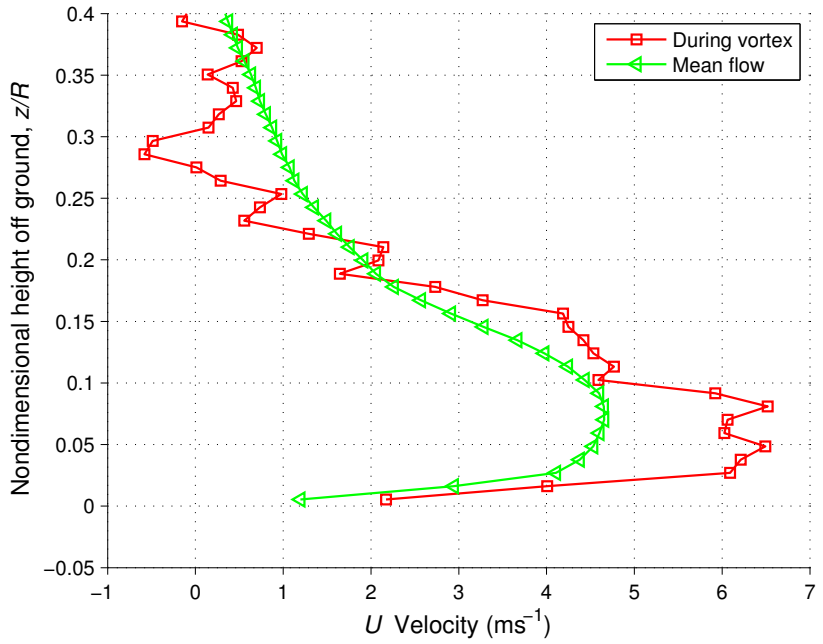

(a) Instantaneous velocity profile during the passage of a tip vortex at $y/R = 2.0$

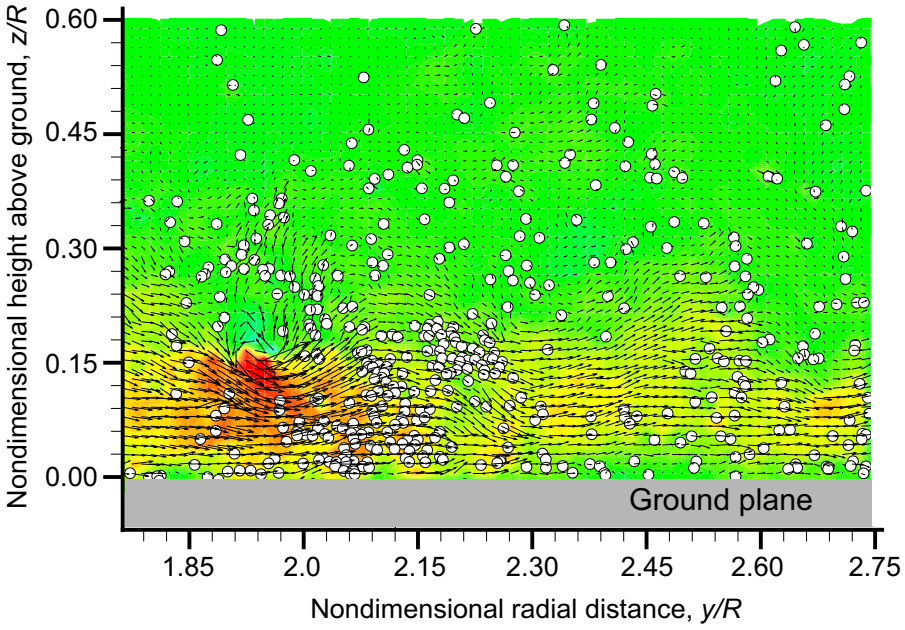

(b) Dual-phase measurement with kaolinite during the passage of a tip vortex

Figure 3.35: Velocity profile during the passage of a vortex at $y/R = 2.0$ and corresponding dual-phase measurement using kaolinite.

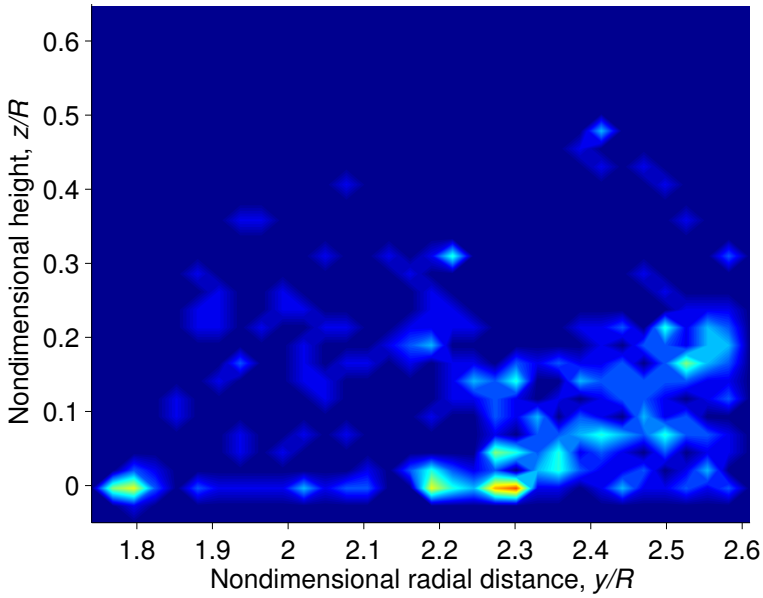

(a) Concentration map with kaolinite before the passage of a tip vortex at $y/R = 2.0$

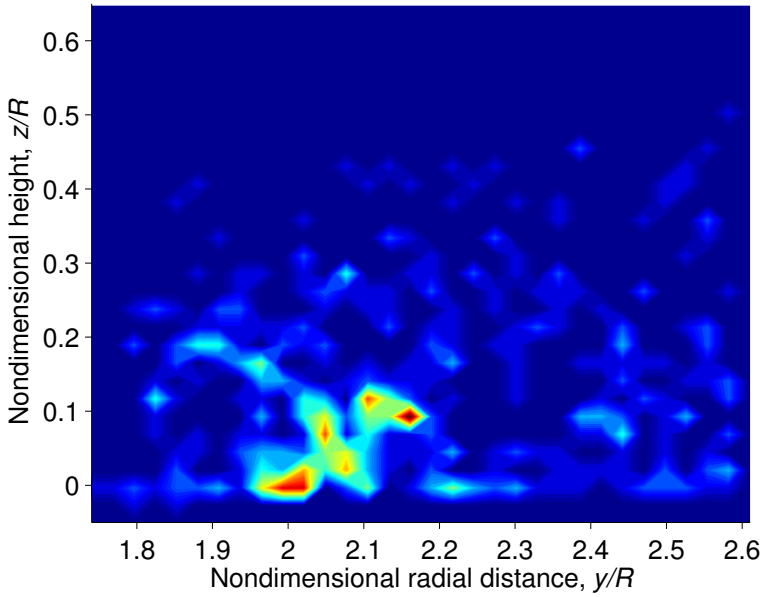

(b) Concentration map with kaolinite during the passage of a tip vortex at $y/R = 2.0$

Figure 3.36: Particle concentration maps of kaolinite before and during the passage of a tip vortex at $y/R = 2.0$.

Figure 3.33(b) shows a detailed region of Fig. 3.33(a) so that the fluctuations in u_* can be identified. It can be seen that several peaks in u_* occur when a vortex passes at $y/R = 2.0$. In this case, the unsteady excursions increase u_* above the value of u_{*_t} for kaolinite.

This observed increase in u^* can be correlated to the initial uplift of sediment particles from the ground plane, as shown in Figs. 3.34 and 3.35. Figure 3.34(a) shows the mean velocity profile and the instantaneous velocity profile before the passage of a vortex at $y/R = 2.0$. A corresponding dual-phase measurement is shown in Fig. 3.34(b). Notice that at $y/R = 2.0$, there are few particles being mobilized, with most of them having been previously uplifted from the passage of an older part of the helicoidal vortex. However, Figs. 3.35(a) and 3.35(b) show the increased velocity at the ground from the passage of a vortex filament and the corresponding sediment uplift, because in this case the friction velocity has exceeded the threshold friction velocity. Figure 3.36 shows the corresponding particle concentration maps of Figs. 3.34(b) and 3.35(b).

In contrast, when the measurements using Ottawa sand (i.e., the least mobile sediment) were analyzed, the observed behavior is different. Figure 3.37 shows the same curve for u_* as shown in Fig. 3.33(b), but now with threshold values given for Ottawa sand. In this case, u_* does not exceed any of the threshold values and the mobilization of any particles would not be expected. This behavior is fully consistent to what was observed in the present experiments.

Figure 3.38(a) and 3.38(b) show the velocity profile and corresponding dual-phase measurement using Ottawa sand before the passage of a tip vortex. No particles are suspended in the flow because the threshold condition has not been met. Figures 3.39(a)

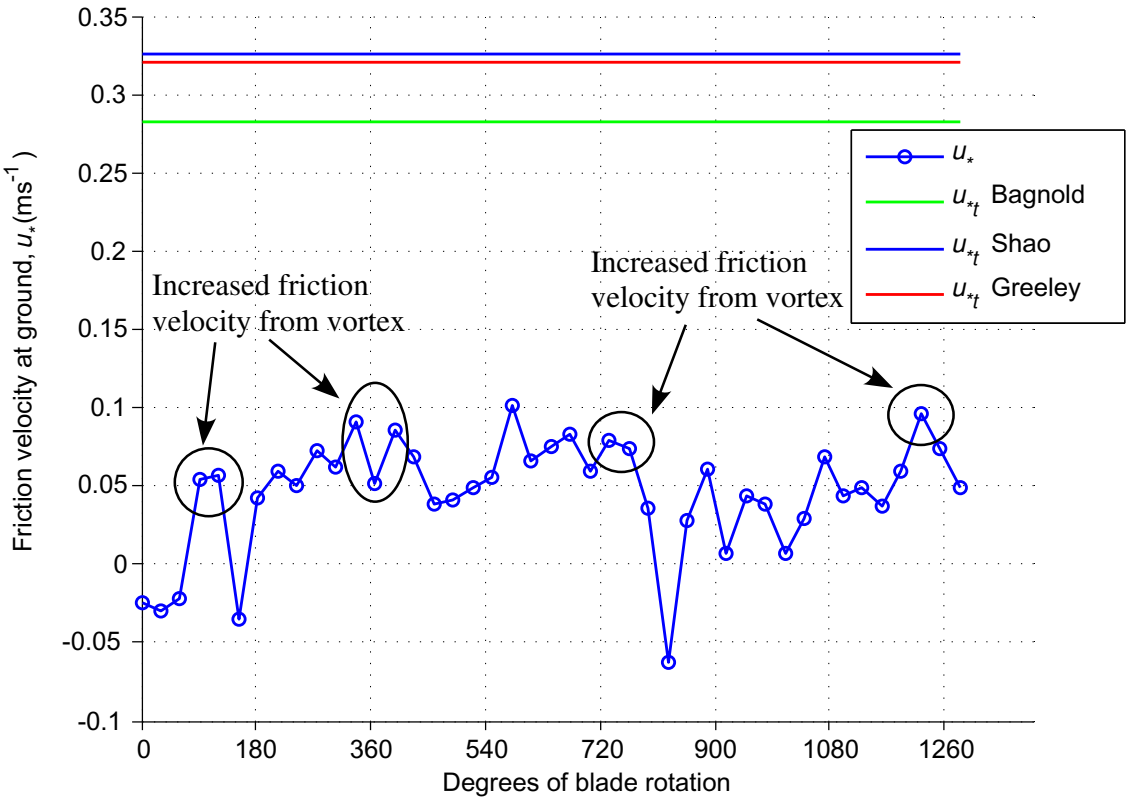

Figure 3.37: Friction velocity at $y/R = 2.0$ versus degrees of blade rotation. Lines denoting the threshold friction velocity for Ottawa sand using three models are also given.

and 3.39(b) show the velocity profile and dual-phase measurement during the passage of a vortex. Figure 3.40 shows the corresponding particle concentration maps of Figs. 3.38(b) and 3.39(b). Although the velocity and shear stress have increased, no mobilization of the sediment particles is observed in this case because the friction velocity, u_*, is below the threshold friction velocity for Ottawa sand.

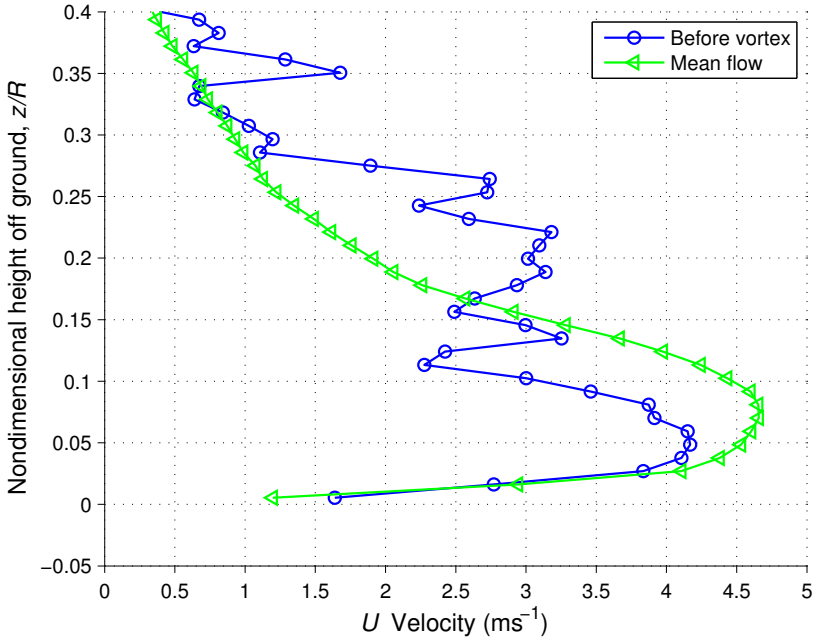

(a) Velocity profile before the passage of a tip vortex at $y/R = 2.0$

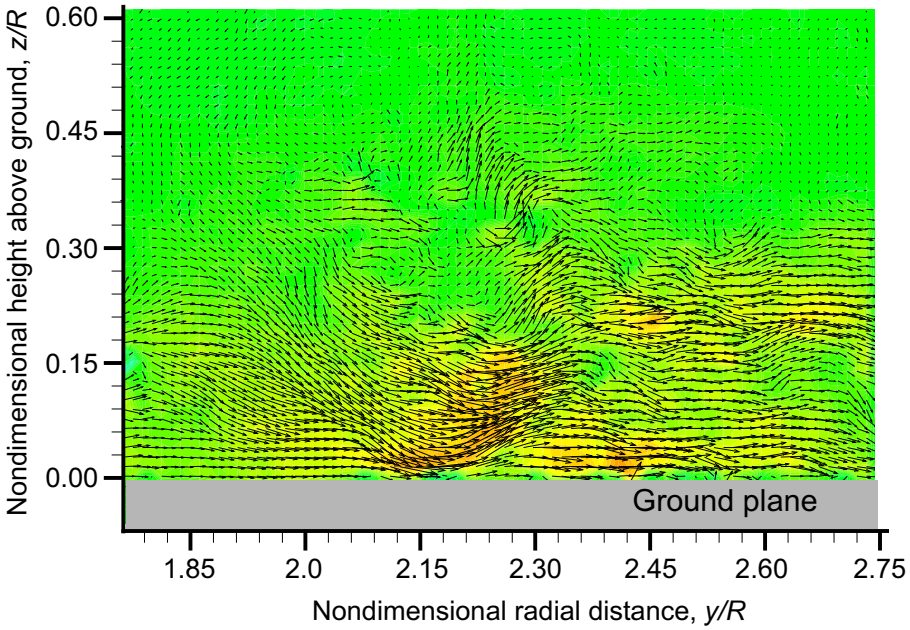

(b) Dual-phase measurement with Ottawa sand before the passage of a tip vortex

Figure 3.38: Velocity profile before the passage of a vortex at $y/R = 2.0$ and corresponding dual-phase measurement with Ottawa sand.

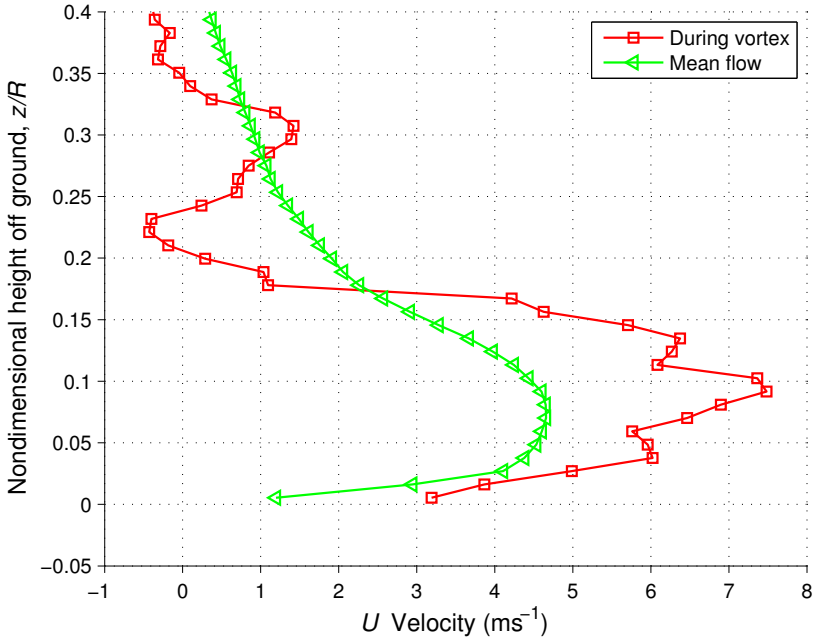

(a) Velocity profile during the passage of a tip vortex at $y/R = 2.0$

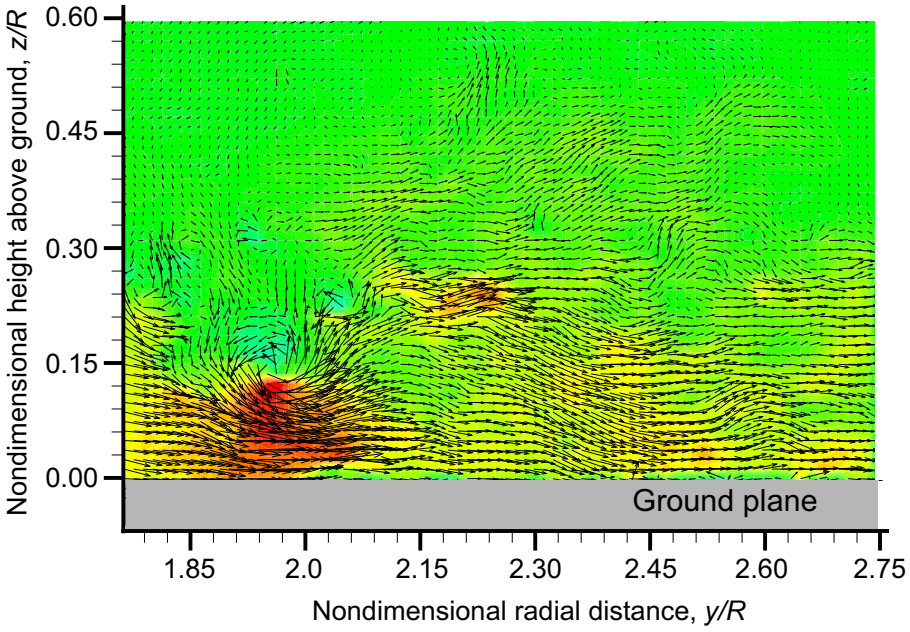

(b) Dual-phase measurement with Ottawa sand during the passage of a tip vortex

Figure 3.39: Velocity profile during the passage of a vortex at $y/R = 2.0$ and corresponding dual-phase measurement with Ottawa sand.

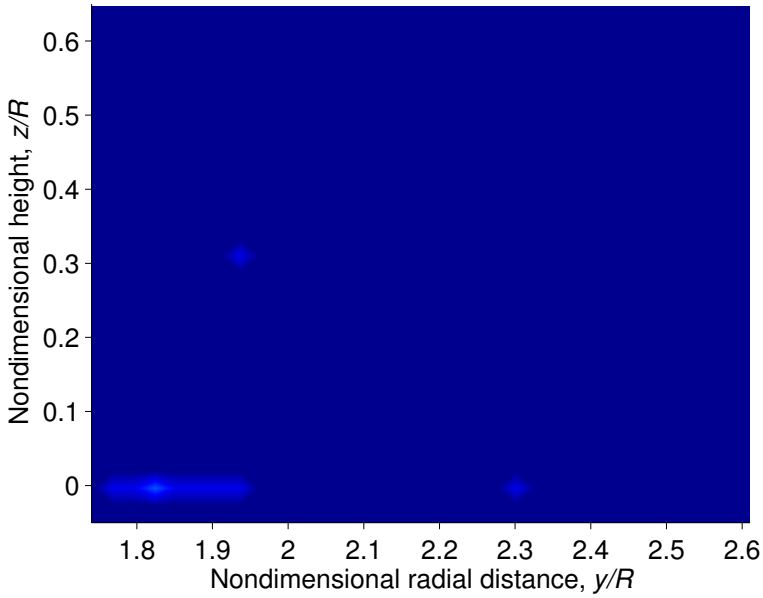

(a) Concentration map with Ottawa sand before the passage of a tip vortex at $y/R = 2.0$

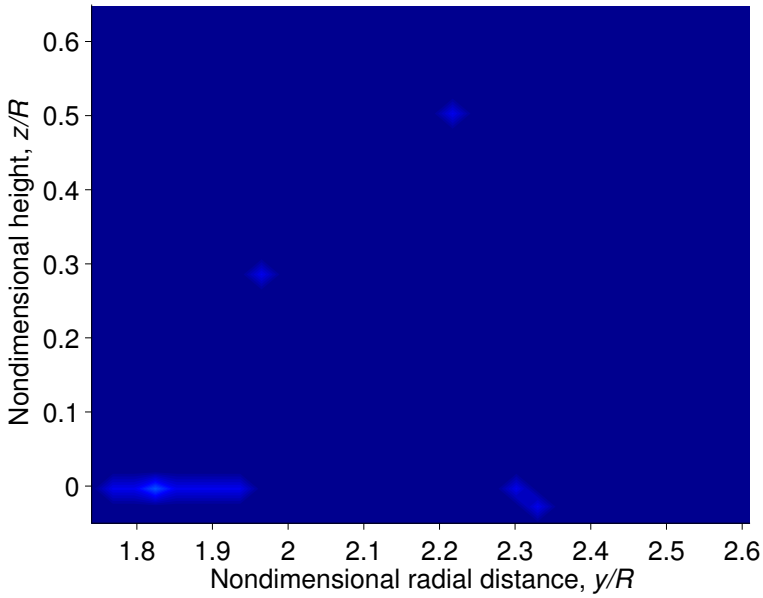

(b) Concentration map with Ottawa sand during the passage of a tip vortex at $y/R = 2.0$

Figure 3.40: Particle concentration maps of Ottawa sand before and during the passage of a tip vortex at $y/R = 2.0$.

Figures 3.41–3.48 show the fluctuations in u^* versus degrees of blade rotation with lines denoting the threshold values for the remaining samples. Corresponding dual-phase measurements and particle concentration maps during the passage of a vortex are shown in Figs. 3.49–3.64. The same flow conditions produced different results depending on the properties of the particles comprising the sediment bed. Clearly, there was a correlation between the vortices passing over the sediment bed causing the friction velocity to increase above the threshold value, and the mobilization and entrainment of sediment particles into the flow. While the vortices clearly cause peaks in the values of u_*, other significant peaks in the friction velocity are observed without the presence of the vortex flow. Such peaks most likely arise from eddies or turbulence in the flow. Further studies obviously will need to be conducted to better understand the turbulent features of the vortical flow near the ground and the effect of turbulence on particle entrainment.

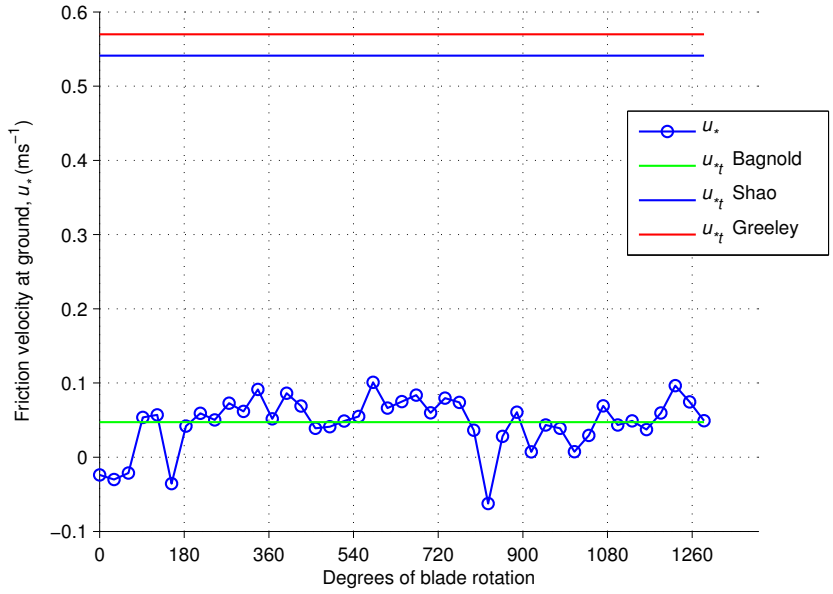

Figure 3.41: Friction velocity at $y/R = 2.0$. Threshold friction velocity for 1–38 μm glass microspheres using three models is also given.

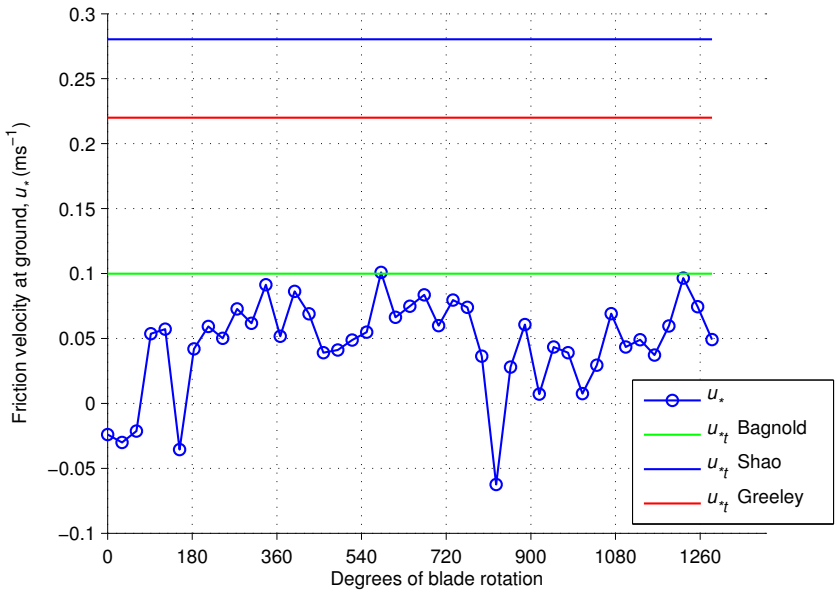

Figure 3.42: Friction velocity at $y/R = 2.0$. Threshold friction velocity for 45–53 μm glass microspheres using three models is also given.

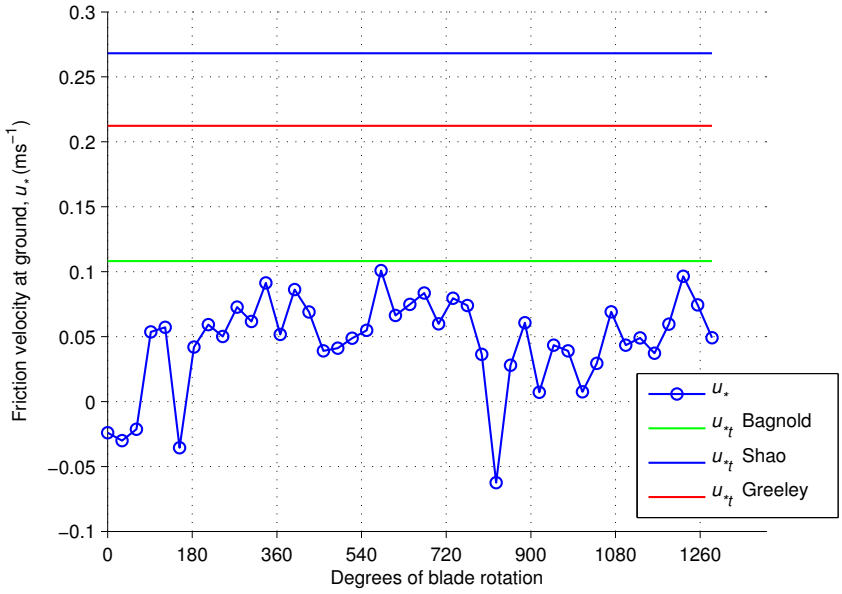

Figure 3.43: Friction velocity at y/R = 2.0. Threshold friction velocity for 53–63 μm glass microspheres using three models is also given.

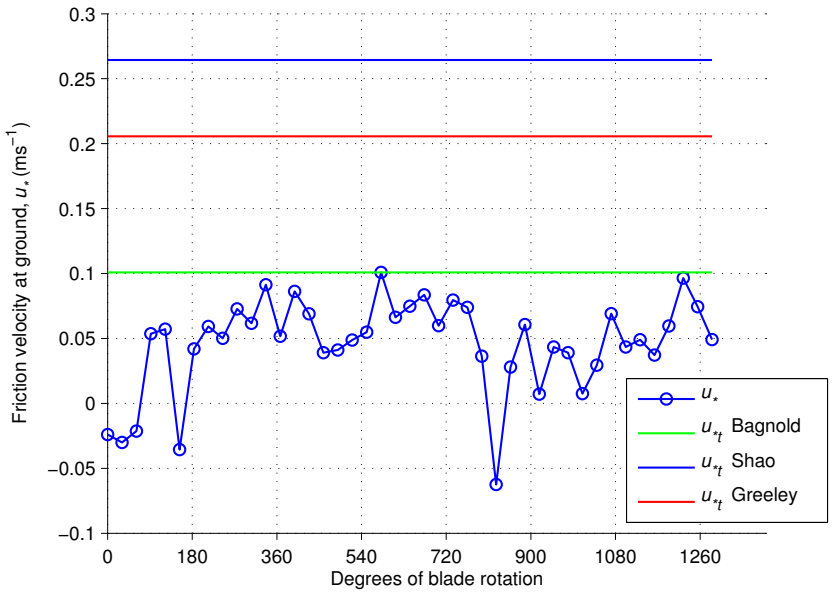

Figure 3.44: Friction velocity at y/R = 2.0. Threshold friction velocity for 45–63 μm glass microspheres using three models is also given.

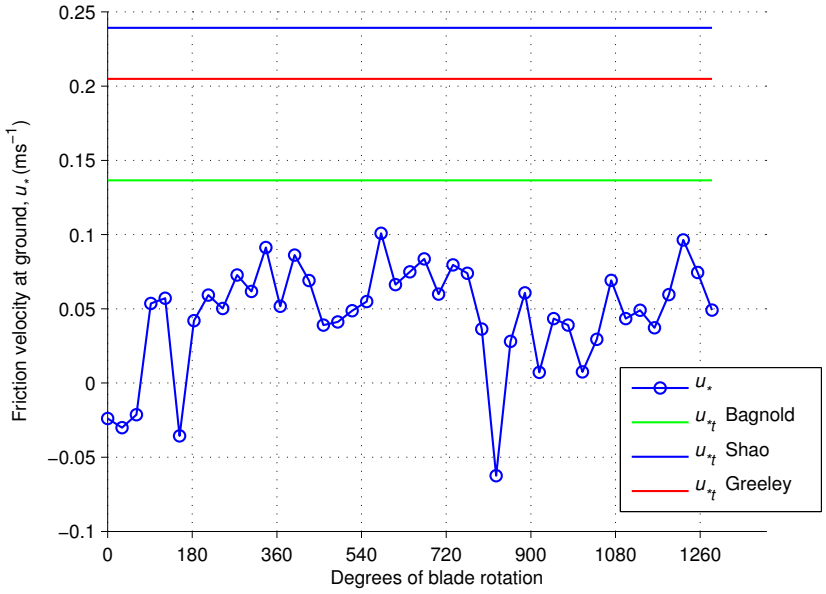

Figure 3.45: Friction velocity at $y/R = 2.0$. Threshold friction velocity for 90–106 μm glass microspheres using three models is also given.

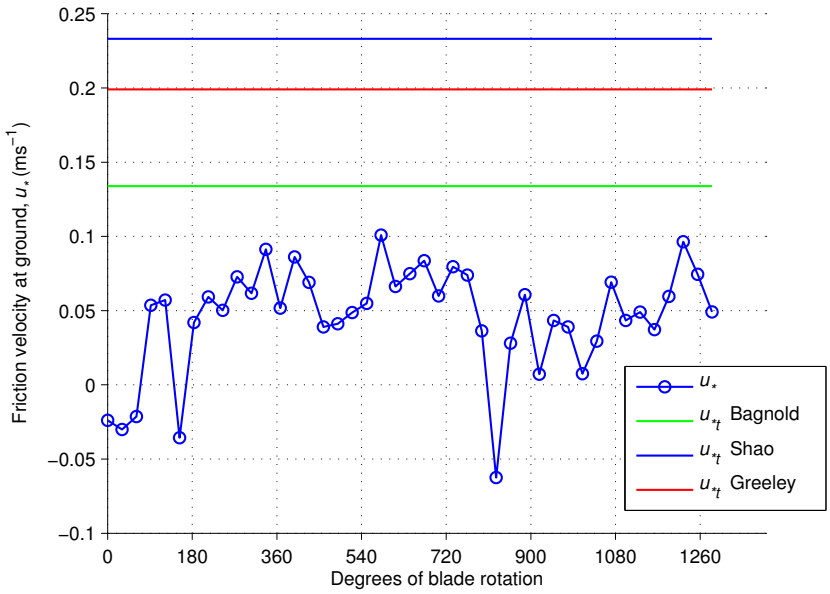

Figure 3.46: Friction velocity at $y/R = 2.0$. Threshold friction velocity for 90–125 μm glass microspheres using three models is also given.

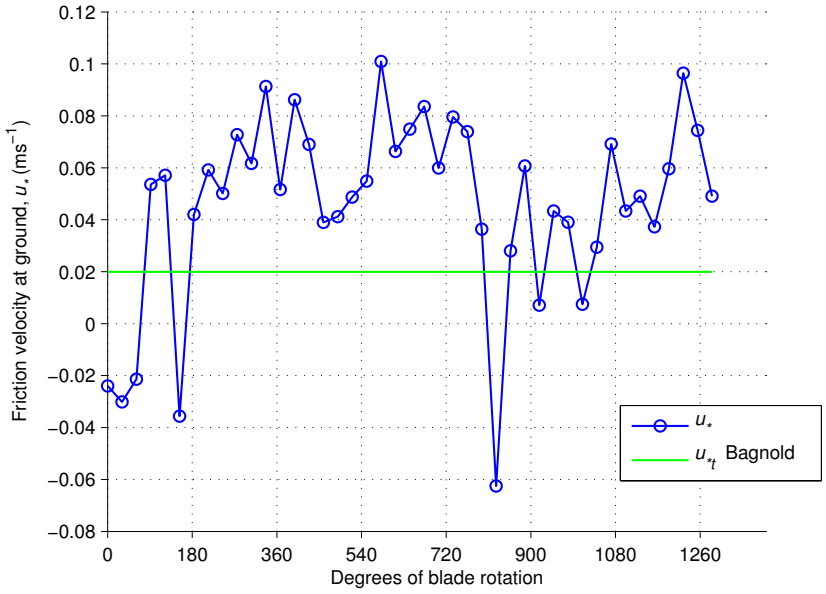

Figure 3.47: Friction velocity at y/R = 2.0 versus degrees of blade rotation. Threshold friction velocity for AZTD 0–5 μm particles using three models is also given.

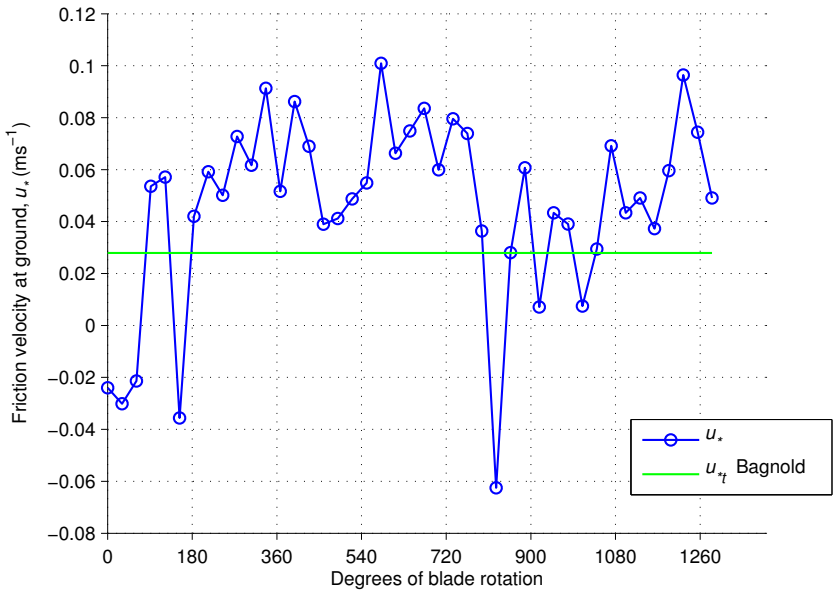

Figure 3.48: Friction velocity at y/R = 2.0 versus degrees of blade rotation. Threshold friction velocity for AZTD 0–10 μm particles using three models is also given.

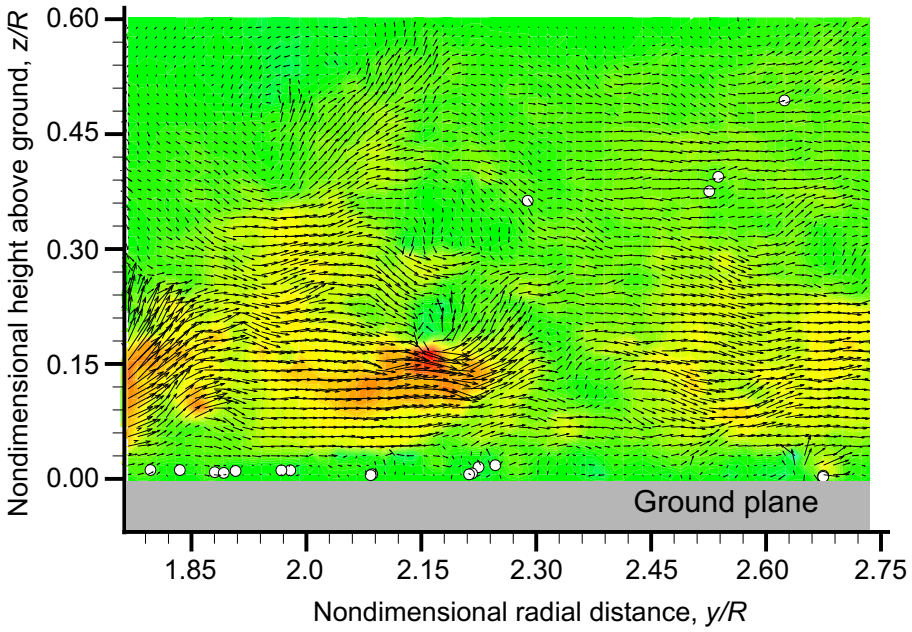

(a) Dual-phase measurement with 1–38 μm diameter glass microspheres before the passage of a tip vortex at $y/R = 2.0$

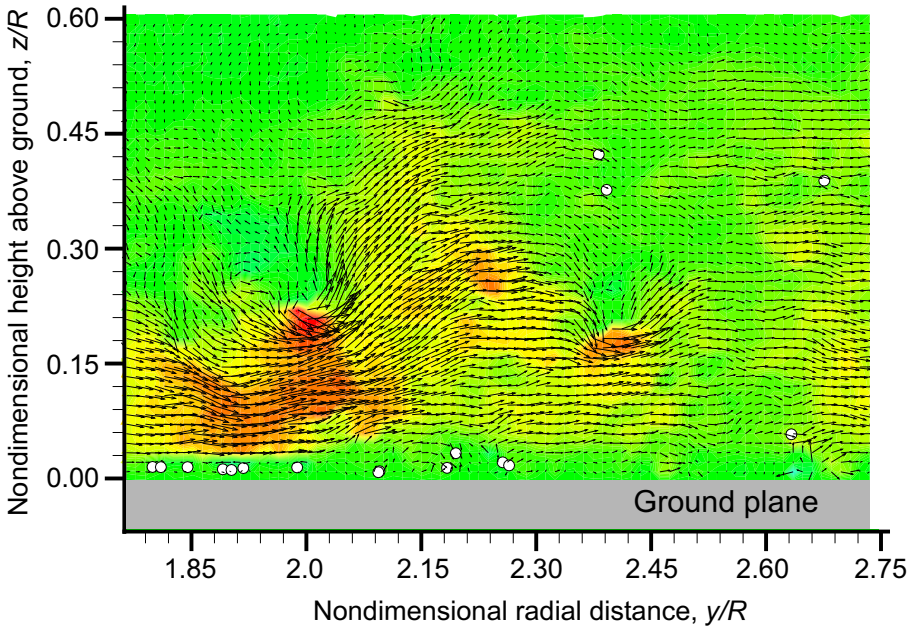

(b) Dual-phase measurement with 1–38 μm diameter glass microspheres during the passage of a tip vortex at $y/R = 2.0$

Figure 3.49: Dual-phase measurement with 1–38 μm diameter glass microspheres before and during the passage of a tip vortex

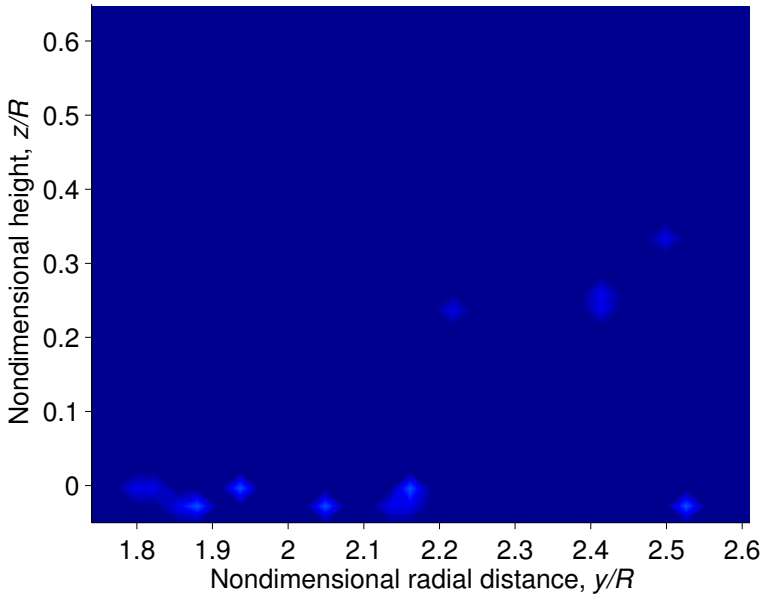

(a) Concentration map with 1–38 μm diameter glass microspheres before the passage of a tip vortex at $y/R = 2.0$

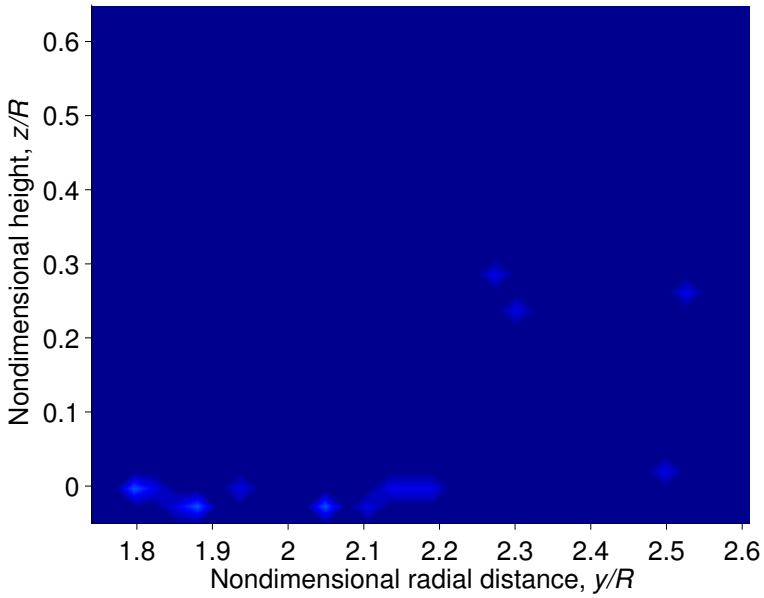

(b) Concentration map with 1–38 μm diameter glass microspheres during the passage of a tip vortex at $y/R = 2.0$

Figure 3.50: Particle concentration maps of 1–38 μm diameter glass microspheres before and during the passage of a tip vortex at $y/R = 2.0$.

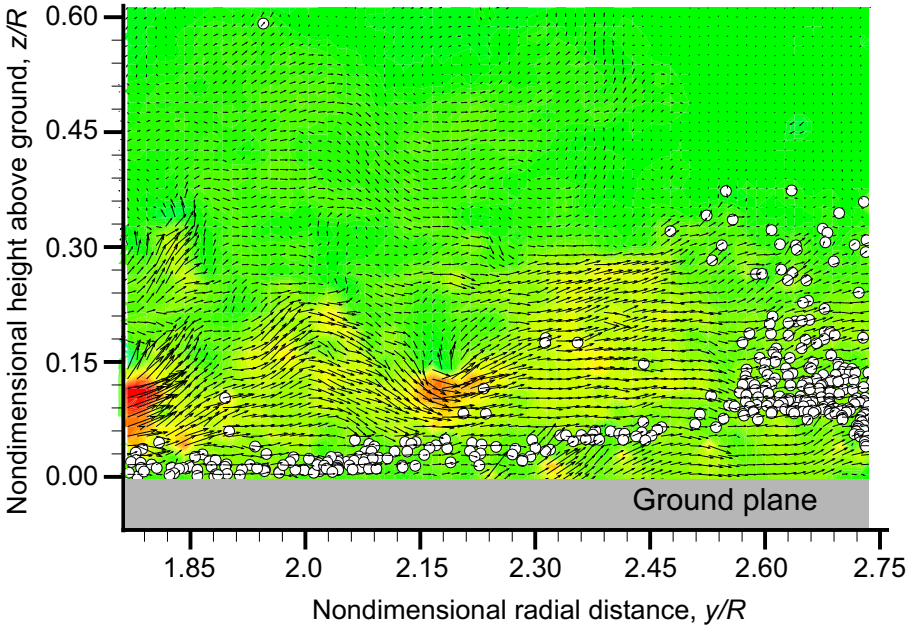

(a) Dual-phase measurement with 45–53 μm diameter glass microspheres before the passage of a tip vortex at $y/R = 2.0$

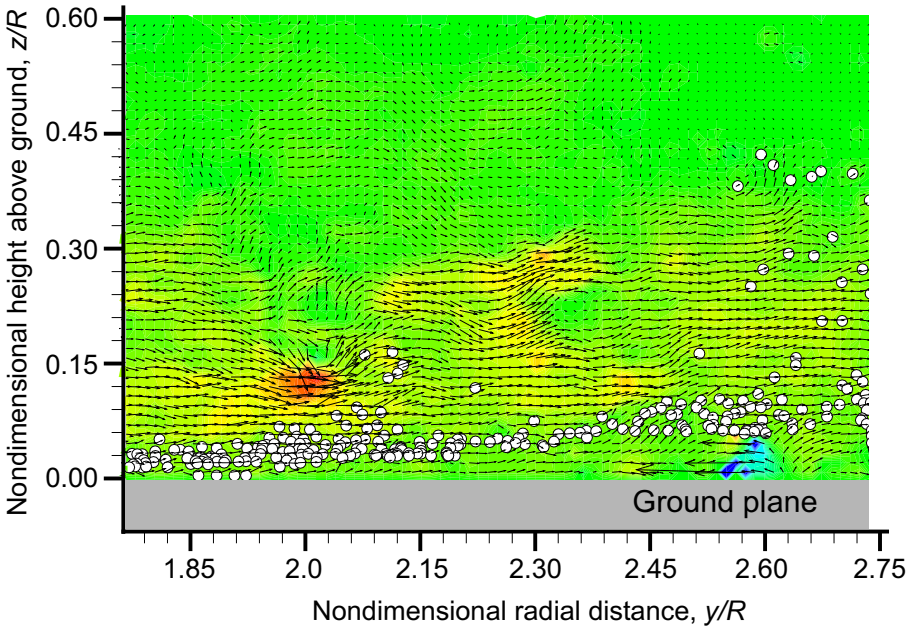

(b) Dual-phase measurement with 45–53 μm diameter glass microspheres before the passage of a tip vortex at $y/R = 2.0$

Figure 3.51: Dual-phase measurement with 45–53 μm diameter glass microspheres before and during the passage of a tip vortex

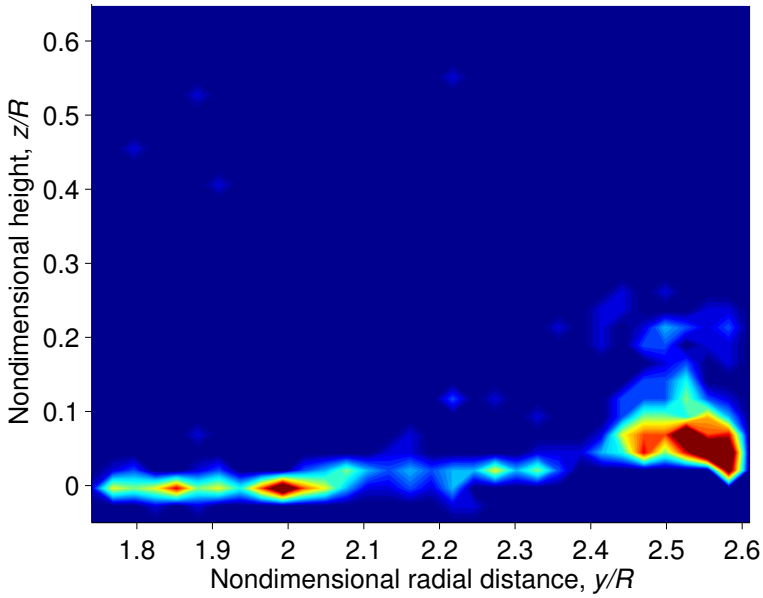

(a) Concentration map with 45–53 μm diameter glass microspheres before the passage of a tip vortex at $y/R = 2.0$

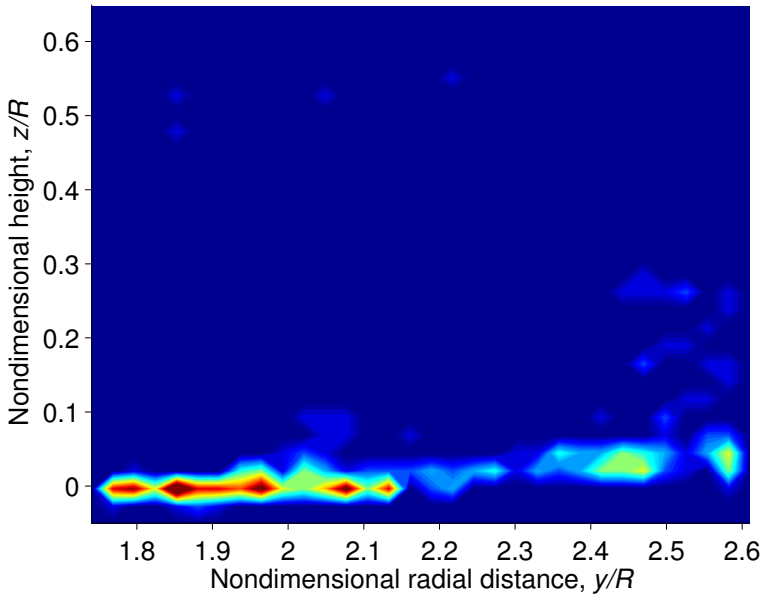

(b) Concentration map with 45–53 μm diameter glass microspheres during the passage of a tip vortex at $y/R = 2.0$

Figure 3.52: Particle concentration maps of 45–53 μm diameter glass microspheres before and during the passage of a tip vortex at $y/R = 2.0$.

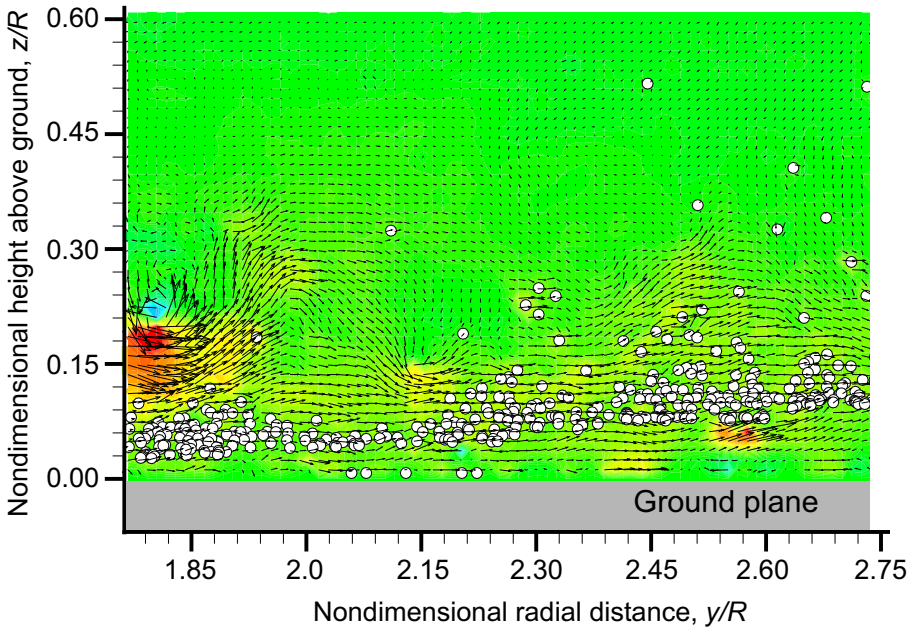

(a) Dual-phase measurement with 53–63 μm diameter glass microspheres before the passage of a tip vortex at $y/R = 2.0$

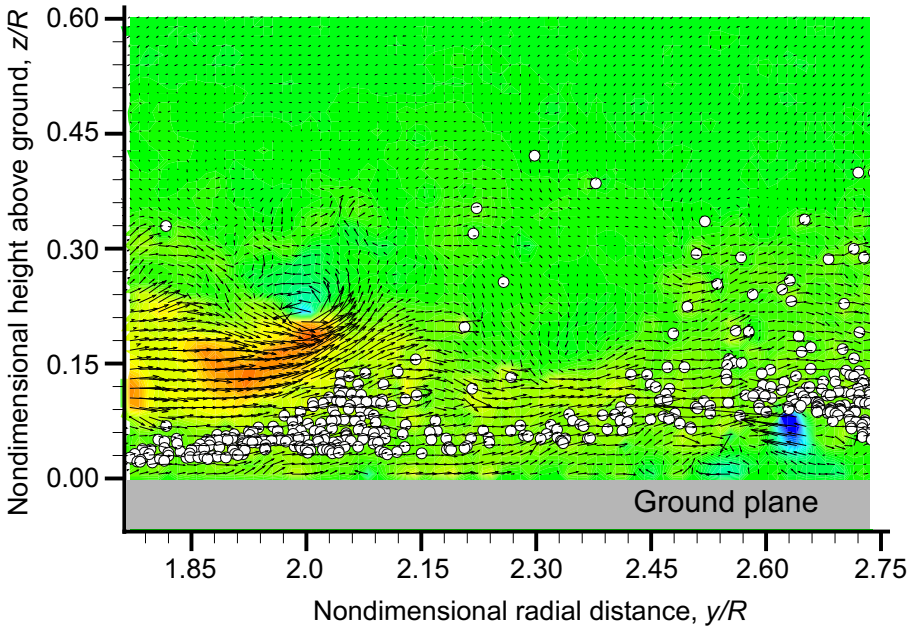

(b) Dual-phase measurement with 53–63 μm diameter glass microspheres during the passage of a tip vortex at $y/R = 2.0$

Figure 3.53: Dual-phase measurement with 53–63 μm diameter glass microspheres before and during the passage of a tip vortex

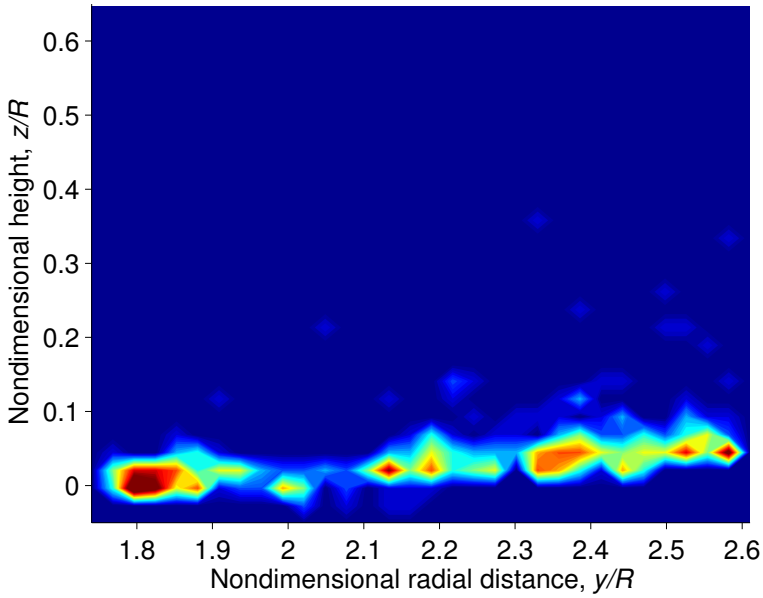

(a) Concentration map with 53–63 μm diameter glass microspheres before the passage of a tip vortex at $y/R = 2.0$

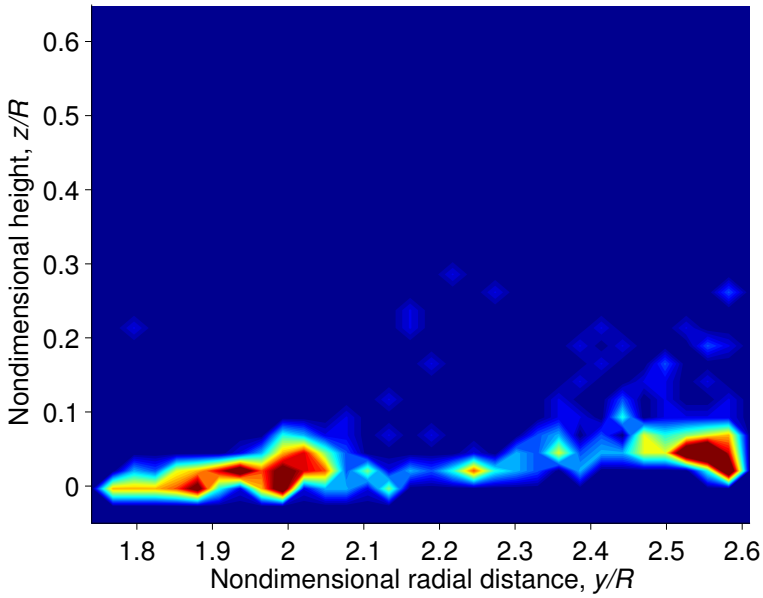

(b) Concentration map with 53–63 μm diameter glass microspheres during the passage of a tip vortex at $y/R = 2.0$

Figure 3.54: Particle concentration maps of 53–63 μm diameter glass microspheres before and during the passage of a tip vortex at $y/R = 2.0$.

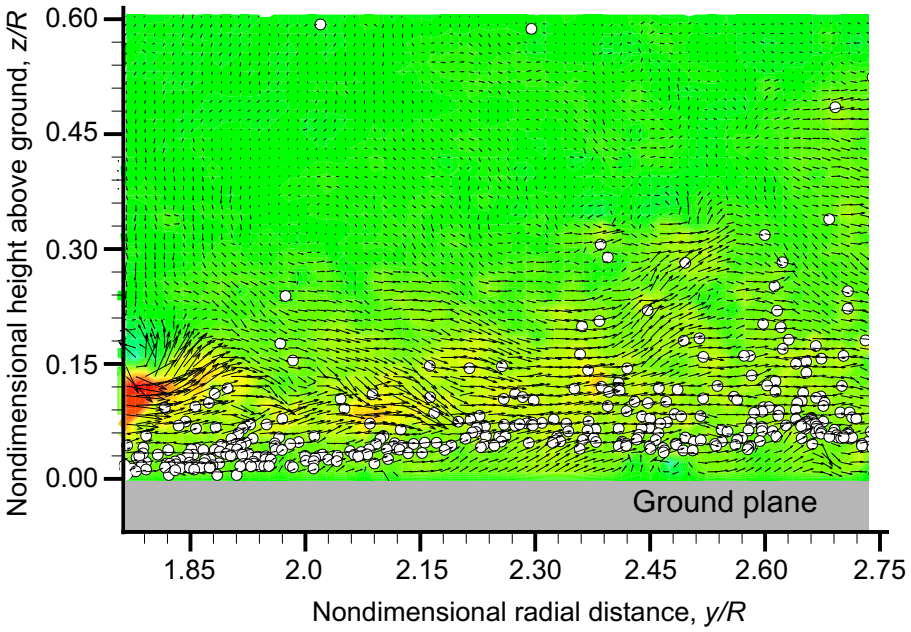

(a) Dual-phase measurement with 45–63 μm diameter glass microspheres before the passage of a tip vortex at $y/R = 2.0$

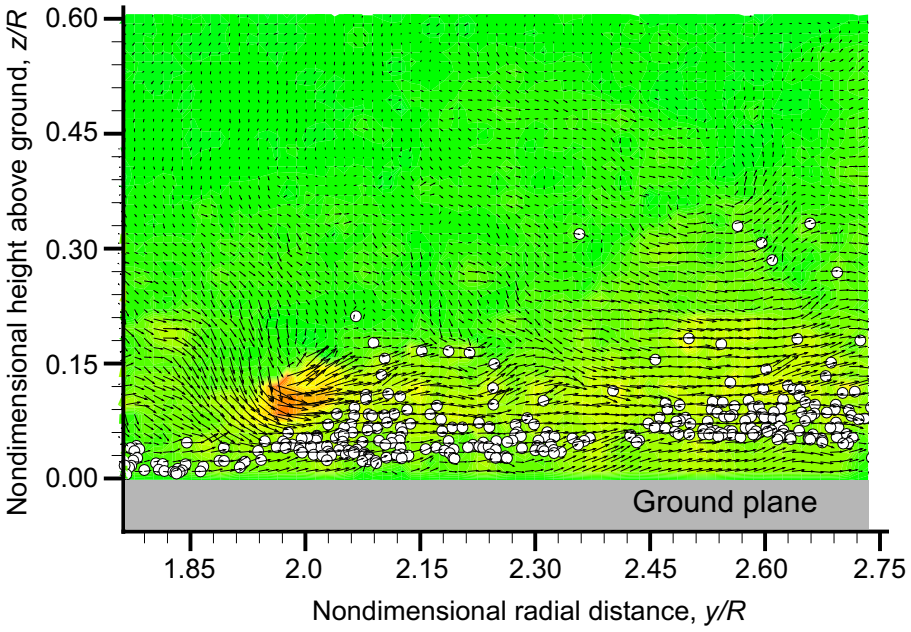

(b) Dual-phase measurement with 45–63 μm diameter glass microspheres during the passage of a tip vortex at $y/R = 2.0$

Figure 3.55: Dual-phase measurement with 45–63 μm diameter glass microspheres before and during the passage of a tip vortex

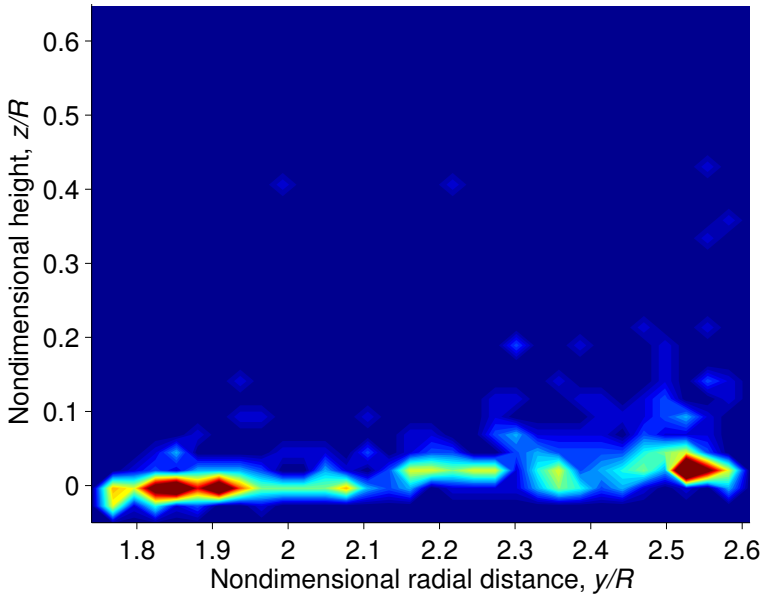

(a) Concentration map with 45–63 μm diameter glass microspheres before the passage of a tip vortex at $y/R = 2.0$

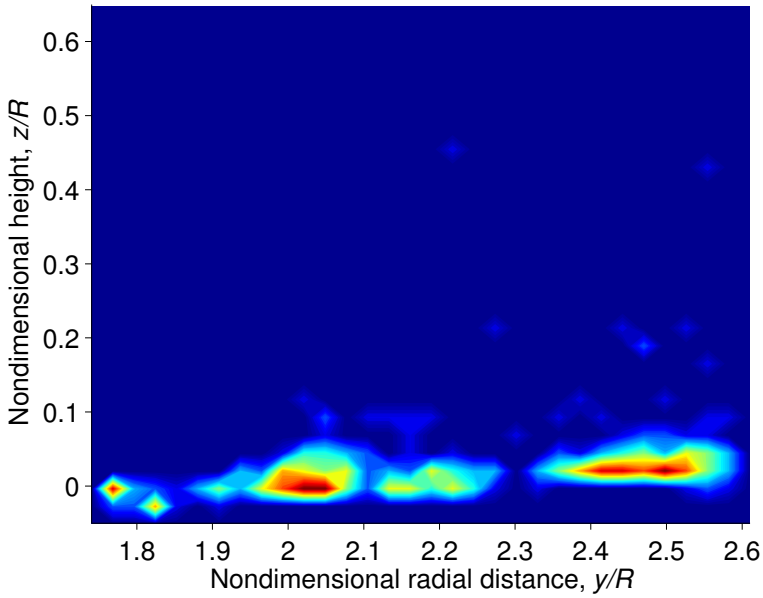

(b) Concentration map with 45–63 μm diameter glass microspheres during the passage of a tip vortex at $y/R = 2.0$

Figure 3.56: Particle concentration maps of 45–63 μm diameter glass microspheres before and during the passage of a tip vortex at $y/R = 2.0$.

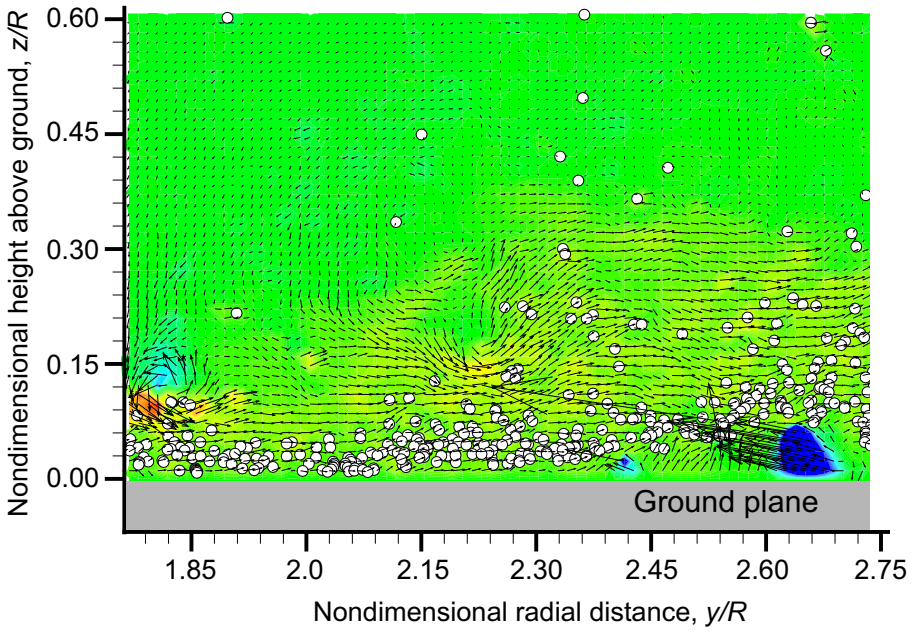

(a) Dual-phase measurement with 90–106 μm diameter glass microspheres before the passage of a tip vortex at $y/R = 2.0$

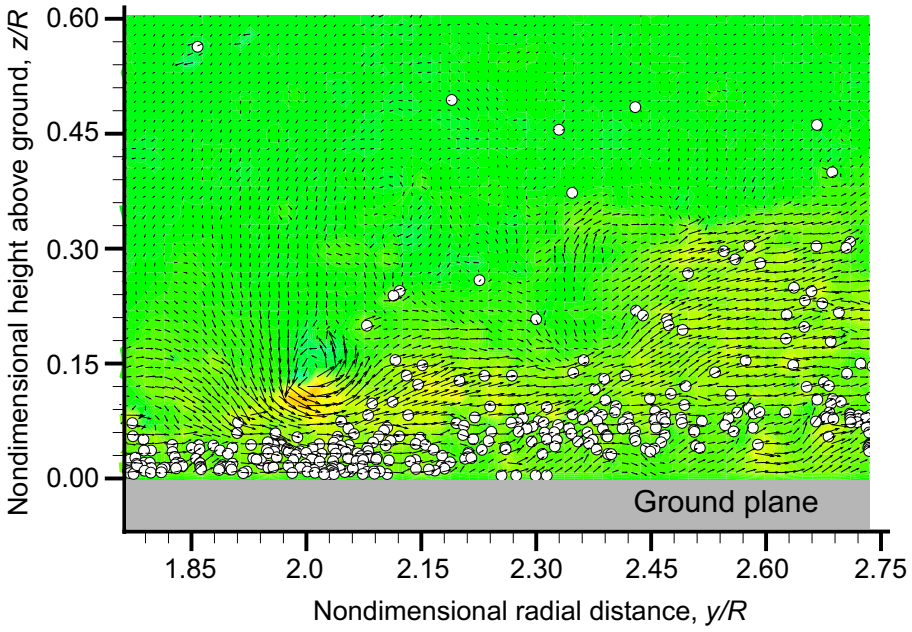

(b) Dual-phase measurement with 90–106 μm diameter glass microspheres during the passage of a tip vortex at $y/R = 2.0$

Figure 3.57: Dual-phase measurement with 90–106 μm diameter glass microspheres before and during the passage of a tip vortex

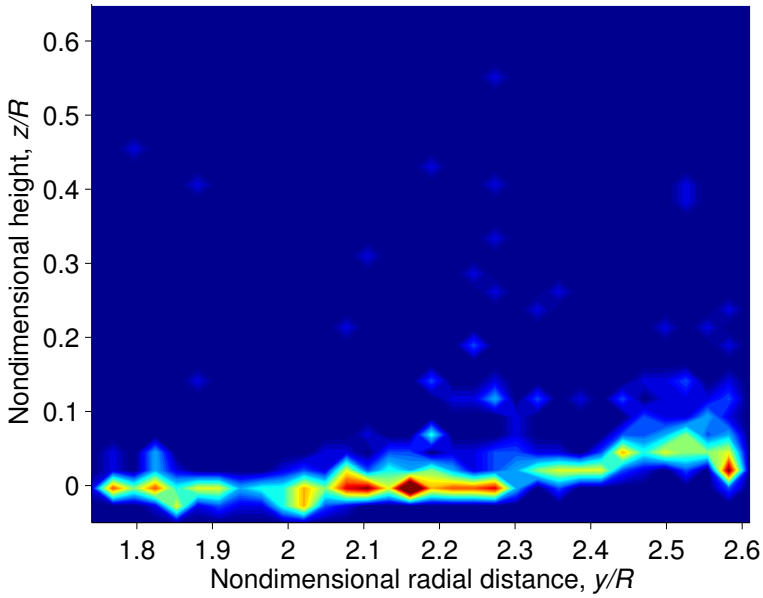

(a) Concentration map with 90–106 μm diameter glass microspheres before the passage of a tip vortex at $y/R = 2.0$

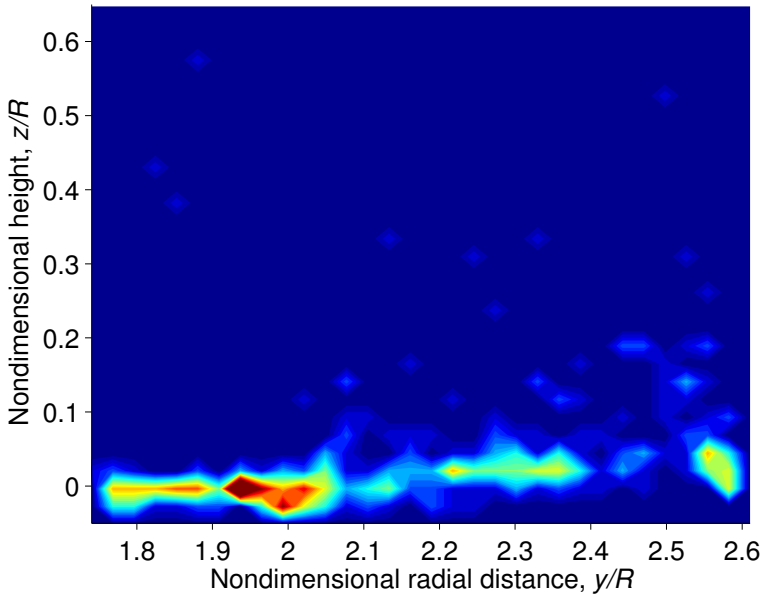

(b) Concentration map with 90–106 μm diameter glass microspheres during the passage of a tip vortex at $y/R = 2.0$

Figure 3.58: Particle concentration maps of 90–106 μm diameter glass microspheres before and during the passage of a tip vortex at $y/R = 2.0$.

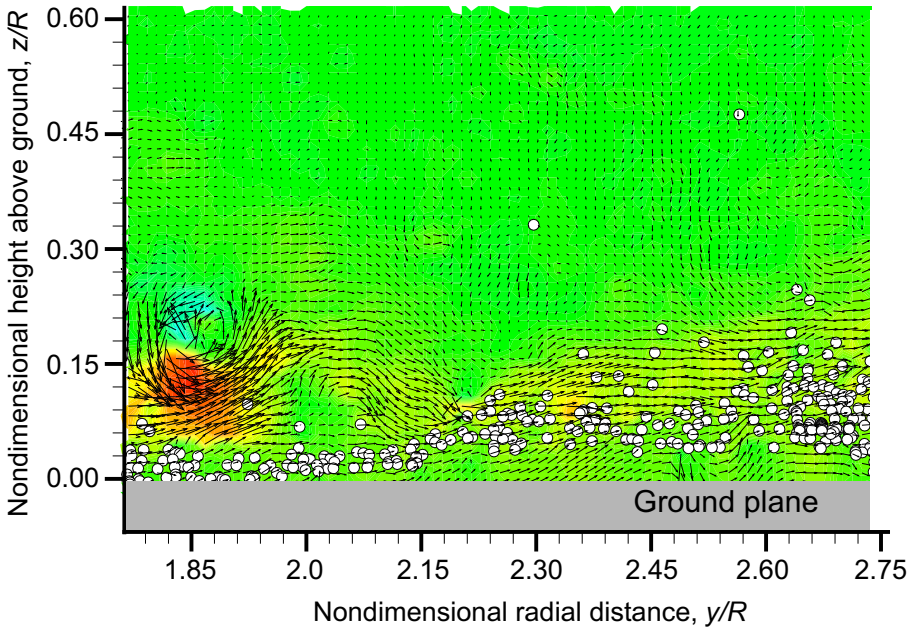

(a) Dual-phase measurement with 90–125 μm diameter glass microspheres before the passage of a tip vortex at $y/R = 2.0$

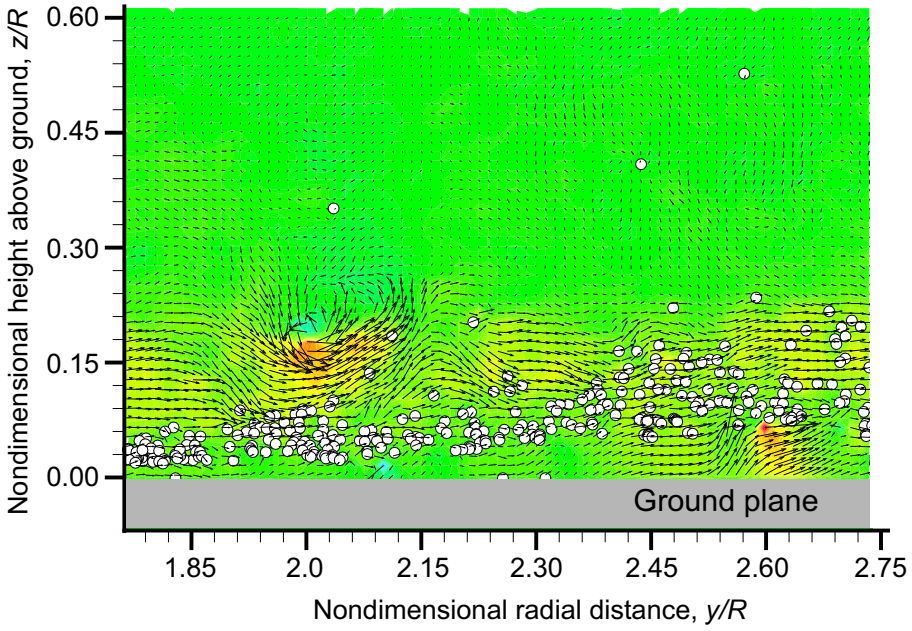

(b) Dual-phase measurement with 90–125 μm diameter glass microspheres during the passage of a tip vortex at $y/R = 2.0$

Figure 3.59: Dual-phase measurement with 90–125 μm diameter glass microspheres before and during the passage of a tip vortex

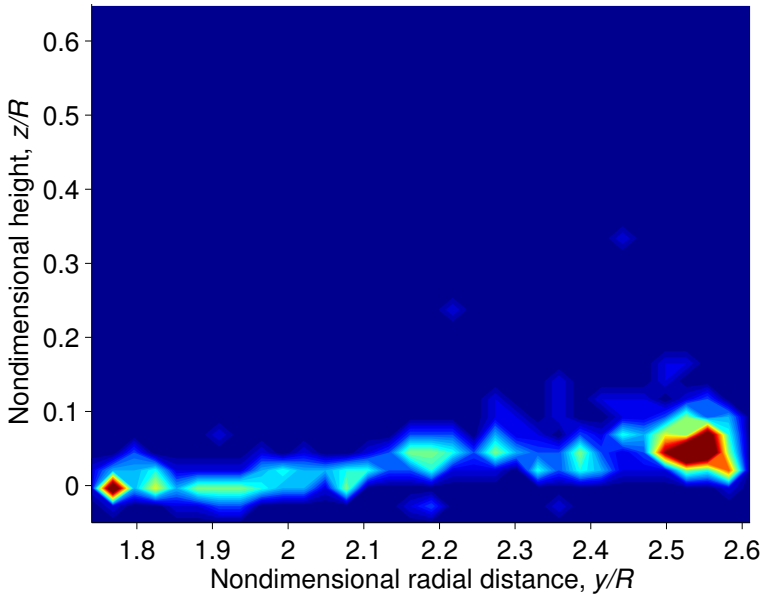

(a) Concentration map with 90–125 μm diameter glass microspheres before the passage of a tip vortex at $y/R = 2.0$

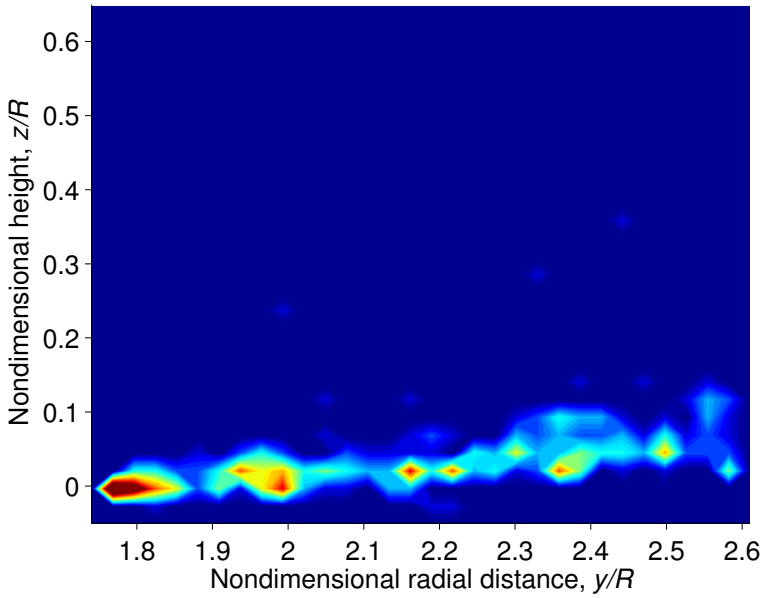

(b) Concentration map with 90–125 μm diameter glass microspheres during the passage of a tip vortex at $y/R = 2.0$

Figure 3.60: Particle concentration maps of 90–125 μm diameter glass microspheres before and during the passage of a tip vortex at $y/R = 2.0$.

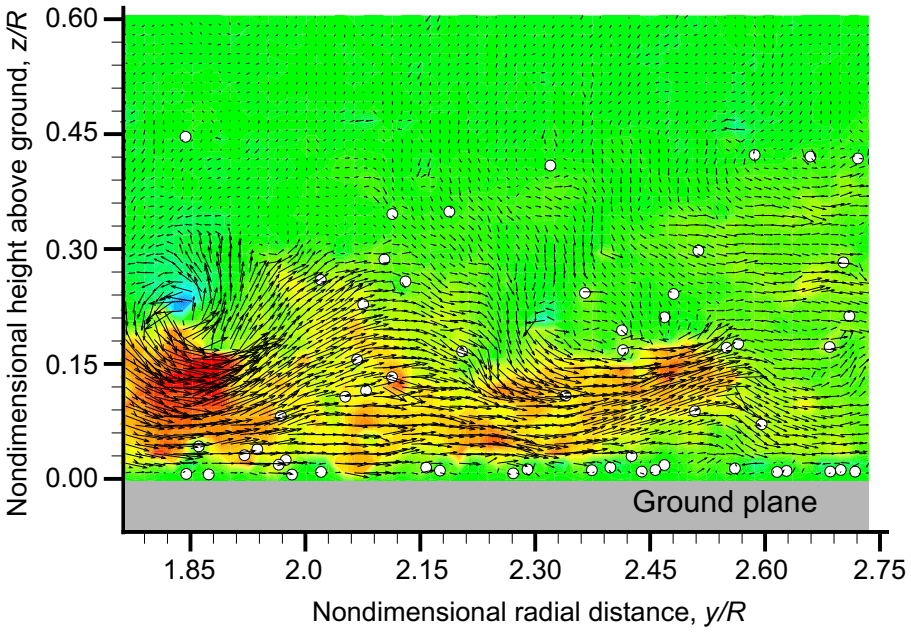

(a) Dual-phase measurement with AZTD 0–5 μm particles before the passage of a tip vortex at $y/R = 2.0$

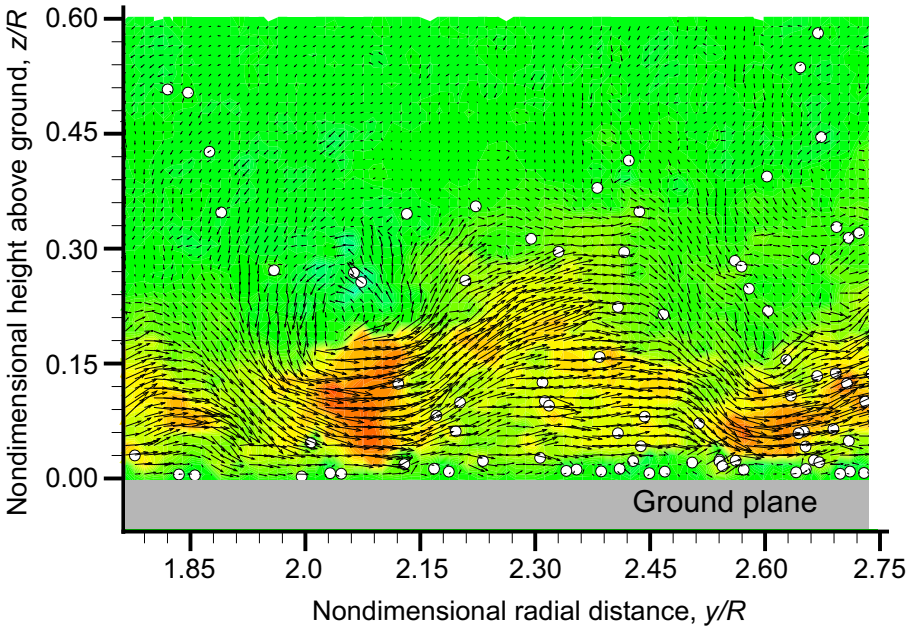

(b) Dual-phase measurement with AZTD 0–5 μm particles during the passage of a tip vortex at $y/R = 2.0$

Figure 3.61: Dual-phase measurement with AZTD 0–5 μm diameter particles before and during the passage of a tip vortex

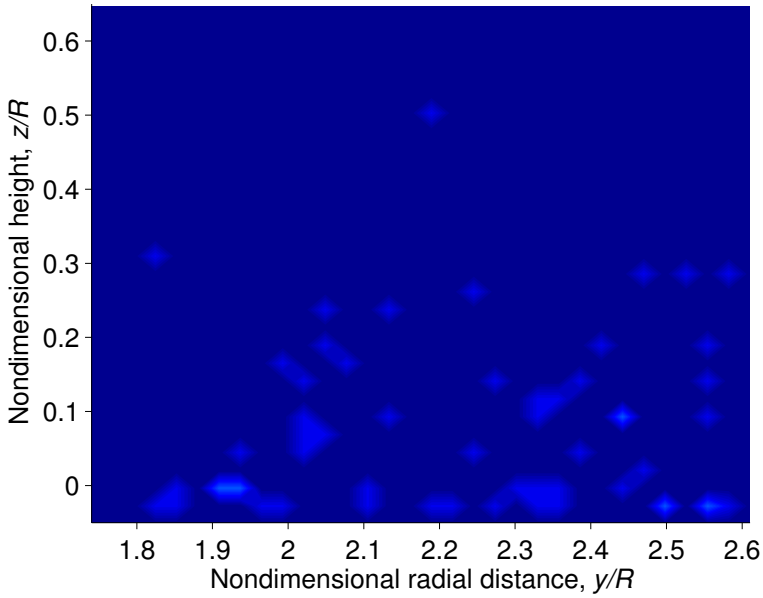

(a) Concentration map with AZTD 0–5 μm diameter glass microspheres before the passage of a tip vortex at $y/R = 2.0$

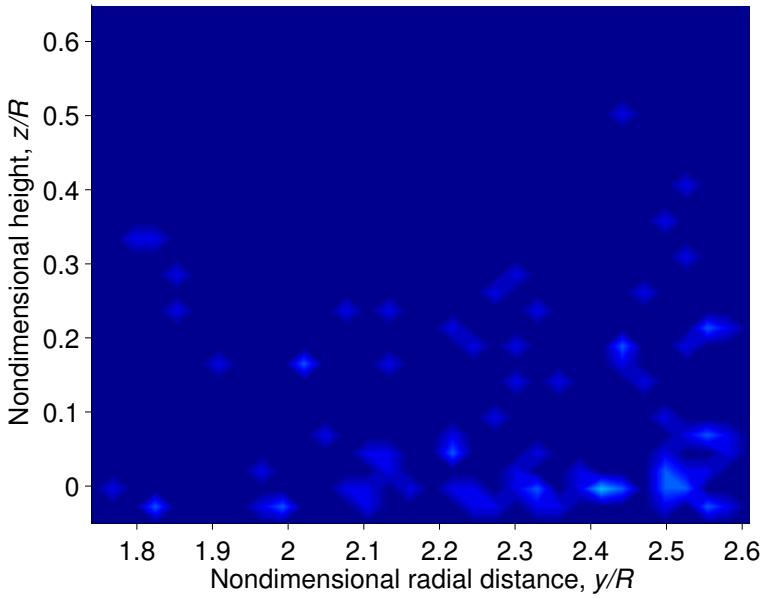

(b) Concentration map with AZTD 0–5 μm diameter glass microspheres during the passage of a tip vortex at $y/R = 2.0$

Figure 3.62: Particle concentration maps of AZTD 0–5 μm diameter glass microspheres before and during the passage of a tip vortex at $y/R = 2.0$.

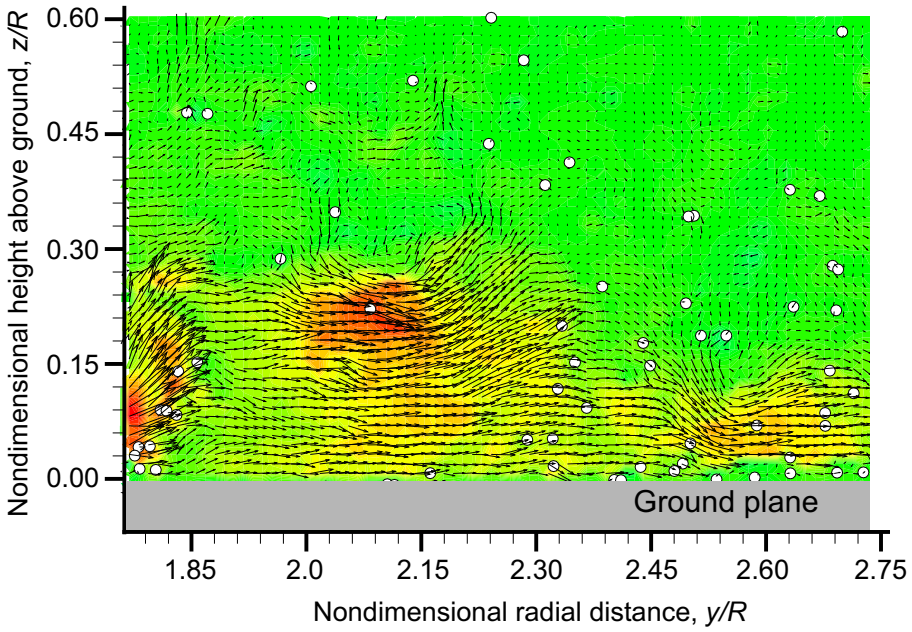

(a) Dual-phase measurement with AZTD 0–10 μm particles before the passage of a tip vortex at $y/R = 2.0$

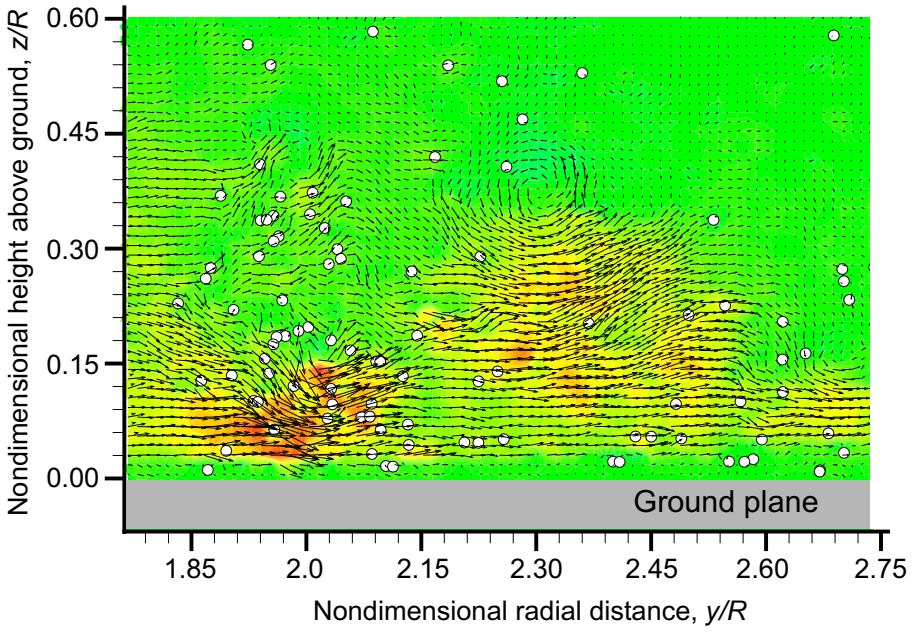

(b) Dual-phase measurement with AZTD 0–10 μm particles during the passage of a tip vortex at $y/R = 2.0$

Figure 3.63: Dual-phase measurement with AZTD 0–10 μm diameter particles before and during the passage of a tip vortex

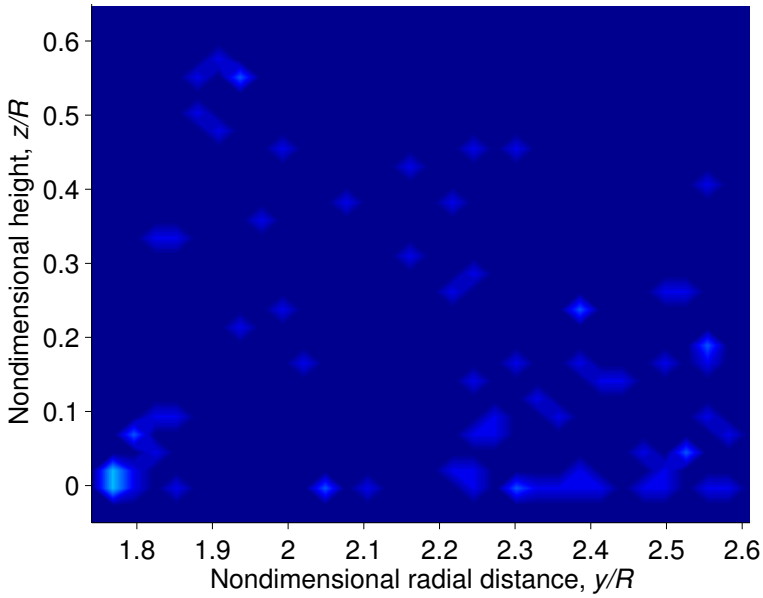

(a) Concentration map with AZTD 0–10 μm diameter glass microspheres before the passage of a tip vortex at $y/R = 2.0$

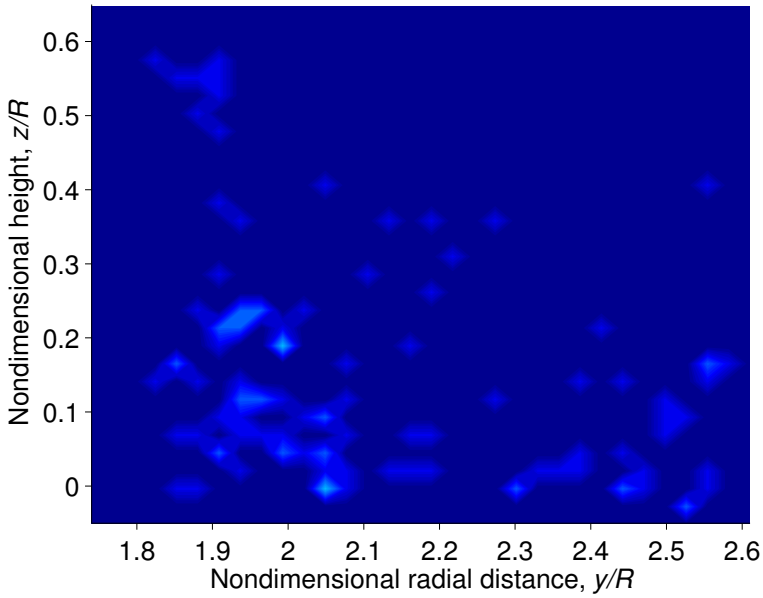

(b) Concentration map with AZTD 0–10 μm diameter glass microspheres during the passage of a tip vortex at $y/R = 2.0$

Figure 3.64: Particle concentration maps of AZTD 0–10 μm diameter glass microspheres before and during the passage of a tip vortex at $y/R = 2.0$.

3.4.10 Summary

The objective of the present work was to examine the effects of five similarity parameters on sediment entrainment and uplift below a hovering rotor. The similarity parameters studied were: 1. Particle diameter-to-rotor radius ratio, D_p/R, 2. Particle-to-fluid density ratio, ρ_s/ρ, 3. Ratio of characteristic flow (or wind) speed to particle terminal speed, U_{char}/U_F, 4. Densimetric Froude number, $U_{\text{char}}/\sqrt{(\rho_s/\rho - 1)gD_p}$, and 5. Threshold friction speed ratio, U_{char}/u_{*_t}.

The time-averaged wall flow below the was analyzed and the characteristic velocity was determined to be $U_{\text{char}} = 4.104$ ms^{-1} for the operating conditions used in the present work. The particle size and density of each sediment sample were also measured. Using this information, the similarity parameters for each sample were then calculated. Differences in the quantity and location of sediment uplift between samples were studied using particle concentration maps.

Measurements of particle entrainment to changes in the values of the similarity parameters were made. Particle entrainment was observed to decrease with increasing D_p/R and decrease with increasing ρ_s/ρ. The particle terminal velocity, U_F, was calculated using a model from [59]. As the ratio U_{char}/U_F increased, particle entrainment was observed to increase. As the Froude number increased, the quantity of suspended particles increased.

While measurements of u_{*_t} were not obtained, the values were calculated using three threshold friction velocity models developed by Bagnold, Shao, and Greeley. Bagnold's model was found to correlate better with the behaviors of sediment mobility that

observed in the experiments. Generally, as U_{char}/u_{*_t} increased, the quantity of suspended particles also increased. In addition, measurements of the friction velocity showed significant excursions in the wall shear with a passing tip vortex. The increased friction velocity was shown to correlate closely with the uplift of sediment particles from the bed.

3.5 Ranking of Similarity Parameters

Identifying the parameters that have the greatest effects on the mobilization and uplift of particles is the first step towards more closely simulating the physics of brownout at the smaller scales needed in laboratory experiments. To this end, the results shown previously can be used to rank the similarity parameters in an order of importance. These rankings were determined from the observations of the sensitivity of the quantity of uplifted particles to changes in the value of a given similarity parameter.

The density ratio, ρ_s/ρ, had the most important effects, with large differences in uplift occurring with only moderate changes in density. Changes in the particle size-to-rotor radius ratio, D_p/R, also had a significant effect, but the glass particle samples did not necessarily follow the same trends. A trend was recognized with changes in the Froude number, but again the glass particles did not seem to follow the trend. For the terminal velocity ratio, U_{char}/U_F, sediment uplift was less sensitive because large changes in uplift required large changes in the value of U_{char}/U_F. The effect of the threshold velocity ratio is clear when using the relatively simple Bagnold model, but the results from the other, more comprehensive models, did not agree with the observations made in the experiments. In this case, the difference in the predicted behavior and the actual

behavior of the sediment particles can be attributed to the fact that these models are semi-empirical in nature, and the values of the empirical constants used may not be the same for the particles samples studied in the present work. Further work will be required to better understand the effect that the threshold friction velocity ratio, U_{char}/u_{*_t}, has on particle entrainment below the rotor.

Using the results obtained in this study, the ranking of importance are assigned as follows: **1)** Particle-to-fluid density ratio, ρ_s/ρ; **2)** Particle diameter-to-rotor radius ratio, D_p/R; **3)** Densimetric Froude number, $U_{\text{char}}/\sqrt{(\rho_s/\rho - 1)gD_p}$; **4)** Ratio of wind speed to particle terminal speed, U_{char}/U_F; and **5)** Threshold friction speed ratio, U_{char}/u_{*t}. These outcomes can be used as a basis for designing future experiments to more closely simulate the physics of brownout in the laboratory.

3.6 Summary

This chapter has described the experimental results and analysis of the effects that varying the similarity parameters has on the dual-phase flow environment below a hovering rotor. The vortices were characterized from the PIV measurements to determine their circulation, vortex Reynolds number, and swirl velocity profile. Phase-averaged measurements also showed that the flow near the ground was unsteady and aperiodic because of the convection of tip vortices over the ground plane, and a characteristic velocity was calculated. The characteristics of the sediment samples that were needed to calculate values of the various similarity parameters were measured and quantified.

Particle concentration maps showed that the processes of sediment entrainment and

transport were sensitive to the values of the similarity parameters. Changes in the density ratio and particle size ratio had the strongest correlations with changes in particle uplift. Changes in the Froude number were correlated with changes in particle uplift, with some samples deviating from the trend. Sediment entrainment was shown to be less sensitive to changes in the terminal velocity ratio. The threshold friction velocity ratio showed different trends depending on the model used to calculate u_{*_t}, but more studies will be required to establish the effects on scaling. Based on the present results, rankings were assigned to the similarity parameters with a view to understanding better ways to simulate the fluid mechanics of brownout in the laboratory environment.

Chapter 4

Conclusions

4.1 Summary

The results obtained during the course of the present work have provided a new understanding into the effects that certain key sedimentology (or aeolian) similarity parameters have on the uplift of sediment particles from a mobile bed underlying a hovering rotor. Questions about producing dynamic similarity of the two-phase flow were addressed. To this end, the work has involved both single-phase and two-phase flow experiments using a small-scale rotor that was hovering at a fixed height over a mobile bed comprised of different particle species. The outcomes from the work have contributed to the understanding of how certain similarity parameters can affect the dusty two-phase flow environment generated by a rotor, and may help in performing better matching of such similarity parameters to simulate the physics of brownout under controlled laboratory conditions. An overall goal of the work was to provide a better physical insight into the physics of the problem of rotorcraft brownout, which continues to be a serious operational problem.

In the experiments that were conducted, high-speed flow visualization and time-resolved particle image velocimetry were used to conduct temporal tracking of the flow features and to make appropriate measurements of the flow field. In the dual-phase experiments, the mobilized sediment particles were identified and tracked through the flow

by using particle identification software. All of the sediment samples used in the present study were carefully characterized with respect to their size and mass density, and in some cases their mineralogy. The two-phase flow field measurements and known sediment properties then allowed for the calculation of the certain groups of similarity parameters for each sediment sample. The quantity and locations of uplifted particles were measured for each sample under the same rotor operating conditions, and any relationships between the sediment uplift with changes in the defined similarity parameters were then examined. In the present work, five similarity parameters were studied in that they were considered to have potentially the most important effects on the developing two-phase flow below the rotor.

In general, the outcomes from the experiments showed that processes of sediment entrainment and transport below the rotor were sensitive to changes in all of the scaling or similarity parameters that were selected. However, it was found that not all the similarity parameters had as large or important effects on the two-phase flow, suggesting that in practice the sediment uplift below a rotor will be more sensitive to some parameters than to others. This outcome also suggests that while designing specific laboratory experiments to study the two-phase flow and particle physics of rotorcraft brownout, it may be sufficient for the purposes of producing a representative two-phase flow to match a few of the similarity parameters that have the most influence on particle entrainment, rather than trying to match all of the relevant similarity parameters simultaneously.

Designing an experiment that would match all of the similarity or scaling parameters of full-scale brownout conditions is clearly a significant challenge if not impossible. Not only are there geometric considerations, such as scaling particle size, but also con-

siderations of the innate properties of the particles, such as density, settling velocity, and threshold friction velocity. It is also not guaranteed that changing one of the properties might not also, as a consequence, change the others. For example, if a small-scale experiment, similar to the one used in the present work, were to be considered where the similarity parameters were perfectly matched to full-scale values (given in Appendix C for a representative helicopter), the particles would have to be 0.05 μm in diameter, have the same density as naturally occurring sediment ($\rho_s \approx 2{,}650\ \mathrm{kg\,m^{-3}}$), have very low settling velocities of 0.0008 $\mathrm{ms^{-1}}$, and have a threshold velocity of 0.147 $\mathrm{ms^{-1}}$. According to the currently used threshold mobility models, the threshold friction velocity for particles of this size and density would be much higher (u_{*_t}= 8.09 $\mathrm{ms^{-1}}$) than what would otherwise be desired. It may be that using custom designed particles (if it is at all possible) in which the properties can be precisely controlled, or changing the fluid (discussed under future work), might be a way forward to accomplish better dynamic similitude.

4.2 Specific Conclusions

The following specific conclusions have been drawn from the present study:

1. The particle-to-fluid density ratio was observed to have the most important effects on sediment uplift below the rotor. As this density ratio increased, the quantity of particles entrained into the flow steadily decreased. This outcome arises because the denser particles have the tendency to descend faster in the carrier flow than the less dense particles. Also, because of their inertia, the denser particles do not respond to changes in the flow velocity as quickly as the less dense particles. One

important outcome of this effect is that fewer particles are uplifted and trapped by the vortical features of the rotor flow as they pass near the bed. Particle size also had obvious effects on sediment entrainment, the larger particles having higher velocity thresholds needed to produce particle mobility and uplift from the bed. However, some of the samples with the smaller particles were also shown to be less mobile than the larger ones, most likely because of inter-particle forces such as cohesion.

2. Changes in the densimetric Froude number and terminal velocity ratio both had observable effects on sediment mobility and entrainment below the rotor. As the Froude number increased, the quantity of entrained particles increased, which is because the inertial forces on the particle became more important relative to their gravitational forces. However, the glass microspheres that were used in the present experiments did not seem to follow the same trends that were shown by some of the other particles; most of the glass microspheres had relatively lower Froude numbers but were entrained into the flow more readily than particles with higher Froude numbers. A similar trend was observed with respect to the terminal velocity ratio; particles with higher terminal velocity ratios experienced greater levels of particle mobilization. However, again the glass microspheres did not seem to follow these trends, showing greater quantities of entrained particles than for the samples with higher terminal velocity ratios.

3. The flow measurements made near the ground revealed that the passage of a tip vortex not only caused unsteady excursions in the wall-parallel flow velocity profile, but it also caused significant increases in the wall shear stress and friction veloc-

ity. The increase in friction velocity from the passing of the tip vortices above the sediment bed could be correlated in some (but not all) cases to the increased mobilization of sediment particles. This observation confirms the premise that the close passage of the blade tip vortices trailed from the rotor and their proximity to the sediment bed is a primary mechanism that is responsible for sediment mobilization as well as uplift (i.e., "trapping") and, ultimately, in the development of rotor-induced brownout conditions.

4. It was found that the semi-empirical threshold friction velocity models that are used in current practice may not be fully applicable to the flow environment found on the bed below the rotor. The results predicting the onset of sediment mobility using the Bagnold threshold friction velocity model was found to correlate well with the behavior shown in the present experiments. It was shown that the kaolinite was the most readily mobilized sediment sample and the Ottawa sand was the least mobile, which agreed with predictions made by Bagnold's threshold friction velocity model. However, the Shao and Greeley threshold friction velocity models predicted that the kaolinite would have the highest threshold friction velocity (i.e., it would be the most difficult to mobilize) and that Ottawa sand would have the lowest threshold friction velocity (i.e., the most easily mobilized). It is recognized that such differences between experimental observations and predicted threshold values can arise because because of several other reasons besides the effect of particle size and density. Nevertheless, these contradictory outcomes suggest that currently used threshold friction velocity models should be used cautiously in the prediction

of rotorcraft brownout conditions.

4.3 Suggestions for Future Work

The specific objectives of the work were to help better the understanding of the effects that certain key aeolian similarity parameters have on the processes of sediment mobilization, uplift, and entrainment from a mobile sediment bed below a rotor. While the present work is by no means complete, it has provided new fundamental insight into the two-phase fluid mechanics below a rotor hovering above a mobile sediment bed. There are obviously still many issues that could be addressed in the future to better understand the scaling effects, and how they contribute to the problem of rotorcraft brownout.

4.3.1 Measurements of Threshold Friction Velocity

The models used in the present work to estimate the threshold friction velocity did not correlate in all cases with the observed movement of the sediment particles. Such differences between experimental observations and predicted values can arise because because of several reasons, including properties of the sediment that go beyond particle size and density. For example, the chemical structure, actual geometric shapes, and mineral content of the particles may also affect their mobilization characteristics. Furthermore, there are pressure forces acting on the particles below the rotor, which may also affect their mobilization thresholds. Actual measurements of the threshold friction velocity for the types of wall-jet type flows found below the rotor would help to better estimate this quantity, and perhaps allow more accurate values of mobilization thresholds to be ob-

tained. For example, measurements of the threshold friction velocity, u_{*_t}, in a wall-jet type of flow would require not only the ability to generate a very controlled flow but also an ability to measure the turbulent velocity profile deeply into the boundary layer region at the wall.

4.3.2 Effects of Unsteadiness

The unsteadiness of the wall flow from the passage of tip vortices has significant effects on the processes of sediment mobilization, as shown in the present work. Therefore, quantifying the unsteadiness of the flow and studying its effects can provide further insight into the mobilization of particles in a rotor flow. For example, a higher frequency of tip vortices passing over the sediment bed may cause the uplift and continued suspension of more particles than a lower frequency [19]. The vortices can also cause unsteady pressure effects that may affect the threshold conditions required for sediment mobilization. The reduced frequency parameter quantifies the unsteadiness of a flow [40] and can be defined as $k = \Omega c/2U_{\text{char}}$ for the wall flow below a rotor. For the present work, k = 1.17 so the wall flow is considered to be highly unsteady, and therefore, the effects of unsteadiness on mobilization needs to be examined in more detail.

4.3.3 Phase Separation

There are obviously many challenges in the accurate measurement of two-phase flows, especially those that involve vortical elements and high velocity gradients. An intensity thresholding method has been used in the present work to separate the carrier phase

and the dispersed phase. While fairly effective at separating the phases under many conditions, the method still leaves locations ("holes") of zero pixel intensity in the carrier phase where the sediment particles used to be. These holes can bias the cross-correlations in the carrier phase leading to less accurate PIV measurements, especially in regions of higher sediment particle concentrations. Furthermore, near the ground plane entire regions of the carrier phase can be masked by the presence of particles, and PIV measurements are much more difficult to make here. Flow measurements in this region are important because it is exactly where the sediment mobilization and uplift occurs.

Several other phase separation techniques are possible, i.e., other than thresholding techniques. These include methods that use fluorescence for separation [63], and methods that use advanced image processing to separate the phases with minimal loss of information [64]. Fluorescence techniques work by doping the dispersed phase with a fluorescent dye and using coplanar red and green light sheets to illuminate the flow. The Mie scattering from the carrier phase and fluorescence from the dispersed phase are then captured by two separate cameras with appropriate filters. In theory, each camera contain information from one phase and the two phases can be processed separately. This technique, however, is difficult to use in practical application.

Advanced image processing techniques have been proposed that make use of a two-dimensional median filter to generate better separate images of the two phases. The median filter sorts the grayscale intensity values of a user-defined small area, A, around a pixel location (i, j) and then selects the median grayscale value in window A to replace the value at (i, j). This method effectively increases the signal-to-noise ratio of the image and has been tested to quantify errors induced by the filter. More information on this

approach is given elsewhere [64]. However, the type of approach still leaves "holes" in the carrier phase images. Obviously, a measurement or processing technique that allows for phase separation while preserving the carrier phase information (i.e., no holes) would be ideal, although there are obviously many challenges to this end.

4.3.4 Selection of Sediment Particles

With the new understanding of sediment mobility and uplift below a rotor flow that has been gained throughout the current study, it is evident that the types of particles comprising the sediment bed can greatly affect the resulting two-phase flow. The current work utilized several different types of particles for the bed that had varying size, densities, shapes, and other properties. When comparing the sediment samples, sometimes more than one property changed from sample-to-sample. To better study the effects of the similarity parameters, it would be useful to conduct more tests with the glass microspheres; such closely spherical particles can be consistent from sample-to-sample while only varying particle size.

4.3.5 Experiments in Water

All of the experiments in the present work were performed with air as the working fluid. However, it might be useful to observe the results obtained when similar experiments are conducted in a different carrier medium such as water, which is about 800 times as dense as air and 50 times as viscous. However, the particles used would also have to be about 800 times as dense as naturally occurring sand or silca-type sediments to match the

particle-to-fluid density ratio to those of the brownout problem. This goal would prove difficult even if the particles were made of the most dense metals (e.g., platinum, iridium, tungsten, etc.) because they are only about 10 times as dense as the naturally occurring materials. Matching of Reynolds numbers and other similarity parameters would also be challenging. Nevertheless, the particles would behave differently in this case, not least of because water has higher viscosity and higher density. In this way, it may be possible to match some similarity parameters to the full-scale values. However performing flow measurements in water have a different set of challenges in the areas of seed particle selection, light refraction, and phase discrimination [65, 66].

Appendix A

Mineral Composition for Naturally Occurring Sediment Samples

The mineral compositions of each of the naturally occurring sediment samples were determined through a diagnostic technique known as X-ray diffraction (XRD). XRD was chosen because it is a standard nondestructive (i.e., the sample is preserved) technique used to identify the minerals or phases present in soil and clay samples.

XRD is conducted by directing a beam of X-rays through the sample. When the X-rays interact with the materials in the sample, they are deflected into a diffraction pattern and captured on an image detector. Every known crystalline material has a unique diffraction pattern. These patterns are then compared with standard diffraction patterns to identify the minerals that comprise the sample. The mass percent of each mineral is determined from an XRD spectrograph, which is a reduced form of the raw XRD data. The spectrograph shows the relative intensity of the signals captured by the image detector, which is used to determine the relative concentration of each mineral.

One of the drawbacks of using XRD is that it can only accurately detect materials that have a crystalline chemical structure. Any amorphous (i.e., non-crystalline) material will not be detected by XRD and requires other techniques such as X-ray fluorescence.

The mineral composition of the naturally occurring samples used in the present work are given in Table A.1. All values in Table A.1 are given as a mass percentage of the sample. More detailed information on the XRD technique is given in [67].

Mineral Name	Chemical Formula	Kaolinite	AZTD 0–5	AZTD 0–10	Ottawa	Yuma
Quartz	SiO_2	<5	29	60	>95	33
Kaolinite	$Al_2Si_2O_5(OH)_4$	90	<3	—	—	—
Mica/illite	$(K,Na,Ca)(Al,Mg,Fe)_2(Si,Al)_4O_{10}(OH,F)_2$	<3	20	—	—	12
Chlorite	$(Mg,Fe,Al)_6(Si,Al)_4OH_{10}(OH)$	<3	—	—	—	>5
Smectite	$(Ca,Na)_x(Al,Mg,Fe)_4(Si,Al)_8O_{20}(OH,F)_4 \bullet nH_2O$	—	20	—	—	—
Plagioclase feldspar	$(Na,Ca)Al(Si,Al)_3O_8$	—	15	20	—	24
K-feldspar	$KAlSi_3O_8$	—	8	12	—	15
Clinoamphibole	$Ca_2(Mg,Fe)_5Si_8O_{22}(OH)_2$	—	—	—	—	<2
Calcite	$CaCO_3$	—	<3	5	—	8
Hematite	Fe_2O_3	—	<3	—	—	—
”Unidentified”	—	<5	<5	<5	<5	<5

Table A.1: Mineral content of the naturally occurring sediment samples as determined by X-ray diffraction.

Appendix B

Particle Sizing Data

The results of the X-ray sedigraph and laser light scattering tests are given in this appendix. The sedigraph data was reported as "Cumulative Mass Finer" and "Mass Frequency" versus the particle size. The cumulative mass finer values represent the mass percentage of particles in a sample that were measured to be smaller than a given particle diameter. The mass frequency values represent the mass percentage of particles in a sample that were of a given particle diameter. The laser light scattering data was reported as the "Differential Volume" versus the particle size, which is equivalent to mass frequency. Some samples are identified with an alias in the data reports. Table B.1 gives the sediment sample, its alias (if applicable), and the method used to determine the particle size distribution. Notice that the data reports are given in the same order as in Table B.1.

Sediment Sample	**Alias**	**Method**
Kaolinite	Sample 1	X-ray sedigraph
AZTD 0–5 μm	Sample 2	X-ray sedigraph
AZTD 0–10 μm	Sample 3	X-ray sedigraph
Yuma Soil	Sample 5	X-ray sedigraph
Ottawa Sand	Sample 6	Laser light scattering
Glass microspheres 90–125 μm	—	Laser light scattering
Glass microspheres 1–38 μm	—	Laser light scattering
Glass microspheres 45–63 μm	—	Laser light scattering

Table B.1: Method used to determine PSD for each sediment sample.

Sample ID: Sample 1
Operator: TN
Submitter: Materials Characterization Services
File: C:\...\11NOV\1006516.SMP
Material/Liquid: Kaolin / 0.05% Sodium Metaphosphate (w/w)
Measurement Principle: X-Ray monitored gravity sedimentation
Calculation Method: Stokes sedimentation and Beer's law of extinction

Test Number: 2
Analyzed: 11/8/2010 10:01:37AM
Reported: 11/8/2010 11:24:12AM
Liquid Visc: 0.7229 mPa·s
Analysis Temp: 35.0 °C
Full Scale Mass: 100.0 %

Analysis Type: High Speed(Adj)
Run Time: 0:34 hrs:min
Sample Density: 2.600 g/cm³
Liquid Density: 0.9941 g/cm³
Mean Base/Full: 132 / 90 kCnts/s
Reynolds Number: 0.21

Comments: 100W

Combined Report

Report by Size Table

Low Diameter (µm)	Cumulative Mass Finer (Percent)	Low Diameter (µm)	Cumulative Mass Finer (Percent)	Low Diameter (µm)	Cumulative Mass Finer (Percent)	Low Diameter (µm)	Cumulative Mass Finer (Percent)
300.0	99.5	100.0	99.5	20.00	99.7	0.500	59.8
250.0	99.5	75.00	99.5	10.00	97.7	0.100	38.3
200.0	99.5	50.00	99.5	5.000	92.6		
150.0	99.5	40.00	99.4	1.000	69.7		

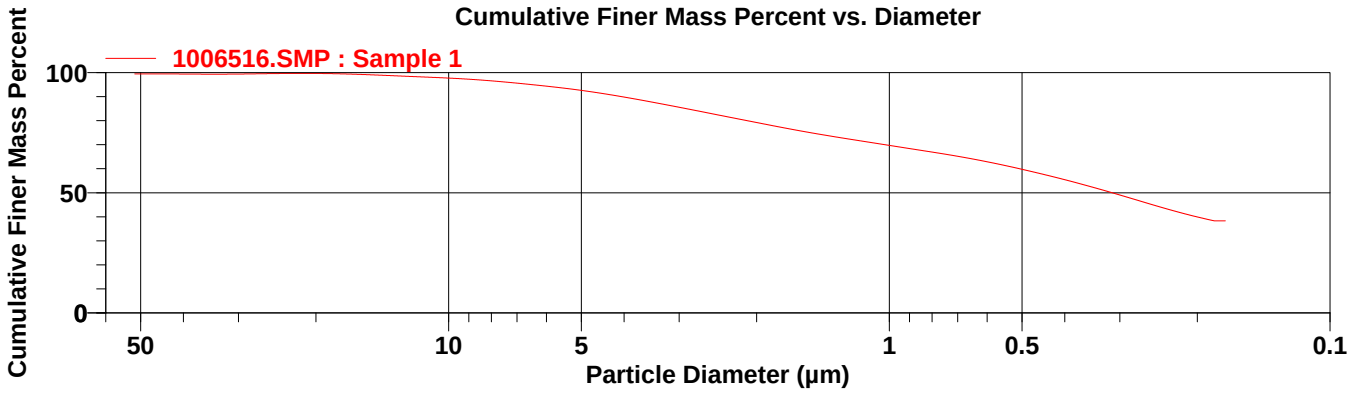

Summary Report

Full scale pump speed: 3
Bubble detection: Medium
Starting Size: 50.00 µm
Ending Size: 0.18 µm

Stir time: 0 s
Stir speed: High
Probe time: 0 s

Weight (g) 6.000 Probe (sec) 300.000 Dispersant 80.000

Mass Distribution Arithmetic Statistics

Mean	2.159	Mode	0.282
Median	0.312		

Sample ID: Sample 1
Operator: TN
Submitter: Materials Characterization Services
File: C:\...\11NOV\1006516.SMP
Material/Liquid: Kaolin / 0.05% Sodium Metaphosphate (w/w)
Measurement Principle: X-Ray monitored gravity sedimentation
Calculation Method: Stokes sedimentation and Beer's law of extinction

Test Number: 2
Analyzed: 11/8/2010 10:01:37AM
Reported: 11/8/2010 11:24:12AM
Liquid Visc: 0.7229 mPa·s
Analysis Temp: 35.0 °C
Full Scale Mass: 100.0 %

Analysis Type: High Speed(Adj)
Run Time: 0:34 hrs:min
Sample Density: 2.600 g/cm³
Liquid Density: 0.9941 g/cm³
Mean Base/Full: 132 / 90 kCnts/s
Reynolds Number: 0.21

Comments: 100W

Report by Size Class

High Diameter (µm)	Low Diameter (µm)	Average Diameter (µm)	Cumulative Mass Finer (Percent)	Mass Frequency (Percent)	Cum. Mass Standard Deviation (2 tests)
51.58	48.70	50.12	99.5	0.0	0.6
48.70	45.97	47.32	99.5	0.0	0.5
45.97	43.40	44.67	99.5	0.0	0.5
43.40	40.97	42.17	99.4	0.0	0.5
40.97	38.68	39.81	99.4	0.0	0.4
38.68	36.52	37.58	99.4	0.0	0.4
36.52	34.47	35.48	99.4	0.0	0.4
34.47	32.55	33.50	99.4	0.0	0.4
32.55	30.73	31.62	99.4	0.0	0.4
30.73	29.01	29.85	99.4	0.0	0.3
29.01	27.38	28.18	99.5	-0.1	0.2
27.38	25.85	26.61	99.6	-0.1	0.2
25.85	24.41	25.12	99.6	-0.1	0.1
24.41	23.04	23.71	99.7	0.0	0.0
23.04	21.75	22.39	99.7	0.0	0.0
21.75	20.54	21.13	99.7	0.0	0.0
20.54	19.39	19.95	99.6	0.0	0.1
19.39	18.30	18.84	99.6	0.1	0.1
18.30	17.28	17.78	99.5	0.1	0.1
17.28	16.31	16.79	99.3	0.1	0.1
16.31	15.40	15.85	99.2	0.2	0.1
15.40	14.54	14.96	99.0	0.2	0.1
14.54	13.72	14.13	98.8	0.2	0.1
13.72	12.96	13.34	98.6	0.2	0.1
12.96	12.23	12.59	98.4	0.2	0.0
12.23	11.55	11.89	98.2	0.2	0.0
11.55	10.90	11.22	98.0	0.2	0.1
10.90	10.29	10.59	97.8	0.2	0.1
10.29	9.716	10.00	97.6	0.2	0.2
9.716	9.173	9.441	97.4	0.3	0.3
9.173	8.660	8.913	97.1	0.3	0.4
8.660	8.175	8.414	96.7	0.3	0.4
8.175	7.718	7.943	96.3	0.4	0.5
7.718	7.286	7.499	95.9	0.4	0.5
7.286	6.879	7.079	95.5	0.4	0.5
6.879	6.494	6.683	95.0	0.5	0.5
6.494	6.131	6.310	94.6	0.5	0.4
6.131	5.788	5.957	94.1	0.5	0.4
5.788	5.464	5.623	93.5	0.5	0.3

Sample ID: Sample 1
Operator: TN
Submitter: Materials Characterization Services
File: C:\...\11NOV\1006516.SMP
Material/Liquid: Kaolin / 0.05% Sodium Metaphosphate (w/w)
Measurement Principle: X-Ray monitored gravity sedimentation
Calculation Method: Stokes sedimentation and Beer's law of extinction

Test Number: 2
Analyzed: 11/8/2010 10:01:37AM
Reported: 11/8/2010 11:24:12AM
Liquid Visc: 0.7229 mPa·s
Analysis Temp: 35.0 °C
Full Scale Mass: 100.0 %

Analysis Type: High Speed(Adj)
Run Time: 0:34 hrs:min
Sample Density: 2.600 g/cm³
Liquid Density: 0.9941 g/cm³
Mean Base/Full: 132 / 90 kCnts/s
Reynolds Number: 0.21

Comments: 100W

Report by Size Class

High Diameter (µm)	Low Diameter (µm)	Average Diameter (µm)	Cumulative Mass Finer (Percent)	Mass Frequency (Percent)	Cum. Mass Standard Deviation (2 tests)
5.464	5.158	5.309	92.9	0.6	0.3
5.158	4.870	5.012	92.3	0.6	0.3
4.870	4.597	4.732	91.6	0.7	0.2
4.597	4.340	4.467	90.9	0.7	0.2
4.340	4.097	4.217	90.2	0.8	0.2
4.097	3.868	3.981	89.4	0.8	0.2
3.868	3.652	3.758	88.5	0.8	0.2
3.652	3.447	3.548	87.7	0.8	0.2
3.447	3.255	3.350	86.8	0.9	0.1
3.255	3.073	3.162	86.0	0.9	0.1
3.073	2.901	2.985	85.1	0.9	0.0
2.901	2.738	2.818	84.2	0.9	0.0
2.738	2.585	2.661	83.3	0.9	0.1
2.585	2.441	2.512	82.3	0.9	0.1
2.441	2.304	2.371	81.4	0.9	0.1
2.304	2.175	2.239	80.5	0.9	0.1
2.175	2.054	2.113	79.6	0.9	0.1
2.054	1.939	1.995	78.7	0.9	0.1
1.939	1.830	1.884	77.8	0.9	0.0
1.830	1.728	1.778	77.0	0.9	0.0
1.728	1.631	1.679	76.1	0.9	0.0
1.631	1.540	1.585	75.3	0.8	0.0
1.540	1.454	1.496	74.5	0.8	0.0
1.454	1.372	1.413	73.7	0.8	0.0
1.372	1.296	1.334	73.0	0.7	0.0
1.296	1.223	1.259	72.2	0.7	0.0
1.223	1.155	1.189	71.5	0.7	0.0
1.155	1.090	1.122	70.8	0.7	0.1
1.090	1.029	1.059	70.1	0.7	0.1
1.029	0.972	1.000	69.4	0.7	0.2
0.972	0.917	0.944	68.6	0.7	0.2
0.917	0.866	0.891	67.9	0.7	0.2
0.866	0.818	0.841	67.2	0.7	0.2
0.818	0.772	0.794	66.5	0.7	0.2
0.772	0.729	0.750	65.7	0.7	0.2
0.729	0.688	0.708	64.9	0.8	0.3
0.688	0.649	0.668	64.1	0.8	0.3
0.649	0.613	0.631	63.2	0.9	0.4
0.613	0.579	0.596	62.3	0.9	0.4

Sample ID: Sample 1
Operator: TN
Submitter: Materials Characterization Services
File: C:\...\11NOV\1006516.SMP
Material/Liquid: Kaolin / 0.05% Sodium Metaphosphate (w/w)
Measurement Principle: X-Ray monitored gravity sedimentation
Calculation Method: Stokes sedimentation and Beer's law of extinction

Test Number: 2
Analyzed: 11/8/2010 10:01:37AM
Reported: 11/8/2010 11:24:12AM
Liquid Visc: 0.7229 mPa·s
Analysis Temp: 35.0 °C
Full Scale Mass: 100.0 %

Analysis Type: High Speed(Adj)
Run Time: 0:34 hrs:min
Sample Density: 2.600 g/cm³
Liquid Density: 0.9941 g/cm³
Mean Base/Full: 132 / 90 kCnts/s
Reynolds Number: 0.21

Comments: 100W

Report by Size Class

High Diameter (µm)	Low Diameter (µm)	Average Diameter (µm)	Cumulative Mass Finer (Percent)	Mass Frequency (Percent)	Cum. Mass Standard Deviation (2 tests)
0.579	0.546	0.562	61.3	1.0	0.4
0.546	0.516	0.531	60.3	1.0	0.5
0.516	0.487	0.501	59.3	1.0	0.5
0.487	0.460	0.473	58.2	1.1	0.5
0.460	0.434	0.447	57.1	1.1	0.4
0.434	0.410	0.422	55.9	1.1	0.4
0.410	0.387	0.398	54.7	1.2	0.4
0.387	0.365	0.376	53.5	1.2	0.4
0.365	0.345	0.355	52.3	1.3	0.4
0.345	0.325	0.335	51.0	1.3	0.5
0.325	0.307	0.316	49.6	1.3	0.5
0.307	0.290	0.299	48.3	1.4	0.6
0.290	0.274	0.282	46.9	1.4	0.7
0.274	0.259	0.266	45.5	1.4	0.8
0.259	0.244	0.251	44.2	1.3	0.8
0.244	0.230	0.237	42.9	1.3	0.8
0.230	0.218	0.224	41.6	1.3	0.8
0.218	0.205	0.211	40.4	1.2	0.8
0.205	0.194	0.200	39.3	1.1	0.7
0.194	0.183	0.188	38.3	1.0	0.7

Sample ID: Sample 1
Operator: TN
Submitter: Materials Characterization Services
File: C:\...\11NOV\1006516.SMP
Material/Liquid: Kaolin / 0.05% Sodium Metaphosphate (w/w)
Measurement Principle: X-Ray monitored gravity sedimentation
Calculation Method: Stokes sedimentation and Beer's law of extinction

Test Number: 2
Analyzed: 11/8/2010 10:01:37AM
Reported: 11/8/2010 11:24:12AM
Liquid Visc: 0.7229 mPa·s
Analysis Temp: 35.0 °C
Full Scale Mass: 100.0 %

Analysis Type: High Speed(Adj)
Run Time: 0:34 hrs:min
Sample Density: 2.600 g/cm³
Liquid Density: 0.9941 g/cm³
Mean Base/Full: 132 / 90 kCnts/s
Reynolds Number: 0.21

Comments: 100W

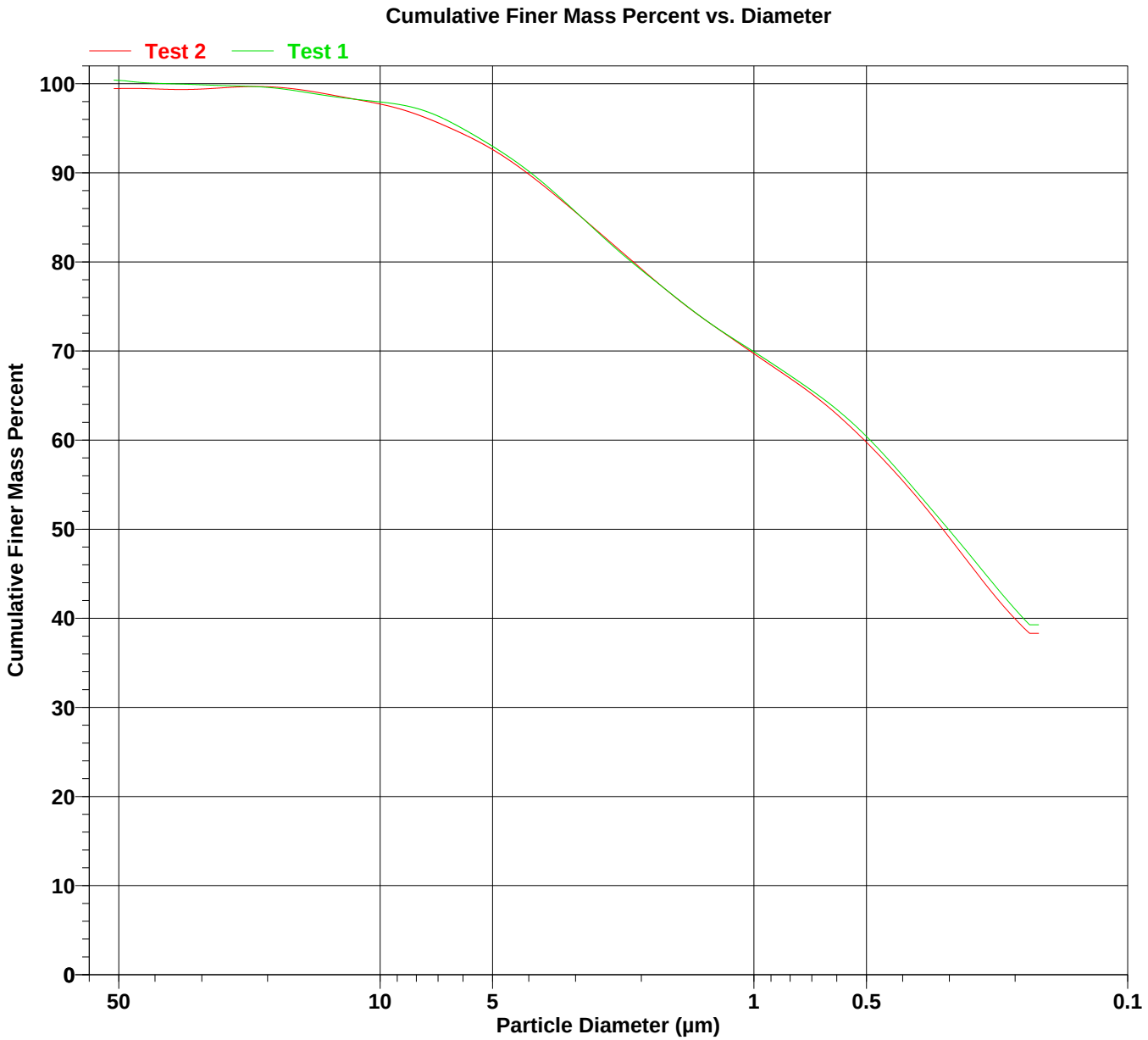

Sample ID: Sample 1
Operator: TN
Submitter: Materials Characterization Services
File: C:\...\11NOV\1006516.SMP
Material/Liquid: Kaolin / 0.05% Sodium Metaphosphate (w/w)
Measurement Principle: X-Ray monitored gravity sedimentation
Calculation Method: Stokes sedimentation and Beer's law of extinction

Test Number: 2
Analyzed: 11/8/2010 10:01:37AM
Reported: 11/8/2010 11:24:12AM
Liquid Visc: 0.7229 mPa·s
Analysis Temp: 35.0 °C
Full Scale Mass: 100.0 %

Analysis Type: High Speed(Adj)
Run Time: 0:34 hrs:min
Sample Density: 2.600 g/cm³
Liquid Density: 0.9941 g/cm³
Mean Base/Full: 132 / 90 kCnts/s
Reynolds Number: 0.21

Comments: 100W

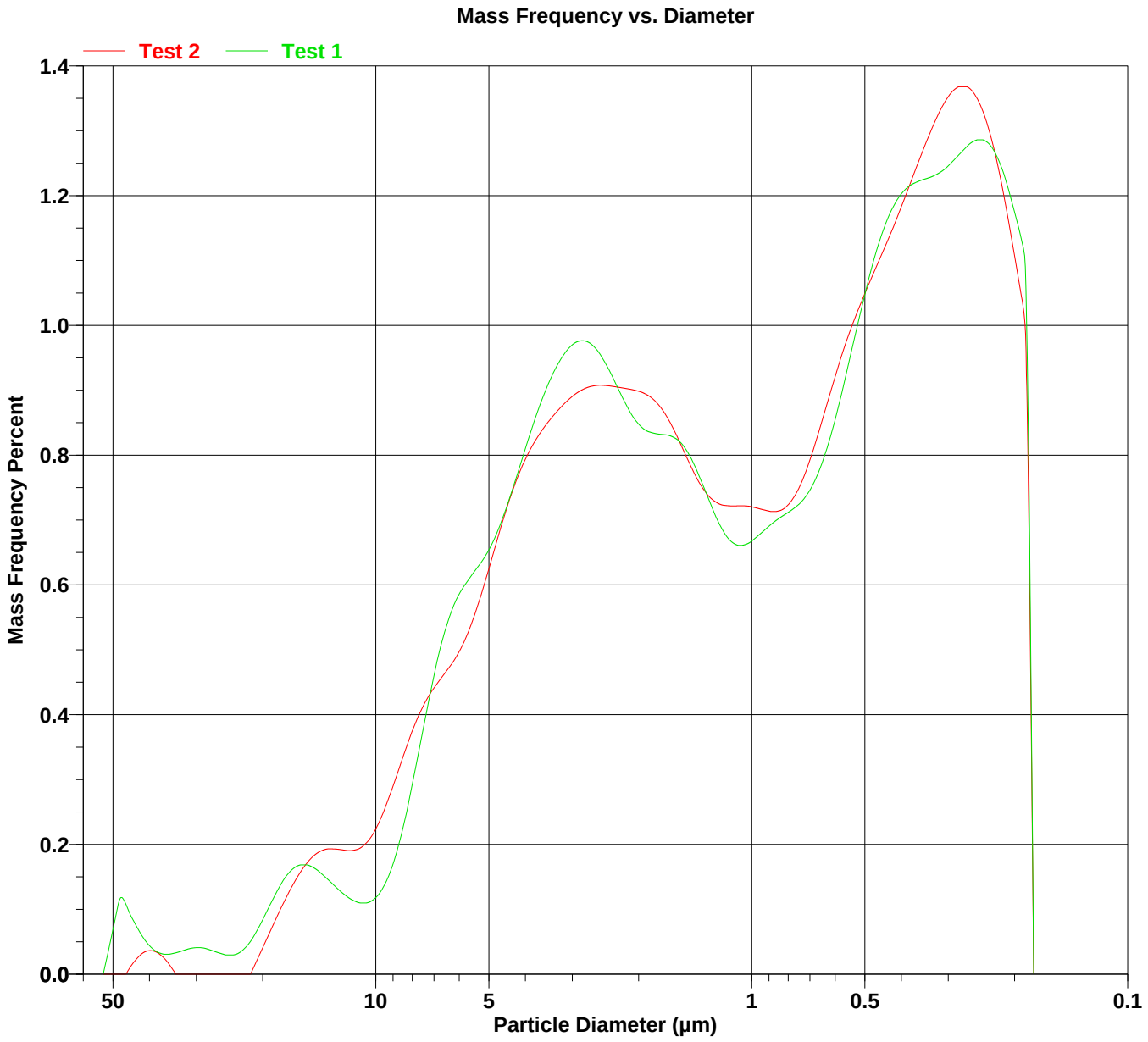

Sample ID: Sample 2
Operator: TN
Submitter: Materials Characterization Services
File: C:\...\11NOV\1006517.SMP
Material/Liquid: Kaolin / 0.05% Sodium Metaphosphate (w/w)
Measurement Principle: X-Ray monitored gravity sedimentation
Calculation Method: Stokes sedimentation and Beer's law of extinction

Test Number: 2
Analyzed: 11/8/2010 10:09:36AM
Reported: 11/9/2010 4:22:25PM
Liquid Visc: 0.7228 mPa·s
Analysis Temp: 35.0 °C
Full Scale Mass: 100.0 %

Analysis Type: High Speed(Adj)
Run Time: 0:32 hrs:min
Sample Density: 2.600 g/cm³
Liquid Density: 0.9941 g/cm³
Mean Base/Full: 129 / 70 kCnts/s
Reynolds Number: 0.21

Comments: 100W

Combined Report

Report by Size Table

Low Diameter (µm)	Cumulative Mass Finer (Percent)	Low Diameter (µm)	Cumulative Mass Finer (Percent)	Low Diameter (µm)	Cumulative Mass Finer (Percent)	Low Diameter (µm)	Cumulative Mass Finer (Percent)
300.0	100.2	100.0	100.2	20.00	100.7	0.500	18.5
250.0	100.2	75.00	100.2	10.00	100.2	0.100	5.7
200.0	100.2	50.00	100.2	5.000	98.7		
150.0	100.2	40.00	100.2	1.000	42.0		

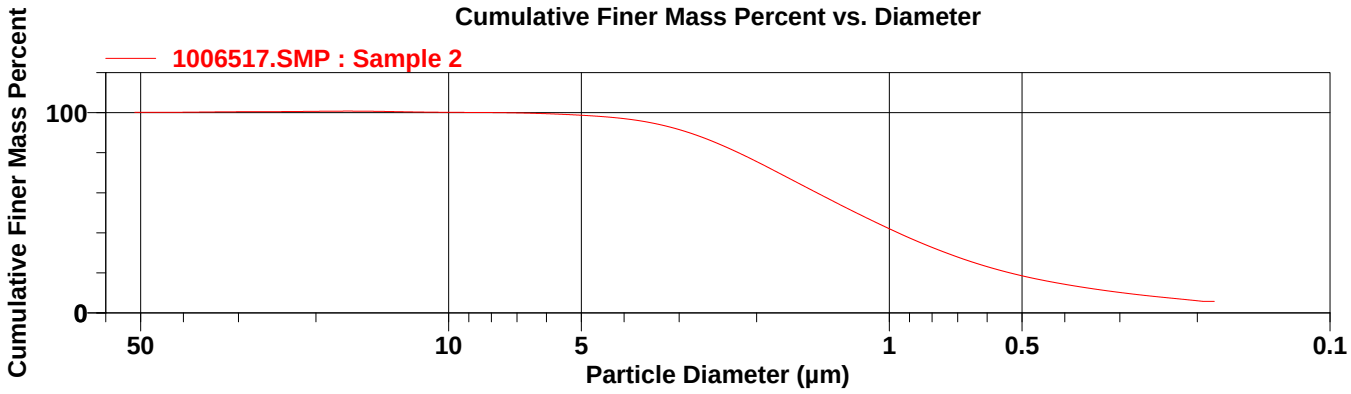

Summary Report

Full scale pump speed: 3
Bubble detection: Medium
Starting Size: 50.00 µm
Ending Size: 0.18 µm

Stir time: 0 s
Stir speed: High
Probe time: 0 s

Weight (g) 6.000 Probe (sec) 300.000 Dispersant 80.000

Mass Distribution Arithmetic Statistics

Mean	1.603	Mode	1.679
Median	1.189		

Sample ID: Sample 2
Operator: TN
Submitter: Materials Characterization Services
File: C:\...\11NOV\1006517.SMP
Material/Liquid: Kaolin / 0.05% Sodium Metaphosphate (w/w)
Measurement Principle: X-Ray monitored gravity sedimentation
Calculation Method: Stokes sedimentation and Beer's law of extinction

Test Number: 2
Analyzed: 11/8/2010 10:09:36AM
Reported: 11/9/2010 4:22:25PM
Liquid Visc: 0.7228 mPa·s
Analysis Temp: 35.0 °C
Full Scale Mass: 100.0 %

Analysis Type: High Speed(Adj)
Run Time: 0:32 hrs:min
Sample Density: 2.600 g/cm³
Liquid Density: 0.9941 g/cm³
Mean Base/Full: 129 / 70 kCnts/s
Reynolds Number: 0.21

Comments: 100W

Report by Size Class

High Diameter (µm)	Low Diameter (µm)	Average Diameter (µm)	Cumulative Mass Finer (Percent)	Mass Frequency (Percent)	Cum. Mass Standard Deviation (2 tests)
51.58	48.70	50.12	100.2	0.0	0.2
48.70	45.97	47.32	100.1	0.0	0.1
45.97	43.40	44.67	100.2	0.0	0.1
43.40	40.97	42.17	100.2	0.0	0.1
40.97	38.68	39.81	100.2	0.0	0.1
38.68	36.52	37.58	100.3	-0.1	0.1
36.52	34.47	35.48	100.4	-0.1	0.1
34.47	32.55	33.50	100.4	-0.1	0.1
32.55	30.73	31.62	100.4	0.0	0.0
30.73	29.01	29.85	100.5	0.0	0.0
29.01	27.38	28.18	100.5	0.0	0.0
27.38	25.85	26.61	100.5	0.0	0.1
25.85	24.41	25.12	100.5	0.0	0.1
24.41	23.04	23.71	100.6	0.0	0.2
23.04	21.75	22.39	100.6	0.0	0.2
21.75	20.54	21.13	100.7	-0.1	0.1
20.54	19.39	19.95	100.7	-0.1	0.1
19.39	18.30	18.84	100.7	0.0	0.0
18.30	17.28	17.78	100.8	0.0	0.0
17.28	16.31	16.79	100.8	0.0	0.1
16.31	15.40	15.85	100.7	0.0	0.1
15.40	14.54	14.96	100.7	0.1	0.1
14.54	13.72	14.13	100.6	0.1	0.1
13.72	12.96	13.34	100.5	0.1	0.0
12.96	12.23	12.59	100.4	0.1	0.0
12.23	11.55	11.89	100.3	0.1	0.1
11.55	10.90	11.22	100.2	0.1	0.1
10.90	10.29	10.59	100.2	0.1	0.1
10.29	9.716	10.00	100.2	0.0	0.1
9.716	9.173	9.441	100.1	0.0	0.1
9.173	8.660	8.913	100.1	0.0	0.1
8.660	8.175	8.414	100.1	0.0	0.1
8.175	7.718	7.943	100.0	0.0	0.1
7.718	7.286	7.499	100.0	0.1	0.1
7.286	6.879	7.079	99.9	0.1	0.2
6.879	6.494	6.683	99.7	0.1	0.2
6.494	6.131	6.310	99.6	0.2	0.2
6.131	5.788	5.957	99.4	0.2	0.3
5.788	5.464	5.623	99.1	0.2	0.3

Sample ID: Sample 2
Operator: TN
Submitter: Materials Characterization Services
File: C:\...\11NOV\1006517.SMP
Material/Liquid: Kaolin / 0.05% Sodium Metaphosphate (w/w)
Measurement Principle: X-Ray monitored gravity sedimentation
Calculation Method: Stokes sedimentation and Beer's law of extinction

Test Number: 2
Analyzed: 11/8/2010 10:09:36AM
Reported: 11/9/2010 4:22:25PM
Liquid Visc: 0.7228 mPa·s
Analysis Temp: 35.0 °C
Full Scale Mass: 100.0 %

Analysis Type: High Speed(Adj)
Run Time: 0:32 hrs:min
Sample Density: 2.600 g/cm³
Liquid Density: 0.9941 g/cm³
Mean Base/Full: 129 / 70 kCnts/s
Reynolds Number: 0.21

Comments: 100W

Report by Size Class

High Diameter (µm)	Low Diameter (µm)	Average Diameter (µm)	Cumulative Mass Finer (Percent)	Mass Frequency (Percent)	Cum. Mass Standard Deviation (2 tests)
5.464	5.158	5.309	98.9	0.3	0.3
5.158	4.870	5.012	98.6	0.3	0.3
4.870	4.597	4.732	98.2	0.4	0.3
4.597	4.340	4.467	97.8	0.4	0.2
4.340	4.097	4.217	97.3	0.5	0.2
4.097	3.868	3.981	96.6	0.7	0.2
3.868	3.652	3.758	95.8	0.8	0.1
3.652	3.447	3.548	94.8	1.0	0.1
3.447	3.255	3.350	93.6	1.2	0.1
3.255	3.073	3.162	92.2	1.4	0.1
3.073	2.901	2.985	90.6	1.6	0.2
2.901	2.738	2.818	88.7	1.8	0.2
2.738	2.585	2.661	86.7	2.0	0.3
2.585	2.441	2.512	84.4	2.2	0.3
2.441	2.304	2.371	82.0	2.4	0.3
2.304	2.175	2.239	79.5	2.6	0.4
2.175	2.054	2.113	76.8	2.7	0.4
2.054	1.939	1.995	74.1	2.8	0.4
1.939	1.830	1.884	71.2	2.8	0.4
1.830	1.728	1.778	68.4	2.9	0.3
1.728	1.631	1.679	65.5	2.9	0.3
1.631	1.540	1.585	62.6	2.9	0.2
1.540	1.454	1.496	59.8	2.9	0.1
1.454	1.372	1.413	56.9	2.8	0.0
1.372	1.296	1.334	54.1	2.8	0.0
1.296	1.223	1.259	51.4	2.8	0.0
1.223	1.155	1.189	48.6	2.7	0.1
1.155	1.090	1.122	45.9	2.7	0.0
1.090	1.029	1.059	43.3	2.6	0.0
1.029	0.972	1.000	40.7	2.6	0.0
0.972	0.917	0.944	38.2	2.5	0.1
0.917	0.866	0.891	35.8	2.4	0.1
0.866	0.818	0.841	33.6	2.3	0.1
0.818	0.772	0.794	31.4	2.2	0.2
0.772	0.729	0.750	29.3	2.1	0.2
0.729	0.688	0.708	27.3	2.0	0.2
0.688	0.649	0.668	25.5	1.9	0.3
0.649	0.613	0.631	23.7	1.7	0.3
0.613	0.579	0.596	22.1	1.6	0.3

Sample ID: Sample 2
Operator: TN
Submitter: Materials Characterization Services
File: C:\...\11NOV\1006517.SMP
Material/Liquid: Kaolin / 0.05% Sodium Metaphosphate (w/w)
Measurement Principle: X-Ray monitored gravity sedimentation
Calculation Method: Stokes sedimentation and Beer's law of extinction

Test Number: 2
Analyzed: 11/8/2010 10:09:36AM
Reported: 11/9/2010 4:22:25PM
Liquid Visc: 0.7228 mPa·s
Analysis Temp: 35.0 °C
Full Scale Mass: 100.0 %

Analysis Type: High Speed(Adj)
Run Time: 0:32 hrs:min
Sample Density: 2.600 g/cm³
Liquid Density: 0.9941 g/cm³
Mean Base/Full: 129 / 70 kCnts/s
Reynolds Number: 0.21

Comments: 100W

Report by Size Class

High Diameter (µm)	Low Diameter (µm)	Average Diameter (µm)	Cumulative Mass Finer (Percent)	Mass Frequency (Percent)	Cum. Mass Standard Deviation (2 tests)
0.579	0.546	0.562	20.6	1.5	0.3
0.546	0.516	0.531	19.2	1.4	0.3
0.516	0.487	0.501	18.0	1.3	0.3
0.487	0.460	0.473	16.8	1.2	0.2
0.460	0.434	0.447	15.7	1.1	0.2
0.434	0.410	0.422	14.7	1.0	0.2
0.410	0.387	0.398	13.7	0.9	0.2
0.387	0.365	0.376	12.9	0.9	0.1
0.365	0.345	0.355	12.0	0.8	0.1
0.345	0.325	0.335	11.2	0.8	0.1
0.325	0.307	0.316	10.5	0.7	0.1
0.307	0.290	0.299	9.8	0.7	0.1
0.290	0.274	0.282	9.2	0.7	0.2
0.274	0.259	0.266	8.5	0.6	0.2
0.259	0.244	0.251	8.0	0.6	0.2
0.244	0.230	0.237	7.4	0.6	0.2
0.230	0.218	0.224	6.9	0.5	0.3
0.218	0.205	0.211	6.3	0.6	0.4
0.205	0.194	0.200	5.7	0.6	0.5

Sample ID: Sample 2
Operator: TN
Submitter: Materials Characterization Services
File: C:\...\11NOV\1006517.SMP
Material/Liquid: Kaolin / 0.05% Sodium Metaphosphate (w/w)
Measurement Principle: X-Ray monitored gravity sedimentation
Calculation Method: Stokes sedimentation and Beer's law of extinction

Test Number: 2
Analyzed: 11/8/2010 10:09:36AM
Reported: 11/9/2010 4:22:25PM
Liquid Visc: 0.7228 mPa·s
Analysis Temp: 35.0 °C
Full Scale Mass: 100.0 %

Analysis Type: High Speed(Adj)
Run Time: 0:32 hrs:min
Sample Density: 2.600 g/cm³
Liquid Density: 0.9941 g/cm³
Mean Base/Full: 129 / 70 kCnts/s
Reynolds Number: 0.21

Comments: 100W

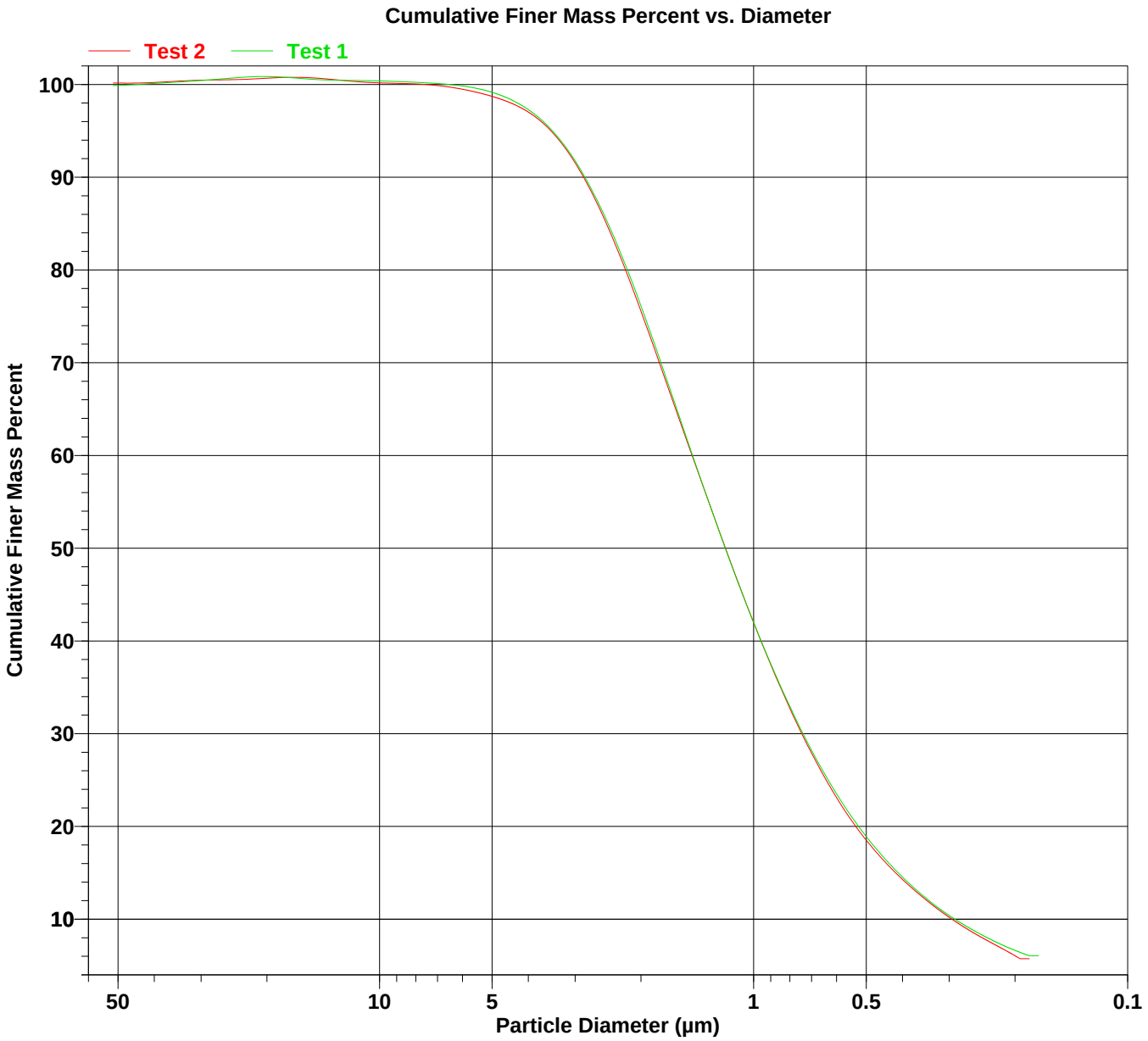

Sample ID: Sample 2
Operator: TN
Submitter: Materials Characterization Services
File: C:\...\11NOV\1006517.SMP
Material/Liquid: Kaolin / 0.05% Sodium Metaphosphate (w/w)
Measurement Principle: X-Ray monitored gravity sedimentation
Calculation Method: Stokes sedimentation and Beer's law of extinction

Test Number: 2
Analyzed: 11/8/2010 10:09:36AM
Reported: 11/9/2010 4:22:25PM
Liquid Visc: 0.7228 mPa·s
Analysis Temp: 35.0 °C
Full Scale Mass: 100.0 %

Analysis Type: High Speed(Adj)
Run Time: 0:32 hrs:min
Sample Density: 2.600 g/cm³
Liquid Density: 0.9941 g/cm³
Mean Base/Full: 129 / 70 kCnts/s
Reynolds Number: 0.21

Comments: 100W

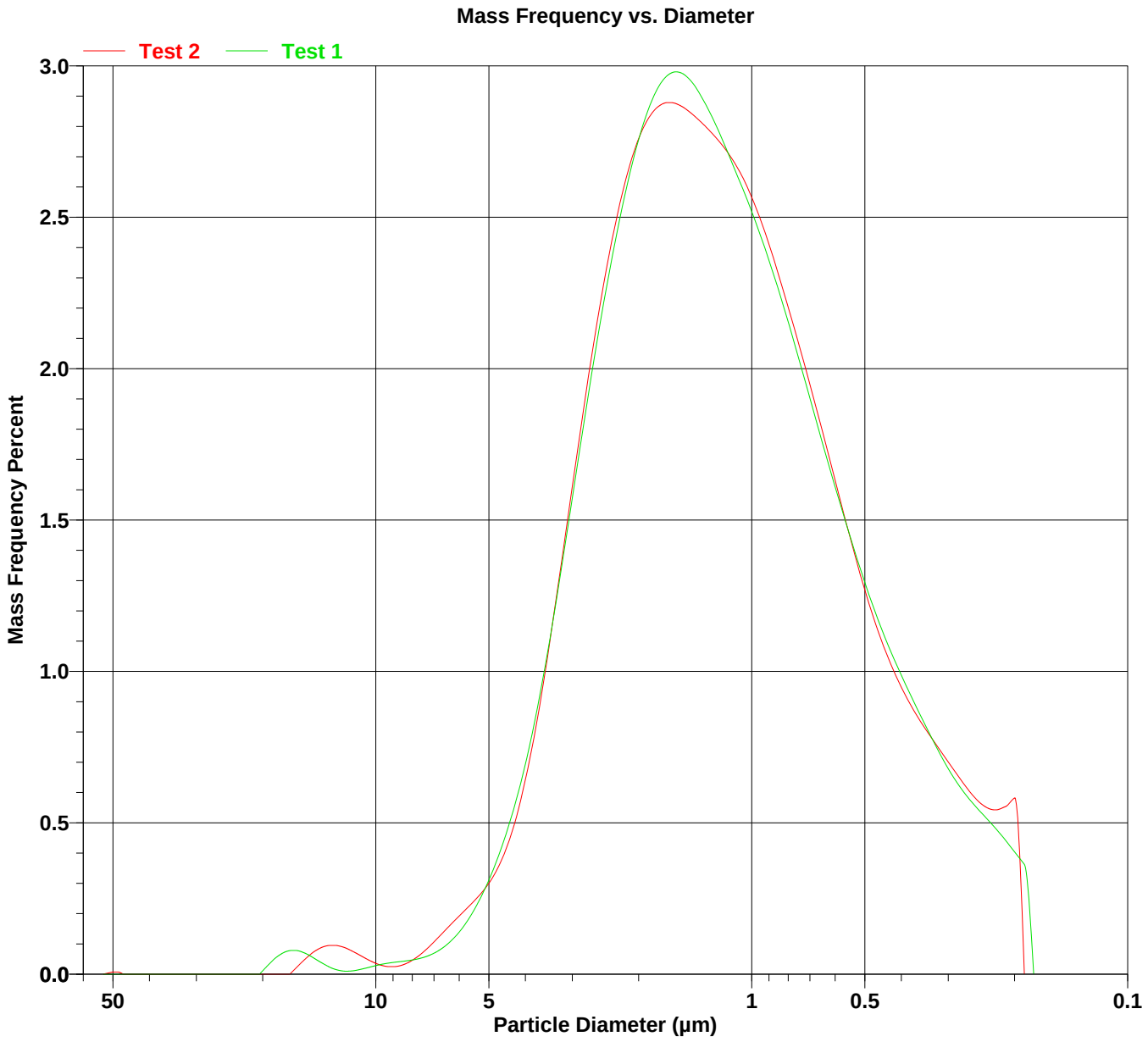

Sample ID: Sample 3
Operator: TN
Submitter: Materials Characterization Services
File: C:\...\11NOV\1006518.SMP
Material/Liquid: Kaolin / 0.05% Sodium Metaphosphate (w/w)
Measurement Principle: X-Ray monitored gravity sedimentation
Calculation Method: Stokes sedimentation and Beer's law of extinction

Test Number: 2
Analyzed: 11/8/2010 12:43:35PM
Reported: 11/8/2010 1:22:53PM
Liquid Visc: 0.7228 mPa·s
Analysis Temp: 35.0 °C
Full Scale Mass: 100.0 %

Analysis Type: High Speed(Adj)
Run Time: 0:32 hrs:min
Sample Density: 2.600 g/cm³
Liquid Density: 0.9941 g/cm³
Mean Base/Full: 129 / 67 kCnts/s
Reynolds Number: 0.21

Comments: 100W

Combined Report

Report by Size Table

Low Diameter (µm)	Cumulative Mass Finer (Percent)	Low Diameter (µm)	Cumulative Mass Finer (Percent)	Low Diameter (µm)	Cumulative Mass Finer (Percent)	Low Diameter (µm)	Cumulative Mass Finer (Percent)
300.0	100.1	100.0	100.1	20.00	100.0	0.500	5.1
250.0	100.1	75.00	100.1	10.00	98.1	0.100	1.8
200.0	100.1	50.00	100.1	5.000	82.5		
150.0	100.1	40.00	100.0	1.000	9.9		

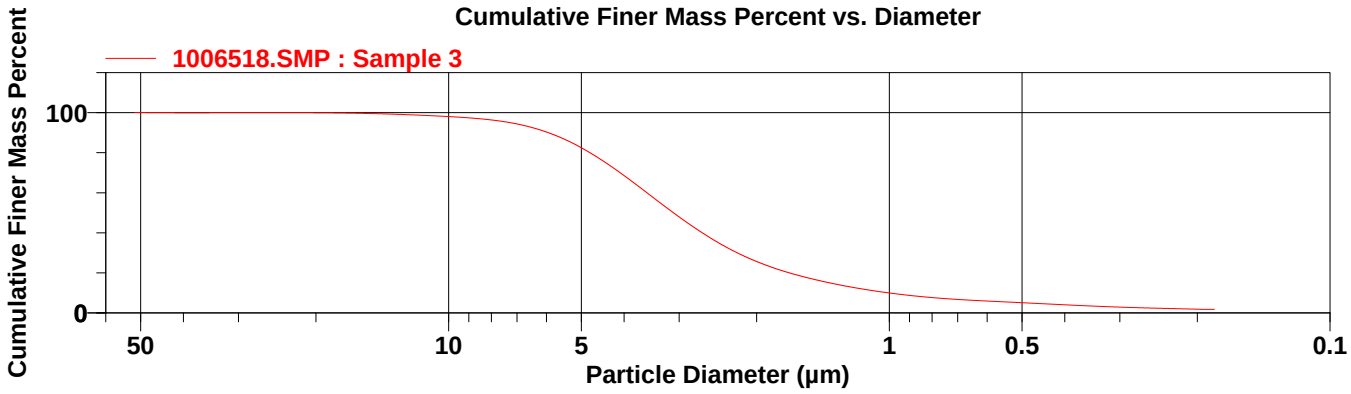

Summary Report

Full scale pump speed: 3
Bubble detection: Medium
Starting Size: 50.00 µm
Ending Size: 0.18 µm

Stir time: 0 s
Stir speed: High
Probe time: 0 s

Weight (g) 6.000 Probe (sec) 300.000 Dispersant 80.000

Mass Distribution Arithmetic Statistics

Mean	3.522	Mode	3.548
Median	3.089		

Sample ID: Sample 3
Operator: TN
Submitter: Materials Characterization Services
File: C:\...\11NOV\1006518.SMP
Material/Liquid: Kaolin / 0.05% Sodium Metaphosphate (w/w)
Measurement Principle: X-Ray monitored gravity sedimentation
Calculation Method: Stokes sedimentation and Beer's law of extinction

Test Number: 2
Analyzed: 11/8/2010 12:43:35PM
Reported: 11/8/2010 1:22:53PM
Liquid Visc: 0.7228 mPa·s
Analysis Temp: 35.0 °C
Full Scale Mass: 100.0 %

Analysis Type: High Speed(Adj)
Run Time: 0:32 hrs:min
Sample Density: 2.600 g/cm³
Liquid Density: 0.9941 g/cm³
Mean Base/Full: 129 / 67 kCnts/s
Reynolds Number: 0.21

Comments: 100W

Report by Size Class

High Diameter (µm)	Low Diameter (µm)	Average Diameter (µm)	Cumulative Mass Finer (Percent)	Mass Frequency (Percent)	Cum. Mass Standard Deviation (2 tests)
51.58	48.70	50.12	100.1	0.0	0.3
48.70	45.97	47.32	100.0	0.0	0.2
45.97	43.40	44.67	100.0	0.0	0.2
43.40	40.97	42.17	100.0	0.0	0.2
40.97	38.68	39.81	100.0	0.0	0.1
38.68	36.52	37.58	100.0	0.0	0.1
36.52	34.47	35.48	100.0	0.0	0.1
34.47	32.55	33.50	100.0	0.0	0.1
32.55	30.73	31.62	100.0	0.0	0.1
30.73	29.01	29.85	100.0	0.0	0.1
29.01	27.38	28.18	100.0	0.0	0.1
27.38	25.85	26.61	100.0	0.0	0.1
25.85	24.41	25.12	100.0	0.0	0.1
24.41	23.04	23.71	100.0	0.0	0.1
23.04	21.75	22.39	100.0	0.0	0.1
21.75	20.54	21.13	100.0	0.0	0.2
20.54	19.39	19.95	99.9	0.0	0.2
19.39	18.30	18.84	99.9	0.0	0.2
18.30	17.28	17.78	99.8	0.1	0.2
17.28	16.31	16.79	99.7	0.1	0.2
16.31	15.40	15.85	99.6	0.1	0.2
15.40	14.54	14.96	99.5	0.1	0.1
14.54	13.72	14.13	99.3	0.2	0.1
13.72	12.96	13.34	99.1	0.2	0.1
12.96	12.23	12.59	98.9	0.2	0.1
12.23	11.55	11.89	98.7	0.2	0.1
11.55	10.90	11.22	98.5	0.2	0.1
10.90	10.29	10.59	98.2	0.3	0.1
10.29	9.716	10.00	97.9	0.3	0.1
9.716	9.173	9.441	97.5	0.4	0.1
9.173	8.660	8.913	97.1	0.4	0.1
8.660	8.175	8.414	96.6	0.5	0.1
8.175	7.718	7.943	95.9	0.7	0.1
7.718	7.286	7.499	95.1	0.8	0.1
7.286	6.879	7.079	94.0	1.1	0.1
6.879	6.494	6.683	92.7	1.3	0.1
6.494	6.131	6.310	91.0	1.6	0.2
6.131	5.788	5.957	89.1	2.0	0.2
5.788	5.464	5.623	86.8	2.3	0.2

Sample ID: Sample 3
Operator: TN
Submitter: Materials Characterization Services
File: C:\...\11NOV\1006518.SMP
Material/Liquid: Kaolin / 0.05% Sodium Metaphosphate (w/w)
Measurement Principle: X-Ray monitored gravity sedimentation
Calculation Method: Stokes sedimentation and Beer's law of extinction

Test Number: 2
Analyzed: 11/8/2010 12:43:35PM
Reported: 11/8/2010 1:22:53PM
Liquid Visc: 0.7228 mPa·s
Analysis Temp: 35.0 °C
Full Scale Mass: 100.0 %

Analysis Type: High Speed(Adj)
Run Time: 0:32 hrs:min
Sample Density: 2.600 g/cm³
Liquid Density: 0.9941 g/cm³
Mean Base/Full: 129 / 67 kCnts/s
Reynolds Number: 0.21

Comments: 100W

Report by Size Class

High Diameter (µm)	Low Diameter (µm)	Average Diameter (µm)	Cumulative Mass Finer (Percent)	Mass Frequency (Percent)	Cum. Mass Standard Deviation (2 tests)
5.464	5.158	5.309	84.1	2.7	0.2
5.158	4.870	5.012	81.1	3.0	0.2
4.870	4.597	4.732	77.7	3.3	0.2
4.597	4.340	4.467	74.1	3.6	0.2
4.340	4.097	4.217	70.3	3.9	0.1
4.097	3.868	3.981	66.2	4.0	0.1
3.868	3.652	3.758	62.1	4.1	0.0
3.652	3.447	3.548	57.9	4.2	0.1
3.447	3.255	3.350	53.7	4.2	0.2
3.255	3.073	3.162	49.6	4.1	0.2
3.073	2.901	2.985	45.6	4.0	0.2
2.901	2.738	2.818	41.9	3.8	0.2
2.738	2.585	2.661	38.3	3.6	0.2
2.585	2.441	2.512	35.0	3.3	0.1
2.441	2.304	2.371	32.0	3.0	0.1
2.304	2.175	2.239	29.2	2.8	0.0
2.175	2.054	2.113	26.7	2.5	0.0
2.054	1.939	1.995	24.5	2.2	0.0
1.939	1.830	1.884	22.5	2.0	0.0
1.830	1.728	1.778	20.7	1.8	0.1
1.728	1.631	1.679	19.1	1.6	0.1
1.631	1.540	1.585	17.6	1.5	0.1
1.540	1.454	1.496	16.3	1.3	0.1
1.454	1.372	1.413	15.1	1.2	0.2
1.372	1.296	1.334	14.0	1.1	0.2
1.296	1.223	1.259	12.9	1.0	0.2
1.223	1.155	1.189	12.0	1.0	0.2
1.155	1.090	1.122	11.1	0.9	0.2
1.090	1.029	1.059	10.3	0.8	0.2
1.029	0.972	1.000	9.6	0.7	0.2
0.972	0.917	0.944	8.9	0.7	0.2
0.917	0.866	0.891	8.4	0.6	0.2
0.866	0.818	0.841	7.8	0.5	0.2
0.818	0.772	0.794	7.4	0.5	0.2
0.772	0.729	0.750	7.0	0.4	0.2
0.729	0.688	0.708	6.6	0.4	0.2
0.688	0.649	0.668	6.3	0.3	0.1
0.649	0.613	0.631	6.0	0.3	0.1
0.613	0.579	0.596	5.8	0.3	0.1

Sample ID: Sample 3
Operator: TN
Submitter: Materials Characterization Services
File: C:\...\11NOV\1006518.SMP
Material/Liquid: Kaolin / 0.05% Sodium Metaphosphate (w/w)
Measurement Principle: X-Ray monitored gravity sedimentation
Calculation Method: Stokes sedimentation and Beer's law of extinction

Test Number: 2
Analyzed: 11/8/2010 12:43:35PM
Reported: 11/8/2010 1:22:53PM
Liquid Visc: 0.7228 mPa·s
Analysis Temp: 35.0 °C
Full Scale Mass: 100.0 %

Analysis Type: High Speed(Adj)
Run Time: 0:32 hrs:min
Sample Density: 2.600 g/cm³
Liquid Density: 0.9941 g/cm³
Mean Base/Full: 129 / 67 kCnts/s
Reynolds Number: 0.21

Comments: 100W

Report by Size Class

High Diameter (µm)	Low Diameter (µm)	Average Diameter (µm)	Cumulative Mass Finer (Percent)	Mass Frequency (Percent)	Cum. Mass Standard Deviation (2 tests)
0.579	0.546	0.562	5.5	0.3	0.1
0.546	0.516	0.531	5.2	0.3	0.1
0.516	0.487	0.501	5.0	0.3	0.1
0.487	0.460	0.473	4.7	0.3	0.1
0.460	0.434	0.447	4.4	0.3	0.2
0.434	0.410	0.422	4.2	0.3	0.2
0.410	0.387	0.398	3.9	0.3	0.2
0.387	0.365	0.376	3.6	0.3	0.2
0.365	0.345	0.355	3.4	0.2	0.2
0.345	0.325	0.335	3.2	0.2	0.2
0.325	0.307	0.316	3.0	0.2	0.2
0.307	0.290	0.299	2.8	0.2	0.2
0.290	0.274	0.282	2.6	0.2	0.2
0.274	0.259	0.266	2.5	0.2	0.2
0.259	0.244	0.251	2.3	0.1	0.1
0.244	0.230	0.237	2.2	0.1	0.1
0.230	0.218	0.224	2.0	0.1	0.1
0.218	0.205	0.211	1.9	0.1	0.0
0.205	0.194	0.200	1.8	0.1	0.0

Sample ID: Sample 3
Operator: TN
Submitter: Materials Characterization Services
File: C:\...\11NOV\1006518.SMP
Material/Liquid: Kaolin / 0.05% Sodium Metaphosphate (w/w)
Measurement Principle: X-Ray monitored gravity sedimentation
Calculation Method: Stokes sedimentation and Beer's law of extinction

Test Number: 2
Analyzed: 11/8/2010 12:43:35PM
Reported: 11/8/2010 1:22:53PM
Liquid Visc: 0.7228 mPa·s
Analysis Temp: 35.0 °C
Full Scale Mass: 100.0 %

Analysis Type: High Speed(Adj)
Run Time: 0:32 hrs:min
Sample Density: 2.600 g/cm³
Liquid Density: 0.9941 g/cm³
Mean Base/Full: 129 / 67 kCnts/s
Reynolds Number: 0.21

Comments: 100W

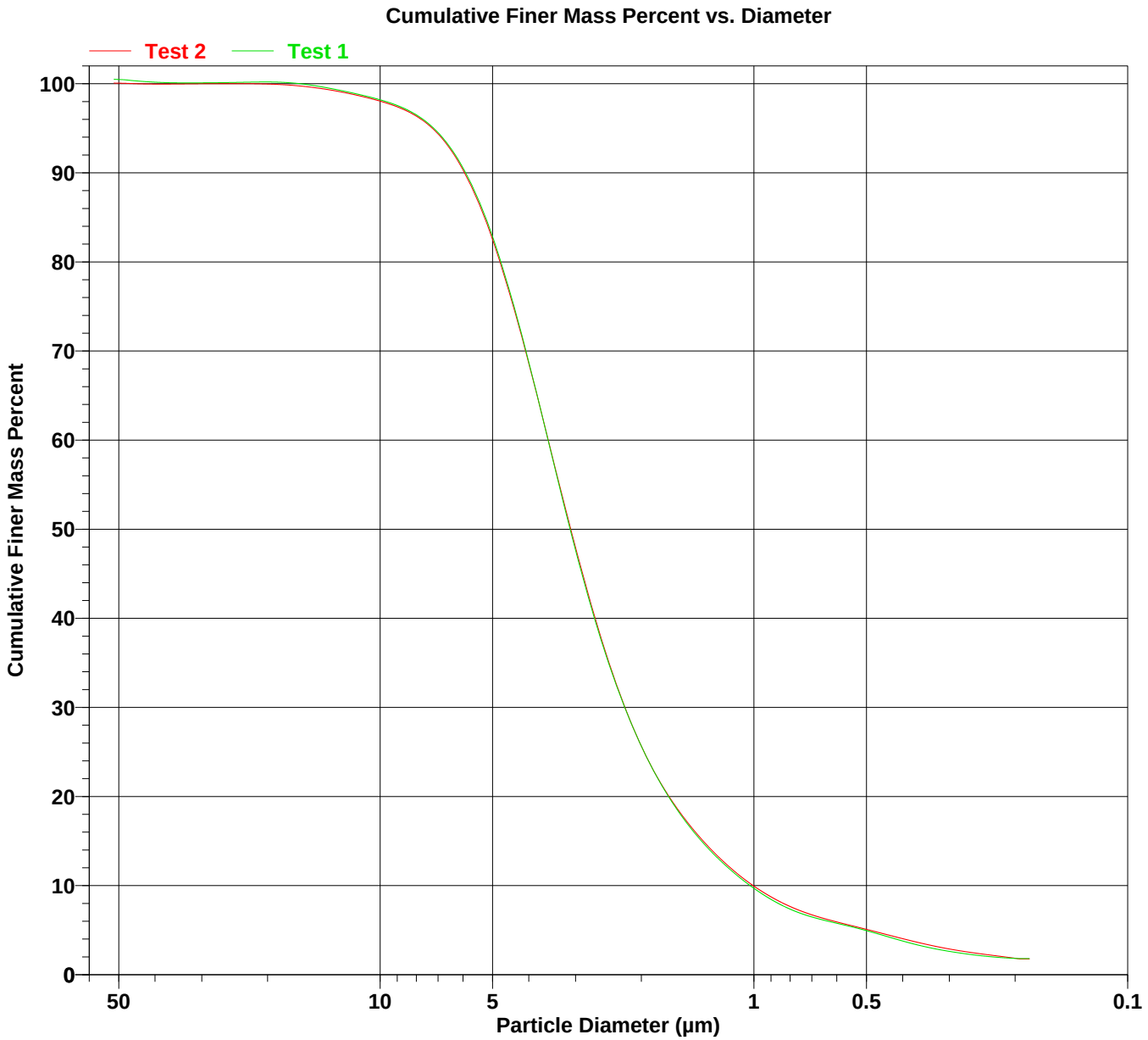

Sample ID: Sample 3
Operator: TN
Submitter: Materials Characterization Services
File: C:\...\11NOV\1006518.SMP
Material/Liquid: Kaolin / 0.05% Sodium Metaphosphate (w/w)
Measurement Principle: X-Ray monitored gravity sedimentation
Calculation Method: Stokes sedimentation and Beer's law of extinction

Test Number: 2
Analyzed: 11/8/2010 12:43:35PM
Reported: 11/8/2010 1:22:53PM
Liquid Visc: 0.7228 mPa·s
Analysis Temp: 35.0 °C
Full Scale Mass: 100.0 %

Analysis Type: High Speed(Adj)
Run Time: 0:32 hrs:min
Sample Density: 2.600 g/cm³
Liquid Density: 0.9941 g/cm³
Mean Base/Full: 129 / 67 kCnts/s
Reynolds Number: 0.21

Comments: 100W

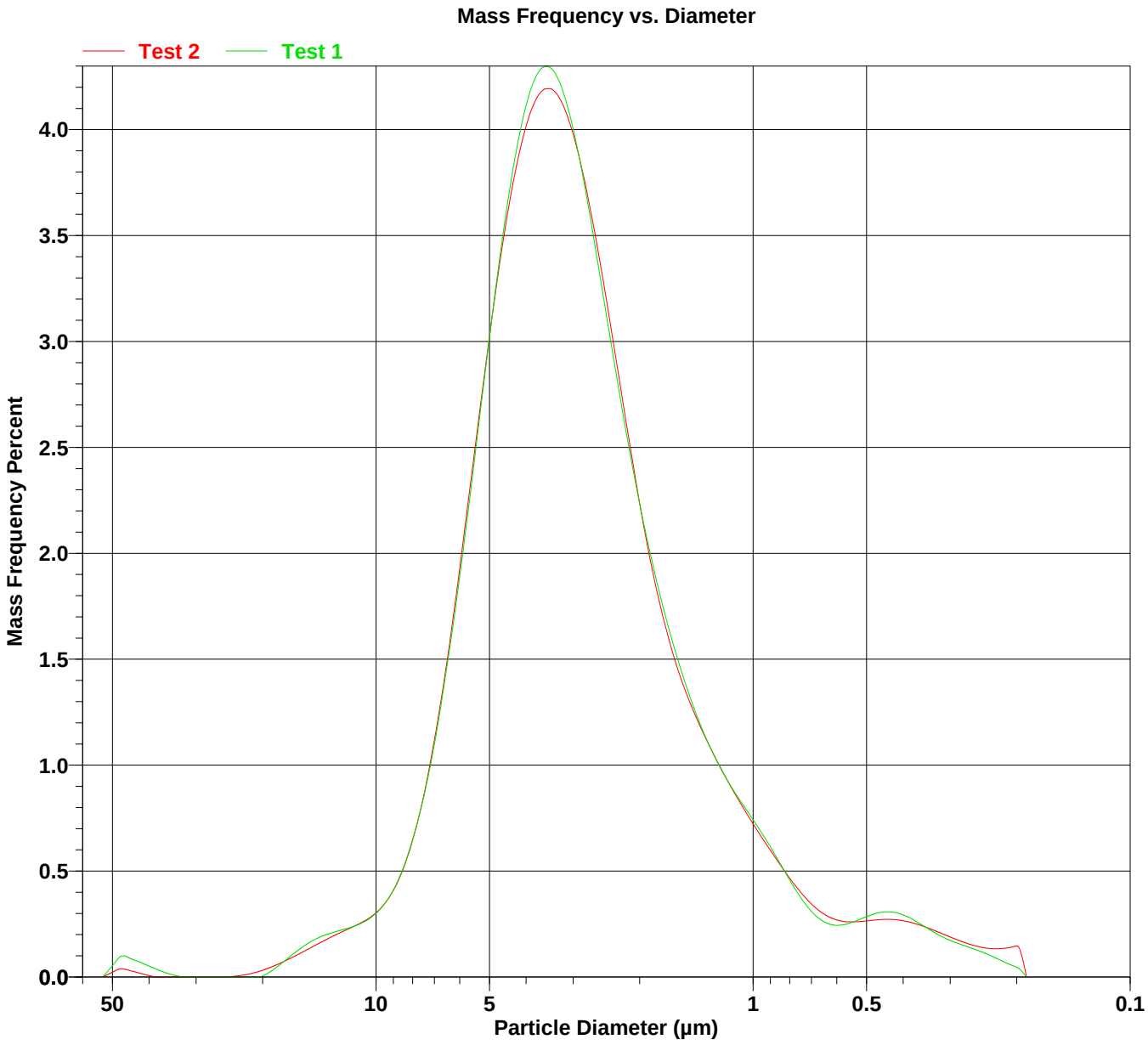

Sample ID: Sample 5
Operator: TN
Submitter: Materials Characterization Services
File: C:\...\REPORTED\1006520.SMP
Material/Liquid: Kaolin / 0.05% Sodium Metaphosphate (w/w)
Measurement Principle: X-Ray monitored gravity sedimentation
Calculation Method: Stokes sedimentation and Beer's law of extinction

Test Number: 2
Analyzed: 11/9/2010 2:52:33PM
Reported: 11/11/2010 7:59:05AM
Liquid Visc: 0.7239 mPa·s
Analysis Temp: 34.9 °C

Analysis Type: High Speed(Adj)
Run Time: 0:35 hrs:min
Sample Density: 2.600 g/cm³
Liquid Density: 0.9941 g/cm³
Mean Base/Full: 129 / 88 kCnts/s
Reynolds Number: 0.21

Comments: 100W. Sieved through #16, 30, 70, and 325.

Combined Report

Report by Size Table

Low Diameter (µm)	Cumulative Mass Finer (Percent)	Low Diameter (µm)	Cumulative Mass Finer (Percent)	Low Diameter (µm)	Cumulative Mass Finer (Percent)	Low Diameter (µm)	Cumulative Mass Finer (Percent)
300.0	68.5	100.0	56.7	20.00	48.2	0.500	10.8
250.0	67.2	75.00	52.8	10.00	45.0	0.100	3.5
200.0	65.6	50.00	49.3	5.000	38.2		
150.0	62.5	40.00	49.0	1.000	17.8		

Cumulative Finer Mass Percent vs. Diameter

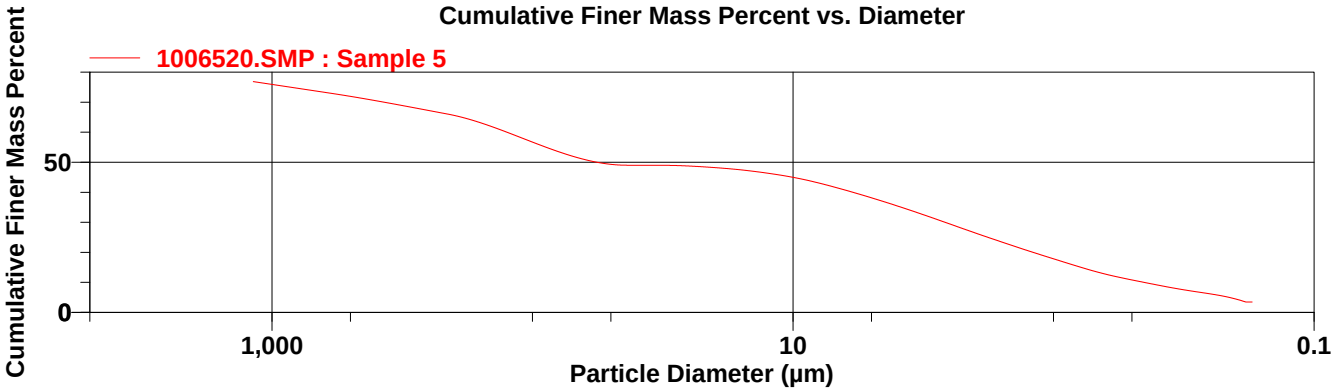

Summary Report

Full scale pump speed: 3
Bubble detection: Coarse
Starting Size: 50.00 µm
Ending Size: 0.18 µm

Stir time: 0 s
Stir speed: High
Probe time: 0 s

Weight (g) 2.000 Probe (sec) 300.000 Dispersant 80.000

Mass Distribution Arithmetic Statistics

Mean	102.8	Mode	97.67
Median	56.61		

Sample ID: Sample 5
Operator: TN
Submitter: Materials Characterization Services
File: C:\...\REPORTED\1006520.SMP
Material/Liquid: Kaolin / 0.05% Sodium Metaphosphate (w/w)
Measurement Principle: X-Ray monitored gravity sedimentation
Calculation Method: Stokes sedimentation and Beer's law of extinction

Test Number: 2
Analyzed: 11/9/2010 2:52:33PM
Reported: 11/11/2010 7:59:05AM
Liquid Visc: 0.7239 mPa·s
Analysis Temp: 34.9 °C

Analysis Type: High Speed(Adj)
Run Time: 0:35 hrs:min
Sample Density: 2.600 g/cm³
Liquid Density: 0.9941 g/cm³
Mean Base/Full: 129 / 88 kCnts/s
Reynolds Number: 0.21

Comments: 100W. Sieved through #16, 30, 70, and 325.

Report by Size Class

High Diameter (µm)	Low Diameter (µm)	Average Diameter (µm)	Cumulative Mass Finer (Percent)	Mass Frequency (Percent)	Cum. Mass Standard Deviation (2 tests)
1029	971.6	1000	75.7	0.3	0.0
971.6	917.3	944.1	75.4	0.3	0.0
917.3	866.0	891.3	75.1	0.3	0.0
866.0	817.5	841.4	74.8	0.3	0.0
817.5	771.8	794.3	74.4	0.3	0.0
771.8	728.6	749.9	74.1	0.3	0.0
728.6	687.9	707.9	73.8	0.3	0.0
687.9	649.4	668.3	73.5	0.3	0.0
649.4	613.1	631.0	73.1	0.3	0.0
613.1	578.8	595.7	72.8	0.3	0.0
578.8	546.4	562.3	72.5	0.3	0.0
546.4	515.8	530.9	72.1	0.3	0.0
515.8	487.0	501.2	71.8	0.4	0.0
487.0	459.7	473.2	71.4	0.4	0.0
459.7	434.0	446.7	71.0	0.4	0.0
434.0	409.7	421.7	70.7	0.4	0.0
409.7	386.8	398.1	70.3	0.4	0.0
386.8	365.2	375.8	69.9	0.4	0.0
365.2	344.7	354.8	69.5	0.4	0.0
344.7	325.5	335.0	69.1	0.4	0.0
325.5	307.3	316.2	68.7	0.4	0.0
307.3	290.1	298.5	68.3	0.4	0.0
290.1	273.8	281.8	67.9	0.4	0.0
273.8	258.5	266.1	67.5	0.4	0.0
258.5	244.1	251.2	67.1	0.4	0.0
244.1	230.4	237.1	66.6	0.4	0.0
230.4	217.5	223.9	66.2	0.4	0.0
217.5	205.4	211.3	65.8	0.4	0.0
205.4	193.9	199.5	65.3	0.5	0.0
193.9	183.0	188.4	64.8	0.5	0.0
183.0	172.8	177.8	64.2	0.6	0.0
172.8	163.1	167.9	63.5	0.7	0.0
163.1	154.0	158.5	62.8	0.7	0.0
154.0	145.4	149.6	62.1	0.7	0.1
145.4	137.2	141.3	61.3	0.8	0.1
137.2	129.6	133.4	60.5	0.8	0.1

Sample ID: Sample 5
Operator: TN
Submitter: Materials Characterization Services
File: C:\...\REPORTED\1006520.SMP
Material/Liquid: Kaolin / 0.05% Sodium Metaphosphate (w/w)
Measurement Principle: X-Ray monitored gravity sedimentation
Calculation Method: Stokes sedimentation and Beer's law of extinction

Test Number: 2
Analyzed: 11/9/2010 2:52:33PM
Reported: 11/11/2010 7:59:05AM
Liquid Visc: 0.7239 mPa·s
Analysis Temp: 34.9 °C

Analysis Type: High Speed(Adj)
Run Time: 0:35 hrs:min
Sample Density: 2.600 g/cm³
Liquid Density: 0.9941 g/cm³
Mean Base/Full: 129 / 88 kCnts/s
Reynolds Number: 0.21

Comments: 100W. Sieved through #16, 30, 70, and 325.

Report by Size Class

High Diameter (µm)	Low Diameter (µm)	Average Diameter (µm)	Cumulative Mass Finer (Percent)	Mass Frequency (Percent)	Cum. Mass Standard Deviation (2 tests)
129.6	122.3	125.9	59.6	0.8	0.1
122.3	115.5	118.9	58.8	0.8	0.1
115.5	109.0	112.2	58.0	0.8	0.1
109.0	102.9	105.9	57.1	0.8	0.1
102.9	97.16	100.0	56.3	0.8	0.2
97.16	91.73	94.41	55.5	0.8	0.2
91.73	86.60	89.13	54.7	0.8	0.2
86.60	81.75	84.14	53.9	0.8	0.2
81.75	77.18	79.43	53.1	0.7	0.2
77.18	72.86	74.99	52.4	0.7	0.2
72.86	68.79	70.79	51.8	0.7	0.2
68.79	64.94	66.83	51.2	0.6	0.2
64.94	61.31	63.10	50.6	0.5	0.2
61.31	57.88	59.57	50.2	0.5	0.2
57.88	54.64	56.23	49.8	0.4	0.1
54.64	51.58	53.09	49.4	0.3	0.1
51.58	48.70	50.12	49.2	0.2	0.1
48.70	45.97	47.32	49.1	0.1	0.0
45.97	43.40	44.67	49.0	0.1	0.0
43.40	40.97	42.17	49.0	0.0	0.1
40.97	38.68	39.81	49.0	0.0	0.1
38.68	36.52	37.58	49.0	0.0	0.1
36.52	34.47	35.48	49.0	0.0	0.1
34.47	32.55	33.50	49.0	0.0	0.1
32.55	30.73	31.62	49.0	0.0	0.1
30.73	29.01	29.85	48.9	0.0	0.1
29.01	27.38	28.18	48.9	0.1	0.0
27.38	25.85	26.61	48.8	0.1	0.0
25.85	24.41	25.12	48.7	0.1	0.0
24.41	23.04	23.71	48.6	0.1	0.0
23.04	21.75	22.39	48.4	0.1	0.0
21.75	20.54	21.13	48.3	0.1	0.0
20.54	19.39	19.95	48.1	0.2	0.0
19.39	18.30	18.84	48.0	0.2	0.1
18.30	17.28	17.78	47.8	0.2	0.1
17.28	16.31	16.79	47.6	0.2	0.1

Sample ID: Sample 5
Operator: TN
Submitter: Materials Characterization Services
File: C:\...\REPORTED\1006520.SMP
Material/Liquid: Kaolin / 0.05% Sodium Metaphosphate (w/w)
Measurement Principle: X-Ray monitored gravity sedimentation
Calculation Method: Stokes sedimentation and Beer's law of extinction

Test Number: 2
Analyzed: 11/9/2010 2:52:33PM
Reported: 11/11/2010 7:59:05AM
Liquid Visc: 0.7239 mPa·s
Analysis Temp: 34.9 °C

Analysis Type: High Speed(Adj)
Run Time: 0:35 hrs:min
Sample Density: 2.600 g/cm³
Liquid Density: 0.9941 g/cm³
Mean Base/Full: 129 / 88 kCnts/s
Reynolds Number: 0.21

Comments: 100W. Sieved through #16, 30, 70, and 325.

Report by Size Class

High Diameter (µm)	Low Diameter (µm)	Average Diameter (µm)	Cumulative Mass Finer (Percent)	Mass Frequency (Percent)	Cum. Mass Standard Deviation (2 tests)
16.31	15.40	15.85	47.3	0.2	0.1
15.40	14.54	14.96	47.1	0.3	0.1
14.54	13.72	14.13	46.8	0.3	0.1
13.72	12.96	13.34	46.5	0.3	0.1
12.96	12.23	12.59	46.2	0.3	0.0
12.23	11.55	11.89	45.9	0.3	0.0
11.55	10.90	11.22	45.6	0.3	0.0
10.90	10.29	10.59	45.2	0.4	0.0
10.29	9.716	10.00	44.8	0.4	0.1
9.716	9.173	9.441	44.3	0.4	0.1
9.173	8.660	8.913	43.8	0.5	0.1
8.660	8.175	8.414	43.3	0.5	0.1
8.175	7.718	7.943	42.8	0.5	0.1
7.718	7.286	7.499	42.2	0.6	0.1
7.286	6.879	7.079	41.6	0.6	0.1
6.879	6.494	6.683	41.0	0.6	0.1
6.494	6.131	6.310	40.4	0.6	0.1
6.131	5.788	5.957	39.8	0.6	0.1
5.788	5.464	5.623	39.2	0.6	0.1
5.464	5.158	5.309	38.5	0.6	0.1
5.158	4.870	5.012	37.9	0.7	0.1
4.870	4.597	4.732	37.2	0.7	0.1
4.597	4.340	4.467	36.5	0.7	0.1
4.340	4.097	4.217	35.8	0.7	0.1
4.097	3.868	3.981	35.1	0.7	0.1
3.868	3.652	3.758	34.4	0.7	0.1
3.652	3.447	3.548	33.7	0.7	0.1
3.447	3.255	3.350	32.9	0.7	0.1
3.255	3.073	3.162	32.2	0.7	0.1
3.073	2.901	2.985	31.4	0.8	0.1
2.901	2.738	2.818	30.7	0.8	0.1
2.738	2.585	2.661	29.9	0.8	0.1
2.585	2.441	2.512	29.1	0.8	0.1
2.441	2.304	2.371	28.3	0.8	0.1
2.304	2.175	2.239	27.6	0.8	0.0
2.175	2.054	2.113	26.8	0.8	0.0

Sample ID: Sample 5
Operator: TN
Submitter: Materials Characterization Services
File: C:\...\REPORTED\1006520.SMP
Material/Liquid: Kaolin / 0.05% Sodium Metaphosphate (w/w)
Measurement Principle: X-Ray monitored gravity sedimentation
Calculation Method: Stokes sedimentation and Beer's law of extinction

Test Number: 2
Analyzed: 11/9/2010 2:52:33PM
Reported: 11/11/2010 7:59:05AM
Liquid Visc: 0.7239 mPa·s
Analysis Temp: 34.9 °C

Analysis Type: High Speed(Adj)
Run Time: 0:35 hrs:min
Sample Density: 2.600 g/cm³
Liquid Density: 0.9941 g/cm³
Mean Base/Full: 129 / 88 kCnts/s
Reynolds Number: 0.21

Comments: 100W. Sieved through #16, 30, 70, and 325.

Report by Size Class

High Diameter (µm)	Low Diameter (µm)	Average Diameter (µm)	Cumulative Mass Finer (Percent)	Mass Frequency (Percent)	Cum. Mass Standard Deviation (2 tests)
2.054	1.939	1.995	26.1	0.8	0.0
1.939	1.830	1.884	25.3	0.7	0.0
1.830	1.728	1.778	24.6	0.7	0.0
1.728	1.631	1.679	23.8	0.7	0.1
1.631	1.540	1.585	23.1	0.7	0.1
1.540	1.454	1.496	22.4	0.7	0.1
1.454	1.372	1.413	21.7	0.7	0.1
1.372	1.296	1.334	20.9	0.7	0.1
1.296	1.223	1.259	20.2	0.7	0.1
1.223	1.155	1.189	19.6	0.7	0.1
1.155	1.090	1.122	18.9	0.7	0.0
1.090	1.029	1.059	18.2	0.7	0.0
1.029	0.972	1.000	17.5	0.7	0.0
0.972	0.917	0.944	16.8	0.7	0.0
0.917	0.866	0.891	16.1	0.7	0.1
0.866	0.818	0.841	15.5	0.7	0.1
0.818	0.772	0.794	14.8	0.7	0.1
0.772	0.729	0.750	14.2	0.6	0.1
0.729	0.688	0.708	13.6	0.6	0.1
0.688	0.649	0.668	13.0	0.6	0.1
0.649	0.613	0.631	12.5	0.5	0.1
0.613	0.579	0.596	12.0	0.5	0.0
0.579	0.546	0.562	11.5	0.5	0.0
0.546	0.516	0.531	11.0	0.5	0.1
0.516	0.487	0.501	10.6	0.4	0.1
0.487	0.460	0.473	10.2	0.4	0.1
0.460	0.434	0.447	9.7	0.4	0.1
0.434	0.410	0.422	9.3	0.4	0.1
0.410	0.387	0.398	8.9	0.4	0.1
0.387	0.365	0.376	8.5	0.4	0.1
0.365	0.345	0.355	8.1	0.4	0.1
0.345	0.325	0.335	7.7	0.4	0.1
0.325	0.307	0.316	7.4	0.4	0.1
0.307	0.290	0.299	7.0	0.3	0.1
0.290	0.274	0.282	6.7	0.3	0.1
0.274	0.259	0.266	6.4	0.3	0.1

Sample ID: Sample 5
Operator: TN
Submitter: Materials Characterization Services
File: C:\...\REPORTED\1006520.SMP
Material/Liquid: Kaolin / 0.05% Sodium Metaphosphate (w/w)
Measurement Principle: X-Ray monitored gravity sedimentation
Calculation Method: Stokes sedimentation and Beer's law of extinction

Test Number: 2
Analyzed: 11/9/2010 2:52:33PM
Reported: 11/11/2010 7:59:05AM
Liquid Visc: 0.7239 mPa·s
Analysis Temp: 34.9 °C

Analysis Type: High Speed(Adj)
Run Time: 0:35 hrs:min
Sample Density: 2.600 g/cm³
Liquid Density: 0.9941 g/cm³
Mean Base/Full: 129 / 88 kCnts/s
Reynolds Number: 0.21

Comments: 100W. Sieved through #16, 30, 70, and 325.

Report by Size Class

High Diameter (µm)	Low Diameter (µm)	Average Diameter (µm)	Cumulative Mass Finer (Percent)	Mass Frequency (Percent)	Cum. Mass Standard Deviation (2 tests)
0.259	0.244	0.251	6.0	0.3	0.1
0.244	0.230	0.237	5.6	0.4	0.1
0.230	0.218	0.224	5.2	0.4	0.0
0.218	0.205	0.211	4.7	0.5	0.0
0.205	0.194	0.200	4.1	0.6	0.1
0.194	0.183	0.188	3.5	0.7	0.2

Sample ID: Sample 5
Operator: TN
Submitter: Materials Characterization Services
File: C:\...\REPORTED\1006520.SMP
Material/Liquid: Kaolin / 0.05% Sodium Metaphosphate (w/w)
Measurement Principle: X-Ray monitored gravity sedimentation
Calculation Method: Stokes sedimentation and Beer's law of extinction

Test Number: 2
Analyzed: 11/9/2010 2:52:33PM
Reported: 11/11/2010 7:59:05AM
Liquid Visc: 0.7239 mPa·s
Analysis Temp: 34.9 °C

Analysis Type: High Speed(Adj)
Run Time: 0:35 hrs:min
Sample Density: 2.600 g/cm³
Liquid Density: 0.9941 g/cm³
Mean Base/Full: 129 / 88 kCnts/s
Reynolds Number: 0.21

Comments: 100W. Sieved through #16, 30, 70, and 325.

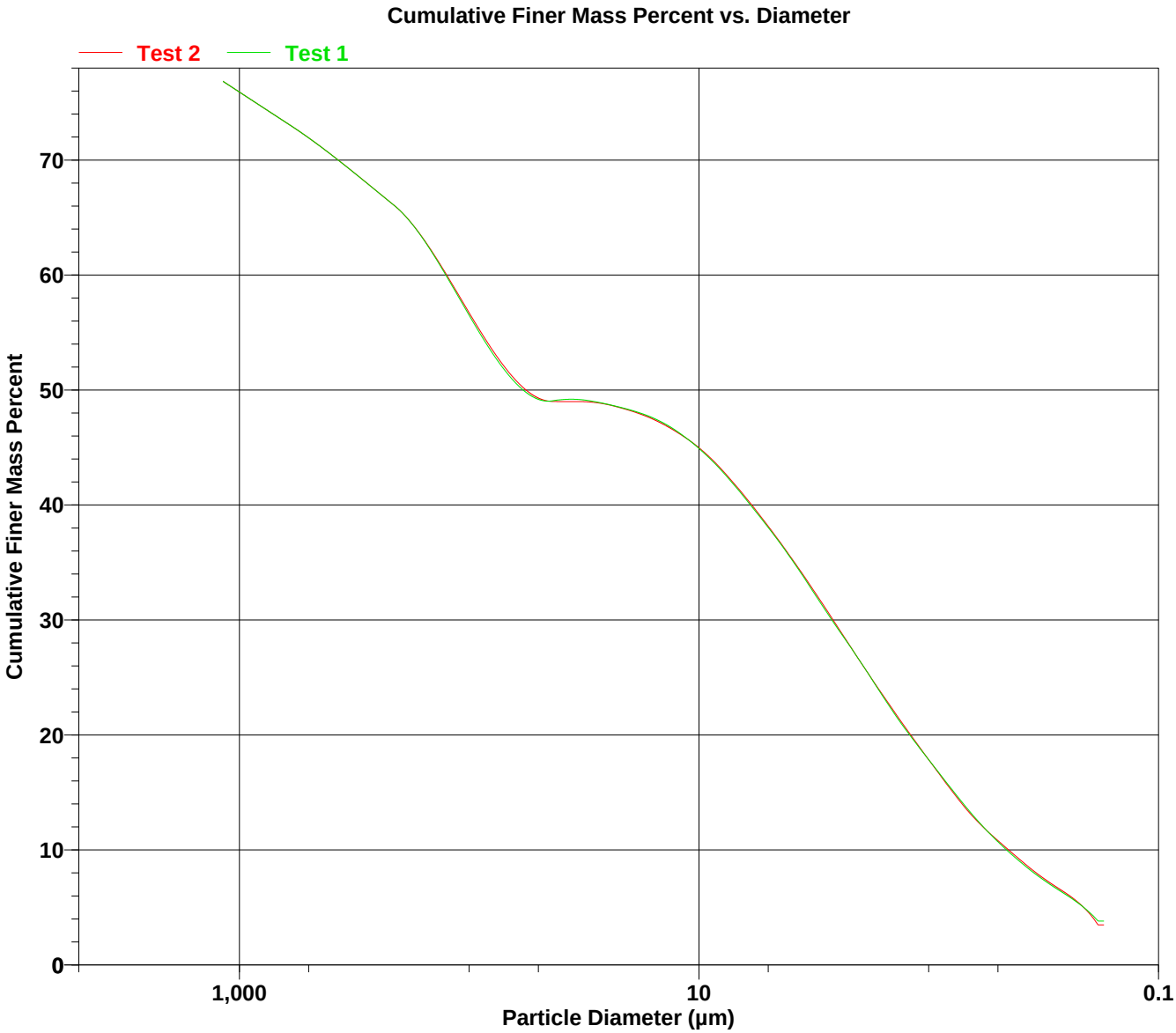

Sample ID:	Sample 5
Operator:	TN
Submitter:	Materials Characterization Services
File:	C:\...\REPORTED\1006520.SMP
Material/Liquid:	Kaolin / 0.05% Sodium Metaphosphate (w/w)
Measurement Principle:	X-Ray monitored gravity sedimentation
Calculation Method:	Stokes sedimentation and Beer's law of extinction

Test Number:	2	Analysis Type:	High Speed(Adj)
Analyzed:	11/9/2010 2:52:33PM	Run Time:	0:35 hrs:min
Reported:	11/11/2010 7:59:05AM	Sample Density:	2.600 g/cm³
Liquid Visc:	0.7239 mPa·s	Liquid Density:	0.9941 g/cm³
Analysis Temp:	34.9 °C	Mean Base/Full:	129 / 88 kCnts/s
		Reynolds Number:	0.21

Comments: 100W. Sieved through #16, 30, 70, and 325.

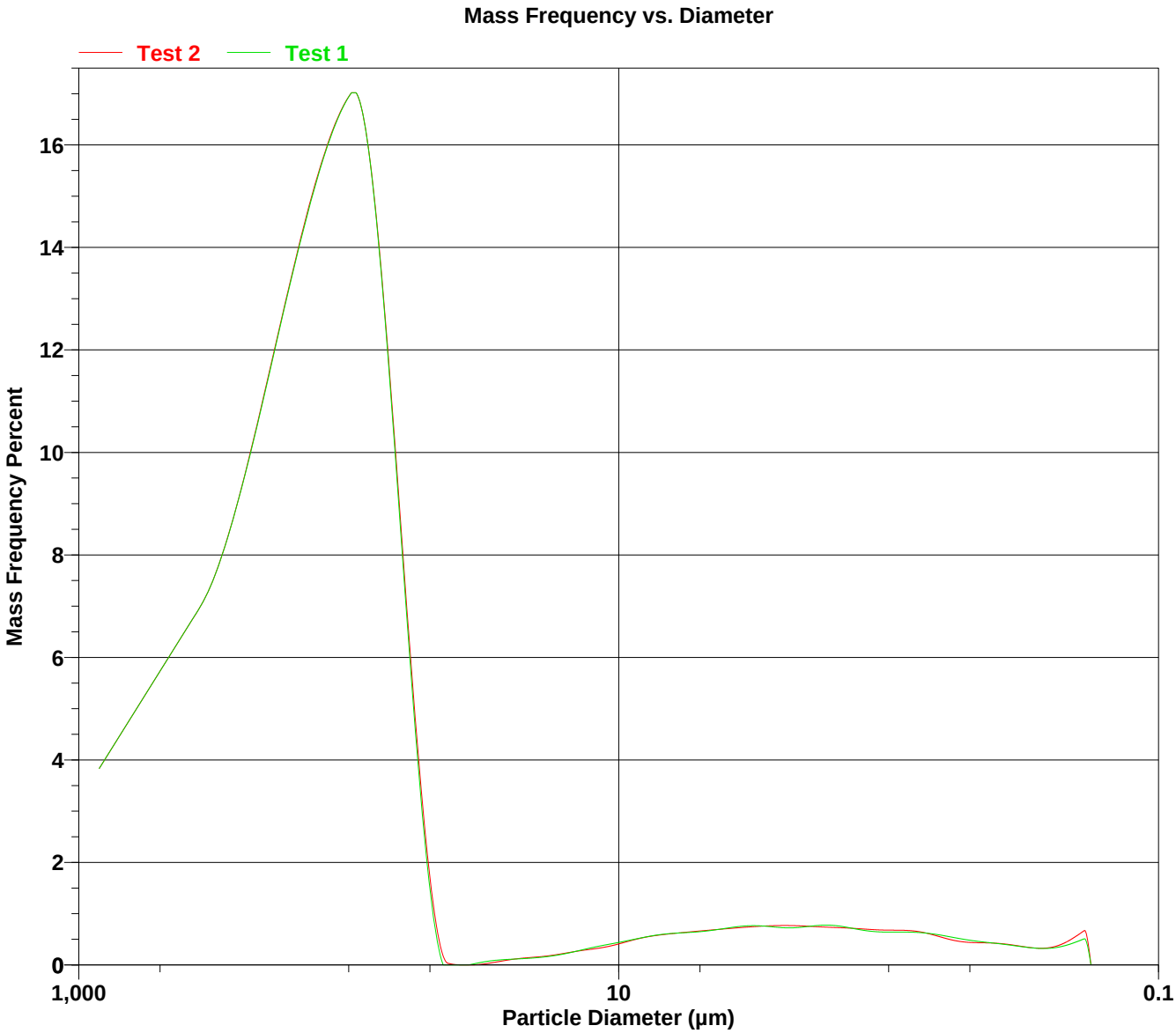

Sample: Sample 6
Operator: TN
Submitter: Materials Characterization Services
File: C:\...\11NOV\1006521.SMP

Test Number: 2
Analyzed: 11/10/2010 3:39:31PM
Reported: 11/10/2010 4:00:21PM
Background: 11/10/2010 9:28:03AM

Model: (1.450, 0.1000000), 1.331
Material: SiO2 / Water
Background: Water RI 1.331
Smoothing: Medium

Combined Report

Incremental Volume Percent vs. Particle Diameter Graph

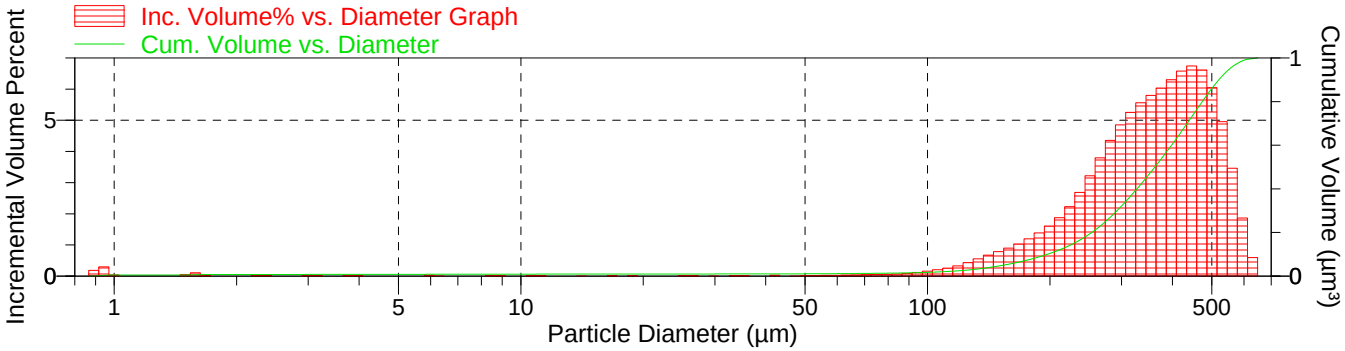

Summary Report

Analysis Conditions

FlowRate: 16.6 l/m
Circulation time: Not Used
Ultrasonic intensity: Not Used
Ultrasonic time: Not Used

Sample

Sample Concentration: 0.38501 %
Obscuration: 38.3 %

Weighted Statistics (Volume Distribution)

		Std Dev of 2			Std Dev of 2
Mean	359.929	0.294	Mode	446.480	0.000
Median	362.173	3.330			

Selected Percentiles by Volume

Percent Finer	Diameter (µm)
90.0	520.303
50.0	362.173
10.0	197.051

Sample: Sample 6
Operator: TN
Submitter: Materials Characterization Services
File: C:\...\11NOV\1006521.SMP

Test Number: 2
Analyzed: 11/10/2010 3:39:31PM
Reported: 11/10/2010 4:00:21PM
Background: 11/10/2010 9:28:03AM

Model: (1.450, 0.1000000), 1.331
Material: SiO2 / Water
Background: Water RI 1.331
Smoothing: Medium

Report by Size Class

High Particle Diameter (µm)	Low Particle Diameter (µm)	Average Particle Diameter (µm)	Cumulative Volume Finer Percent	Incremental Volume Percent	Cumulative Volume Percent (StdDev)
1029.201	1029.201	1029.201	100.0	0.0	0.0
1029.201	971.628	1000.000	100.0	0.0	0.0
971.628	917.276	944.061	100.0	0.0	0.0
917.276	865.964	891.251	100.0	0.0	0.0
865.964	817.523	841.395	100.0	0.0	0.0
817.523	771.792	794.328	100.0	0.0	0.0
771.792	728.618	749.894	100.0	0.0	0.0
728.618	687.860	707.946	100.0	0.0	0.0
687.860	649.382	668.344	100.0	0.0	0.0
649.382	613.056	630.957	99.4	0.6	0.1
613.056	578.762	595.662	97.6	1.9	0.3
578.762	546.387	562.341	94.1	3.4	0.6
546.387	515.822	530.884	89.2	4.9	0.7
515.822	486.968	501.187	83.1	6.0	0.6
486.968	459.727	473.151	76.5	6.6	0.3
459.727	434.010	446.684	69.8	6.7	0.0
434.010	409.732	421.697	63.2	6.6	0.4
409.732	386.812	398.107	56.9	6.3	0.7
386.812	365.174	375.837	50.8	6.0	0.9
365.174	344.747	354.813	45.0	5.8	1.0
344.747	325.462	334.965	39.5	5.6	0.9
325.462	307.256	316.228	34.2	5.3	0.7
307.256	290.068	298.538	29.4	4.9	0.5
290.068	273.842	281.838	25.0	4.4	0.2
273.842	258.523	266.073	21.2	3.8	0.0
258.523	244.062	251.189	18.0	3.2	0.1
244.062	230.409	237.137	15.3	2.7	0.2
230.409	217.520	223.872	13.1	2.2	0.1
217.520	205.353	211.349	11.2	1.9	0.0
205.353	193.865	199.526	9.6	1.6	0.1
193.865	183.021	188.365	8.2	1.4	0.1
183.021	172.783	177.828	7.0	1.2	0.1
172.783	163.117	167.880	6.0	1.0	0.1
163.117	153.993	158.489	5.1	0.9	0.1
153.993	145.378	149.624	4.3	0.8	0.0
145.378	137.246	141.254	3.6	0.7	0.0
137.246	129.569	133.352	3.0	0.6	0.1
129.569	122.321	125.893	2.6	0.4	0.1
122.321	115.478	118.850	2.3	0.3	0.1
115.478	109.018	112.202	2.0	0.3	0.1
109.018	102.920	105.925	1.8	0.2	0.1
102.920	97.163	100.000	1.7	0.2	0.1
97.163	91.728	94.406	1.5	0.1	0.1
91.728	86.596	89.125	1.5	0.1	0.0

Sample: Sample 6
Operator: TN
Submitter: Materials Characterization Services
File: C:\...\11NOV\1006521.SMP

Test Number: 2
Analyzed: 11/10/2010 3:39:31PM
Reported: 11/10/2010 4:00:21PM
Background: 11/10/2010 9:28:03AM

Model: (1.450, 0.1000000), 1.331
Material: SiO2 / Water
Background: Water RI 1.331
Smoothing: Medium

Report by Size Class

High Particle Diameter (µm)	Low Particle Diameter (µm)	Average Particle Diameter (µm)	Cumulative Volume Finer Percent	Incremental Volume Percent	Cumulative Volume Percent (StdDev)
86.596	81.752	84.140	1.4	0.1	0.0
81.752	77.179	79.433	1.3	0.1	0.0
77.179	72.862	74.989	1.3	0.1	0.0
72.862	68.786	70.795	1.2	0.0	0.0
68.786	64.938	66.834	1.2	0.0	0.0
64.938	61.306	63.096	1.1	0.0	0.0
61.306	57.876	59.566	1.1	0.0	0.0
57.876	54.639	56.234	1.1	0.0	0.0
54.639	51.582	53.088	1.1	0.0	0.0
51.582	48.697	50.119	1.1	0.0	0.0
48.697	45.973	47.315	1.0	0.0	0.0
45.973	43.401	44.668	1.0	0.0	0.0
43.401	40.973	42.170	1.0	0.0	0.0
40.973	38.681	39.811	1.0	0.0	0.0
38.681	36.517	37.584	1.0	0.0	0.0
36.517	34.475	35.481	1.0	0.0	0.0
34.475	32.546	33.497	1.0	0.0	0.0
32.546	30.726	31.623	1.0	0.0	0.0
30.726	29.007	29.854	1.0	0.0	0.0
29.007	27.384	28.184	1.0	0.0	0.0
27.384	25.852	26.607	1.0	0.0	0.0
25.852	24.406	25.119	1.0	0.0	0.0
24.406	23.041	23.714	1.0	0.0	0.0
23.041	21.752	22.387	1.0	0.0	0.0
21.752	20.535	21.135	1.0	0.0	0.0
20.535	19.387	19.953	1.0	0.0	0.0
19.387	18.302	18.836	0.9	0.0	0.0
18.302	17.278	17.783	0.9	0.0	0.0
17.278	16.312	16.788	0.9	0.0	0.0
16.312	15.399	15.849	0.9	0.0	0.0
15.399	14.538	14.962	0.9	0.0	0.0
14.538	13.725	14.125	0.9	0.0	0.0
13.725	12.957	13.335	0.9	0.0	0.0
12.957	12.232	12.589	0.9	0.0	0.0
12.232	11.548	11.885	0.9	0.0	0.0
11.548	10.902	11.220	0.9	0.0	0.0
10.902	10.292	10.593	0.9	0.0	0.0
10.292	9.716	10.000	0.9	0.0	0.0
9.716	9.173	9.441	0.9	0.0	0.0
9.173	8.660	8.913	0.9	0.0	0.0
8.660	8.175	8.414	0.9	0.0	0.0
8.175	7.718	7.943	0.9	0.0	0.0
7.718	7.286	7.499	0.9	0.0	0.0
7.286	6.879	7.079	0.9	0.0	0.0

Sample: Sample 6
Operator: TN
Submitter: Materials Characterization Services
File: C:\...\11NOV\1006521.SMP

Test Number: 2
Analyzed: 11/10/2010 3:39:31PM
Reported: 11/10/2010 4:00:21PM
Background: 11/10/2010 9:28:03AM

Model: (1.450, 0.1000000), 1.331
Material: SiO2 / Water
Background: Water RI 1.331
Smoothing: Medium

Report by Size Class

High Particle Diameter (µm)	Low Particle Diameter (µm)	Average Particle Diameter (µm)	Cumulative Volume Finer Percent	Incremental Volume Percent	Cumulative Volume Percent (StdDev)
6.879	6.494	6.683	0.9	0.0	0.0
6.494	6.131	6.310	0.9	0.0	0.0
6.131	5.788	5.957	0.8	0.0	0.0
5.788	5.464	5.623	0.8	0.0	0.0
5.464	5.158	5.309	0.8	0.0	0.0
5.158	4.870	5.012	0.8	0.0	0.0
4.870	4.597	4.732	0.8	0.0	0.0
4.597	4.340	4.467	0.8	0.0	0.0
4.340	4.097	4.217	0.8	0.0	0.0
4.097	3.868	3.981	0.8	0.0	0.0
3.868	3.652	3.758	0.8	0.0	0.0
3.652	3.447	3.548	0.8	0.0	0.0
3.447	3.255	3.350	0.8	0.0	0.0
3.255	3.073	3.162	0.8	0.0	0.0
3.073	2.901	2.985	0.8	0.0	0.0
2.901	2.738	2.818	0.8	0.0	0.0
2.738	2.585	2.661	0.8	0.0	0.0
2.585	2.441	2.512	0.8	0.0	0.0
2.441	2.304	2.371	0.7	0.0	0.0
2.304	2.175	2.239	0.7	0.0	0.0
2.175	2.054	2.113	0.7	0.0	0.0
2.054	1.939	1.995	0.7	0.0	0.0
1.939	1.830	1.884	0.7	0.0	0.0
1.830	1.728	1.778	0.7	0.0	0.0
1.728	1.631	1.679	0.7	0.0	0.0
1.631	1.540	1.585	0.6	0.1	0.0
1.540	1.454	1.496	0.5	0.1	0.0
1.454	1.372	1.413	0.5	0.0	0.0
1.372	1.296	1.334	0.5	0.0	0.0
1.296	1.223	1.259	0.5	0.0	0.0
1.223	1.155	1.189	0.5	0.0	0.0
1.155	1.090	1.122	0.5	0.0	0.0
1.090	1.029	1.059	0.5	0.0	0.0
1.029	0.972	1.000	0.5	0.0	0.0
0.972	0.917	0.944	0.2	0.3	0.1
0.917	0.866	0.891	0.0	0.2	0.0
0.866	0.818	0.841	0.0	0.0	0.0
0.818	0.772	0.794	0.0	0.0	0.0
0.772	0.729	0.750	0.0	0.0	0.0
0.729	0.688	0.708	0.0	0.0	0.0
0.688	0.649	0.668	0.0	0.0	0.0
0.649	0.613	0.631	0.0	0.0	0.0
0.613	0.579	0.596	0.0	0.0	0.0
0.579	0.546	0.562	0.0	0.0	0.0

Sample: Sample 6
Operator: TN
Submitter: Materials Characterization Services
File: C:\...\11NOV\1006521.SMP

Test Number: 2
Analyzed: 11/10/2010 3:39:31PM
Reported: 11/10/2010 4:00:21PM
Background: 11/10/2010 9:28:03AM

Model: (1.450, 0.1000000), 1.331
Material: SiO2 / Water
Background: Water RI 1.331
Smoothing: Medium

Report by Size Class

High Particle Diameter (µm)	Low Particle Diameter (µm)	Average Particle Diameter (µm)	Cumulative Volume Finer Percent	Incremental Volume Percent	Cumulative Volume Percent (StdDev)
0.546	0.516	0.531	0.0	0.0	0.0
0.516	0.487	0.501	0.0	0.0	0.0
0.487	0.460	0.473	0.0	0.0	0.0
0.460	0.434	0.447	0.0	0.0	0.0
0.434	0.410	0.422	0.0	0.0	0.0
0.410	0.387	0.398	0.0	0.0	0.0
0.387	0.365	0.376	0.0	0.0	0.0
0.365	0.345	0.355	0.0	0.0	0.0
0.345	0.325	0.335	0.0	0.0	0.0
0.325	0.307	0.316	0.0	0.0	0.0
0.307	0.290	0.299	0.0	0.0	0.0
0.290	0.274	0.282	0.0	0.0	0.0
0.274	0.259	0.266	0.0	0.0	0.0
0.259	0.244	0.251	0.0	0.0	0.0
0.244	0.230	0.237	0.0	0.0	0.0
0.230	0.218	0.224	0.0	0.0	0.0
0.218	0.205	0.211	0.0	0.0	0.0
0.205	0.194	0.200	0.0	0.0	0.0
0.194	0.183	0.188	0.0	0.0	0.0
0.183	0.173	0.178	0.0	0.0	0.0
0.173	0.163	0.168	0.0	0.0	0.0
0.163	0.154	0.158	0.0	0.0	0.0
0.154	0.145	0.150	0.0	0.0	0.0
0.145	0.137	0.141	0.0	0.0	0.0
0.137	0.130	0.133	0.0	0.0	0.0
0.130	0.122	0.126	0.0	0.0	0.0
0.122	0.115	0.119	0.0	0.0	0.0
0.115	0.109	0.112	0.0	0.0	0.0
0.109	0.103	0.106	0.0	0.0	0.0
0.103	0.097	0.100	0.0	0.0	0.0

Sample: Sample 6
Operator: TN
Submitter: Materials Characterization Services
File: C:\...\11NOV\1006521.SMP

Test Number: 2
Analyzed: 11/10/2010 3:39:31PM
Reported: 11/10/2010 4:00:21PM
Background: 11/10/2010 9:28:03AM

Model: (1.450, 0.1000000), 1.331
Material: SiO2 / Water
Background: Water RI 1.331
Smoothing: Medium

Cumulative Volume Finer Percent vs. Particle Diameter Graph

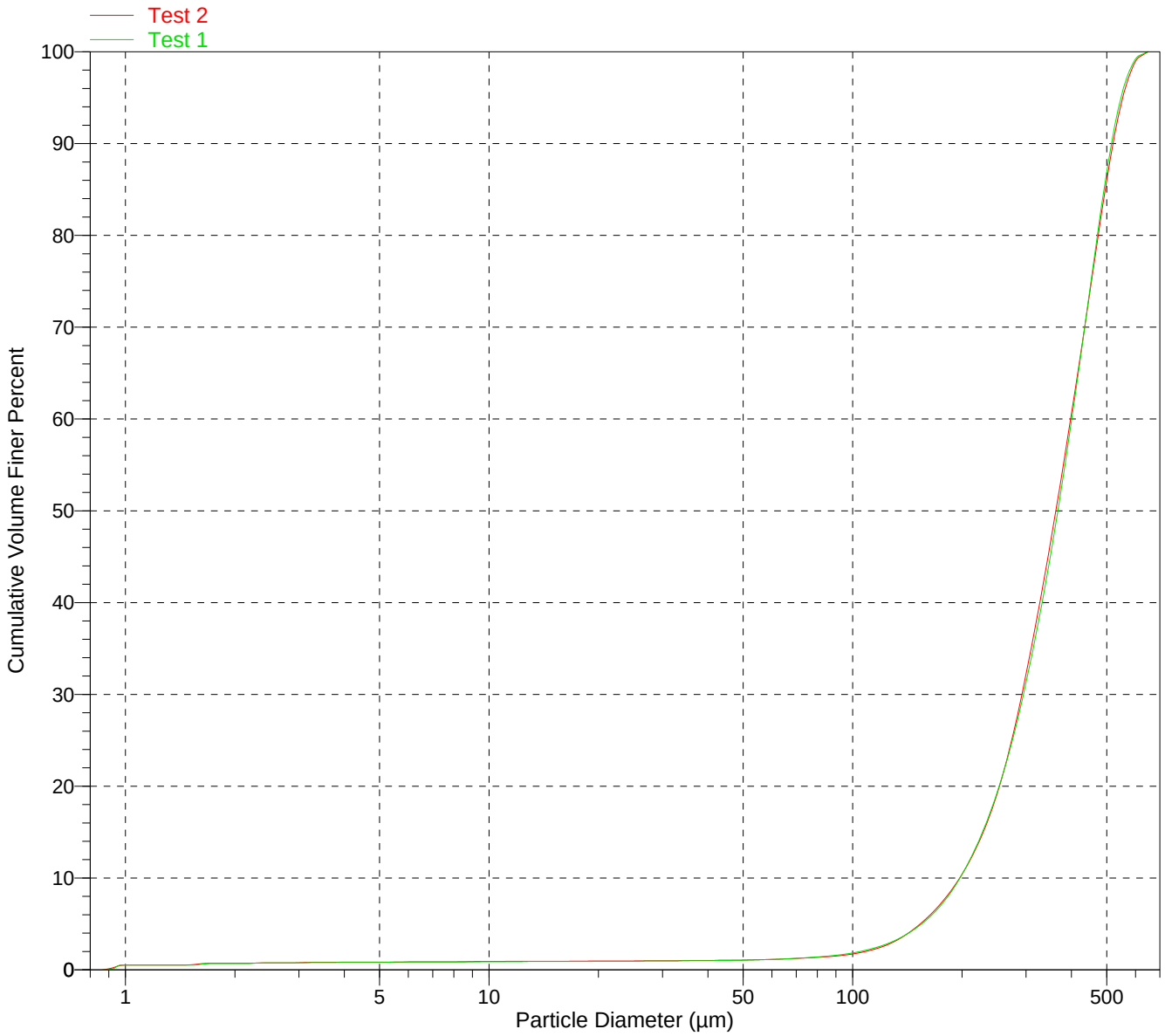

Sample: Sample 6
Operator: TN
Submitter: Materials Characterization Services
File: C:\...\11NOV\1006521.SMP

Test Number: 2
Analyzed: 11/10/2010 3:39:31PM
Reported: 11/10/2010 4:00:21PM
Background: 11/10/2010 9:28:03AM

Model: (1.450, 0.1000000), 1.331
Material: SiO2 / Water
Background: Water RI 1.331
Smoothing: Medium

Incremental Volume Percent vs. Particle Diameter Graph

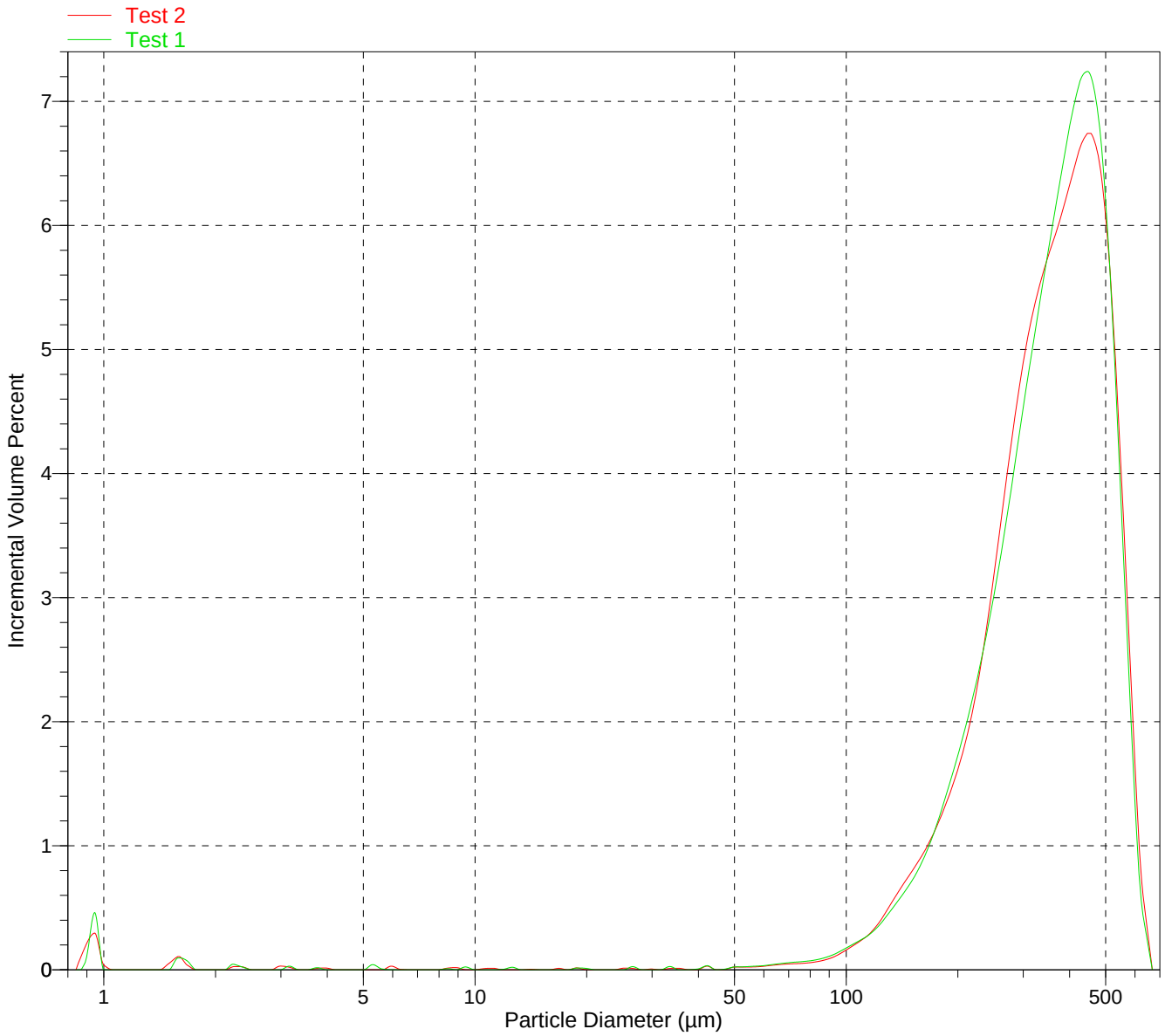

Sample: Sample 6
Operator: TN
Submitter: Materials Characterization Services
File: C:\...\11NOV\1006521.SMP

Test Number: 2
Analyzed: 11/10/2010 3:39:31PM
Reported: 11/10/2010 4:00:21PM
Background: 11/10/2010 9:28:03AM

Model: (1.450, 0.1000000), 1.331
Material: SiO2 / Water
Background: Water RI 1.331
Smoothing: Medium

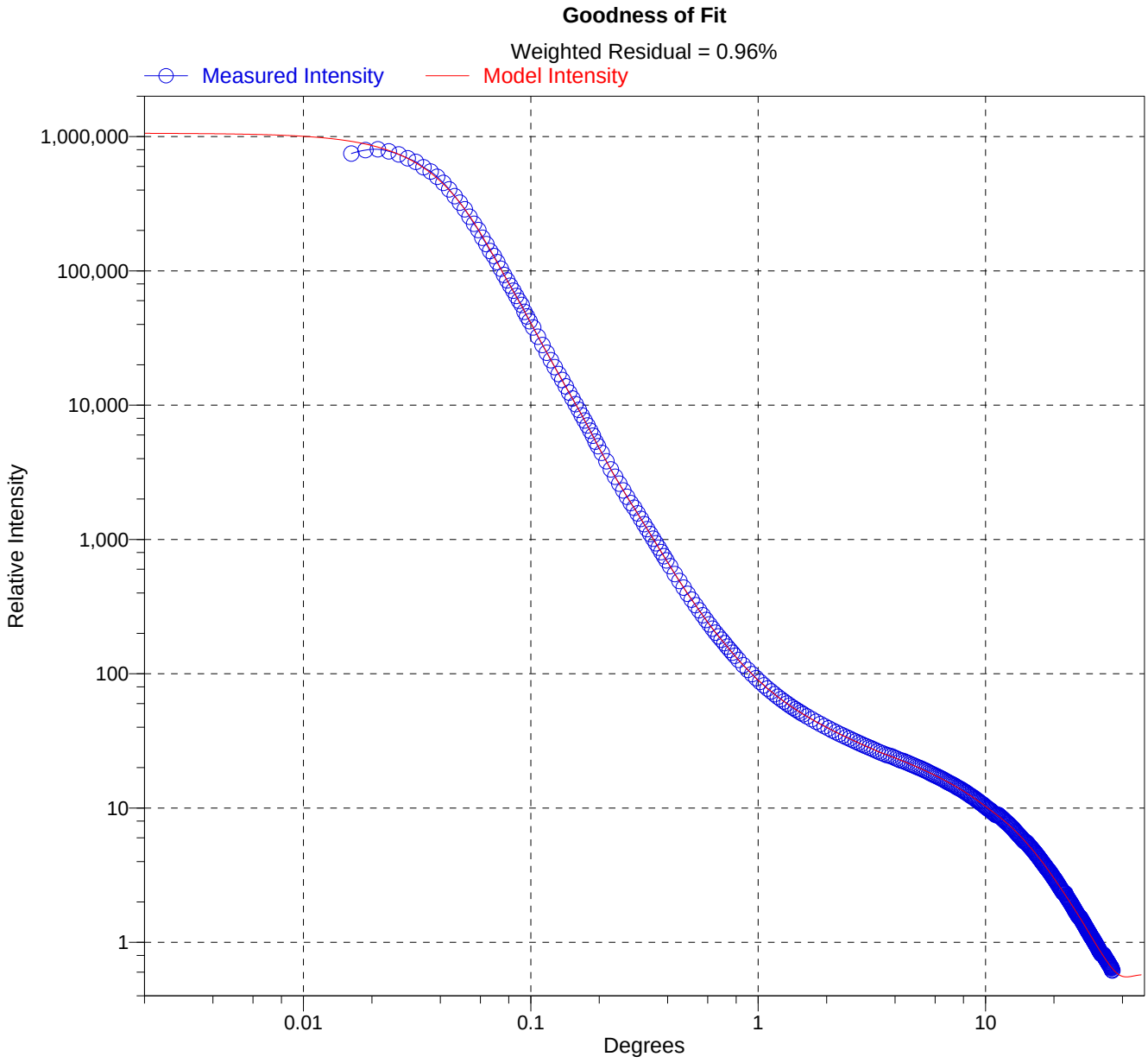

BECKMAN COULTER™

LS Particle Size Analyzer

22 Sep 2011 11:02

Beckman Coulter LS 13 320

Volume Statistics (Arithmetic)

Calculations from 0.375 µm to 2000 µm

Volume:	100%		
Mean:	97.04 µm	S.D.:	9.156 µm
Median:	96.70 µm	Variance:	83.82 µm^2
Mean/Median ratio:	1.004	C.V.:	9.43%
Mode:	96.49 µm		
Specific Surf. Area:	623.8 cm^2/mL		

d_{10}: 85.12 µm d_{50}: 96.70 µm d_{90}: 109.7 µm

<10%	<50%	<90%
85.12 µm	96.70 µm	109.7 µm

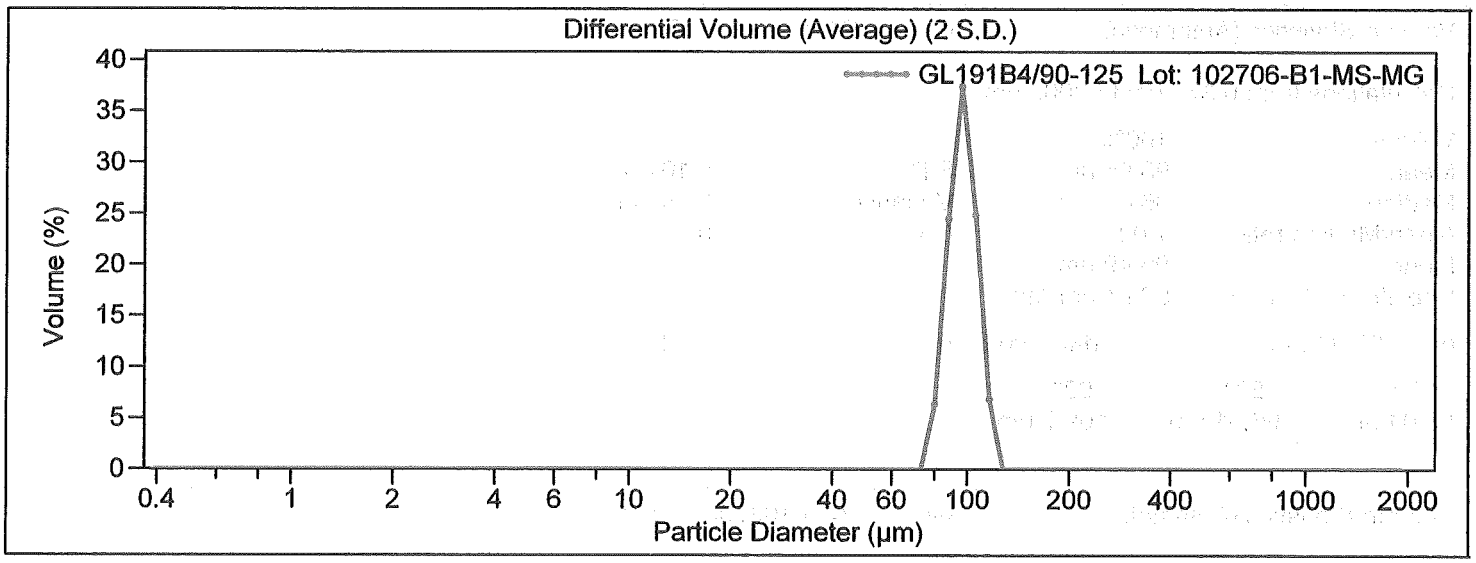

Sample ID:	L102706-B1-MS-MG
Comment 1:	sonicated 10min H2O
Optical model:	glass.rf780d

LS Particle Size Analyzer

22 Sep 2011 11:02

Beckman Coulter LS 13 320

Sample ID:	L102706-B1-MS-MG
Comment 1:	sonicated 10min H2O
Optical model:	glass.rf780d

(Untitled)

Channel Diameter (Lower) µm	Diff. Volume %	-2 S.D. Diff. Volume %	+2 S.D. Diff. Volume %
0.375	0	0	0
0.412	0	0	0
0.452	0	0	0
0.496	0	0	0
0.545	0	0	0
0.598	0	0	0
0.657	0	0	0
0.721	0	0	0
0.791	0	0	0
0.869	0	0	0
0.954	0	0	0
1.047	0	0	0
1.149	0	0	0
1.261	0	0	0
1.385	0	0	0
1.520	0	0	0
1.669	0	0	0
1.832	0	0	0
2.011	0	0	0
2.208	0	0	0
2.423	0	0	0
2.660	0	0	0
2.920	0	0	0
3.206	0	0	0
3.519	0	0	0
3.863	0	0	0
4.241	0	0	0
4.656	0	0	0
5.111	0	0	0
5.610	0	0	0
6.159	0	0	0
6.761	0	0	0
7.422	0	0	0
8.148	0	0	0
8.944	0	0	0
9.819	0	0	0
10.78	0	0	0
11.83	0	0	0
12.99	0	0	0
14.26	0	0	0
15.65	0	0	0
17.18	0	0	0
18.86	0	0	0
20.71	0	0	0
22.73	0	0	0
24.95	0	0	0
27.39	0	0	0
30.07	0	0	0
33.01	0	0	0
36.24	0	0	0
39.78	0	0	0
43.67	0	0	0
47.94	0	0	0
52.63	0	0	0
57.77	0	0	0
63.42	0	0	0
69.62	0	0	0
76.43	6.36	5.01	7.71
83.90	24.5	22.9	26.1
92.10	37.5	36.4	38.5
101.1	24.8	23.3	26.4
111.0	6.83	6.43	7.23
121.8	0	0	0
133.8	0	0	0
146.8	0	0	0
161.2	0	0	0
176.9	0	0	0
194.2	0	0	0
213.2	0	0	0
234.1	0	0	0
256.9	0	0	0
282.1	0	0	0
309.6	0	0	0
339.9	0	0	0
373.1	0	0	0
409.6	0	0	0
449.7	0	0	0
493.6	0	0	0
541.9	0	0	0
594.9	0	0	0
653.0	0	0	0
716.9	0	0	0
787.0	0	0	0
863.9	0	0	0
948.3	0	0	0
1041	0	0	0
1143	0	0	0
1255	0	0	0
1377	0	0	0
1512	0	0	0
1660	0	0	0
1822	0	0	0
2000			

BECKMAN COULTER™

LS Particle Size Analyzer

22 Sep 2011 10:56

Beckman Coulter LS 13 320

Volume Statistics (Arithmetic)

Calculations from 0.375 µm to 2000 µm

Volume:	100%		
Mean:	10.80 µm	S.D.:	7.770 µm
Median:	9.341 µm	Variance:	60.37 µm^2
Mean/Median ratio:	1.156	C.V.:	71.9%
Mode:	11.29 µm		
Specific Surf. Area:	12528 cm^2/mL		

d_{10}: 2.134 µm d_{50}: 9.341 µm d_{90}: 21.34 µm

<10%	<50%	<90%
2.134 µm	9.341 µm	21.34 µm

File ID:	GL0191B4
Sample ID:	L0400R1403-1-2
Comment 1:	sonicated 10min H2O
Optical model:	glass.rf780d

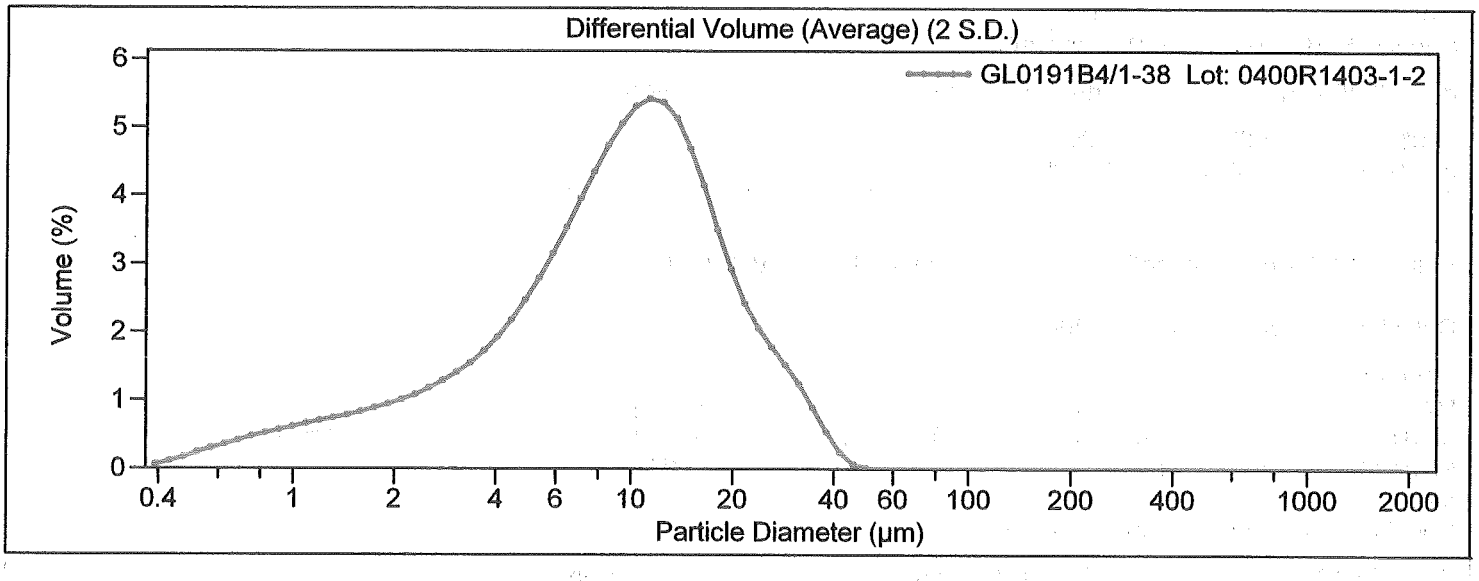

LS Particle Size Analyzer

22 Sep 2011 10:56

Beckman Coulter LS 13 320

File ID:	GL0191B4
Sample ID:	L0400R1403-1-2
Comment 1:	sonicated 10min H2O
Optical model:	glass.rf780d

(Untitled)

Channel Diameter (Lower) µm	Diff. Volume %	-2 S.D. Diff. Volume %	+2 S.D. Diff. Volume %
0.375	0.062	0.050	0.073
0.412	0.11	0.090	0.13
0.452	0.17	0.13	0.20
0.496	0.24	0.19	0.28
0.545	0.30	0.24	0.36
0.598	0.36	0.29	0.42
0.657	0.41	0.33	0.49
0.721	0.47	0.38	0.56
0.791	0.52	0.42	0.63
0.869	0.57	0.45	0.68
0.954	0.61	0.48	0.74
1.047	0.66	0.51	0.81
1.149	0.70	0.54	0.86
1.261	0.74	0.56	0.92
1.385	0.78	0.59	0.98
1.520	0.83	0.62	1.05
1.669	0.89	0.65	1.13
1.832	0.95	0.68	1.21
2.011	1.01	0.72	1.29
2.208	1.08	0.77	1.39
2.423	1.18	0.84	1.52
2.660	1.29	0.92	1.65
2.920	1.41	1.02	1.80
3.206	1.54	1.13	1.96
3.519	1.72	1.28	2.16
3.863	1.93	1.46	2.40
4.241	2.18	1.69	2.68
4.656	2.47	1.96	2.98
5.111	2.79	2.26	3.32
5.610	3.15	2.61	3.70
6.159	3.54	2.99	4.09
6.761	3.96	3.42	4.49
7.422	4.35	3.84	4.85
8.148	4.74	4.29	5.19
8.944	5.06	4.69	5.42
9.819	5.31	5.08	5.55
10.78	5.42	5.33	5.51
11.83	5.36	5.19	5.53
12.99	5.13	4.73	5.53
14.26	4.69	4.05	5.32
15.65	4.15	3.30	4.99
17.18	3.50	2.54	4.47
18.86	2.92	1.92	3.93
20.71	2.42	1.47	3.38
22.73	2.05	1.16	2.94
24.95	1.78	0.94	2.62
27.39	1.52	0.71	2.32
30.07	1.24	0.46	2.01
33.01	0.90	0.21	1.58
36.24	0.54	0.025	1.05
39.78	0.24	0	0.52
43.67	0.065	0	0.16
47.94	0.0090	0	0.024
52.63	0.00032	0	0.00099

Channel Diameter (Lower) µm	Diff. Volume %	-2 S.D. Diff. Volume %	+2 S.D. Diff. Volume %
57.77	0	0	0
63.42	0	0	0
69.62	0	0	0
76.43	0	0	0
83.90	0	0	0
92.10	0	0	0
101.1	0	0	0
111.0	0	0	0
121.8	0	0	0
133.8	0	0	0
146.8	0	0	0
161.2	0	0	0
176.9	0	0	0
194.2	0	0	0
213.2	0	0	0
234.1	0	0	0
256.9	0	0	0
282.1	0	0	0
309.6	0	0	0
339.9	0	0	0
373.1	0	0	0
409.6	0	0	0
449.7	0	0	0
493.6	0	0	0
541.9	0	0	0
594.9	0	0	0
653.0	0	0	0
716.9	0	0	0
787.0	0	0	0
863.9	0	0	0
948.3	0	0	0
1041	0	0	0
1143	0	0	0
1255	0	0	0
1377	0	0	0
1512	0	0	0
1660	0	0	0
1822	0	0	0
2000			

LS Particle Size Analyzer

22 Sep 2011 11:00

Beckman Coulter LS 13 320

Volume Statistics (Arithmetic)

Calculations from 0.375 µm to 2000 µm

Volume:	100%		
Mean:	54.61 µm	S.D.:	4.212 µm
Median:	54.71 µm	Variance:	17.74 µm^2
Mean/Median ratio:	0.998	C.V.:	7.71%
Mode:	55.14 µm		
Specific Surf. Area:	1105 cm^2/mL		

d_{10}: 48.77 µm d_{50}: 54.71 µm d_{90}: 61.05 µm

<10%	<50%	<90%
48.77 µm	54.71 µm	61.05 µm

File ID:	GL0191B4
Comment 1:	sonicated 10min H2O
Optical model:	glass.rf780d

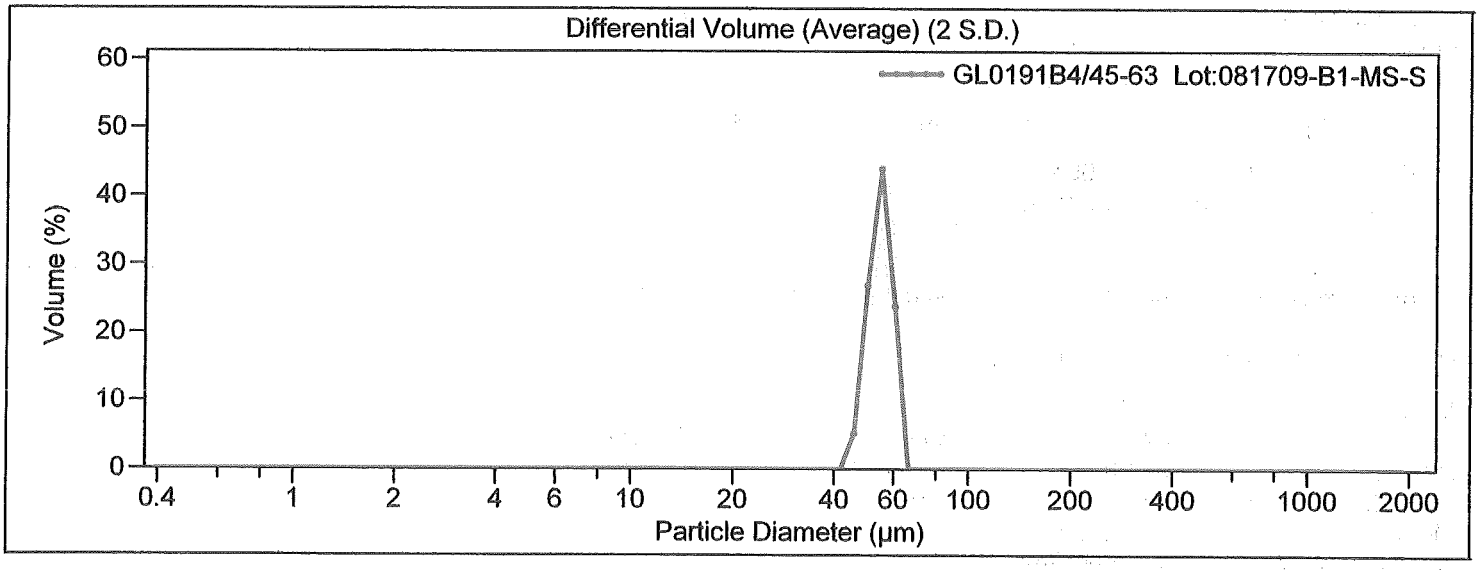

LS Particle Size Analyzer

22 Sep 2011 11:00

Beckman Coulter LS 13 320

File ID:	GL0191B4
Comment 1:	sonicated 10min H2O
Optical model:	glass.rf780d

(Untitled)

Channel Diameter (Lower) µm	Diff. Volume %	-2 S.D. Diff. Volume %	+2 S.D. Diff. Volume %
0.375	0	0	0
0.412	0	0	0
0.452	0	0	0
0.496	0	0	0
0.545	0	0	0
0.598	0	0	0
0.657	0	0	0
0.721	0	0	0
0.791	0	0	0
0.869	0	0	0
0.954	0	0	0
1.047	0	0	0
1.149	0	0	0
1.261	0	0	0
1.385	0	0	0
1.520	0	0	0
1.669	0	0	0
1.832	0	0	0
2.011	0	0	0
2.208	0	0	0
2.423	0	0	0
2.660	0	0	0
2.920	0	0	0
3.206	0	0	0
3.519	0	0	0
3.863	0	0	0
4.241	0	0	0
4.656	0	0	0
5.111	0	0	0
5.610	0	0	0
6.159	0	0	0
6.761	0	0	0
7.422	0	0	0
8.148	0	0	0
8.944	0	0	0
9.819	0	0	0
10.78	0	0	0
11.83	0	0	0
12.99	0	0	0
14.26	0	0	0
15.65	0	0	0
17.18	0	0	0
18.86	0	0	0
20.71	0	0	0
22.73	0	0	0
24.95	0	0	0
27.39	0	0	0
30.07	0	0	0
33.01	0	0	0
36.24	0	0	0
39.78	0	0	0
43.67	5.24	0	14.4
47.94	26.9	19.8	34.0
52.63	44.0	35.6	52.5
57.77	23.8	16.0	31.6
63.42	0	0	0
69.62	0	0	0
76.43	0	0	0
83.90	0	0	0
92.10	0	0	0
101.1	0	0	0
111.0	0	0	0
121.8	0	0	0
133.8	0	0	0
146.8	0	0	0
161.2	0	0	0
176.9	0	0	0
194.2	0	0	0
213.2	0	0	0
234.1	0	0	0
256.9	0	0	0
282.1	0	0	0
309.6	0	0	0
339.9	0	0	0
373.1	0	0	0
409.6	0	0	0
449.7	0	0	0
493.6	0	0	0
541.9	0	0	0
594.9	0	0	0
653.0	0	0	0
716.9	0	0	0
787.0	0	0	0
863.9	0	0	0
948.3	0	0	0
1041	0	0	0
1143	0	0	0
1255	0	0	0
1377	0	0	0
1512	0	0	0
1660	0	0	0
1822	0	0	0
2000			

Appendix C

Estimation of Full-Scale Similarity Parameters

The similarity parameters studied in this thesis were estimated for full-scale helicopters to examine the differences in the similarity parameters between those at the laboratory scale and those at full-scale. Groundwash velocity data for a CH-54 hovering near the ground [68] was used to calculate the characteristic flow velocity. The particle characteristics (i.e., mean diameter and mass density) were measured using a soil sample from Yuma Proving Ground (YPG) that was analyzed in the same manner as the other sediment samples. Table C.1 shows the values of the dimensional variables (i.e., rotor radius, particle diameter, etc.) that were used for this analysis. From these values, the nondimensional similarity parameters for the full-scale problem were calculated, which are given in Table C.2.

R (m)	D_p (m)	U_{char} (ms^{-1})	U_F (ms^{-1})	u_{*_t} (ms^{-1})	ρ_s (kg m^{-3})	ρ (kg m^{-3})
10.97	6.82×10^{-6}	18.98	0.0036	0.679	2,650	1.225

Table C.1: Values of the dimensional variables at full-scale for a CH-54.

D_p/R	ρ_p/ρ	U_{char}/U_F	$U_{\text{char}}/\sqrt{(\rho_s/\rho - 1)gD_p}$	U_{char}/u_{*_t}
6.22×10^{-7}	2,250	5,313	48.93	27.94

Table C.2: Values of similarity parameters at full-scale for a CH-54.

Compared to the values at the laboratory scale given in Table 3.2, some of the similarity parameters are very different, in some cases by an order or orders of magnitude. In this case, the value of D_p/R at the full-scale for this helicopter is two orders of magnitude smaller than was used at the laboratory-scale. The value of U_{char}/u_{*_t} is about 1.5 times greater than the largest value obtained at the laboratory-scale, meaning that the flow velocities are more likely to be above the threshold required for particle mobilization. The value of ρ_s/ρ is similar to the values obtained at the laboratory scale because the densities of the fluid and sediment were similar between the different scales. U_{char}/U_F is larger than most of the values at the laboratory-scale, but smaller than the values for the AZTD 0–5 μm and kaolinite samples. The Froude number at full-scale is almost twice as high as the most mobile particles in the laboratory-scale experiments, meaning that the gravity forces are less significant here. The differences in the values of the similarity parameters will obviously have quantitative differences in sediment entrainment and uplift between scales.

Bibliography

[1] Lee, T. E., Leishman, J. G., and Ramasamy, M., "Fluid Dynamics of Interacting Blade Tip Vortices With a Ground Plane," *Journal of the American Helicopter Society*, Vol. 55, No. 2, April 2010, pp. 1–16.

[2] Sydney, A., Baharani, A., and Leishman, J. G., "Understanding Brownout using Near-Wall Dual-Phase Flow Measurements," 67th Annual Forum Proceedings of the American Helicopter Society, Virginia Beach, VA, May 3–5, 2011.

[3] Mapes, P., Kent, R., and Wood, R., "DoD Helicopter Mishaps FY85-05: Findings and Recommendations," U.S. Air Force, 2008.

[4] "NTSB Accident Briefs: LAX01LA283, LAX01LA304, LAX04LA285, SEA05CA173, LAX08LA198," National Transportation Safety Board, 2001, 2004, 2005, 2009.

[5] Thomas, W., Hong, S. C., Yu, C. J., Rosenzweig, E. L., "Enhanced Erosion Protection For Rotor Blades," 65th Annual Forum Proceedings of the American Helicopter Society, Grapevine, TX, May 27–29, 2009.

[6] Jansen, C., Wennemers, A., and Groen, E., "FlyTact: A Tactile Display Improves a Helicopter Pilots Landing Performance in Degraded Visual Environments," *Haptics: Perception, Devices and Scenarios*, Vol. 502, No. 4, 2008, pp. 867–875.

[7] "Sandblaster 2 Support of See-Through Technologies for Particulate Brownout," Task 1 Technical Report, Sponsored by Defense Advanced Research Projects

Agency (DOD) Strategic Technology Office, Issued by U.S. Army Aviation and Missile Command under Contract No. W31P4Q-07-C-0215, MRI Project No. 110565, October 31, 2007.

[8] "Sandblaster 2 Support of See-Through Technologies for Particulate Brownout,," Task 5 Final Technical Report, Sponsored by Defense Advanced Research Projects Agency (DOD) Strategic Technology Office, Issued by U.S. Army Aviation and Missile Command under Contract No. W31P4Q-07-C-0215, MRI Project No. 110565, October 31, 2007.

[9] Harrington, W. W., Braddom, S. R., Savage, J. C., Szoboszlay, Z. P., McKinley, R. A., and Burns, H. N., "3D-LZ Brownout Landing Solution," Proceedings of the 66^{th} Annual Forum of the American Helicopter Society International, Phoenix, AZ, May 11–13 2010.

[10] Haehnel, R. B., Moulton, M. A., Wenren, W., and Steinhoff, J., "A Model to Simulate Rotorcraft-Induced Brownout," American Helicopter Society 64th Annual Forum Proceedings, Montréal, Canada, April 29–May 1, 2008.

[11] Syal, M., Govindarajan, B., and Leishman, J. G., "Mesoscale Sediment Tracking Methodology to Analyze Brownout Cloud Developments," 66th Annual Forum of the American Helicopter Society, Phoenix, AZ, May 10–13, 2010.

[12] Syal, M., and Leishman, J. G., "Comparisons of Predicted Brownout Dust Clouds with Photogrammetry Measurements," 67th Annual Forum Proceedings of the American Helicopter Society, Virginia Beach, VA, May 3–5, 2011.

[13] Thomas, S., Lakshminarayan, V. K., Kalra, T. S., and Baeder, J. D., "Eulerian-Lagrangian Analysis of Cloud Evolution using CFD Coupled with a Sediment Tracking Algorithm," 67th Annual Forum Proceedings of the American Helicopter Society, Virginia Beach, VA, May 3–5, 2011.

[14] D'Andrea, A., "Numerical Analysis of Unsteady Vortical Flows Generated by a Rotorcraft Operating on Ground: A First Assessment of Helicopter Brownout," American Helicopter Society 65th Annual Forum Proceedings, Grapevine, Texas, May 27–29 2009.

[15] Morales, F. Naqvi, I., Squires, K. D., and Piomelli, U., "Euler-Lagrange Simulations of Particle Interactions with Coherent Vortices in Turbulent Boundary Layers," *Bulletin of the American Physical Society*, Vol. 54, No. 19, 2009.

[16] Ryerson, C. C., Haehnel, R. B., Koenig, G. G., and Moulton, M. A., "Visibility Enhancement in Rotorwash Clouds," Paper AIAA-2005-263, 43rd AIAA Aerospace Sciences Meeting and Exhibit, Reno, Nevada, January 10–13, 2005.

[17] Greeley, R., and Iversen, J. D., *Wind as a Geological Process on Earth, Mars, Venus and Titan,* Cambridge University Press, New York, NY, 1985.

[18] Leishman, J. G., "Challenges in Understanding the Fluid Dynamics of Brownout: Review and Update," Proceedings of the AHS International Meeting on Advanced Rotorcraft Technology and Safety Operations, Omiya, Japan, Novermber 1–3 2010.

[19] Milluzzo, J., and Leishman, J. G., "Assessment of Rotorcraft Brownout Severity in Terms of Rotor Design Parameters," *Journal of the American Helicopter Society*, Vol. 55, No. 3, DOI: 10.4050/JAHS.55.032000, October 2010.

[20] Fradenburgh, E. A., "The Helicopter and the Ground Effect Machine," *Journal of the American Helicopter Society*, Vol. 5, No. 4, 1960, pp. 26–28.

[21] Knight, M., and Hefner, R. A., "Analysis of Ground Effect on the Lifting Airscrew," NACA TN 835, 1941.

[22] Hayden, J.S., "The Effect of the Ground on Helicopter Hovering Power Required," American Helicopter Society 32th Annual National V/STOL Forum Proceedings, Washington D.C., May 10–12, 1976.

[23] Curtiss, H. C., Sun, M., Putman, W. F., and Hanker, E. J., "Rotor Aerodynamics in Ground Effect at Low Advance Ratios," *Journal of the American Helicopter Society*, Vol. 29, No. 1, 1984, pp. 48–55.

[24] Light, J. S., and Norman, T., "Tip Vortex Geometry of a Hovering Helicopter Rotor in Ground Effect," American Helicopter Society 45th Annual Forum Proceedings, Boston, MA, May 22–24, 1989.

[25] Prouty, R. W., "Ground Effect and the Helicopter," AIAA Paper 85-4034, AIAA/AHS/ASEE Aircraft Design Systems and Operations Meeting, Colorado Springs, CO, October 14–16, 1985.

[26] Ramasamy, M., Johnson, B., and Leishman, J. G., "Understanding the Aerodynamic Efficiency of a Hovering Micro-Rotor," *Journal of American Helicopter Society*, Vol. 53, No. 4, October, 2008, pp. 412–428.

[27] Milluzzo, J., Sydney, A., Rauleder, J., and Leishman, J. G., "In-Ground-Effect Aerodynamics of Rotors with Different Blade Tips," 66th Annual Forum Proceedings of the American Helicopter Society, Phoenix, AZ, May 10–13, 2010.

[28] Johnson, B., Sydney, A., and Leishman, J. G., "Investigation of Sediment Entrainment Using Dual-Phase, High-Speed Particle Image Velocimetry," *Journal of the American Helicopter Society*, Vol. 55, No. 4, 2010, p. 042003.

[29] Ramasamy, M., and Leishman, J. G., "Interdependence of Diffusion and Straining of Helicopter Blade Tip Vortices," *Journal of Aircraft*, Vol. 41, No. 5, 2004, pp. 1014–1024.

[30] Ananthan S. and Leishman, J. G., "Role of Filament Strain in the Free-Vortex Modeling of Rotor Wakes," *Journal of the American Helicopter Society*, Vol. 49, No. 2, 2004, pp. 176–191.

[31] Bagnold, R. A., *The Physics of Blown Sand and Desert Dunes,* Dover Publications, Inc., Mineola, NY, 1941.

[32] Buffington, J. M., "The Legend of A.F. Shields.," *Journal of Hydraulic Engineering*, Vol. 125, No. 4, 1999, p. 376.

[33] Shields, A., *Application of similarity principles and turbulence research to bed-load movement,* PhD thesis, Hydrodynamics Laboratory Publ. No. 167, W. P. Ott, and J.

C. van Uchelen,, trans., U.S. Dept. of Agr., Soil Conservation Service Cooperative Laboratory, California Institute of Technology, Pasadena, Calif., 1936.

[34] Zhixian, C., Pender, G., and Jian, M., "Explicit Formulation of the Shields Diagram for Incipient Motion of Sediment.," *Journal of Hydraulic Engineering*, Vol. 132, No. 10, 2006, pp. 1097 – 1099.

[35] Shao, Y., Raupach, M. R., and Findlater, P. A., "Effect of Saltation Bombardment on the Entrainment of Dust by the Wind," *Journal of Geophysical Research*, Vol. 98, No. D7, "1993", pp. 12,719–12,726.

[36] Nathan, N. D., and Green, R. B., "Measurements of a rotor flow in ground effect and visualisation of the brown-out phenomenon," Proceedings of the 64th Annual Forum of the American Helicopter Society International, Montreal, Canada, April 29–May 1 2008.

[37] Wong, O. D., and Tanner, P. E., "Photogrammetric Measurements of an EH-60L Brownout Cloud," 66th Annual Forum of the American Helicopter Society, Phoenix, AZ, May 10–13, 2010.

[38] Tanner, P., "Photogrammetric Characterization of a Brownout Cloud," Proceedings of the 67th Annual Forum of the American Helicopter Society International, Virginia Beach, VA, May 3–5 2011.

[39] Anderson, J. D., *Fundamentals of Aerodynamics,* McGraw-Hill, New York, NY, 2007.

[40] Leishman, J. G., *Principles of Helicopter Aerodynamics*, 2nd ed., Cambridge University Press, New York, NY, 2006.

[41] Iversen, J. D. and Greeley, R. and Marshall, J. R. and Pollack, J. B., "Aeolian saltation threshold: the effect of density ratio," *Sedimentology*, Vol. 34, No. 4, 1987, pp. 699–706.

[42] CONCEPT ENGINEERING LTD, *Concept ViCount 180 Smoke System,* 7 Woodlands Business Park, Woodlands Park Avenue, Maidenhead, Berks SL6 3UA, UK, May 2009.

[43] R. P. Dring, "Sizing Criteria for Laser Anemometry Particles," *Journal of Fluids Engineering*, Vol. 104, No. 1, 1982, pp. 15–17.

[44] TSI INCORPORATED, *Laser Diagnostics: Seed Particles for LDV and PIV,* 500 Cardigan Road, Shoreview, MN 55126 U.S.A., 2006.

[45] Leishman, J. G., "Seed Particle Dynamics in Tip Vortex Flows," *Journal of Aircraft*, Vol. 33, No. 4, 1996, pp. 823–825.

[46] Willert, C. E., and Gharib, M., "Digital Particle Image Velocimetry," *Experiments in Fluid*, Vol. 10, No. 4, January 1991, pp. 181–193.

[47] Scarano, F., "Iterative Image Deformations Methods in PIV," *Measurement Science and Technology*, Vol. 13, 2002, pp. R1–R19.

[48] Raffel, M., Willert, C., Wereley, S., Kompenhans, J., *Particle Image Velocimetry*, 2nd ed., Springer Publishing Company, New York, NY, 2007.

[49] Keane, R. D., and Adrian R. J., "Theory of Cross-Correlation Analysis of PIV Images," *Measurement Science and Technology*, Vol. 49, No. 3, July 1991, pp. 191–215.

[50] Westerweel, J., "Fundamentals of Digital Particle Image Velocimetry," *Measurement Science and Technology*, Vol. 8, No. 12, December 1997, pp. 1379–1392.

[51] Adrian, R. J., "Particle-Imaging Techniques For Experimental Fluid Mechanics," *Annual Review of Fluid Mechanics*, Vol. 23, 1991, pp. 261–304.

[52] Keane, R. D., and Adrian R. J., "Optimization of Particle Image Velocimeters," *Measurement Science and Technology*, Vol. 1, No. 11, November 1991, pp. 1202–1215.

[53] TROPEA, C., YARIN, A. L., AND FOSS, J. F.,, Ed. *Springer Handbook of Experimental Fluid Mechanics* Springer, 2007.

[54] Huang, H., Dabiri, D., and Gharib, M., "On Errors of Digital Particle Image Velocimetry," *Measurement Science and Technology*, Vol. 8, No. 12, December 1991, pp. 1427–1440.

[55] Bhagwat, M. J., and Leishman, J. G., "Stability Analysis of Helicopter Rotor Wakes in Axial Flight," *Journal of the American Helicopter Society*, Vol. 45, No. 3, 2000, pp. 165–178.

[56] Martin, P. B., and Leishman, J. G., and Pugliese, G. J., and Anderson, S. L., *Stereoscopic PIV measurements in the wake of a hovering rotor* American Helicopter Society, Inc., 2000, p. 402420.

[57] Webb, Paul A., "The SediGraph Method of Particle Sizing," Micromeritics Instrument Corporation, January 8, 2004.

[58] Webb, Paul A., "Technical Workshop Series: Introduction to the Latest ANSI/ISO Standard for Laser Particle Size Analysis," Micromeritics Instrument Corporation, January, 2000.

[59] Ferguson, R. I., and Church, M., "A Simple Universal Equation for Grain Settling Velocity," *Journal of Sedimentary Research*, Vol. 74, No. 6, November 2004, pp. 933–937.

[60] Aguirre-Pe, J., Olivero, M. L., and Moncada A. T., "Particle Densimetric Froude Number for Estimating Sediment Transport," *Journal of Hydraulic Engineering*, Vol. 129, No. 6, June 1, 2003, pp. 428–437.

[61] Shao, Y., and Hua, L., "A Simple Expression for Wind Erosion Threshold Friction Velocity," *Journal of Geophysical Research*, Vol. 105, No. D17, September 16, 2000, pp. 22437–22443.

[62] Eckelmann, H., "The Structure of the Viscous Sublayer and the Adjacent Wall Region in a Turbulent Channel Flow," *Journal of Fluid Mechanics*, Vol. 65, No. 03, 1974, pp. 439–459.

[63] Towers D.P. and Towers C.E. and Buckberry C.H. and Reeves M., "A Colour PIV System Employing Fluorescent Particles for Two-Phase Flow Measurements," *Measurement Science and Technology*, Vol. 10, No. 9, 1999, pp. 824–830.

[64] Kiger, K. T., and Pan, C., "PIV Technique for the Simultaneous Measurement of Dilute Two-Phase Flows," *Journal of Fluids Engineering*, Vol. 122, No. 4, 2000, pp. 811–818.

[65] Techet, A.H. and McDonald, A.K., "High Speed PIV of Breaking Waves on Both Sides of the Air-Water Interface," 6th International Symposium on Particle Image Velocimetry, Pasadena, California, USA, September 21–23 2005.

[66] Wulff, D. L., "PIV Measurements in Pumps," Design and Analysis of High Speed Pumps, TU Braunschweig Institut fr Strmungsmaschinen Langer Kamp 6 D-38106 Braunschweig, Germany, 2006.

[67] Moore, D. M., and Reynolds, R. C., *X-Ray Diffraction and the Identification and Analysis of Clay Minerals*, Vol. ISBN:0.19. Oxford University Press, 1997.

[68] Leese, G. W., and Knight, J. T., Jr., "Helicopter Downwash Data," US Army Engineer Waterways Experiment Station, Soils and Pavement Laboratory, Vicksburg, Mississippi, June 1974.